Inaugural dissertation

for

obtaining the doctoral degree

of the

Combined Faculty of Mathematics, Engineering and Natural Sciences

of the

Ruprecht - Karls - University

Heidelberg

Presented by

M.Sc. Marcel Johannes Catharinus Piepers

born in: Swalmen, The Netherlands

Oral examination: 17 November 2025

Feeling the force: SOSEKI proteins at the interface of mechanics and the cell cycle

Referees: Prof. Dr. Alexis Maizel

Prof. Dr. Karin Schumacher

Abstract

Multicellular development requires coordination of polarity, growth, and division both within individual cells and between neighboring cells. In plants, where cells are immobile and interconnected by cell walls, this cross-scale coordination is critical. Yet, the mechanisms that link cellular processes to multicellular organization remain poorly understood.

The recently discovered plant-specific SOSEKI proteins provide robust 'global' polarity markers and are a promising new tool to investigate how global polarity is formed. In most contexts, their localization reflects a higher-order 'global' polarity field, whereas in the post-embryonic lateral root they instead reflect an organ-autonomous polarity field. Using fluorescent SOSEKI reporters, I investigated how this global polarity field transforms into an organ-autonomous field during lateral root organogenesis. I found that SOSEKI polarity is not globally fixed, but instead exhibits features of a local, mechano-sensitive polarity field. Indeed, mechanical perturbations and analysis of root mechanics showed that SOSEKI localization is responsive to mechanical cues, dissipating in mechanically stressed environments and accumulating in the mechanically heterogeneous environments. Complementary analyses in mutants and chemically treated plants further revealed that intercellular interfaces are critical for stable SOSEKI polarity, implicating the cell wall as a conduit for polarity signals.

Furthermore, I show that SOSEKI5, one of the essential family members, has dynamic cell-cycle-linked expression, peaking before division and declining just prior to cytokinesis. To circumvent the lethality of complete SOSEKI loss-of-function, collaborators generated a higher-order mutant combining loss-of-function with knockdown. I found that this mutant exhibited reduced regenerative divisions during wound healing. Together with collaborative data, these results implicate SOSEKI5 in the punctual execution of cell division. These findings establish SOSEKIs as mechano-sensitive proteins that may link multicellular mechanics to the cell cycle.

In addition to these functional and conceptual insights, this work takes steps towards plant optogenetics by piloting a strategy for cell-level control of gene expression, and it introduces GreenBraid, a GreenGate-based molecular cloning tool for efficient transgene stacking.

Zusammenfassung

Die Entwicklung vielzelliger Organismen erfordert eine Koordination von Polarität, Wachstum und Teilung sowohl innerhalb einzelner Zellen als auch zwischen benachbarten Zellen. Bei Pflanzen, deren Zellen unbeweglich und durch Zellwände miteinander verbunden sind, ist diese Koordination über Maßstabsebenen hinweg besonders entscheidend. Dennoch sind die Mechanismen, die zelluläre Prozesse mit der Organisation des Gesamtgewebes verknüpfen, bislang nur unzureichend verstanden.

Die kürzlich entdeckten, pflanzenspezifischen SOSEKI-Proteine dienen als robuste Polaritätsmarker: In den meisten Kontexten spiegelt ihre Lokalisation ein übergeordnetes „globales“ Polaritätsfeld im Pflanzenkörper wider, während sie in der postembryonalen Seitenwurzel stattdessen ein organautonomes Polaritätsfeld anzeigen. Mithilfe fluoreszierender SOSEKI-Reporters habe ich untersucht, wie sich dieses globale Polaritätsfeld während der Organogenese der Seitenwurzel in ein organautonomes Feld umwandelt. Ich stellte fest, dass die SOSEKI-Polarität nicht global fixiert ist, sondern Merkmale eines lokalen, mechanosensitiven Polaritätsfeldes aufweist. Tatsächlich zeigten mechanische Störungen und die Analyse der Wurzelmechanik, dass die SOSEKI-Lokalisation auf mechanische Signale reagiert: Sie zerfällt unter Stress und akkumuliert in mechanisch heterogenen Umgebungen. Ergänzende Analysen an Mutanten und chemisch behandelten Pflanzen ergaben außerdem, dass interzelluläre Grenzflächen für eine stabile SOSEKI-Polarität unerlässlich sind, was die Zellwand als Vermittler von Polaritätssignalen nahelegt.

Darüber hinaus zeigt SOSEKI5, eines der wesentlichsten Familienmitglieder, eine dynamische, mit dem Zellzyklus verknüpfte Expression, die kurz vor der Teilung ihren Höhepunkt erreicht und unmittelbar vor der Cytokinese wieder abnimmt. Um die Letalität eines vollständigen SOSEKI-Verlustes zu umgehen, generierten Kollaborationspartner eine höherstufige Mutante, die Verlustfunktion mit Knockdown kombiniert. Ich konnte zeigen, dass diese Mutante während der Wundheilung eine verringerte regenerative Teilungsaktivität aufweist. Zusammen mit kollaborativen Daten deuten diese Ergebnisse darauf hin, dass SOSEKI5 eine Rolle bei der präzisen Durchführung von Zellteilungen spielt.

Insgesamt etablieren diese Befunde SOSEKIs als mechanosensitive Proteine, die mechanische Signale mit der Zellzyklusregulation verknüpfen könnten, und liefern damit Einblicke in die Frage, wie mehrzellige Mechanik den Zellzyklus beeinflussen kann.

Neben diesen funktionellen und konzeptionellen Erkenntnissen leistet diese Arbeit Beiträge zur pflanzlichen Optogenetik, indem sie eine Strategie zur zellulären Kontrolle der Genexpression pilotiert, und sie stellt mit GreenBraid ein auf GreenGate basierendes molekulares Klonierungssystem für effizientes Stapeln von Transgenen vor.

Contributions

This work was written independently, and all sources consulted have been acknowledged. The text was proofread with the assistance of colleagues and digital tools, including ChatGPT and Overleaf. All suggestions were carefully reviewed and selectively incorporated to improve clarity and grammar.

Other than the author and the supervisor, the following people contributed to this work:

- **Neva Bölke**
  - Creation of the pXPP:SOK1:Gamillus plant transformation vector and the GreenGate entry vector with the SOSEKI2 coding sequence.

- **Kathrin Distel**
  - Creation of the pre-assembled GreenBraid fluorescent markers (pUBQ10::PiP1;4:fluorescent protein and pUBQ10::H2B:fluorescent protein).
  - Oryzalin treatment of plants expressing a SOSEKI marker.
  - Plant staining of oryzalin-treated plants and of the AURORA KINASE double mutant.

- **Laura Schütz**
  - Preliminary investigations into whether SOSEKIs respond to mechanical cues in the developmental context where the endodermis does not accomodate for lateral root emergence.

- **Anika Seppelt**
  - Construction of optogenetic components in plasmids.

- **Babette Knoblauch**
  - Testing optimal light conditions for induction of optogenetic gene expression.

- **Dr. Jazmín Reyes-Hernández**
  - Assistance with experimental setup for multi-photon imaging of genomic SOSEKI markers.
  - Experimental setup and completion of the molecular cloning of inducible SOSEKI knockdown constructs.
  - Preparation of plants for ablation experiments in the root apical meristem, to observe genomic and ectopic SOSEKI5 expression post-ablation using light sheet microscopy.
  - Major contribution to the collaborative work mentioned in Chapter 4.

Publication

The GreenBraid toolkit mentioned in **Annex 2** has been published: Piepers M, Erbstein K, Reyes-Hernandez J, Song C, Tessi T, et al. (2023). GreenGate 2.0: Backwards compatible addons for assembly of complex transcriptional units and their stacking with GreenGate. *PLOS ONE*, 18(9): e0290097. https://doi.org/10.1371/journal.pone.0290097

Publication strategy

Most of **Chapter I** and perhaps parts of **Chapter II and III** will be included in a manuscript on the development of post-embryonic growth axes in *Arabidopsis*, for which I will be first author.

Parts of **Chapter II and IV** will be included in a manuscript that addresses the function of SOSEKI proteins, for which I will be a contributing author.

Contents

List of Figures

List of Tables

List of Movies

Click here to download all movies

List of Abbreviations

Agrobacterium *Agrobacterium tumefaciens*. 115

Arabidopsis *Arabidopsis thaliana*. 6

E.coli *Escherichia coli*. 127

N. benthamiana *Nicotiana benthamiana*. 98

S. pombe *Schizosaccharomyces pombe*. 83

BASL BREAKING OF ASYMMETRY IN THE STOMATAL LINEAGE. 8

BDP Big Data Processor. 138

BOR1 Boron Transporter 1. 8

BP band pass. 137

Col-0 Columbia-0. 120

DAG days after germination. 121

DEX dexamethasone. 46

EL222 erythrobacter litoralis 222. 98

FP fluorescent protein. 17

G2 gap 2 phase. 78

gSOK::YFP genomic SOK:yellow fluorescent protein. 14

HU hydroxy urea. 89

iaaM indoleacetic acid tryptophan monooxygenase. 103

IL inner cell layer. 10

KD knock down. 32

LOF loss-of-function. 32

LR lateral roots. 6

LRP lateral root primordia. 10

LTi6B low temperature induced protein 6B. 17

MAP4 microtubule-associated protein 4. 46

MBD microtubule binding domain. 50

mCherry monomeric cherry. 17

MS Murashige and Skoog. 121

mScarlet-I monomeric scarlet-I. 17

NAA 1-naphthaleneacetic acid. 58

NIP5;1 Nodulin 26-like Intrinsic Protein 5;1. 8

OL outer cell layer. 10

p35S cauliflower mosaic virus 35S promoter. 16

PBS phosphate-buffered saline. 124

PDG principal direction of growth. 11

PE pericycle-endodermis. 10

PFA paraformaldehyde. 124

PhyB phytochrome B. 98

PiP1;4 plasma membrane intrinsic protein 4;1. 17

PR primary root. 6

pRPS5A ribosomal Protein S5A promoter. 16

pUBQ10 UBIQUITIN10 promoter. 17

RAM root apical meristem. 6

ROS reactive oxygen species. 54

RPM round per minute. 123

RT room temperature. 124

SAM shoot apical meristem. 6

SOK SOSEKI. 8

TU transcriptional unit. 108

UEG universal entry vector generation. 125

VP16 virion protein 16. 98

XPP xylem pole pericycle. 10

Preamble

The recently discovered SOSEKI proteins (2019) exhibit robust and unique polar localization relative to organismal axes, suggesting that their polarity patterns reflect a higher order 'global' polarity field. Interestingly, the orientation of this global polarity differs in post-embryonically formed lateral roots.

Chapter I describes when the orientation of this global polarity changes during lateral root formation.

Chapter II explores the nature of the signals to which SOSEKI proteins respond.

Chapter III explores which factors guide the polar localization of SOSEKI proteins.

Chapter IV addresses the function of the SOSEKI proteins.

Annex 1 and 2 discuss technological advancements in optogenetics and molecular cloning, respectively.

Chapter 1

From global to local: axis formation during lateral root organogenesis

1.1 Introduction

1.1.1 Multicellular development

Multicellular organisms have a striking spatial organization that is dependent on the precise coordination of individual cells. This coordination is similar to the way a conductor directs an orchestra, providing cues that guide all players simultaneously (Figure 1.1). However, the biological equivalent of such a conductor, and the nature of corresponding instructive cues, are poorly understood in many biological systems. To achieve coordination beyond the scale of individual cells, instructive cues must be global in nature and operate at larger scales, such as at the level of tissues, organs, or the whole organism. Research across kingdoms suggests that such global instructive cues can be gradients of morphogens, environmental signals such as gravity, polarized cellular contents, or mechanical forces [Hamant and Haswell, 2017, Butler and Wallingford, 2017, Li and Bowerman, 2010, Takahashi et al., 2021]. Historically, much more is known about cellular coordination in animals than in plants, and plants lack many molecular homologs of animal coordination mechanisms [Kania et al., 2014, Dettmer and Friml, 2011]. From an evolutionary perspective, plants evolved multicellularity independently, making the mechanisms that coordinate their development comparatively more elusive. This thesis focuses on plant development, where immobile cells are encased and mechanically connected by a rigid cell wall, offering a unique context to provide insight into instructive signals, with a particular focus on the role of mechanical signals.

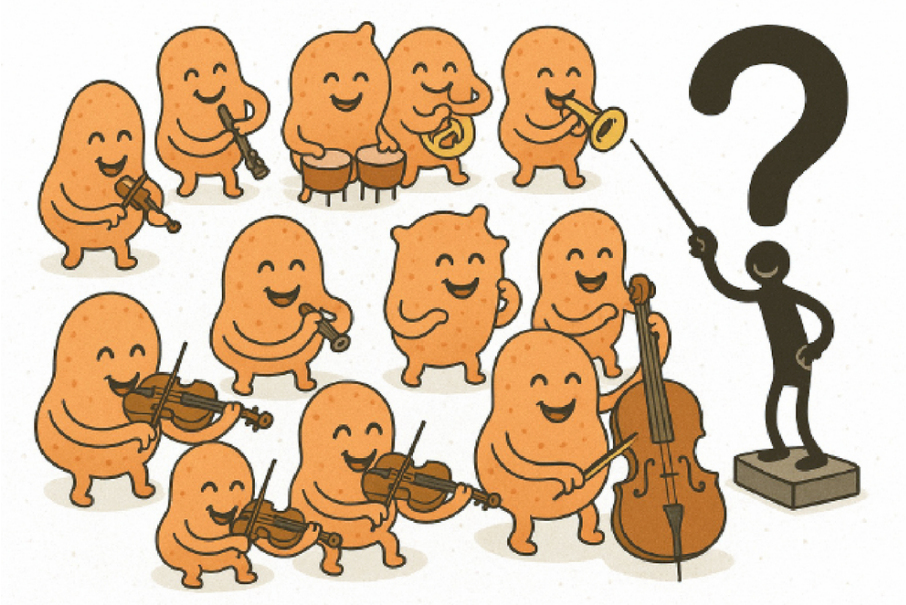

Figure 1.1: Multicellular development is analogous to an orchestra, where an instructive cues is responsible for coordinating cells. ChatGPT was used to draft this image, which was refined in Adobe Photoshop.

1.1.2 Principles of cell polarity

Many fundamental cellular processes, including growth and division, are inherently directional and therefore depend on cells being polarized. Cell polarity is defined as an asymmetry in cell shape, protein distribution, or cellular functions [Nelson, 2003]. Polarity is established in response to an internal or external cue, often subtle or elusive, that initiates the acquisition of an asymmetric state. Such signals can include internal landmarks, such as localized proteins or organelles, as well as external signals such as chemical gradients, cell-cell interactions, or mechanical cues [Mammoto and Ingber, 2010, Asnacios and Hamant, 2012, Arkowitz, 2009, St Johnston and Ahringer, 2010]. In some cases, stochastic fluctuations alone can trigger polarity by amplification through a self-organizing feedback loop [Goehring et al., 2011, St Johnston and Ahringer, 2010].

The first polarization event that breaks the symmetric state of a cell is called symmetry breaking, often a crucial step that determines how the cell will develop afterward [Li and Bowerman, 2010]. Establishing or adjusting polarity also plays a role in asymmetric cell division, where the internal polarity of a cell ensures that cellular components are unequally divided between two daughter cells (Figure 1.2). This unequal distribution is essential for generating cells with different fates or specialized functions [Sunchu and Cabernard, 2020].

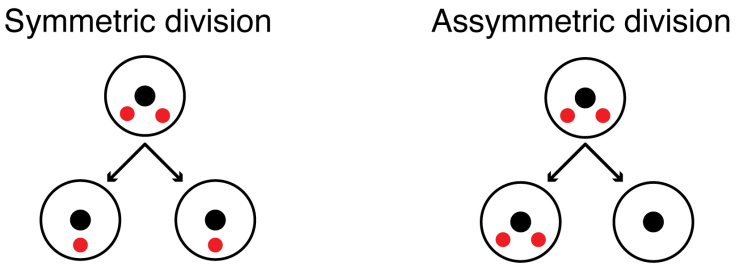

Figure 1.2: Simplistic schematic of symmetric and asymmetric division. A cellular component (red) is either distributed symmetrically or asymmetrically. The nucleus is depicted as a black dot.

In multicellular organisms, cell polarity can be coordinated between cells in a tissue, organ, or entire body [Petersen and Reddien, 2009, Butler and Wallingford, 2017, Ramalho et al., 2022a]. This multicellular polarity is apparent by polarization relative to growth axes or in a cell plane, and is distinct from cellular or transient polarity [Ramalho et al., 2022a]. Multicellular polarity is essential to establish and maintain the spatial organization of cells within tissues and organs [Klunder et al., 2017, Butler and Wallingford, 2017]. This coordinated polarity often emerges during the early stages of development, when cells align relative to the major spatial axes of the organism. In animals, these axes include the anterior-posterior (head-back), dorsal-ventral (back-belly), and left-right dimensions [Abas et al., 2022]. In plants, the spatial axes are termed apical–basal (shoot–root) and radial (inside–outside) (Figure 1.3) [Baskin et al., 2010].

Polarization relative to the body axes is often established in a sequential way. For example in *Drosophila Melanogaster*, anterior-posterior polarization is established prior to fertilization, dorsal-ventral polarization during fertilization, and left-right polarization during embryogenesis [Roth and Lynch, 2009]. Similarly, in *Arabidopsis*, shoot-root polarization is established during the first zygotic division, whereas in-out polarization becomes apparent two division cycles later [Matsumoto and Ueda, 2024, Liao and Weijers, 2018]. These polarization patterns are usually retained in the adult organism.

The fundamental principles of establishing polarity are marking a site for polarity establishment, reinforcing that polarity, and propagating this polarity. This principle is conserved between kingdoms, yet the molecular machinery and cues involved can differ, as is evident in plants [Drubin and Nelson, 1996, Dettmer and Friml, 2011]).

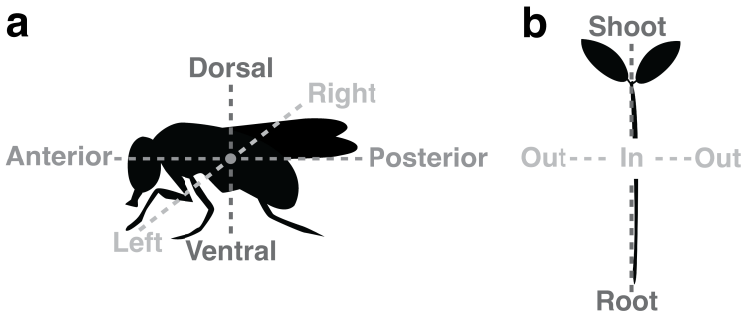

Figure 1.3: Organismal axes in animals and plants. (a) The three organismal in *D. Melanogaster*. (b) The two organismal axes of *Arabidopsis thaliana*.

1.1.3 Plant development

Plant development is characterized by striking contrasts. On the one hand, plants are physically immobile; on the other hand, their developmental fate remains remarkably flexible. Their immobility increases their reliance on adaptable developmental programs that, unlike in animals, occur mainly after embryogenesis, when new nutrient scavenging organs are formed to meet changing nutritional needs [Meyerowitz, 1997].

Similar contrasts appear at the cellular level. Plant cells are encased in cell walls that physically isolate them. Yet, these same walls mechanically connect them, and the symplastic links between cells allow direct cytoplasmic exchange [Roberts and Oparka, 2003, Cosgrove, 2005]. Thus, plant cells are isolated yet highly connected, allowing coordination between cells during plant development.

The plant cell wall

The plant cell wall is an organized and dynamic structure composed of multiple layers of cellulose microfibrils. These microfibrils are interwoven with cross-linking glycans (hemicelluloses) that tether them into a flexible yet robust network. Pectins are particularly abundant in the middle lamella, where they function as a ”glue” that binds the primary cell walls of adjacent cells together (Figure 1.4) [Peaucelle et al., 2012, Obomighie et al., 2025]. This complex matrix maintains cell integrity, facilitates intercellular communication, and enables the wall to respond dynamically to developmental and environmental signals [Cosgrove, 2005, Lu et al., 2025].

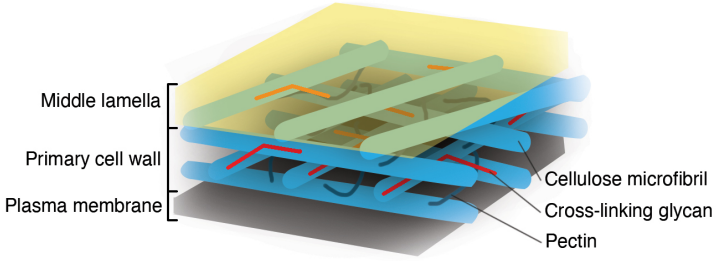

Figure 1.4: Schematic representation of the cell wall. The diagram shows the layered structure including the middle lamella, primary cell wall, and the underlying plasma membrane. Cellulose microfibrils (blue) form a rigid scaffold that provides mechanical strength, while pectins (dark-blue) ’glue’ and cross-linking glycans (red) tether the microfibrils into a flexible, interconnected network. Figure inspired by [Alberts et al., 2002b]

Plant growth

Plant growth is driven by turgor pressure, which pushes outward against the cell wall and generates tensile stress. Growth occurs when the cell wall yields in response to this stress [Jonsson et al., 2022a, Baskin, 2005]. The composition of the cell wall plays a key role in determining how stress is distributed and where the cell wall yields. A heterogeneous cell wall composition can create an uneven stress distribution, promoting anisotropic (directional) growth, whereas a homogeneous wall composition tends to support isotropic (uniform) growth [Jonsson et al., 2022b].

Moreover, the composition of the cell wall is closely linked to the mechanical stress pattern, where walls are typically reinforced in the direction parallel to the direction of maximal tensile stress [Jonsson et al., 2022b]. This reinforcement arises from a feedback loop involving mechanosensitive cortical microtubules and directional cellulose microfibril deposition. Cortical microtubules usually align with the direction of maximal tensile stress, and cellulose microfibrils, which are synthesized by cellulose synthase complexes at the cell cortex, are deposited into the cell wall under microtubule guidance, reinforcing the wall parallel to the stress direction [Hamant et al., 2008, Jonsson et al., 2022a]. This results in a heterogeneous cell wall composition, which in turn directs growth and ultimately feeds back into the stress patterns that initially directed the growth.

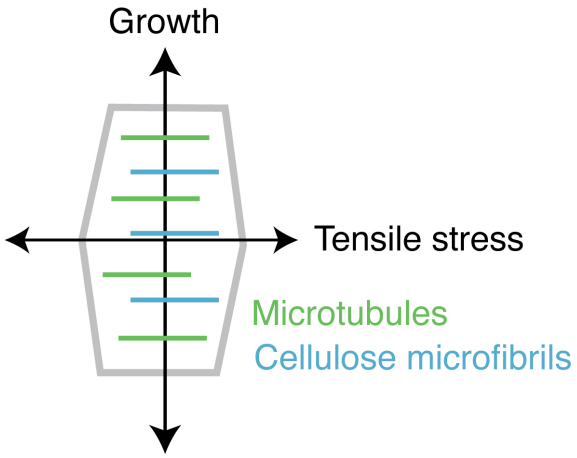

Figure 1.5: Schematic of cell growth and corresponding orientation of stress, microtubules, and cellulose microfibrils.

Principles of Arabidopsis development

Plant development is shaped by a dynamic integration of chemical, hormonal, mechanical, and environmental signals that trigger specific developmental programs, allowing plants to respond and adapt to their surroundings with remarkable precision [Xiao et al., 2017, Waadt et al., 2022, Jonsson et al., 2022a].

In the model plant *Arabidopsis thaliana* (*Arabidopsis*), developmental processes are highly predictable. The basic body plan of *Arabidopsis*, with the shoot-root and in-out growth axes, is established during embryogenesis [ten Hove et al., 2015, Breuninger et al., 2008]. After fertilization, the zygote undergoes an asymmetric division that defines the shoot–root axis: the apical (shootward) cell gives rise to most of the embryo, while the basal (rootward) cell produces the suspensor, a structure that anchors the embryo and facilitates nutrient transport. Although most of the suspensor is extra-embryonic and terminal, its uppermost cell, the hypophysis, contributes to formation of the root meristem organizer [ten Hove et al., 2015]. Development along the radial (in–out) axis occurs later, in the four-cell stage [Liao and Weijers, 2018], with clear distinctions in cell fate becoming evident in the eight-cell (octant) stage [Breuninger et al., 2008].

Furthermore, during embryogenesis, the meristems that maintain post-embryonic development are established: the shoot apical meristem (SAM), responsible for generating aerial organs, and the root apical meristem (RAM), which orchestrates root development in the primary root (PR) (Figure 1.6a) [ten Hove et al., 2015]. During post-embryonic development, stem cells in the SAM give rise to its layered structure, while the peripheral zone of the meristem produces new organs such as leaves, stems, and flowers (Figure 1.6b) [Fuchs and Lohmann, 2020]. Similarly, in the RAM, the quiescent center plays a key role in maintaining the surrounding stem cells, which give rise to the various tissues of the root. These stem cells differentiate into the epidermis, cortex, endodermis, pericycle, and vascular tissues (Figure 1.6e) [Dolan et al., 1993a], where the pericycle retains the capacity to form secondary lateral roots (LR) later in development (Figure 1.6c, d) [Zhang et al., 2022].

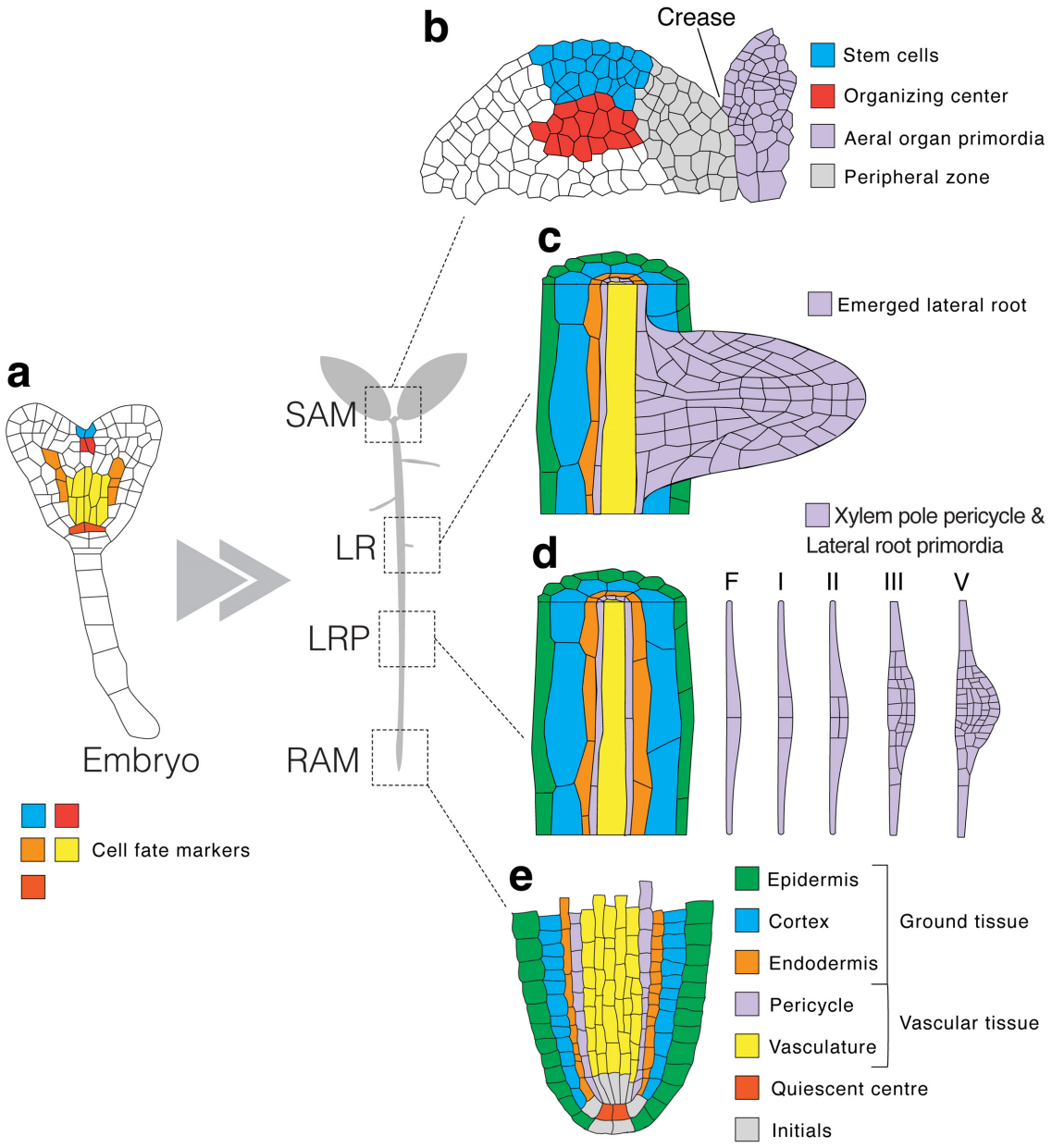

Figure 1.6: Organs and tissues in *Arabidopsis*. (a) Heart stage embryo where the colors indicate cell fate markers of the corresponding tissue in the RAM and SAM. (b) SAM with colors of the distinct domains and formation of an aerial organ. (c) A LR emerging from the PR. (d) LR organogenesis originating from xylem pole pericycle cells and various developmental stages of LR primordia. (e) RAM where the different tissues, quiescent center, and initials are colored. SAM outlines replicated from [Fuchs and Lohmann, 2020]. Embryo outlines replicated from [Armenta-Medina et al., 2021]. RAM outlines inspired by [Detlef Weigel and Peter Doerner, 1996].

Plant polarity

Plants evolved multicellularity independently from animals and lack many of the canonical polarity proteins that are central to animal development. Instead, plants have developed distinct mechanisms to establish polarity [Kania et al., 2014, Dettmer and Friml, 2011].

One of the most critical players in plant polarity is the hormone auxin, which acts as a morphogenetic trigger in almost all plant development programs [Vanneste and Friml, 2009]. Auxin is locally synthesized and directionally transported in a process known as polar auxin transport. This creates local auxin maxima, which are essential for activating genetic patterning pathways, helping to initiate organogenesis and specify developmental axes [Friml et al., 2003, Benková et al., 2003, Robert et al., 2013, Dubrovsky et al., 2008, Tang et al., 2017, Vanneste and Friml, 2009].

Polar auxin transport is mediated by auxin efflux and influx carriers, such as the PIN-FORMED and AUXIN RESISTANT 1 and LIKE AUX protein families [Vanneste and Friml, 2009]. These carriers polarize to specific domains of the plasma membrane through membrane trafficking processes [Geldner et al., 2003]. Notably, PINs polarize in tissue-specific and context-dependent manner, and their localization does not appear to be guided by an unified, (organism-wide) global polarity, but rather reflects local cellular context [Kania et al., 2014, Ramalho et al., 2022a].

Although most known polar plant proteins exhibit such context-specific polarity, some exceptions stand out. In particular, the recently discovered SOSEKI (SOK) proteins, which have consistent polarization relative to organismal axes, and appear to reflect a polarity system at a higher 'global' organizational level [Yoshida et al., 2019]. Similarly, the transcription factor BREAKING OF ASYMMETRY IN THE STOMATAL LINEAGE (BASL), as well as Boron Transporter 1 (BOR1) and Nodulin 26-like Intrinsic Protein 5;1 (NIP5;1), exhibit polarization relative to a 'global' polarity field [Dong et al., 2009, Takano et al., 2010, Liao and Weijers, 2018]. These proteins are valuable tools for studying such a 'global' polarity system.

SOSEKIs: markers of global polarity

The SOK protein family, comprising five proteins in *Arabidopsis*, were identified as potential auxin-dependent mediators of cell division orientation in the embryo. SOKs stand out for their consistent polarization relative to the global organismal axes in various developmental contexts [Yoshida et al., 2019].

Each SOK displays a distinct stereotyped polarity in the embryo and RAM that is maintained upon ectopic expression. Namely, SOK1 polarizes shootward and toward the endodermis–cortex interface; SOK2 polarizes rootward and inward; SOK3 is unique in polarizing to each cell corner; SOK4's polarization has not been characterized in detail; and SOK5 mirrors SOK2 but with a tendency to polarize slightly more inward than rootward (Figure 1.7) [Yoshida et al., 2019].

SOK polarization relies on two conserved elements, a DIX-like domain and a CG motif (Figure 1.8). The DIX-like domain is evolutionarily conserved and mediates head-to-tail polymerization in a manner functionally equivalent to the DIX domain of Dishevelled, a core component of the Wnt/planar cell polarity pathway [van Dop et al., 2020, Schwarz-Romond et al., 2007]. Notably, the DIX(-like) domain is found in most eukaryotes and is thought to play a role in polarity [van Dop et al., 2020, Kostareli et al., 2025]. Meanwhile, the CG motif mediates association with the plasma membrane, and is a likely palmitoylation site that allows anchoring into the lipid bilayer through post-transcriptional attachment of palmitoyl [Ren et al., 2008].

The SOKs maintain their localization in a robust way. That is, they are not affected by perturbation of polar auxin transport, temperature, cytoskeleton dynamics, or membrane trafficking [Yoshida et al., 2019]. Notably, SOK localization is only affected by loss of cell wall integrity [Yoshida et al., 2019], suggesting that SOKs may be sensitive to cell wall mechanics.

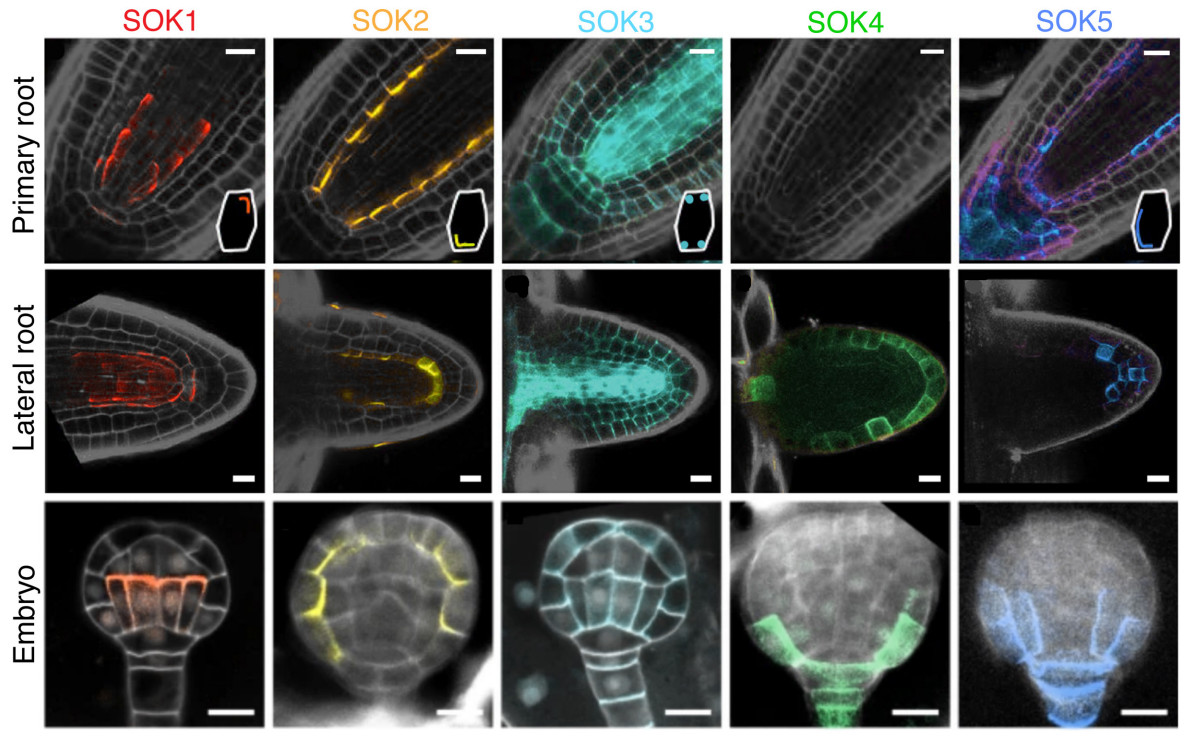

Figure 1.7: Characteristic polarization of each genomic SOK protein in the PR, LR, and embryo. The SOK proteins polarize relative to organismal axes, indicating integration of a global polarity cue. Interestingly, in the LR, SOK polarization is relative to the LR organ axes, indicating that global polarity is reorientated during LR organogenesis (Figure adapted from Yoshida et al., 2019). Scale bars 10µm.

Notably, the SOK polarity pattern in the emerged LR is relative to the newly established organ axes rather than the original PR organismal axes (Figure 1.7), suggesting that the orientation of global polarity shifts during LR development [Yoshida et al., 2019]. The SOK proteins may be a valuable tool to explore how this global polarity is reoriented during LR organogenesis.

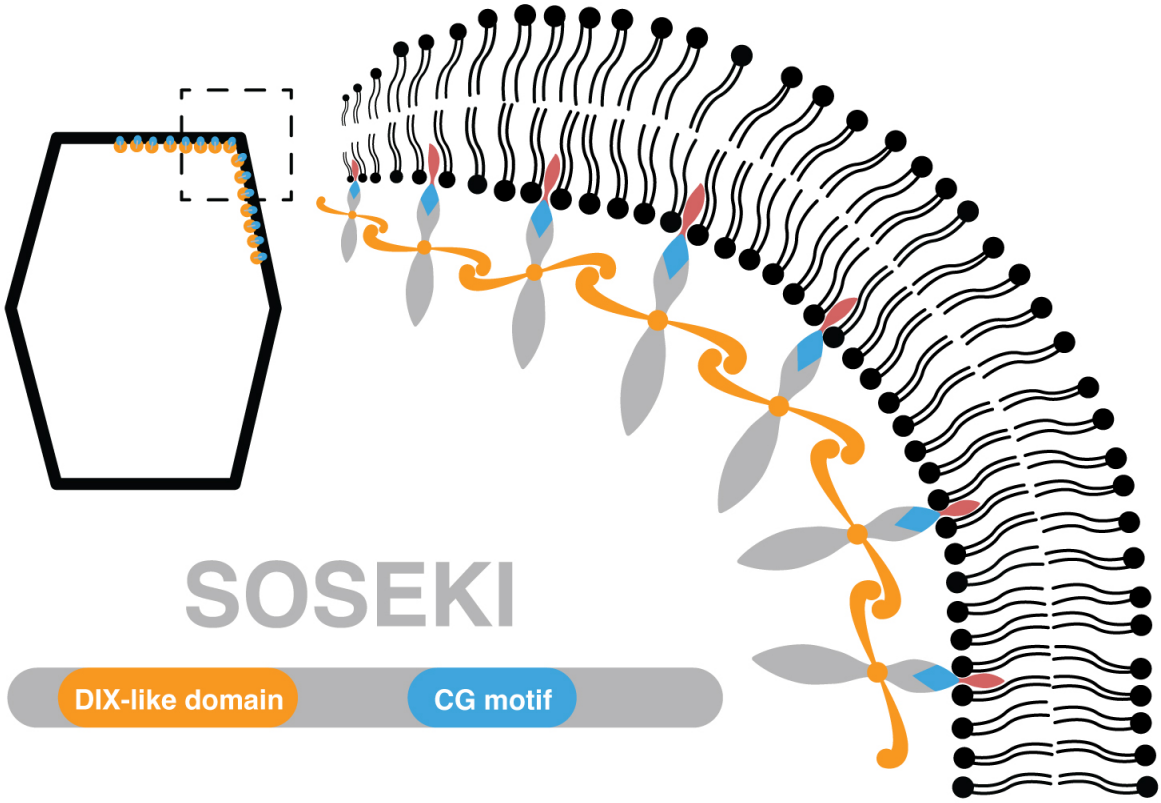

Figure 1.8: Schematic of SOSEKI proteins with their DIX-like polymerisation domain, and CG motif for membrane association. The zoomed in region illustrates polymerization between SOK proteins and (potential) anchoring in the lipid bilayer through a palmitoyl group (red) attached to the CG motif.

Lateral root organogenesis

The development of LRs exemplifies how plants establish new organ axes within an existing body plan. LR organogenesis begins in two adjacent pericycle cells, located along the xylem pole known as xylem pole pericycle (XPP) cells. These XPP cells undergo asymmetric swelling to form the so-called founder cells, where the central domain is more swollen than the pheripheral domain (Figure 1.9a, b) [Malamy and Benfey, 1997, Vilches Barro et al., 2019]. The founder cells perform an asymmetric anticlinal division, resulting in a stage I lateral root primordia (LRP) composed of two smaller central cells, flanked by two larger peripheral cells (Figure 1.9c). Subsequently the smaller central cells shift their division plane orientation and undergo an asymmetric periclinal division, producing a stage II LRP with an inner cell layer (IL) and an outer cell layer (OL) [Malamy and Benfey, 1997]. This layered structure reflects the fundamental radial organization of the PR, where the inner layer will develop into vascular tissue, and the outer layer differentiates into ground tissue [Serrano-Ron et al., 2021a]. The boundary between these layers is the prospective pericycle-endodermis (PE) interface (Figure 1.9,1.17b).

Up to stage II, LR development follows a stereotyped sequence of precisely oriented asymmetric divisions that bifurcate cell fates [Serrano-Ron et al., 2021b, Von Wangenheim et al., 2016, Schütz et al., 2021]. From stage III onward, development becomes self-organized, where additional periclinal divisions characterize stages III through VII, progressively establishing radial patterning and delineating boundaries between distinct tissue types (Figure 1.9) [Von Wangenheim et al., 2016]. By the time the LR emerges from the PR, it has reconstructed a similar radial tissue organization as the PR (Figure 1.9c) [Dolan et al., 1993b].

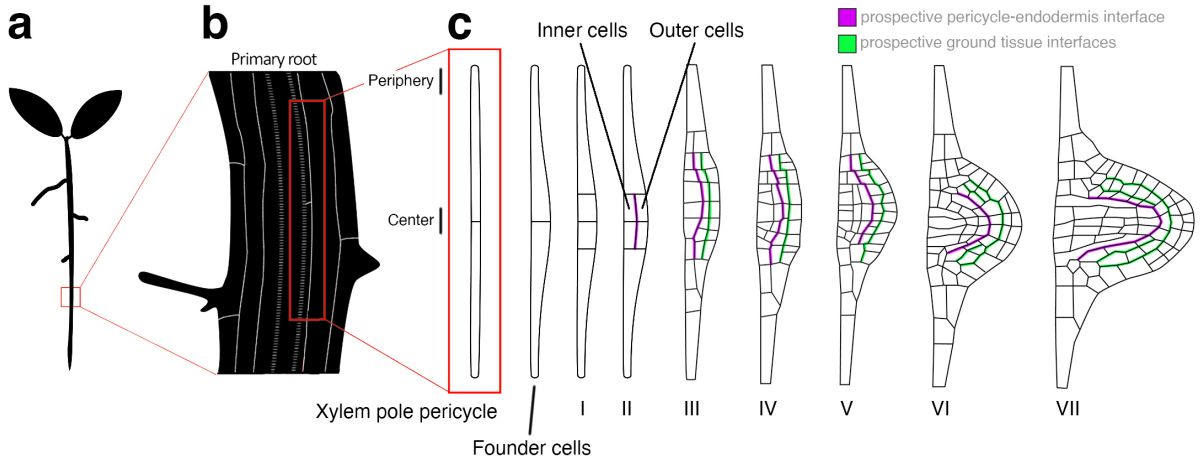

Figure 1.9: LR organogenesis. (a) Schematic of an *Arabidopsis thaliana* seedling showing the PR and LRs, with a zoom-in highlighting the LR initiation site. (b) Illustration of the PR tissue layers at the LR initiation site, focusing on XPP cells. (c) Developmental sequence of LR organogenesis, starting with asymmetric swelling of xylem pole pericycle cells that forms founder cells. A subsequent asymmetric anticlinal division generates a stage I LRP with central and peripheral cells. A further subsequent asymmetric periclinal division produces a stage II LRP with distinct inner and outer cell layers. After this point, development becomes self-organized, where further periclinal divisions add additional cell layers, defining stages III through VII. The cell interfaces that seperates the IL and OL is marked in magenta and is the prospective pericycle-endodermis interface. Furthermore, ground tissue interfaces are marked in green. Upon reaching stage VII, the LRP is emerged from the PR and is then termed an emerged LR. The outlines of stage III to VII were adapted from [Torres-Martínez et al., 2019].

Computer models of LR organogenesis have successfully reproduced the characteristic LR cell pattern by linking the orientation of cell divisions to the principal direction of growth (PDG) [Szymanowska-Pułka et al., 2012, Szymanowska-Pułka, 2007]. Specifically, several distinct growth domains were defined, including regions corresponding to provascular cells, ground tissue precursors, the QC region, the shootward domain, and peripheral zones; each with its own characteristic growth profile (Figure 1.10) [Szymanowska-Pułka et al., 2012]. The model showed that the local growth field within the developing LRP is dynamic. Namely, as tissues expand, the growth directions change, guiding successive divisions that shape the LR pattern [Szymanowska-Pułka et al., 2012].

Understanding how cells maintain or reinterpret global polarity is fundamental to understanding plant development. LR organogenesis exemplifies how plants establish new growth axes within an existing body plan, and provides an ideal context to investigate how global polarity may change during post-embryonic development.

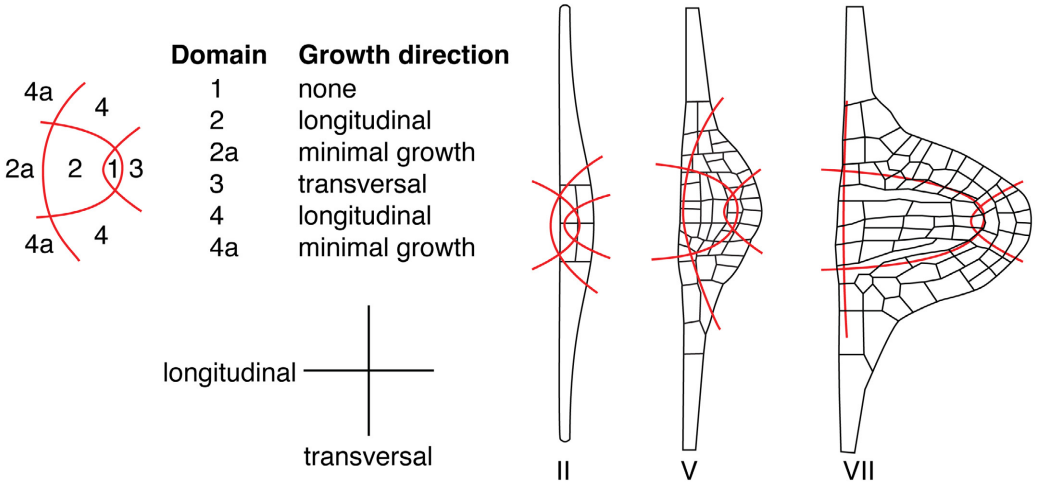

Figure 1.10: Predicted growth domains and principal directions of growth during LR organogenesis as defined by Szymanowska-Pułka *et al*. In their computer model, distinct growth regions were defined in provascular tissue (2), vascular bridge zone (2a), ground tissue precursors (4), the quiescent center (1), shootward domain (3), and peripheral zones (4a). Figure inspired by [Szymanowska-Pułka et al., 2012, Szymanowska-Pułka, 2007]. The outlines of stage V and VII were adapted from [Torres-Martínez et al., 2019].

1.1.4 Objective

The SOKs mark global polarity, exemplified by their polarization relative to organismal axes throughout the plant body [Yoshida et al., 2019]. Interestingly, in emerged LRs, the SOKs polarize relative to the new organ axes rather than the original organismal axes, suggesting that the orientation of global polarity changed during LR development (Figure 1.11b, d) [Yoshida et al., 2019]. This raised a fundamental question: **At what point during LR organogenesis does the orientation of global polarity change?**

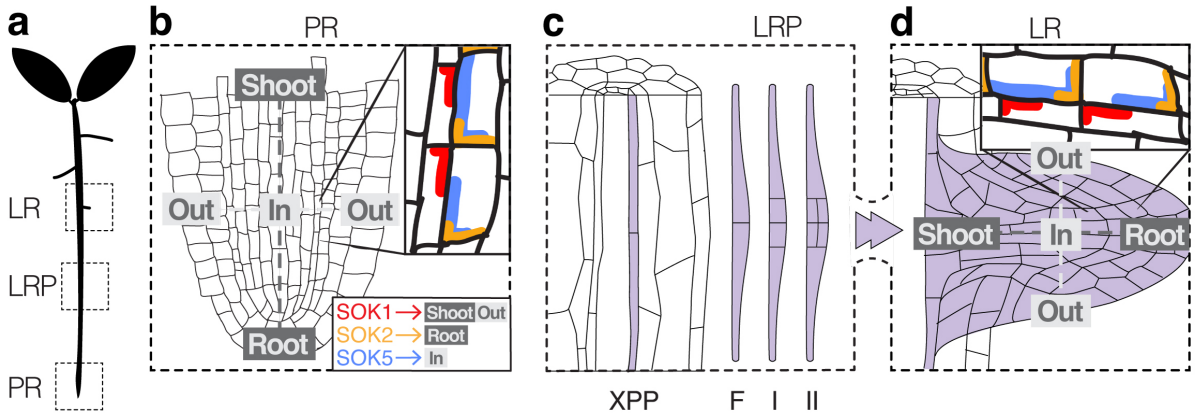

Figure 1.11: Objective of Chapter I: use the SOK proteins as global polarity markers to clarify when the orientation of global polarity changes during LR organogenesis (a) *Arabidopsis* seedling with three marked zones (LR: LR emergence, LRP: LR primordia, PR: primary root meristem). (b) The PR meristem overlaid with organismal axes to indicate the direction of the global polarity. The polarization of SOK1, SOK2, and SOK5 is relative to the these global organismal axes. (c) Schematic representation of LR development from XPP cells to a stage II LRP. In these early developmental stages, the polarization of the SOKs is unknown and characterizing this may provide insight into how the orientation of global polarity changes during post-embryonic development. (d) An emerged LR overlaid with organ axes to indicate that the direction of global polarity has changed during LR development. This shift in orientation is also reflected by the polarization of the SOKs. RAM outlines inspired by [Detlef Weigel and Peter Doerner, 1996].

1.2 Results

1.2.1 New organ axes may appear early during lateral root development

To assess whether the SOKs could be used to investigate when the orientation of global polarity changes during LR organogenesis, the expression patterns of genomic SOK:yellow fluorescent protein (gSOK::YFP) markers [Yoshida et al., 2019] were examined in the early stages of LR development. Namely, LR organogenesis was induced through gravistimulation and gSOK::YFP markers were live-imaged in the resulting primordia using two-photon microscopy.

All gSOK markers were observed in the early stages of LR organogenesis. gSOK1::YFP was seen in all LRP cells, whereas gSOK2::YFP, gSOK3::YFP, gSOK4::YFP and gSOK5::YFP showed a more restricted expression pattern. Specifically, gSOK2::YFP and gSOK4::YFP were limited to the outer central cells, and gSOK3::YFP was limited to the central cells. Whereas, gSOK5::YFP had dynamic signal that varied between individual LRPs (Figure 1.13). Based on the observed pattern, gSOK1::YFP may be the most useful polarity marker in early LR organogenesis, as it has a broad expression pattern, whereas the expression pattern of the other genomic SOK markers is limited or dynamic.

Regarding polarization, gSOK1::YFP exhibited divergent corner polarization relative to the LRP center in stage I (Figure 1.13). This polarity pattern is different from the polarity pattern seen in the RAM (Figure 1.12), and suggests that global polarity already changed orientation in stage I. To deduce the orientation of the new LRP organ axes, the gSOK1::YFP polarity pattern in the LRP was compared with the polarity pattern in the RAM and the emerged LR. However, the new LRP pattern did not align with either the PR or emerged LR (Figure 1.12). This suggests that the development of the LRP organ axes is incomplete in stage I. The other SOK markers did not provide more insight due to their limited expression domain. gSOK3::YFP was polarized in every corner, making it difficult to infer the orientation of polarity, and gSOK4::YFP was not expressed in the RAM, leaving no reference point for determining orientation. Consequently, the orientation of the organ axes in LRP remains unclear.

In conclusion, all SOKs are endogenously expressed during LR initiation, and the polarization of gSOK1::YFP suggests that global polarity changes early in development. However, the corresponding orientation remains unclear. Utilization of additional polarity markers may be provide more insight.

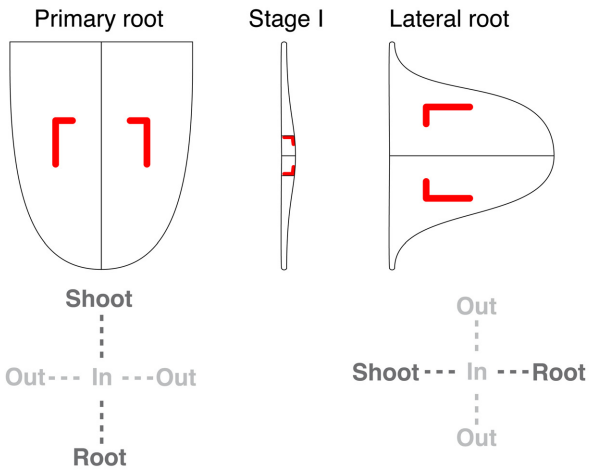

Figure 1.12: Schematic of polar SOK1 localization in the PR, stage I LRP, and emerged LR. In stage I LRP, SOK1 polarity does not align with either the PR or emerged LR, suggesting that new organ axes are established early during LR initiation and that they are incomplete.

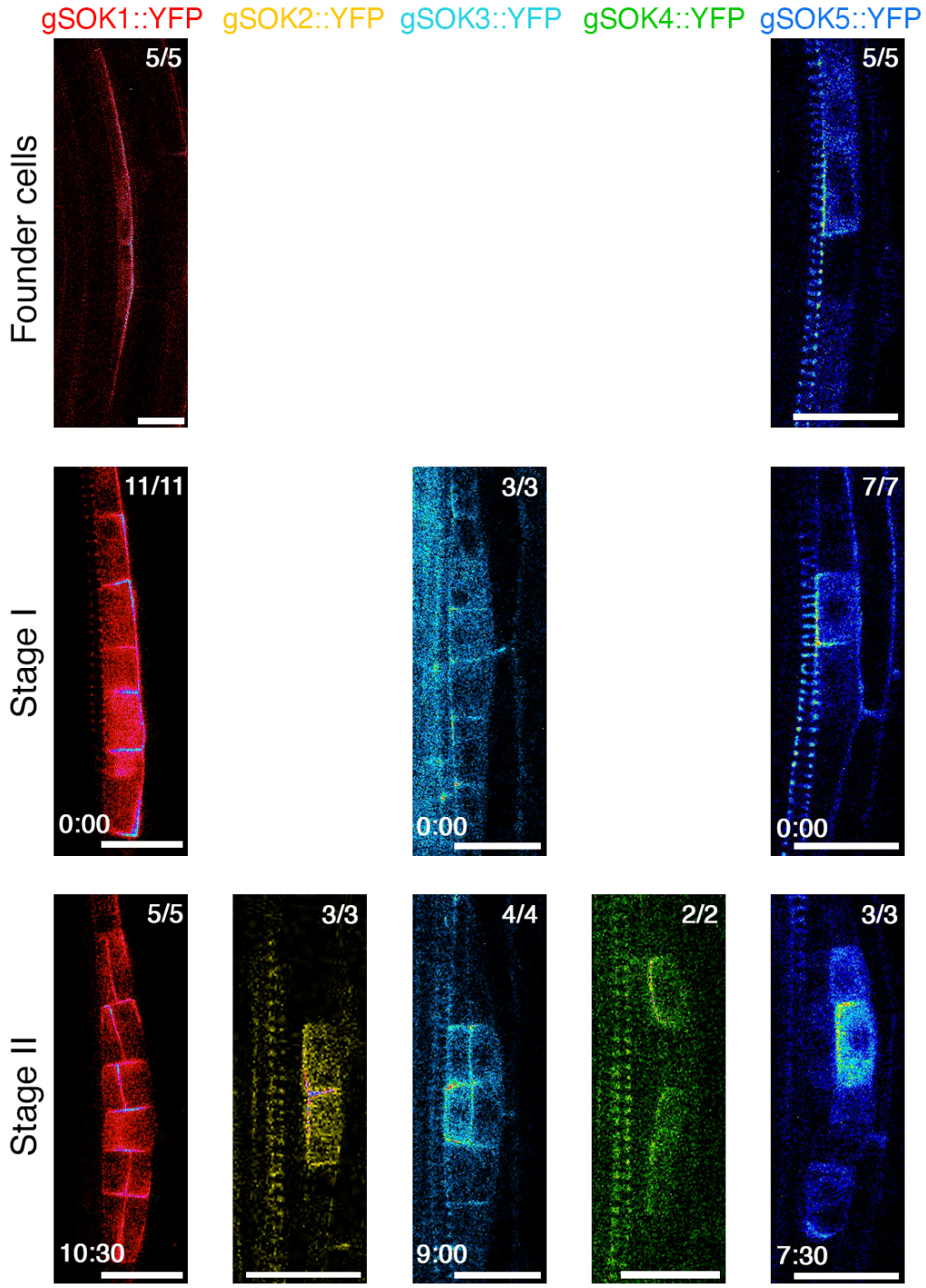

Figure 1.13: Expression patterns and polar localisation of genomic SOK markers during early LR development, from founder cells to stage II. SOK1 is consistently expressed across all LRP cells, while SOK2 to SOK5 exhibit a restricted expression domains. And, all SOK proteins, except SOK3, display unidirectional polar localisation. Timestamps are provided for timelapse images (hour:min). The number of identical observations relative to the total number of samples is indicated in the top right corner of each panel. Scale bar: 20µm.

1.2.2 SOSEKI:YFP misexpression can be used to mark polarity

The polarity pattern of gSOK1::YFP in stage I LRP suggests that new organ axes are established early in LR development. However, the orientation of these young axes is unclear because they do not align with the organismal axes nor with the emerged LR organ axes (Figure 1.12). To better define the orientation of the LRP organ axes, I sought to characterize the polarity pattern of the young LRP in greater detail. Given that the genomic SOK markers had a limited resolution for determining polarity, I evaluated the use of established global polarity markers and SOK misexpression lines as complementary tools to characterize the polarity pattern. In addition to pRPS5A::SOK:YFP misexpression markers, I investigate the utility of p35::GFP:BASL, pRPS5A::BOR1:mCitrine and pRPS5A::NIP5;1:mCitrine (Table 1.1) [Yoshida et al., 2019, Dong et al., 2009, Liao and Weijers, 2018, Alassimone et al., 2010, Takano et al., 2010]. These markers were either misexpressed in all cells from the strong, constitutive cauliflower mosaic virus 35S promoter (p35S) [Odell et al., 1985] or the ribosomal Protein S5A promoter (pRPS5A), active in all proliferating cells [Weijers et al., 2001].

Table 1.1: Potential global polarity markers. Polarization is indicated as observed in the RAM.

Gene	Marker	Polarization	Reference
BASL	p35S::GFP:BASL	rootward	[Dong et al., 2009]
BOR1	pRPS5A::BOR1:mCitrine	outward	[Liao and Weijers, 2018]
NIP5;1	pRPS5A::NIP5;1:mCitrine	inward	[Liao and Weijers, 2018]
SOK1	pRPS5A::SOK1:YFP	shootward & to ground tissue	[Yoshida et al., 2019]
SOK2	pRPS5A::SOK2:YFP	rootward and inward	[Yoshida et al., 2019]
SOK4	pRPS5A::SOK4:YFP	unknown	this thesis
SOK5	pRPS5A::SOK5:YFP	rootward and inward	[Yoshida et al., 2019]

The seeds of the *p35S::GFP:BASL* plant did not germinate. And, the characteristic polarization of pRPS5A::BOR1:mCitrine (outward) and pRPS5A::NIP5;1:mCitrine (inward) along the radial axis was not observed in the RAM. Namely, their polarization was multi-directional in the RAM (Figure 1.14) and in the LR (not shown). Thus, p35S::GFP:BASL, pRPS5A::BOR1:mCitrine, pRPS5A::NIP5;1:mCitrine were unsuitable as reliable polarity markers.

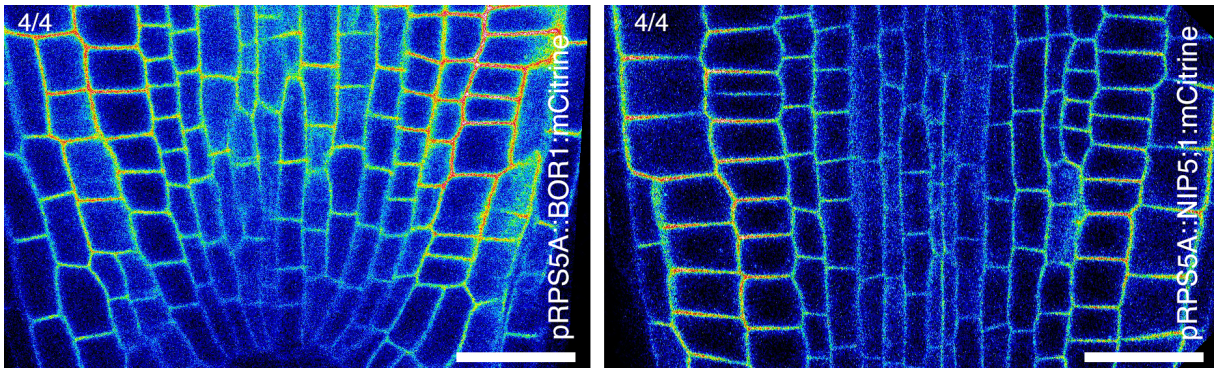

Figure 1.14: Ectopic pRPS5A::BOR1mCitrine and pRPS5A::NIP5;1mCitrine lack their characteristic inward (BOR1) and outward (NIP5;1) polarity. Number of replicates is indicated in the top left corner. Scale bar: 20µm.

The pRPS5A::SOK1/2/4/5:YFP misexpression markers were the most promising because they had unidirectional polarization, allowing for axis orientation to be deduced from the polarity pattern in the RAM [Yoshida et al., 2019]. However, pRPS5A::SOK4:YFP was primarily localized to the cytosol, making it

challenging to infer polarity (Figure 1.15a, b). In contrast, pRPS5A::SOK1/2/5:YFP consistently maintained their characteristic polarization in the PR or emerged LR (Figure 1.15a, b) [Yoshida et al., 2019]. To visualize all cell contours, the *pRPS5A::SOK1/2/5:YFP* misexpression lines were crossed with a plasma membrane marker line (*pUBQ10::LTi6B:mCherry(x2)*) expressing a membrane localized fluorescent fusion protein consisting of low temperature induced protein 6B (LTi6B) and two monomeric cherry (mCherry) proteins activated from the UBIQUITIN10 promoter (pUBQ10) [Elsayed et al., 2016].

Importantly, all crossed *pRPS5A::SOK:YFP* lines developed normal LRs, and their polarization matched the polarization seen in the native *SOK* expression domain (Figure 1.15, 1.7; 1.13, 1.16). However, homozygous *pRPS5A::SOK1:YFP* lines were not recovered, and selected wildtype-like plants showed weak YFP, suggesting that there may be developmental defects at higher expression levels. Thus, *pRPS5A::SOK1/2/5:YFP* lines are reliable polarity markers provided that misexpression is kept sufficiently low to avoid perturbation.

Furthermore, to confirm that the orientation of global polarity cues changes during the developmental transition from XPP cells to stage I LRP, the polarity in XPP cells would have to be determined. To this end, I examined whether pRPS5A::SOK1/2/5:YFP could be observed in XPP cells. I detected pRPS5A::SOK2:YFP and pRPS5A::SOK5:YFP signals in ”young” XPP cells, but pRPS5A::SOK1:YFP signal was not observed, likely due to its weaker expression. To overcome this, I generated a new transgenic line expressing SOK1 fused to the fluorescent protein (FP) Gamillus, under the control of an XPP-specific promoter (*pXPP::SOK1:Gamillus*, constructed jointly with Neva Bölke) [Andersen et al., 2018], and included a cell outline marker on the same transgenic construct (*pUBQ10::PiP1;4:mScarlet-I*) consisting of plasma membrane intrinsic protein 4;1 (PiP1;4) fused to monomeric scarlet-I (mScarlet-I).

With this, I established a toolkit of polarity markers suitable for characterizing the polarity pattern in the early stages of LR organogenesis.

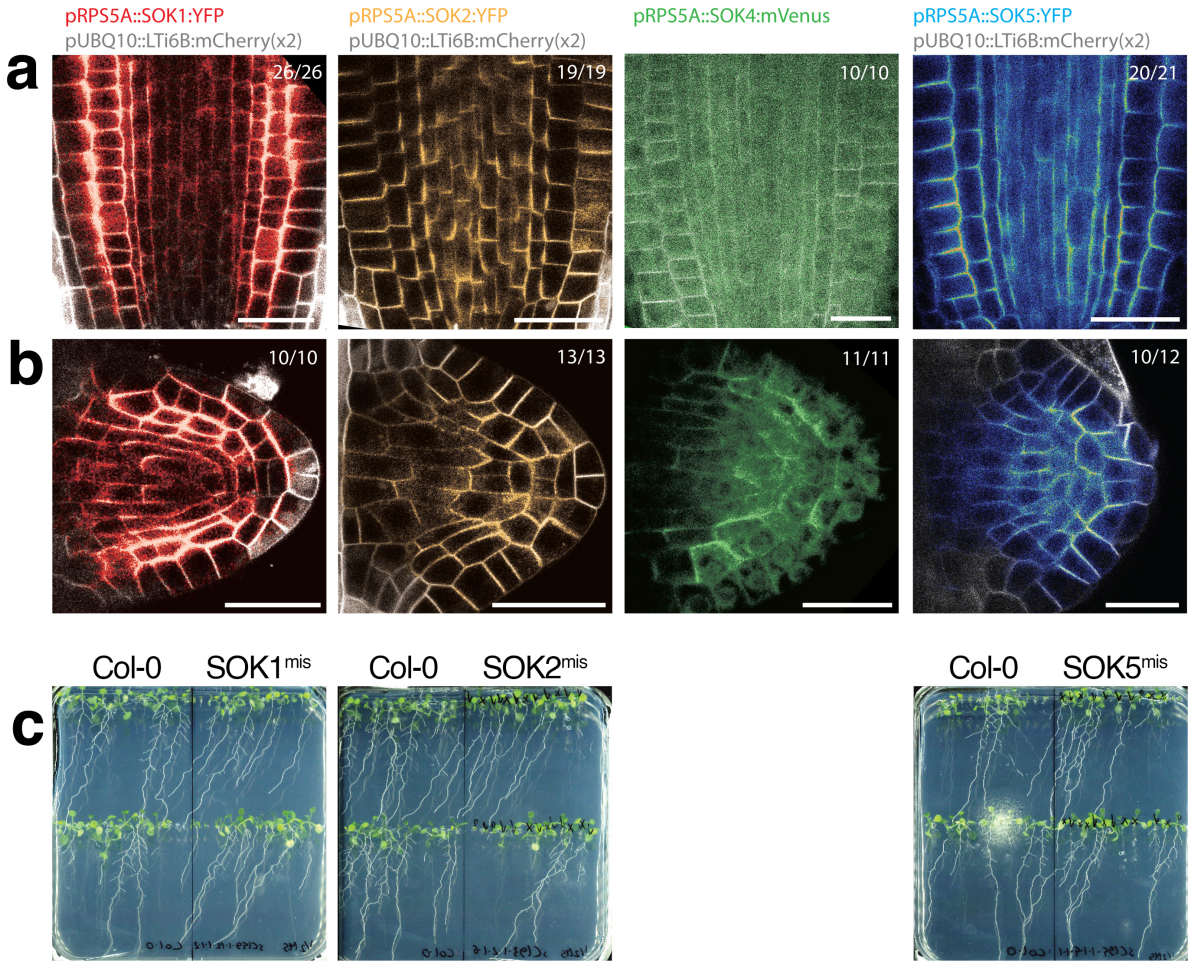

Figure 1.15: Heterozygous ectopic expression of SOK1, SOK2, SOK4, and SOK5 under the pRPS5A promoter does not alter root patterning. (a) Representative images of the RAM in heterozygous *pRPS5A::SOK1/2/4/5* lines show no noticeable disruption to cell layout. (b) Emerged LRs in the same lines display normal tissue organization. (c) Whole-root phenotype on ½MS plates has no apparent abnormal phenotype compared to wildtype (Col-0). Markings on the plates (✓,✗) denote seedlings with and without pRPS5A::SOK:YFP signal as observed under a dissection microscope. Images were flipped horizontally. Numbers in the top right of each panel indicate the number of replicates. Scale bar: 20µm.

1.2.3 SOSEKIs may not sense global polarity cues

To deduce the orientation of the LRP organ axes, I used genomic SOK markers (gSOK::YFP) and ectopic SOK markers (pXPP::SOK1:YFP and pRPS5A::SOK1/2/5:YFP) to track changes in polarity from XPP cells to stage II [Yoshida et al., 2019]. This was done by capturing 2D images of the SOK markers in each developmental stage using confocal microscopy, and drawing a consensus of SOK polarity for each developmental stage. Notably, the observed polarity patterns were consistent between biological samples (Figure 1.25, 1.26, 1.27). When referring to SOKs in the text below, I refer to the polarity conensus seen among both the genomic and ectopic markers.

In XPP cells, SOK1:YFP, SOK2:YFP, and SOK5:YFP displayed polarization consistent with the PR organismal axes, indicating that XPP cells obey the organismal axes (Figure 1.16). Upon transition to founder cells, the polarity patterns changed. SOK1:YFP, SOK2:YFP, and SOK5:YFP were now oriented relative to the center of the developing LRP rather than relative to the organismal axes. Notably, SOK1:YFP showed divergent localization, while SOK2:YFP and SOK5:YFP exhibited convergent localization, relative to the LRP center (Figure 1.16a, b). These results suggest that when symmetry is broken in founder cells, the orientation of global polarity changes and the formation of new LRP organ axes is initiated.

The divergent and convergent polarity patterns of founder cells became more pronounced in stage I LRP. Notably for SOK1:YFP, in stage I, a divergent corner localization pattern appeared (Figure 1.13, 1.16). Similarly, for SOK2:YFP and SOK5:YFP, their convergent polarity patterns were maintained. These observations indicate that the characteristic divergent (SOK1) or convergent (SOK2/5) polarity patterns were established in founder cells and are maintained in stage I LRP (Figure 1.16a, b).

In stage II, the periclinal divisions established the IL and OL, where the IL is destined to become the vasculature and the OL will develop into ground tissue [Serrano-Ron et al., 2021a]. Intriguingly, the SOK1:YFP, SOK2:YFP, and SOK5:YFP polarity pattern changed from stage I to stage II, where the IL and OL were polarized differently. This observation contradicts previous assumptions that SOK proteins are guided solely by a global polarity cue [Yoshida et al., 2019], and suggests that SOKs respond to a tissue-specific cue. This differential polarization complicates assignment of a single orientation to the LRP organ axes (Figure 1.16c), and suggests that the SOK polarity pattern may not reflect a global polarity field. Instead, it seems to reflect a local polarity field shaped by tissue divergence.

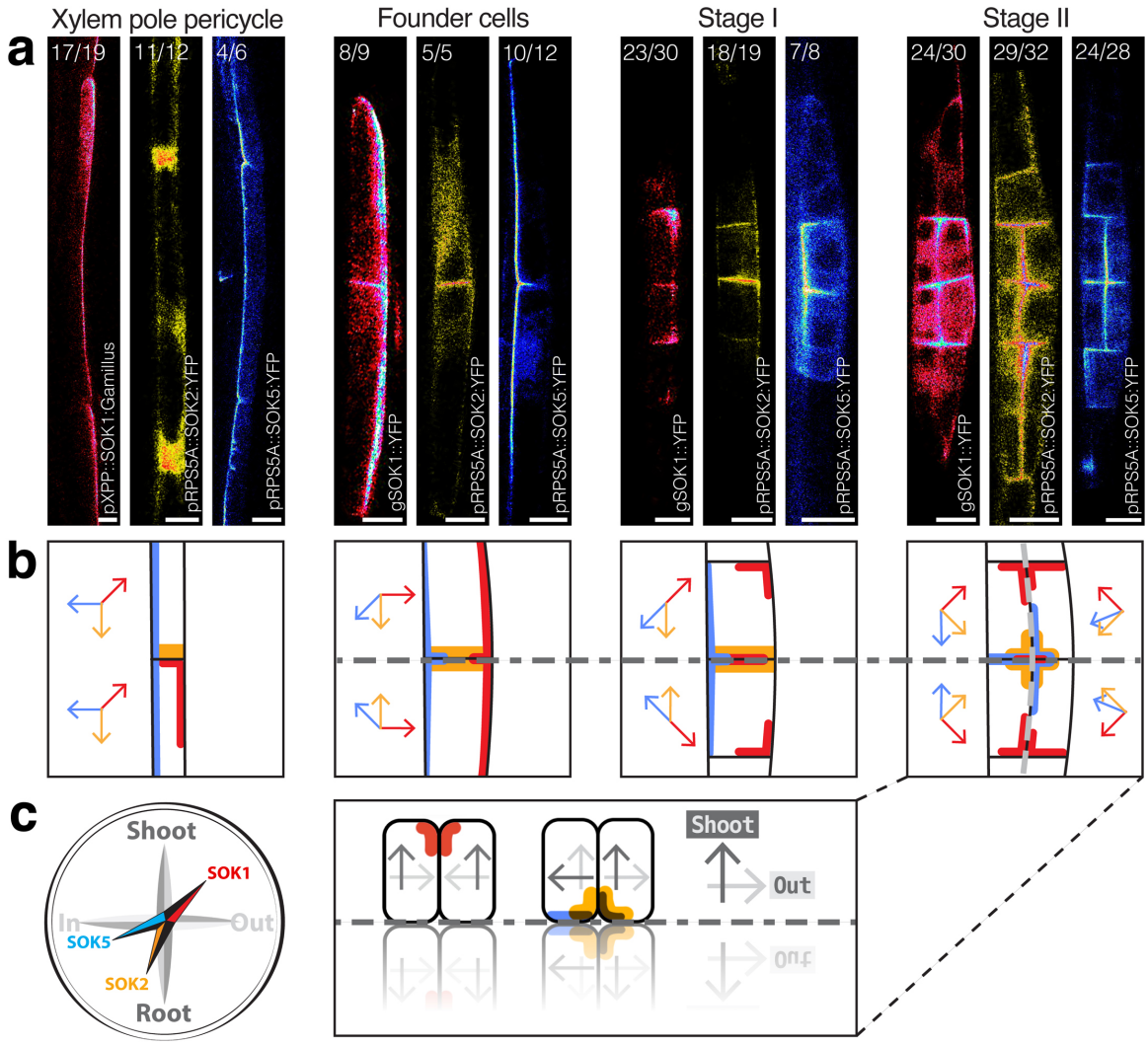

Figure 1.16: SOK proteins may not follow global polarity cues during early LR organogenesis. (a) Representative images showing the polarity pattern of SOK1:YFP, SOK2:YFP, and SOK5:YFP during early stages of LR development. Each image reflects the consensus, with the number of replicates in the top left corner. Scale bars: 10µm. (b) Schematic summary of the SOK polarity patterns in each developmental stage. Arrows indicate the direction of polarization per individual cell (red: SOK1, yellow: SOK2, blue: SOK5). (c) in stage II there are inconsistencies in the orientation of global polarity. The cartoon depicts central LRP cells, where grayscale arrows represent the inferred direction from the compass. This indicate that the polarity in the IL and OL is different. Furthermore, the inferred orientations is different between SOK1 and SOK2/5. This raises the possibility that the cells are polarized relative to a local system rather than a global polarity system.

1.2.4 SOSEKIs accumulate at tissue interfaces that separate domains of differential growth

The SOK polarity pattern was initially thought to reflect a global polarity field. Surprisingly, the heterogeneous pattern in stage II LRP suggests that SOK polarity reflects a local polarity field shaped by tissue separation (Figure 1.16). However, the polarity pattern in the mature LR and PR have a uniform SOK polarity pattern [Yoshida et al., 2019]. It is unknown how the heterogeneous polarity pattern in stage II LRP transforms into a uniform pattern during LR development. To explore this, I live-imaged pRPS5A::SOK1:YFP, pRPS5A::SOK2:YFP, and pRPS5A::SOK5:YFP (pRPS5A::SOK1/2/5:YFP) from stage II to emergence using light sheet and took 2D images using confocal microscopy [Yoshida et al., 2019].

Strikingly, despite *pRPS5A* driving uniform expression throughout LR development (Figure 1.17a, 2.7c), the pRPS5A::SOK1/2/5:YFP signal was not evenly distributed. Instead, there were differences in signal intensity between different domains. Namely, the pRPS5A::SOK1/2/5:YFP signal was more intense near the interface that separates the provascular cells and ground tissue precursors, which corresponds to the PE interface (Figure 1.17b, Figure 1.18a).

To quantify this, I processed the live-imaging data (stages II to emergence) and 2D images (stage I - emergence) through a custom bioinformatics pipeline that determined the positions of the pRPS5A::SOK1/2/5:YFP signal maxima across developmental stages (Method 8.4.1, 462 images, 1388 maxima). The results revealed that pRPS5A::SOK1/2/5:YFP consistently localized near the PE interface during organogenesis. Specifically, each SOK marker accumulated in a slightly different region. That is, pRPS5A::SOK1:YFP accumulated near the ground tissue interfaces, likely marking the position of the prospective endodermis-cortex interface, as this interface has been reported to attract SOK1 in the RAM [Yoshida et al., 2019]. pRPS5A::SOK2:YFP accumulation aligned more precisely with the position of the PE interface. And, pRPS5A::SOK5:YFP accumulated in the provascular cells near the PE interface (Figure 1.18b). These observations suggest that the SOK proteins are consistently attracted to a region near the PE interface.

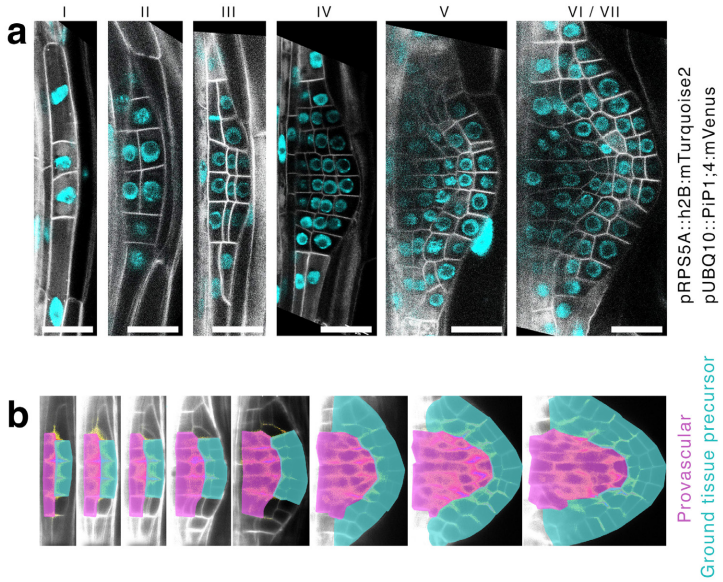

Figure 1.17: (a) Nuclear pRPS5A::H2B:mTurquoise2 signal indicates that the *RPS5A* promoter is active in every LR cell. Scale bar: 20µm. (b) The provascular (magenta) and ground tissue precursor domains (cyan) throughout LR organogenesis. The pericycle–endodermis (PE) junction lies at the interface between these colored domains. Timestamp: hour:min.

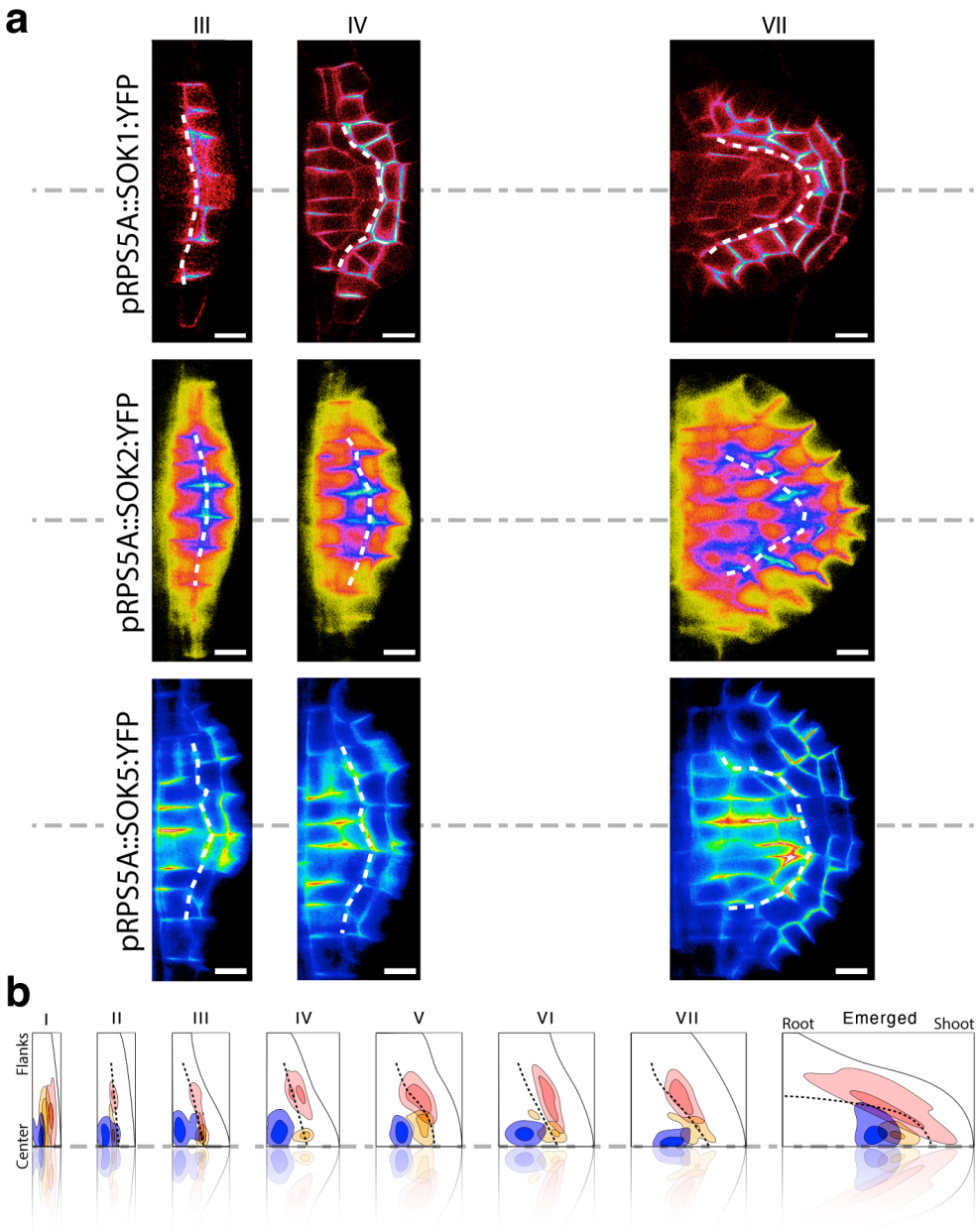

Figure 1.18: SOSEKI proteins accumulate near the PE interface. (a) Microscopy images showing uneven distribution of pRPS5A::SOK1:YFP, pRPS5A::SOK2:YFP, and pRPS5A::SOK5:YFP signal in various stages of LR development. Notably SOKs appear to accumulate near the PE interface (dashed white line). Symmetry axis (dashed gray line). Scale bar: 10µm. (2D images of pRPS5A::SOK1:YFP were captured with confocal microscopy, whereas pRPS5A::SOK2:YFP and pRPS5A::SOK5:YFP timelapses were captured with light sheet microscopy). (b) Spatial distribution of pRPS5A::SOK:YFP maxima plotted relative to LR dimensions for each developmental stage. Each "cloud" (red: SOK1, yellow: SOK2, blue: SOK5) indicates the region with the highest density of maxima points. Developmental stages and sample sizes: I (n = 126), II (n = 216), III (n = 294), IV (n = 234), V (n = 122), VI (n = 69), VII (n = 114), emerged (n = 213). LR widths taken during data processing of each stage: (I: 8-15µm, II: 15-23µm, III: 23-30µm, IV: 30-38µm, V: 38-45µm, VI: 45-50µm, VII: 50-60µm, emerged: 60-130µm). Across all stages, SOK maxima density is highest near the PE interface (black dashed line).

Importantly, the PE interface distinguishes two domains with differential growth. Namely, provascular cells appeared to undergo anisotropic growth, while ground tissue precursors appeared to undergo isotropic growth. This differential growth underlaid the transformation of the heterogeneous polarity pattern into a uniform polarity pattern (Figure 1.19, Movie 1). Namely, the differential growth shapes the tissue organization in such a way that the polarity pattern appears uniform. There was a small but notable exception for SOK1:YFP, whose polarity shifts in elongating provascular cells at stage IV, likely in response to newly formed ground tissue interfaces, which are known to attract SOK1 (Figure 1.20; Movie 2; Figure 3.6a, h) [Yoshida et al., 2019].

Together, these findings suggest that SOK proteins are attracted to a regions with differential growth, suggesting that there is a link between growth-derived mechanics and SOK accumulation.

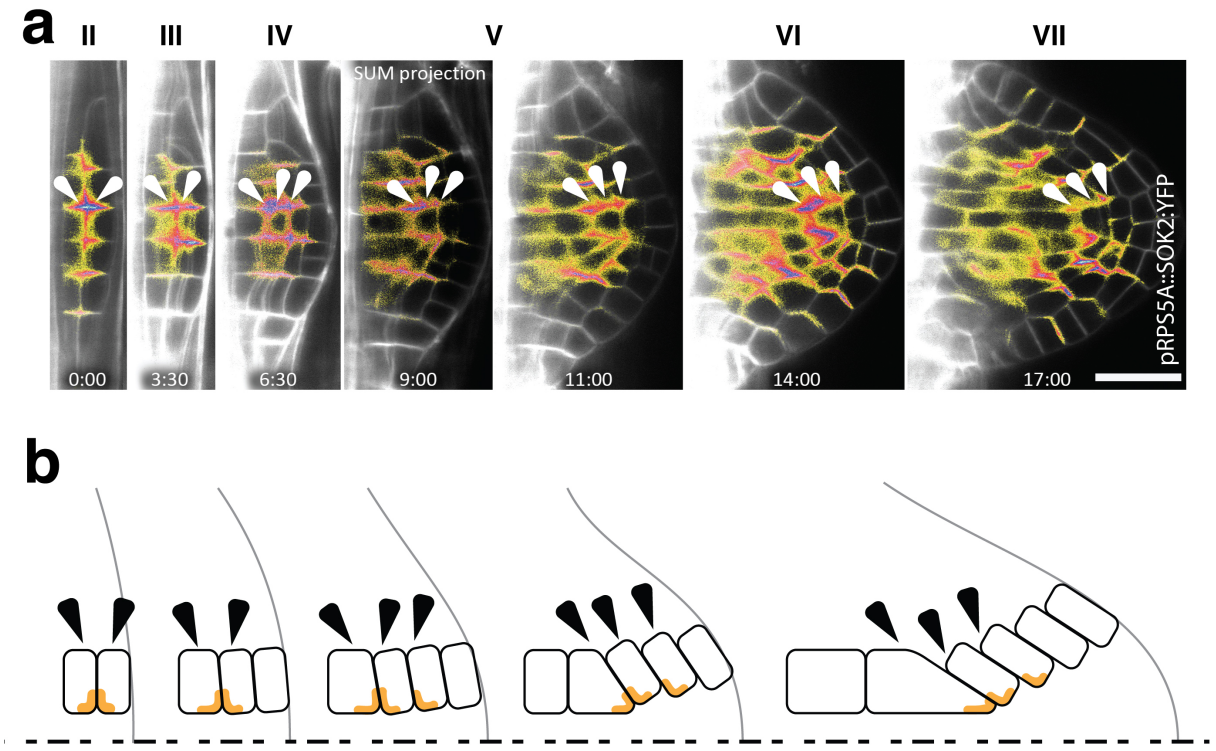

Figure 1.19: Cellular polarity gradually becomes visually uniform during differential growth in the developing LR. (a) Timelapse of pRPS5A::SOK2:YFP and pUBQ10::LTi6B:mCherry(x2). Pointers indicate the cells in the schematic below. (b) Schematic of cell layout during LR organogenesis. Pointers represent the indicated cells in the timelapse above. SOK2 polarization is indicated in orange/yellow, and gradually becomes uniform throughout development. The same phenomenon is illustrated in (Movie 1). Timestamp: hour:min. Scale bar 20µm.

Movie 1: pRPS5A::SOK2:YFP polarity pattern becomes coherent as a result of differential tissue growth.

Click here to view Movie 1
Click here to download Movie 1

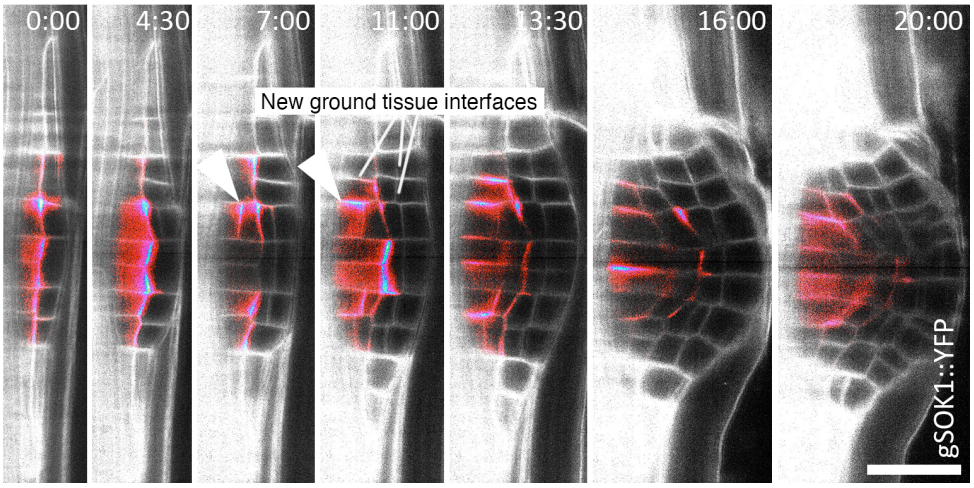

Figure 1.20: Timelapse of gSOK1::YFP reveals a polarity change in elongating provascular cells during stage IV (arrowhead; timestamp: 7:00–11:00), indicating a correlation between SOK1 polarization and either anisotropic growth or the formation of ground tissue interfaces in adjacent cells. Scale bar: 20µm. Timestamp: hour:min

Movie 2: Polarization change of gSOK1::YFP in elongating vascular cells of stage IV LRP.

Click here to view Movie 2
Click here to download Movie 2

1.2.5 SOSEKI proteins respond to tissue-level growth and mechanical cues

The SOK proteins accumulate at regions with differential growth, suggesting that there is a correlation between directional growth and SOK accumulation. Interestingly, when overlaying hypothetical growth domains as predicted by [Szymanowska-Pułka et al., 2012] on the the pRPS5A::SOK5:YFP signal, the pRPS5A::SOK5:YFP polarization was distinct in the different growth domains [Szymanowska-Pułka et al., 2012] (Figure 1.21). This observation suggests that there may be a quantifiable relationship between directional growth and SOK accumulation. To investigate this, I measured the PDGs and cellular growth anisotropy in timelapses with pRPS5A::SOK:YFP signal, for each SOK, using MorphoGraphX [de Reuille et al., 2015].

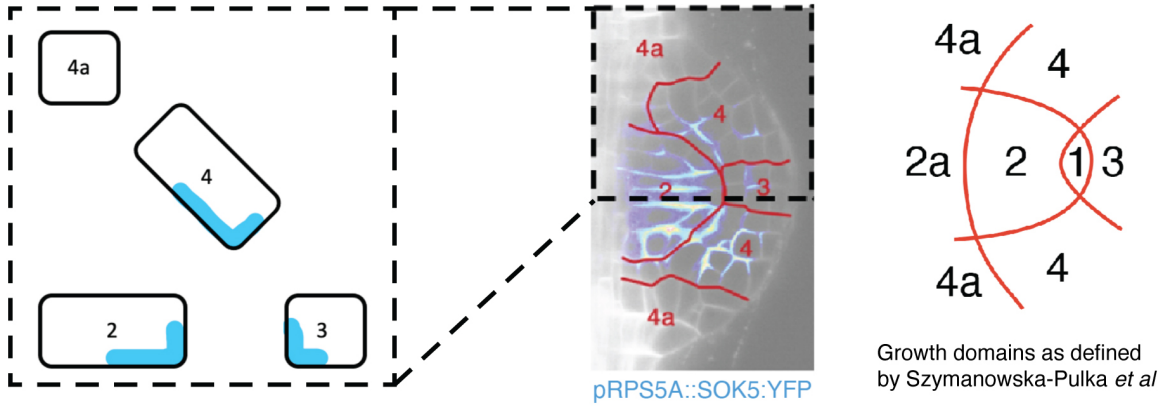

Figure 1.21: pRPS5A::SOK5:YFP polarization and intensity is distinct between different growth domains defined in the model by [Szymanowska-Pułka et al., 2012, Szymanowska-Pułka, 2007]. The figure is inspired by the spatial organization of growth domains in their simulation.

As expected, the resulting growth maps revealed that elongating provascular cells had anisotropic growth, whereas ground tissue precursors had an isotropic growth profile (Figure 1.22a). The PDGs in the provascular cells were parallel to the shoot-root axis of the LR, and PDGs in ground tissue precursors were predominantly parallel to the curvature of the LRP (Figure 1.22a). In line with previous results (Figure 1.18), when overlaying the pRPS5A::SOK:YFP signal, the highest intensities occurred near the region with differential growth (Figure 1.22b).

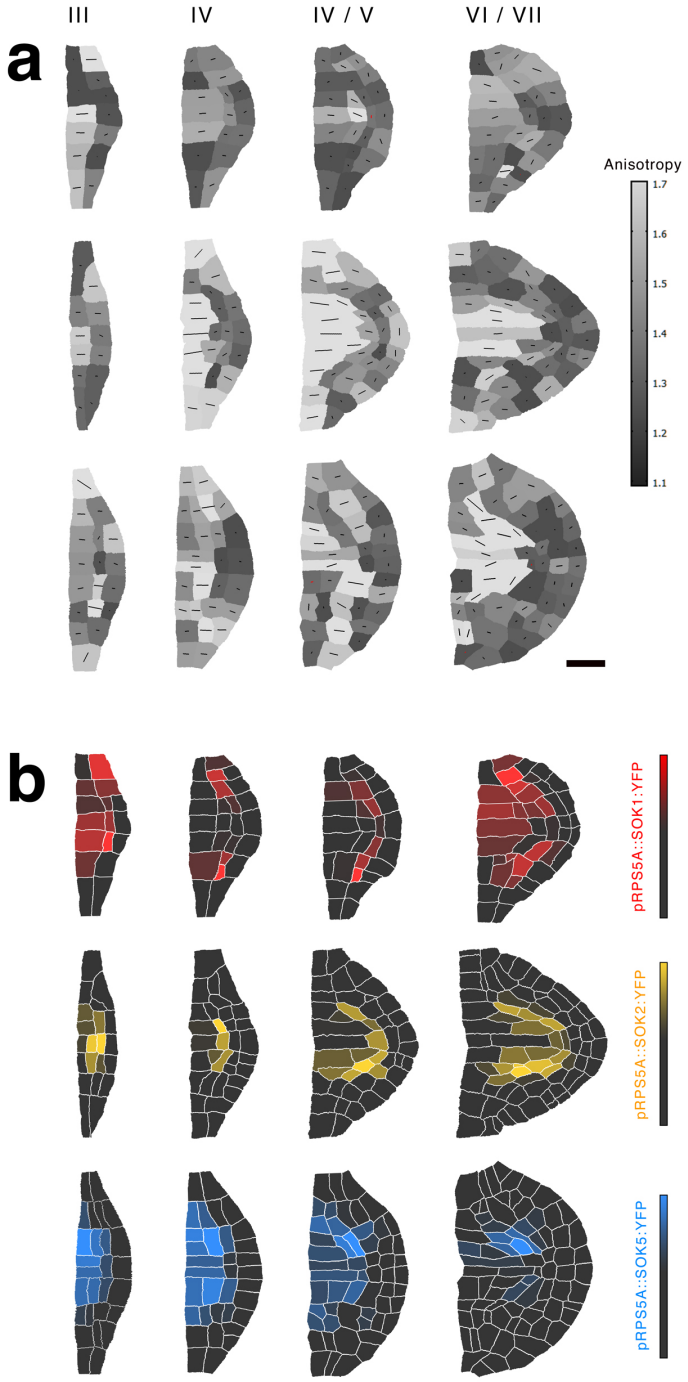

Figure 1.22: pRPS5A::SOK:YFP markers accumulate at the interface of differential growth. (a) Quantification of growth anisotropy and PDGs during LR organogenesis, indicating distinct growth patterns between provascular cells and ground tissue precursors. Grayscale shading indicates the degree of anisotropy (bright: high anisotropy; dark: low anisotropy), while PDG lines indicate the orientation of growth (StretchMax – StretchMin; line length reflects anisotropy, with longer lines indicating directional growth and shorter lines indicating isotropic growth; red lines are artefacts). (b) Signal intensity of pRPS5A::SOK1:YFP, pRPS5A::SOK2:YFP, and pRPS5A::SOK5:YFP overlaid on the developmental stages analyzed in (a), showing accumulation near regions with differential growth. Scale bar: 20µm.

There is no prominent correlation between SOK accumulation and anisotropic growth at the cellular level

To determine whether there is a correlation between pRPS5A::SOK:YFP signal intensity and anisotropic growth at the cellular level, I plotted cellular signal intensities (cortical or cytosolic) against cellular anisotropy. Although in general no strong or consistent correlation was observed, pRPS5A::SOK2:YFP and pRPS5A::SOK5:YFP exhibit moderate associations (Figure 1.23a).

To examine whether there is a correlation with differential growth between two adjacent cells and pRPS5A::SOK5:YFP signal intensity at the corresponding cell-cell interface, I measured two parameters: (i) the difference in growth anisotropy and (ii) the acute angle between the two PDGs of adjacent cells. Both metrics showed weak, non-significant, correlations (Figure 1.23b). In other words, there was a lack of a consistent cell-level correlation between pRPS5A::SOK:YFP signal intensity and directional growth.

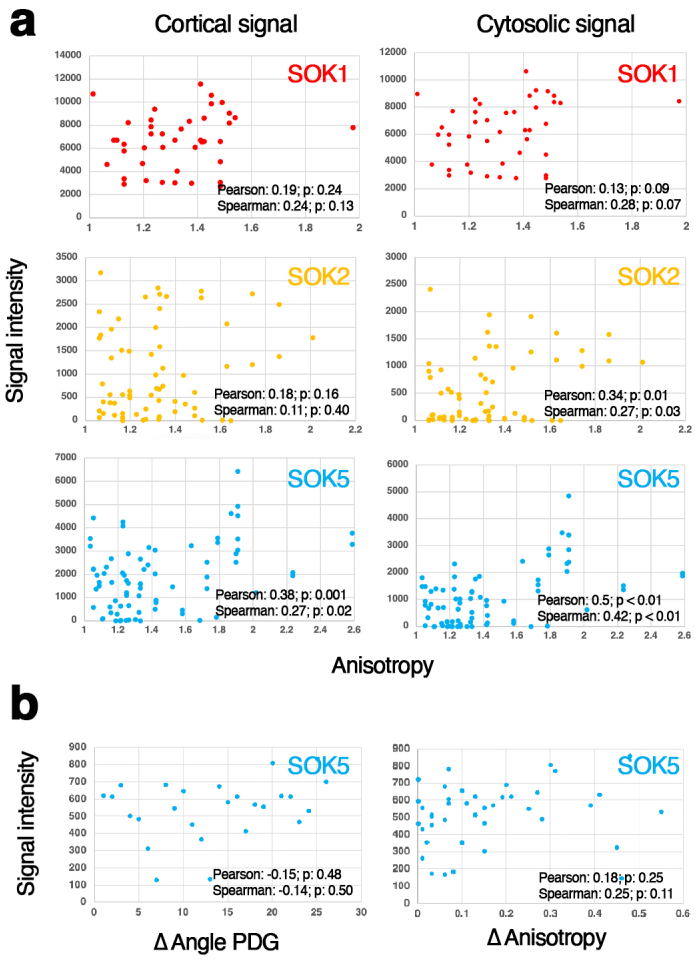

Figure 1.23: No consistent correlation was observed between pRPS5A::SOK:YFP signal intensity and growth at the cellular level. (a) Datapoints represent cells where either cortical or cytosolic signal intensity (signal/area) is plotted against anisotropic growth, for SOK1 (red), SOK2 (orange/yellow), and SOK5 (blue). (b) Signal intensity at the interface between two adjacent cells showed no correlation with the difference in anisotropy (ΔAnisotropy) or the difference in PDG angle between adjacent cells (ΔAngle PDG). Pearson and Spearman correlations were calculated with the help of ChatGPT, and then manually confirmed in Microsoft Excel.

SOKs dissipate in regions with mechanical stress in the SAM

The lack of a prominent cell-level correlation suggests that the relationship between SOK proteins and growth may be complex and that a prominent correlation may only be apparent at the organ level, because such a prominent visual correlation was observed consistently at the organ level (Figure 1.18b, 1.22b).

To test whether the organ-level relationship extended to other organs, I examined pRPS5A::SOK1/2/5:YFP in the different zones of the SAM, which are shaped by tissue dynamics [Alonso-Serra et al., 2024, Shi et al., 2018, Hamant et al., 2008, Uyttewaal et al., 2012]. Similar to LR organogenesis, despite the uniform activity of *pRPS5A*, microscopy revealed that the pRPS5A::SOK1/2/5:YFP signal was specifically absent in the creases (Figure 1.6b) near the peripheral zone and newly initiated aerial organs. This region is characterized by minimal growth and elevated mechanical stress arising from tissue dynamics (Figure 1.24) [Hamant et al., 2008], and suggests that SOK proteins respond to mechanical stress generated by tissue dynamics.

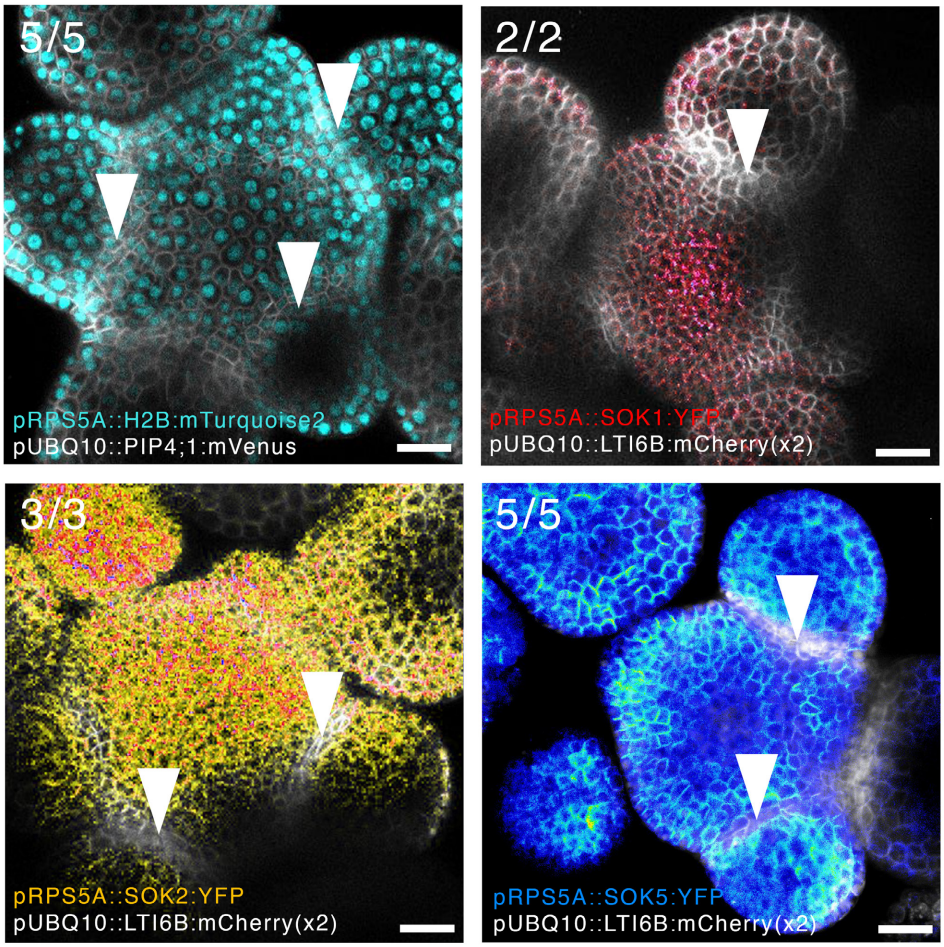

Figure 1.24: SOK proteins appear to be affected by tissue-derived mechanical stress. pRPS5A::SOK1:YFP, pRPS5A::SOK2:YFP, and pRPS5A::SOK5:YFP are absent in the creases of the SAM (white arrowhead), an area of minimal growth and high mechanical stress. Whereas, pRPS5A::H2B:mTurquoise2 shows uniform expression throughout the SAM. Replicate numbers shown in top-left. (b) Stress pattern deduced from microtubule orientation by [Hamant et al., 2008]. Schematic replicated from Hamant *et al*., 2008. Scale bar: 20µm.

1.3 Conclusion

Together, the findings in this chapter suggest that SOK proteins accumulate in specific regions at the organ level that are associated with differential tissue growth. Mechanical cues arising from these growth differences may influence SOK accumulation, as exemplified in the SAM, where SOKs are notably absent from crease regions (known to experience high mechanical stress). Together, the data support a model in which SOK proteins respond to local growth dynamics and mechanical context, rather than serving as markers of global polarity.

1.4 Discussion

I began this work with the question of how the orientation of global polarity changes during LR organogenesis. Unexpectedly, the results suggest that SOKs, initially thought to be stable markers of global polarity, instead sense local cues related to growth and tissue mechanics [Yoshida et al., 2019]. This interpretation fits within the unique constraints of plant development. Plant cells are physically isolated by rigid cell walls that limit their movement, yet cells remain mechanically connected through the same walls. In this context, plants rely on transmission of mechanical signals to coordinate multicellular development [Coen and Cosgrove, 2023, Hamant and Haswell, 2017]. This raises three questions about how SOKs may participate in such a mechanism:

1. Do SOSEKIs respond to mechanical cues?
2. What are determinants of SOSEKI polarity?
3. Do SOSEKIs link mechanics to intracellular responses?

1.4.1 Do SOSEKIs respond to mechanical cues?

During LR development, the SOKs accumulate near the PE region, whereas in the SAM, the SOKs are absent in the crease region (Figure 1.18, 1.24). The crease region is known to experience mechanical stress, whereas the mechanical stress pattern near the PE region is unknown [Hamant et al., 2008]. This raises the question whether SOK proteins respond to mechanical cues and how they respond to these mechanical cues.

To investigate this, it may be insightful to investigate the behaviour of SOKs in additional contexts where mechanical forces play a role. Namely, during the LR emergence, where the LRP pushes through the overlying PR tissues that provide mechanical resistance [Stöckle et al., 2022]. In addition, wound healing in the RAM could be used, where targeted laser ablation changes local mechanics [Hoermayer et al., 2024].

Furthermore, the SAM has a well-characterized mechanical stress pattern that is inferred from the orientation of cortical microtubules. Namely, supracellular alignment of cortical microtubules indicates a high level of mechanical stress [Hamant et al., 2008, Uyttewaal et al., 2012, Sampathkumar et al., 2014, Louveaux et al., 2016, Jacques et al., 2013, Li et al., 2023]. Characterizing the cortical microtubule orientation during LR organogenesis may provide insight into the mechanics that play a role during organogenesis.

Additionally, a new molecular tag, CarboTag-BDP, that binds to cell wall components offers a promising tool to approximate cell wall mechanics, potentially providing further insight into the mechanical state of the LR [Besten et al., 2024].

1.4.2 What are the determinants for SOSEKI polarity?

The SOK polarity pattern likely reflects a local polarity pattern. Yet, it is unknown what cue guides the polarization of the SOK proteins. In this chapter, there were indications that anisotropic growth, tissue-specific cues, interfaces, and mechanical cues may direct SOK polarity (Figure 1.16, 1.18, 1.20). During LR organogenesis, all these cues play a role in shaping the organ [Von Wangenheim et al., 2016, Banda et al., 2019], suggesting that organ patterning may affect SOK polarity. Investigating the SOK polarity pattern in mutants with aberrant organ patterning may help identify determinants of SOK polarity.

1.4.3 Do SOSEKIs link mechanics to intracellular responses?

The idea that SOKs respond to mechanics fits naturally with the constraints of plant development, where immobile cells must coordinate division within a mechanically connected network. Given the dependence of SOKs on cell wall integrity [Yoshida et al., 2019], it is tempting to speculate that SOKs connect external mechanical cues to intracellular responses, where the mechanical cues are propagated through the cell wall network [Gorelova et al., 2021, Ramalho et al., 2022b]. The exact cellular function(s) of SOK proteins remain speculative and experiments using loss-of-function (LOF) mutants will be essential to clarify this. Single LOF mutants do not have an apparent phenotype [van Dop, 2018], likely due to functional redundancy between the different SOKs, and generating a complete LOF mutant has been challenging, likely due to lethality (Andriy Volkov, pers. comm.). To address this, a strategy to induce a complete LOF mutant in a controlled way has been developed (Andriy Volkov, Dr. Reyes-Hernández). Their approach uses a quadruple *sok1/2/3/4* LOF mutant, with inducible knock down (KD) of SOK5. This approach provides a valuable system for investigating the function of SOK proteins.

Supplemental figures

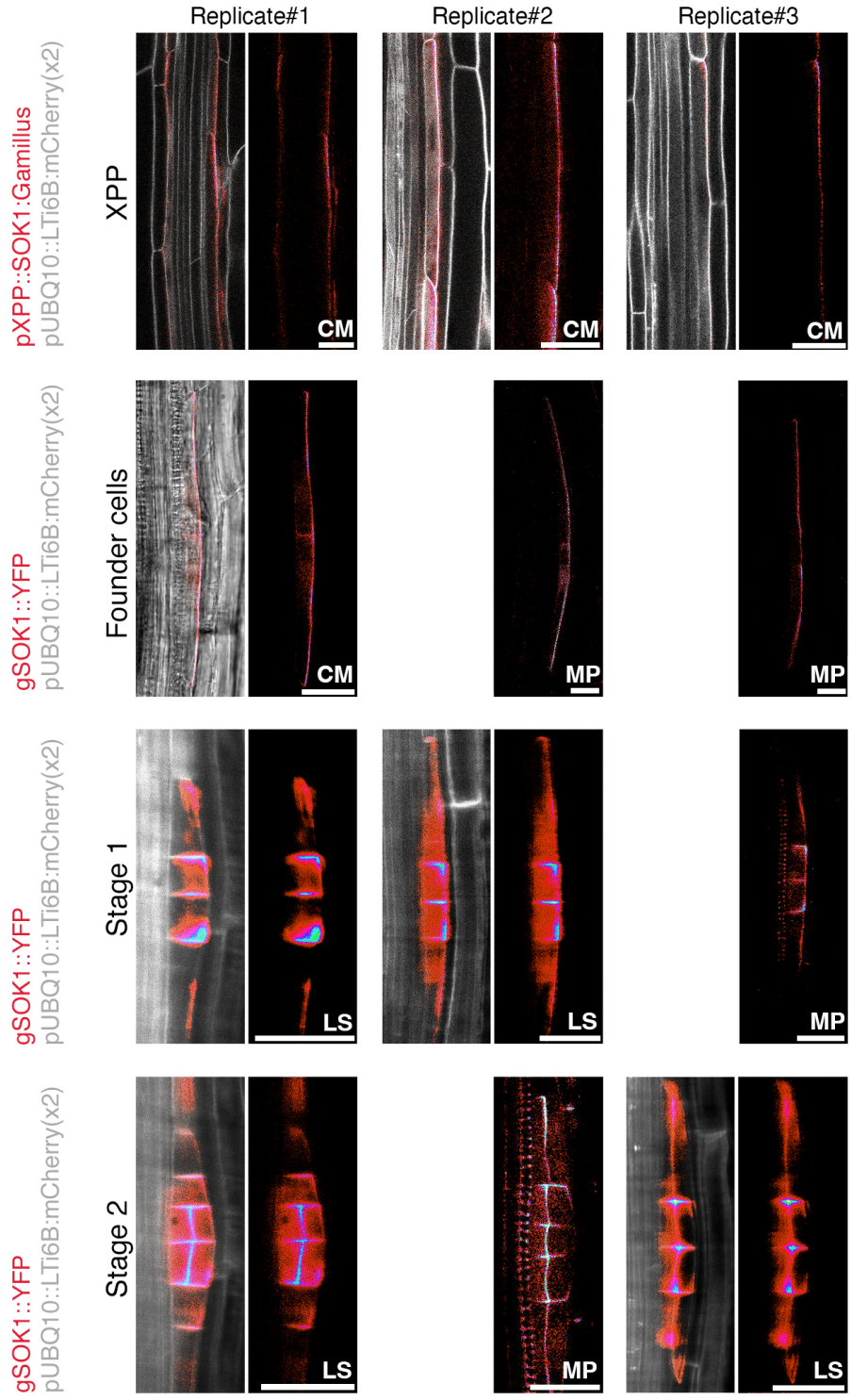

Figure 1.25: Three replicates of pXPP::SOK1:Gamillus and gSOK1::YFP polarization to illustrate their consistent polarity patterns between different biological replicates. Aquisition method is indicated in bottom right: confocal microscopy (CM), light sheet microscopy (LS), multiphoton microscopy (MP). Scale bar 20µm.

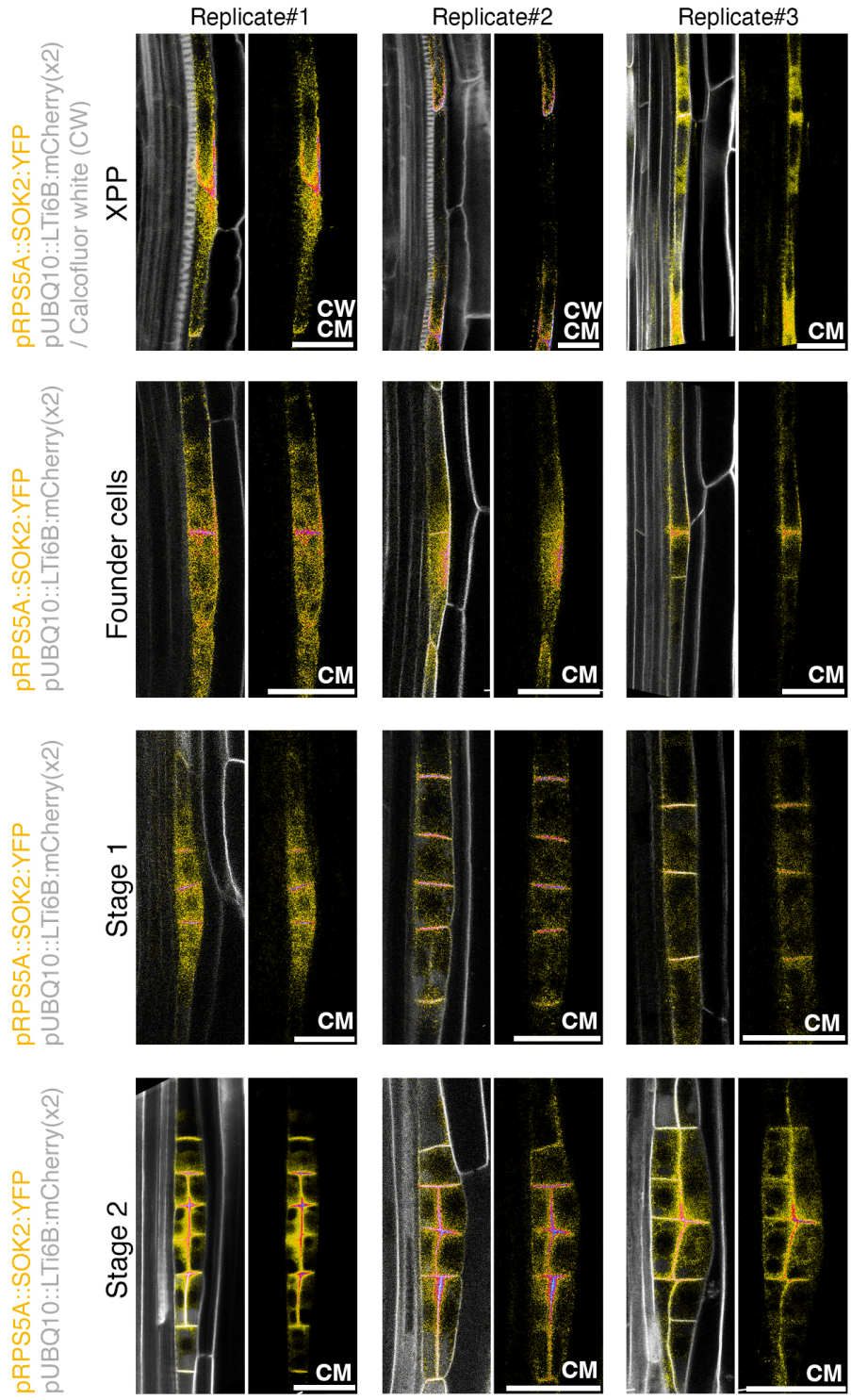

Figure 1.26: Three replicates of pRPS5A::SOK2:YFP polarization to illustrate their consistent polarity patterns between different biological replicates. Aquisition method is indicated in bottom right: confocal microscopy (CM). Staining method is indicated with: calcufluor white (CW). Scale bar 20µm.

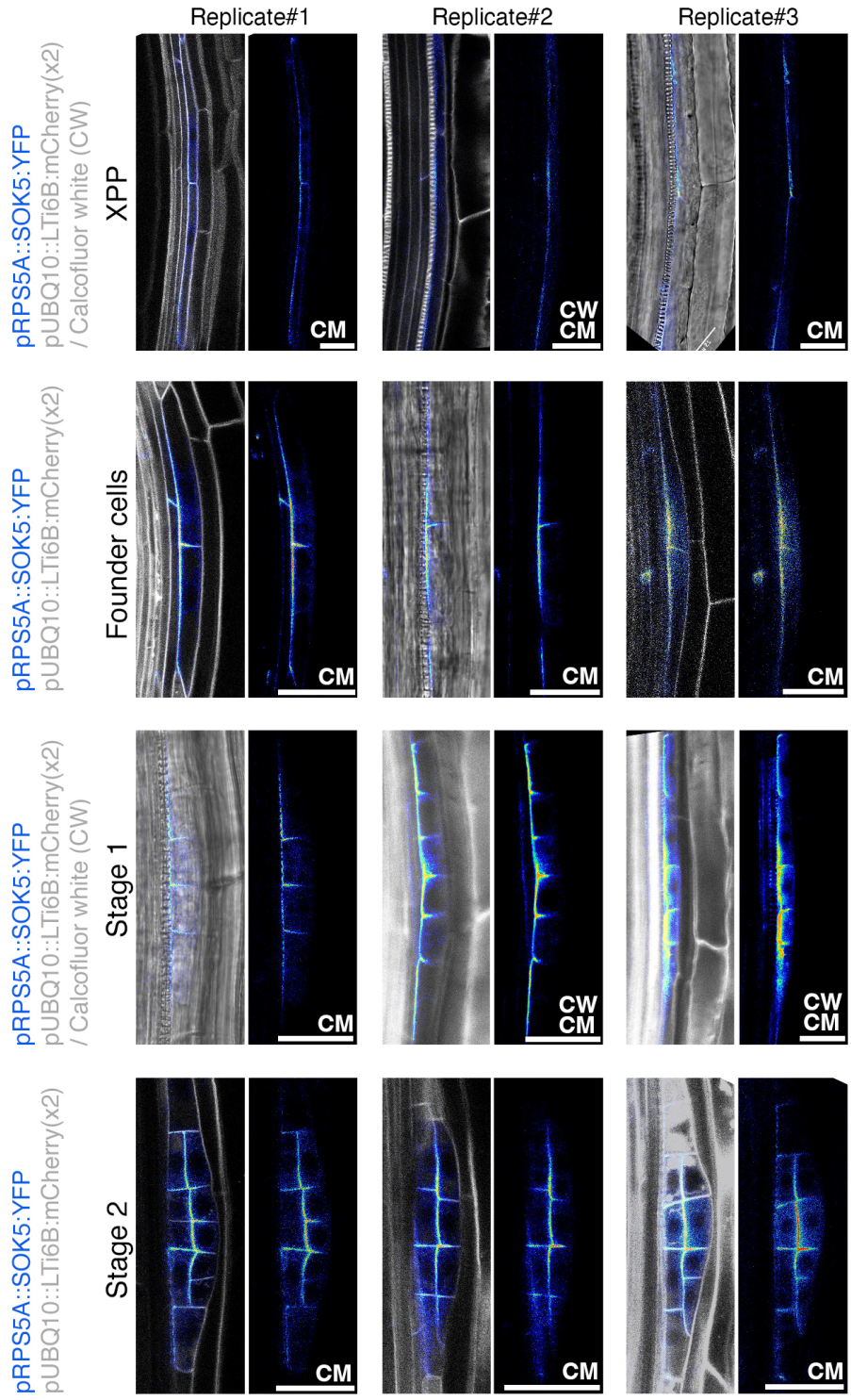

Figure 1.27: Three replicates of pRPS5A::SOK5:YFP polarization to illustrate their consistent polarity patterns between different biological replicates. Aquisition method is indicated in bottom right: confocal microscopy (CM). Staining method is indicated with: calcufluor white (CW). Scale bar 20µm.

Chapter 2

Heterogeneity attracts and stress repels: localization dynamics of SOSEKI proteins

2.1 Introduction

Plant development is characterized by its immobile yet interconnected nature, where plant cells are fixed in place, encased by a cell wall that mechanically links them to the continuum of the cell wall network. To coordinate multicellular development under these conditions, mechanical signaling between cells is essential, with forces and stress patterns transmitted through the continuum of the cell wall [Hamant et al., 2008, Cosgrove, 2016, Sampathkumar, 2020, Gorelova et al., 2021].

2.1.1 The cell wall continuum as a relay for mechanical signals

Under normal conditions, the cell wall network is in a stable mechanical state, where the internal turgor pressure of the cells is balanced by the resistance of the cell wall. If this balance changes, for example through changes in turgor pressure, it allows cells to quickly detect mechanical changes over long distances [Gorelova et al., 2021]. This principle has been compared to a spiderweb, where a change in tension at one point in the web can be felt at another point in the web [Gorelova et al., 2021] (Figure 2.1).

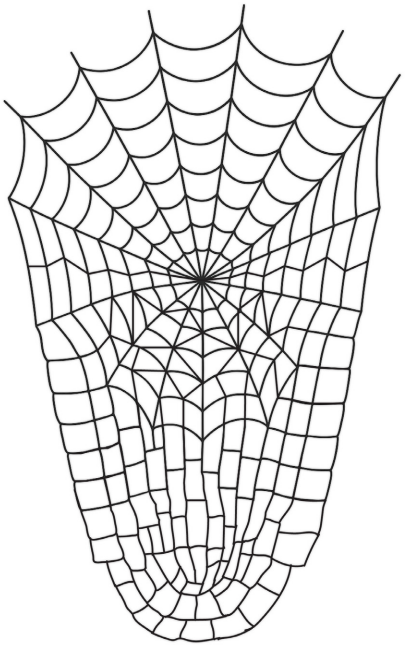

Figure 2.1: Mechanical cues may be transmitted through the cell wall network analogous to a spiderweb. Concept developed in ChatGPT; figure created in Illustrator.

Chapter 1 revealed that SOK proteins respond to local, probably mechanical, cues (Figures 1.22, 1.24). Importantly, SOK localization depends on cell wall integrity, as exemplified by disrupting cellulose synthesis or degrading the cell wall, both of which lead to protein internalization [Yoshida et al., 2019]. This raises the possibility that SOKs are sensitive to mechanical cues transmitted through the cell wall network. However, the exact relationship between SOKs and mechanics remains unclear. Specifically, it is unclear whether SOKs accumulate or dissipate in regions of high mechanical stress, as conflicting observations have been reported. For instance, in the LRP, SOKs accumulate near regions of differential growth (Figure 1.18, 1.22), which suggests that these are regions of mechanical stress [Trinh et al., 2021]. Whereas, in the creases of the SAM, which are known to experience high mechanical stress, SOKs are absent (Figure 1.24) [Hamant et al., 2008].

2.1.2 Objective

In this chapter, I aim to clarify whether there is a relationship between mechanical stress and SOK accumulation and what conditions favor SOK accumulation or dissipation. To this end, I will investigate the behavior of SOKs in response to compressive stress generated during LR emergence. During LR emergence, a growing LR must push through overlying tissues, exerting compressive stress on the LRP. Additionally, to investigate changes in subcellular localization of the SOKs in response to mechanical changes, the tractable wound healing assay in the RAM will be used [Hoermayer et al., 2024]. Here, a change in tissue mechanics is induced by ablation of a single cell in the RAM, and thus allows temporal control over mechanical changes and the investigation of subsequent subcellular localization changes. Furthermore, to clarify the type of mechanical state that allows the SOKs to accumulate in the developing LRP, I will use a new molecular probe for assessing cell wall mechanics together with mapping the microtubule orientation pattern in the developing LR [Besten et al., 2024, Hamant et al., 2008].

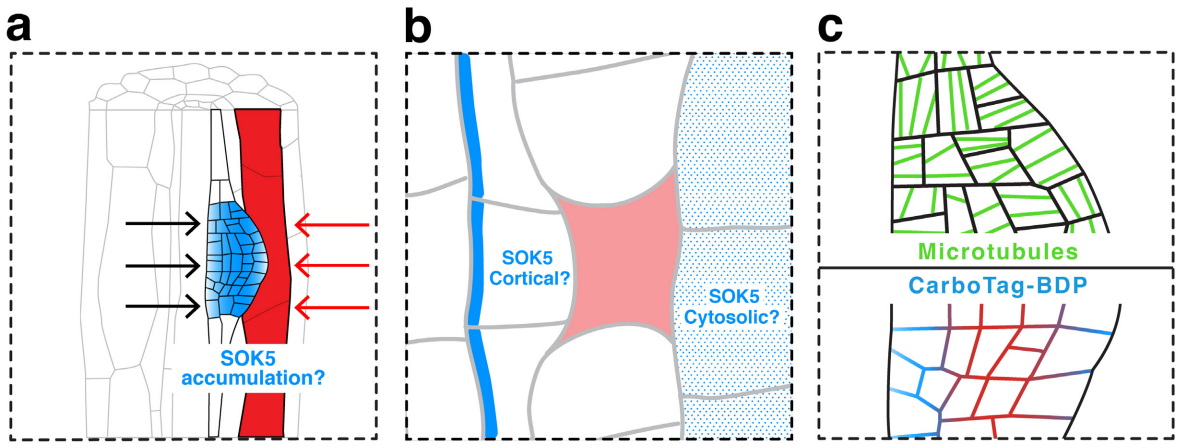

Figure 2.2: How do mechanical cues affect the SOK proteins? (a) During LR, the overlying tissues (red) exert compressive stress on the developing LR. How does compressive stress affect SOK accumulation? (b) The developmental context of targeted cell ablation in the RAM is a tractable system to perturb mechanical forces and observe resulting changes in SOK localization at the cellular scale. How is subcellular localization affected by changes in mechanics? (c) Cortical microtubule orientation may serve as a reporter of the mechanical stress pattern, while CarboTag-BDP can provide insights into cell wall mechanics. What is the mechanical state of the LRP?

2.1.3 Mechanics during LR emergence

During LR emergence, the growing LR encounters mechanical obstacles posed by the overlying tissues (the endodermis, cortex, and epidermis). To accommodate for LR emergence, these overlying tissues are modified with precise spatio-temporal control [Vilches-Barro and Maizel, 2015].

The endodermis naturally limits outward proliferation of pericycle cells, which is exemplified by its removal that results in a periclinal division in the pericycle rather than an anticlinal division [Marhavý et al., 2016]. During LR initiation, an auxin-dependent signal is relayed to the overlying endodermis, triggering its spatial accommodation [Marhavý et al., 2013, Marhavý et al., 2016, Stöckle et al., 2022, Ramos et al., 2024, Vermeer et al., 2014]. This accommodation response is polarized, where the cortical microtubules at the interface, facing the developing LRP, are reorganized [Stöckle et al., 2022]. This reorganization accommodates for LR emergence, as was exemplified by disrupting this reorganization that resulted in delayed emergence. Furthermore, it is thought that this lack of microtubule reorganization increases compressive stress on the LRP [Stöckle et al., 2022]. This

disruption of the endodermal microtubules was done by endodermis-specific and inducible depolymerizing of microtubules using a truncated version of PROPYZAMIDE-HYPERSENSITIVE 1 (PHS1ΔP) [Stöckle et al., 2022]. This is a valuable genetic tool to investigate how increased compressive stress in the LRP may affect SOK accumulation.

When a LRP emerges through the endodermis, it encounters the cortex and epidermis that are additional barriers. The emergence through these layers is regulated by a spatially controlled auxin response [Vilches-Barro and Maizel, 2015]. Specifically, outward polar auxin transport from the LRP induces auxin accumulation in the overlying tissues, which in turn activates the expression of cell wall-modifying enzymes in the cortex and epidermis. These enzymes loosen the surrounding tissues, allowing the LRP to grow and emerge [Benková et al., 2003, Swarup et al., 2008, Vilches-Barro and Maizel, 2015]. Due to the rapid growth of the developing LRP, the LRP emerges through the cortex and epidermis in rapid succession.

The growth of the LRP itself is regulated by an auxin-dependent spatial expression pattern of aquaporins, particularly PLASMA MEMBRANE INTRINSIC PROTEINS (PIPs). These proteins facilitate asymmetric water uptake, generating hydraulic forces that are believed to push the LRP through the overlying tissues [Maure et al., 2008, Péret et al., 2012].

Although the overlying tissues are remodeled to accommodate for emergence, LR growth has been anecdotally reported and personally observed to accelerate after passing through each tissue layer. This implies that growth against these accommodating layers mechanically restricts the LR and generates compressive stress within the LRP. Monitoring SOK behavior during the transient phases of constrained growth and associated compressive stress could provide insight into how such stress affects SOK accumulation.

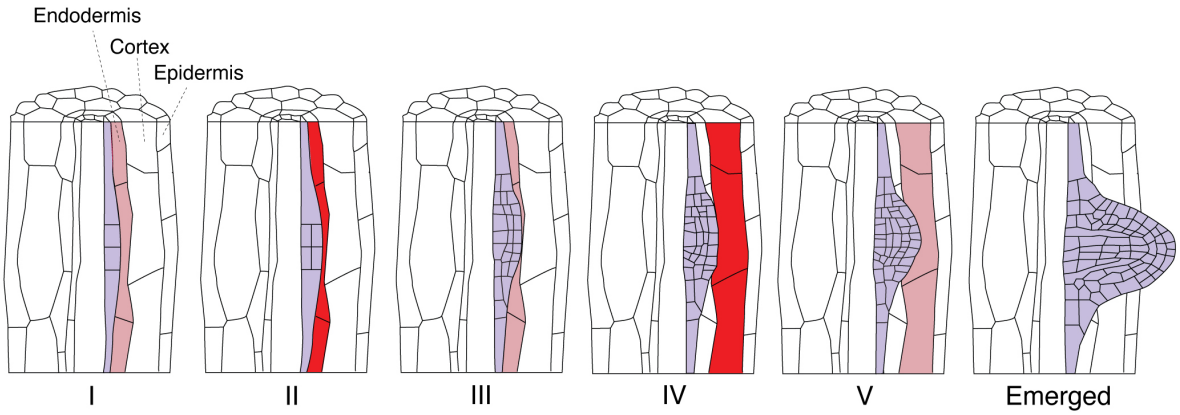

Figure 2.3: Mechanical barriers and corresponding compressive stress (red) during LR emergence. During development up to stage II, the endodermis acts as the primary mechanical barrier; afterwards, the cortex (and epidermis) become the main barriers. The shading of red indicates the magnitude of compressive stress, dark red being more intense than light red.

2.1.4 Wound healing assay: a mechanical response to targeted cell ablation

The removal of a cell alters the surrounding mechanical stress pattern [Robinson and Kuhlemeier, 2018, Demes and Verger, 2023, Melogno et al., 2024, Hoermayer et al., 2020]. This was exemplified with the wound healing assay, where a ground tissue cell was removed through targeted laser ablation, which results in a local pressure drop [Hoermayer et al., 2024]. In cells adjacent to the ablation site, the mechanical strain increases, where surrounding cells expand towards the ablation site. Vascular cells expand more than ground tissue cells, likely reflecting differences in the underlying mechanical stress pattern. That is, the vasculature is thought to be under compression, while surrounding ground tissues are under circumferential tension (Figure 2.4) [Gorelova et al., 2021, Hoermayer et al., 2024, Kutschera and Niklas, 2007, Asaoka et al., 2023]. The mechanical changes induced by cell ablation trigger the reorientation of cortical microtubules, which in turn guides the orientation of the cell division plane, a process essential to restore tissue organization [Hoermayer et al., 2024]. Observing SOKs at the subcellular level following ablation may reveal how SOK proteins respond to changes in mechanics.

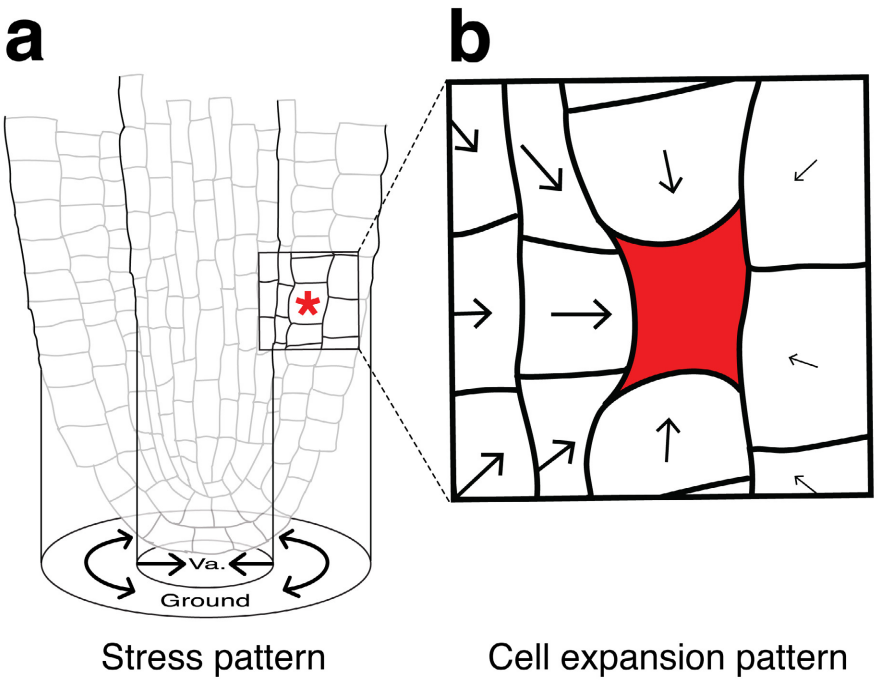

Figure 2.4: Ablation in the RAM induces expansion of surrounding cells. (a) Schematic of the RAM with its hypothetical mechanical stress pattern, where the vascular tissue is under compression and the ground tissue experiences circumferential tension. A region is highlighted where a cortex cell is targeted for laser ablation (red asterisk). (b) Magnified view of the ablated region. Cells adjacent to the ablation site, as well as distant cells, expand toward the site of ablation. Ground tissue cells expand less than vascular cells, indicated by the scale of the arrows.

2.1.5 CarboTag-BDP: a proxy for cell wall mechanics

Differential growth in the developing LR likely generates local mechanical stress, which in turn can influence the composition of the cell wall [Jonsson et al., 2022a, Willats et al., 2001, Jarvis et al., 2003]. To examine the effects of differential growth on the cell wall, the recently developed fluorescent molecular probe, CarboTag-BDP, may be used [Besten et al., 2024, Michels et al., 2020]. CarboTag-BDP measures the local molecular crowdedness in the cell wall. It does this by binding to cell wall components, where its fluorescence lifetime, which is the time spend in the excited state after absorbing light, increases when the local environment is more viscous or crowded [Besten et al., 2024, Michels et al., 2020]. This effect arises because molecular rotation of CarboTag-BDP is hindered in a crowded environment. Consequently, it remains longer in the excited state before returning to the ground state in crowded environments, resulting in a longer lifetime. Conversely, in a less crowded or less viscous environment, the probe can rotate more freely, resulting in a shorter fluorescence lifetime. Thus, the fluorescence lifetime of CarboTag-BDP is a proxy for cell wall crowdedness [Besten et al., 2024, Michels et al., 2020]. This has been used to verify cell wall mechanics in three developmental contexts in *Arabidopsis* [Besten et al., 2024]. That is, (i) by treating plants with isoxaben, which inhibits cellulose synthesis and triggers pectin de-esterification as a potential rescue response. Here, CarboTag-BDP has a higher fluorescence lifetime in root epidermal cells compared to mock-treated samples, reflecting a denser pectin network. (ii) FERONIA is a pectin-binding receptor-like kinase that functions in the maintenance of cell wall integrity [Malivert et al., 2021, Feng et al., 2018]. In *feronia* mutants, with impaired cell wall integrity, there is a decrease in fluorescence lifetime in the root compared to wildtype, consistent with the expected increase in cell wall porosity. (iii) Before and after hormone-induced stomatal closure there is a significant difference in fluorescence lifetime in the cell wall of guard cells, reflecting changes in cell wall mechanics. These findings illustrate that CarboTag-BDP can detect biologically relevant cell wall mechanics, and is thus a promising new tool [Besten et al., 2024].

2.1.6 Microtubule orientation as an indicator of mechanical stress

Cortical microtubules are well established indicators of mechanical stress. They typically align with the direction of maximal tensile stress at the cellular level, and at the tissue level, sufficiently strong tissue-derived stress can produce supracellular anisotropic alignment patterns. In contrast, isotropic alignment of microtubules usually reflects heterogenous stress patterns [Jonsson et al., 2022a, Hamant et al., 2008, Uyttewaal et al., 2012, Sampathkumar et al., 2014, Louveaux et al., 2016, Jacques et al., 2013].

On the cellular level, the response to mechanics is most apparant in pavement cells, where the cortical microtubules show anisotropic alignment at indentations, where the tensile stress is relatively high [Sampathkumar et al., 2014].

At the tissue level, striking supracellular alignments are observed in the crease region of the SAM, where cells experience compressive stress (Figure 2.5) [Hamant et al., 2008, Louveaux et al., 2016, Uyttewaal et al., 2012], and after targeted cell ablation in the hypocotyl, which induces a ring-like alignment pattern in cells surrounding the ablation site [Robinson and Kuhlemeier, 2018, Demes and Verger, 2023, Melogno et al., 2024]. Such patterns may become detectable after roughly two hours [Jacques et al., 2013, Louveaux et al., 2016, Hamant et al., 2008, Hoermayer et al., 2024, Uyttewaal et al., 2012]. Observing cortical microtubule orientation in the LRP may help identify regions with tissue-derived mechanical stress.

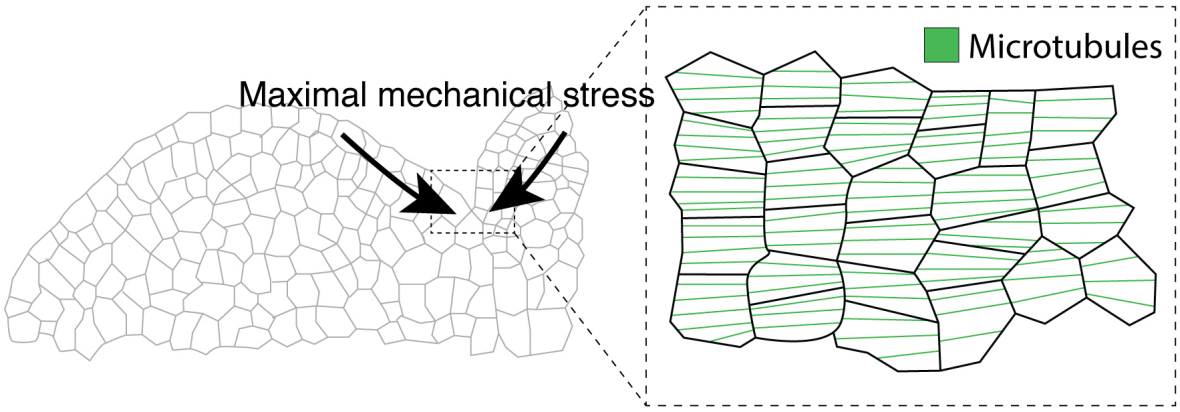

Figure 2.5: In the SAM, cortical microtubules exhibit supracellular anisotropic alignment in the crease region, which is a zone with maximal mechanical stress. Figure inspired by [Hamant et al., 2008]. SAM outlines replicated from [Fuchs and Lohmann, 2020].

2.2 Results

2.2.1 SOSEKIs dissipate in LRP experiencing compressive stress

During LR emergence, the LRP passes through the endodermis, cortex and epidermis [Vilches-Barro and Maizel, 2015]. Experimental data suggest that the endodermis acts as a mechanical barrier, generating compressive stress on stage II LRP as it grows outward and presses against the endodermis [Stöckle et al., 2022]. Much less is known about the mechanical stress experienced by the LRP as it pushes against the cortex and epidermis. I hypothesized that a similar compressive stress acts on the growing LRP. To test this, I ablated cortex cells overlying a stage IV LRP and measured the resulting change in LRP length. Indeed, a noticeable increase in length was observed almost immediately after ablation (Figure 2.6; n=5 LRP). This rapid increase in length indicates a release of mechanical tension and suggests that LRP experience mechanical compression in stage IV.

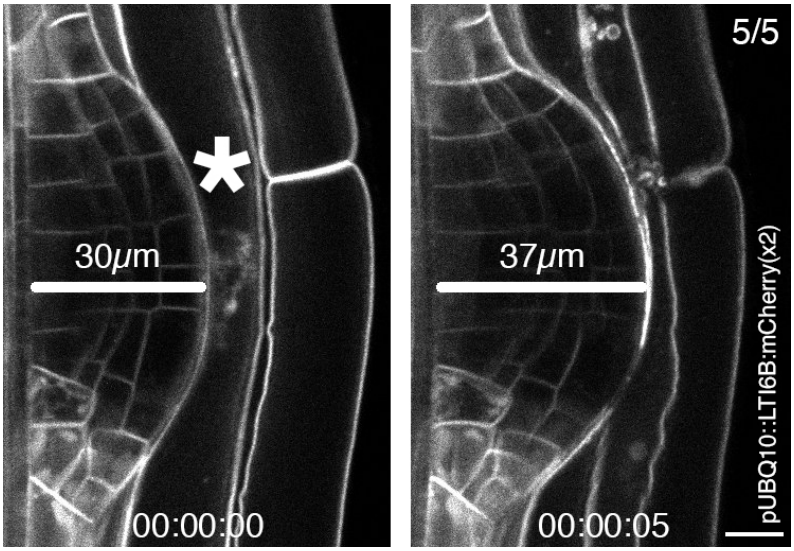

Figure 2.6: Immediate pressure release post cortex ablation. The cortex was ablated (asterisks) and imaged roughly five seconds later. The PR length increased by 7µm, indicating a release of pressure. Similar increases in LR length were observed in five independent samples (top right). Scale bar 10µm. Timestamp: (hour:min:sec)

Thus, the LRP experiences compressive stress, where compressive stress may peak in stage II prior to endodermis emergence and in stage IV prior to cortex emergence (Figure 2.3). To investigate how SOKs respond to this compressive stress, I live-imaged pRPS5A::SOK5:YFP from stage II to emergence using light sheet microscopy [Yoshida et al., 2019]. From the resulting timelapse, I quantified LRP length and measured the normalized pRPS5A::SOK5:YFP signal intensity. These values were plotted alongside each other, over time, to assess a potential correlation between growth and pRPS5A::SOK5:YFP accumulation (Figure 2.7a). Strikingly, the pRPS5A::SOK5:YFP signal increased during phases of growth and dropped sharply during periods of little to no growth (n=3 timelapses). This dynamic pattern occurred despite the RPS5A promoter being active throughout organogenesis (Figure 2.7c). Furthermore, there was no correlation between *RPS5A* promoter activity and LRP length, which suggests that changes in pRPS5A::SOK5:YFP signal intensity are independent of transcriptional regulation (Figure 2.7c). The periods of minimal growth and decreased pRPS5A::SOK5:YFP signal intensity corresponded to the period prior to emergence through the endodermis and cortex, suggesting that compressive stress suppresses SOK accumulation (Movie 3). Furthermore, a similar trend was observed for pRPS5A::SOK2:YFP in an

independent experiment, suggesting that SOK2 responds to compressive stress in a similar way.

To confirm the role of compressive stress, I ablated cortex cells using a UV laser to relieve compressive stress and tracked pRPS5A::SOK5:YFP dynamics in the developing LRP (n=2 timelapses). Remarkably, pRPS5A::SOK5:YFP signal remained consistently high throughout organogenesis (Figure 2.7b). On average, signal intensity was approximately 3.5-fold higher than in unablated samples (data not shown due to normalization). This consistent and strong pRPS5A::SOK5:YFP signal in the absence of overlying tissues suggests that compressive stress triggers the dissipation of the SOKs.

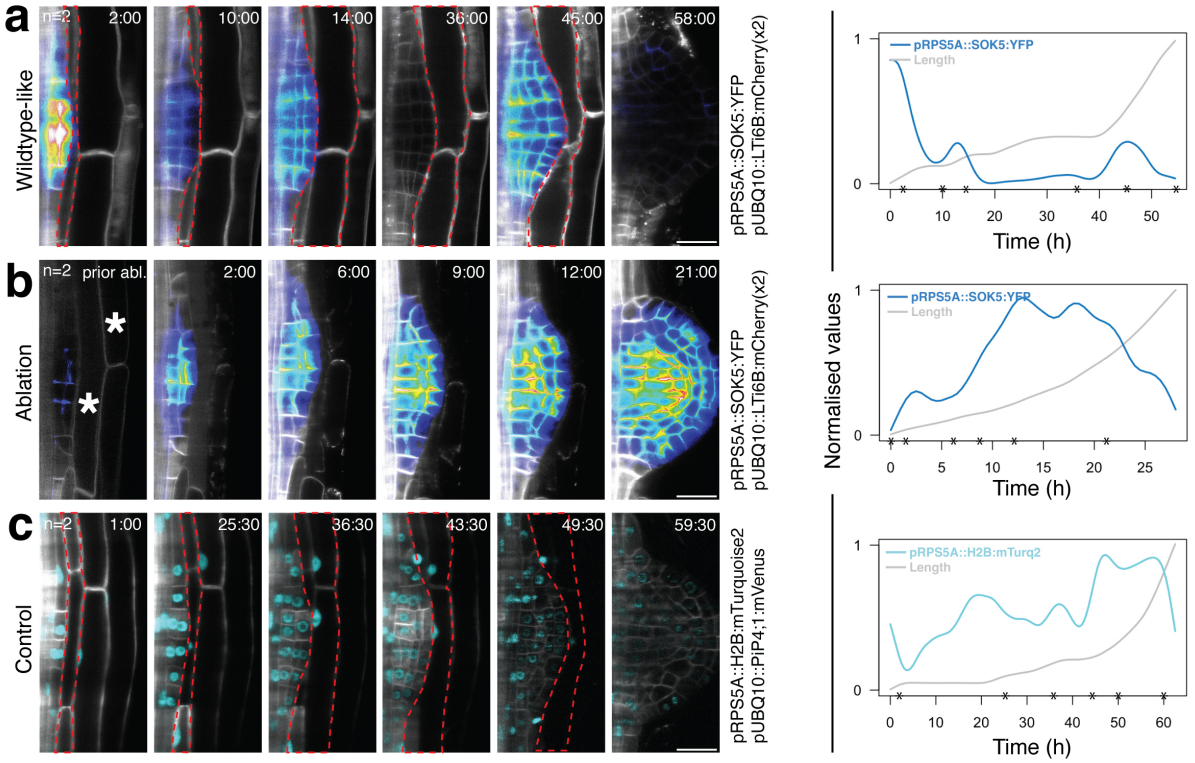

Figure 2.7: Compressive stress during LR emergence affects pRPS5A::SOK5:YFP accumulation. (a) In wildtype roots, pRPS5A::SOK5:YFP signal intensity decreases during periods of little to no growth and reappeared once the LRP emerged through the endodermis or cortex. (b) In samples where the overlying cortex and epidermis were ablated (asterisks), pRPS5A::SOK5:YFP signal remains consistently high throughout the emergence process. (c) pRPS5A::H2B:mTurquoise2 expression with nuclear signal throughout LR organogenesis indicates that there is no correlation between pRPS5A promoter activity and LR length. Time: (hours:min). Endodermis and cortex are outlined in red in the relevant stages. Scale bars: 20µm.

Movie 3: pRPS5A::SOK5:YFP signal and LR length during LR emergence with and without ablation of overlying tissues. The ablated movie starts later so that the developmental stages are synchronous.

Click here to view Movie 3
Click here to download Movie 3

For an additional and more targeted analysis, I focused on the emergence through the endodermis during LRP stage II. This process depends on reorganization of cortical microtubules in the overlying endodermis, where disruption of this reorganization is thought to generate compressive stress in the growing LRP [Stöckle et al., 2022]. To induce microtubule depolymerisation I used a verified two-component driver-reporter system (pCASP1»PHS1ΔP), of which the driver was coupled to the promoter of casparian strip membrane protein 1 (pCASP1) [Roppolo et al., 2011], and the reporter expressed PHS1ΔP. [Fujita et al., 2013, Vilches Barro et al., 2019, Stöckle et al., 2022, Moore et al., 2006]. Expression was induced by treating *pCASP1»PHS1ΔP* plants with dexamethasone (DEX), which specifically depolymerizes microtubules in the endodermis. To verify that microtubules were depolymerized, the plants had an additional microtubule marker consisting of microtubule-associated protein 4 (MAP4) fused to mVenus driven from *pCASP1*. Indeed, in DEX-treated plants, the MAP4:mVenus signal was noticeably lower, indicating that the LRP is experiencing compressive stress (Figure 2.8). To assess the effect of this compressive stress on pRPS5A::SOK5:YFP accumulation, *pRPS5A::SOK5:YFP* was transformed into the *pCASP1»PHS1ΔP* background, and the mean pRPS5A::SOK5:YFP signal intensity was determined in Mock- and DEX-treated samples. Strikingly, signal intensity was significantly reduced in the DEX-treated group, suggesting that compressive stress caused dissipation of pRPS5A::SOK5:YFP, which is consistent with the previous experiment.

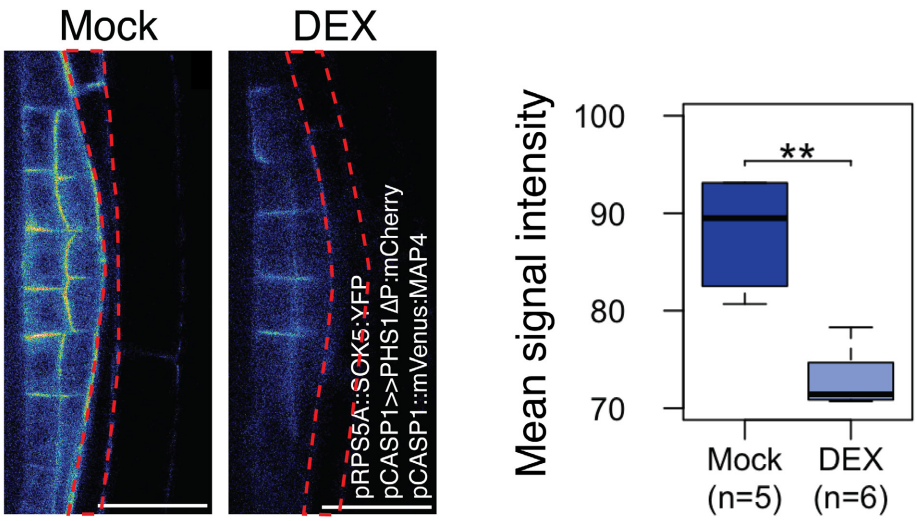

Figure 2.8: pRPS5A::SOK5:YFP signal intensity is significantly lower in stage II LRP when microtubules in the overlying endodermis are depolymerised (DEX). Dashed red line outlines the endodermis. Statistical test: Wilcoxon rank-sum test (** indicates P < 0.01). Scale bar 20µm. Data generated jointly with Laura Schütz.

2.2.2 Cortical SOSEKI localisation is affected during the wound healing assay

The SOKs dissipate in regions experiencing high mechanical stress (Figure 1.24, 2.7, 2.8), which suggests that SOKs internalize in response to mechanical stress. To examine how subcellular SOK localization is influenced by mechanics, I used the tractable wound-healing assay to induce a local pressure drop by targeted laser ablation of a cortex cell in the RAM, and monitored the subsequent localization of pRPS5A::SOK5:YFP (n=6 timelapses) [Yoshida et al., 2019, Hoermayer et al., 2024, Marhava et al., 2019, Hoermayer et al., 2024].

Strikingly, following ablation, there was a rapid (<1min) and visually apparent decrease in cortical pRPS5A::SOK5:YFP signal in all cells throughout the organ (Movie 4. This suggests that the pressure drop is sensed throughout the organ. To investigate whether the SOK proteins internalized, I measured the normalized pRPS5A::SOK5:YFP signal intensity at the cortex and in the cytosol. Indeed, the cortical signal decreased within the first 120 seconds, whereas the cystolic signal increased in the same period. This indicates that SOK proteins internalize in response to mechanical changes.

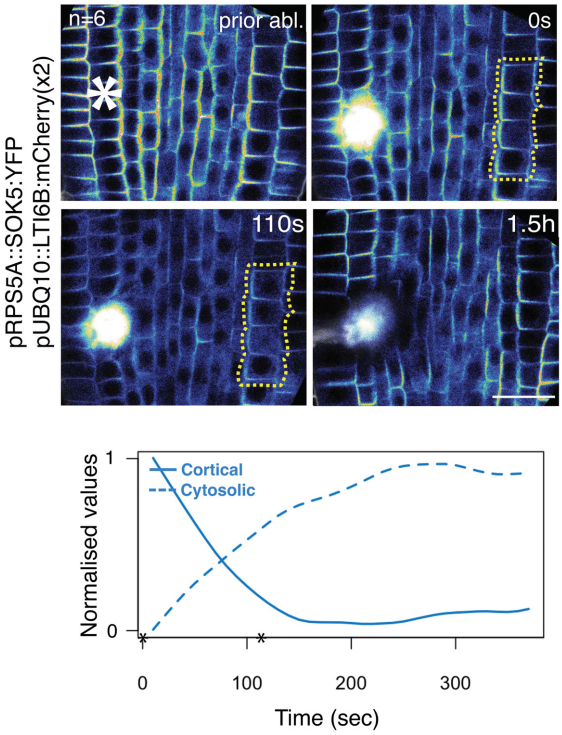

Figure 2.9: pRPS5A::SOK5:YFP localization is affected throughout the organ following a pressure drop in the RAM. The cortical pRPS5A::SOK5:YFP signal decreases shortly after ablation, whereas the cytosolic signal increases. Cell contours are marked by pUBQ10::LTI6B:mCherry(x2). Normalized values are the ratio of pRPS5A::SOK5:YFP over the LTI6B:mCherry(x2) values, normalized between 0 and 1. Asterisks (*) on the image indicates the ablation site. Asterisks (*) on the graph indicate the timepoint from the images. Scale bars: 20µm.

Movie 4: pRPS5A::SOK5:YFP post ablation of a cortex cell in the RAM. Cortical signal decreases and cytosolic signal increases throughout the organ. Control is an independent recording without ablation.

Click here to view Movie 4
Click here to download Movie 4

2.2.3 The lateral root has a heterogenous mechanical state

SOK proteins appear to respond to mechanical stress in a magnitude-dependent way where they are absent in cells experiencing high mechanical stress (Figures 1.24, 2.7). However, SOKs accumulate in the developing LR, where differential growth between provascular cells and ground tissue precursors may generate mechanical stress (Figure 1.18, 1.22). Thus, the relationship between SOKs and mechanics remains speculative. To clarify this, it is important to characterize the mechanical state of the developing LR to determine which conditions favor SOK accumulation in the developing LR. To this end, I used both CarboTag-BDP and microtubule markers to infer the mechanical state of the developing LRP, where CarboTag-BDP fluorescence lifetime is a proxy for cell wall mechanics (or porosity) and microtubule orientation a proxy for mechanical stress patterns [Besten et al., 2024, Hamant et al., 2008].

CarboTag–BDP patterns reveal a graded pattern of cell wall mechanics along the radial axis

Fluorescence lifetime measurements of CarboTag-BDP were taken in each developmental stage from XPP cells to emergence. In XPP cells through to stage IV, there were no apparent differences in fluorescence lifetime at the organ level (Figure 2.10a). Whereas, in LRP stages beyond stage IV, which actively undergo differential growth, the inner cell walls appeared different from the cell walls near the boundary of the organ (Figure 2.10a, b). To systematically assess this, I quantified the intensity-weighted fluorescence lifetimes at key interfaces in LRP beyond developmental stage IV. That is, interfaces between epidermis cells (edge), cortex–endodermis (ground), pericycle–endodermis (PE), and between vascular cells. The measurements revealed subtle but consistent differences in fluorescence lifetimes between tissue interfaces, with a significant graded pattern along the radial axis (Friedman test, p=0.0036) (Figure 2.10b). However, pairwise comparisons were mainly significant between tissues located far apart, suggesting that mechanical differences are subtle overall, but become more apparent between the innermost and outermost layers.

To investigate the mechanical pattern in a mature root, I measured intensity-weighted fluorescence lifetimes at the same tissue interfaces in the RAM. Here, a similar significant pattern emerged, where vascular and PE cell walls exhibited significantly distinct lifetimes compared to ground tissue and edge interfaces (p = 0.0036, Figure 2.10c). Notably, the overall fluorescence lifetime was higher in the RAM, suggesting that in addition to the graded pattern, there is an overall mechanical change in the organ that affects each tissue interface similarly. Furthermore, the difference in fluorescence lifetime between vascular and ground tissue was more distinct than in the developing LR, with a significant difference between the PE and ground tissue interfaces, suggesting that there may be a more distinct mechanical separation between the vasculature and ground tissue in mature roots.

Together, the CarboTag-BDP results suggest that young LRP initially have a relatively uniform mechanical state, but post differential growth begins, a graded radial pattern of cell wall mechanics emerges. This pattern is largely maintained throughout development when the overall mechanical properties of the organ continue to change, yet a more distinct separation between the vasculature and ground tissue may be formed.

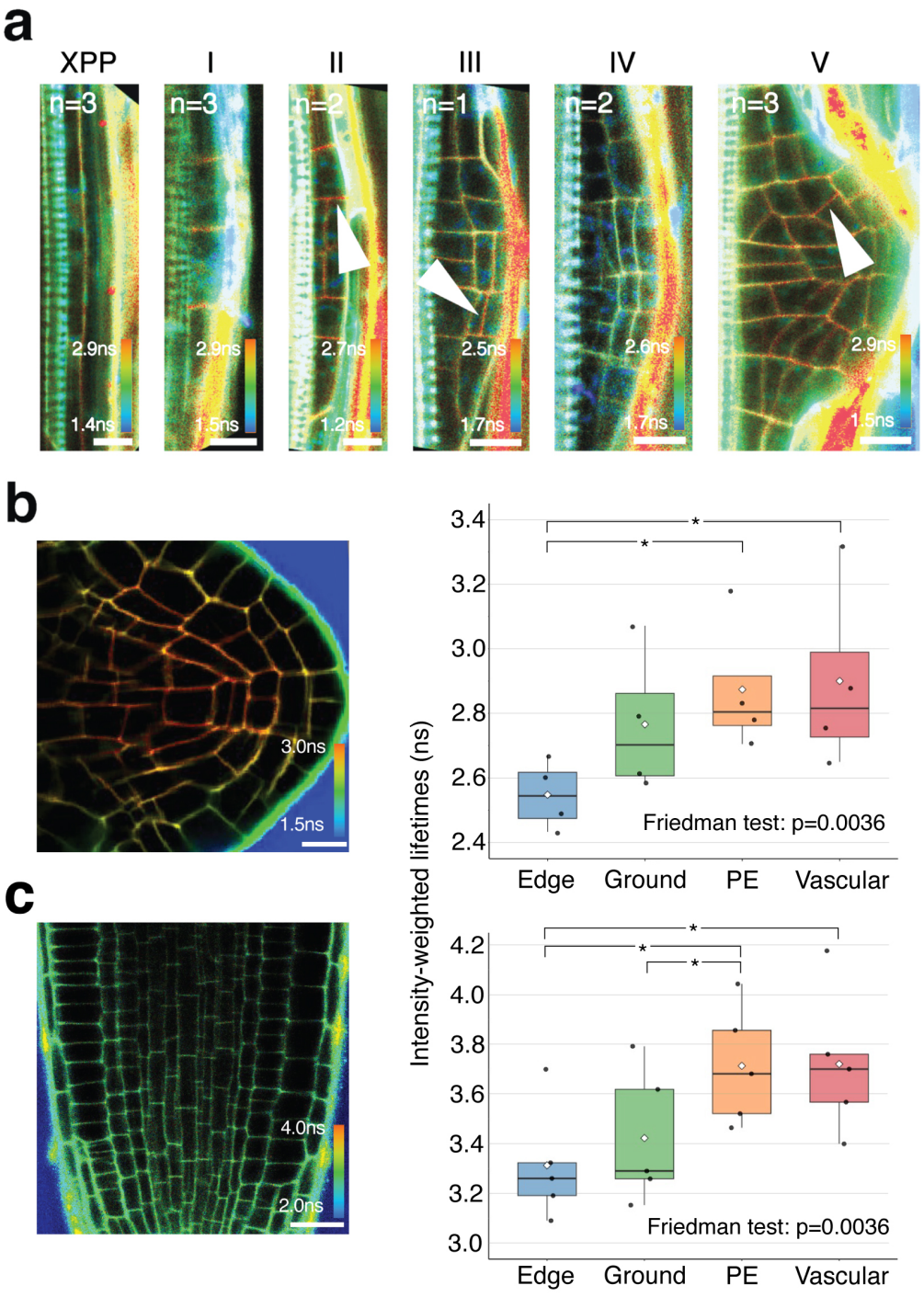

Figure 2.10: Fluorescence lifetime measurements of CarboTag-BDP reveal a graded mechanical pattern along the radial axis. (a) Representative lifetime images of CarboTag-BDP at various developmental stages (XPP to stage V). There are no apparent visual differences in lifetimes between tissue interfaces at the organ level in early developmental stages. Arrowheads indicate a few cell walls that have a noticeably different lifetime. (b & c) Representative fluorescent lifetime image and boxplot of intensity-weighted fluorescence lifetimes for tissue interfaces in the LR (n=4) and RAM (n=5). Data indicate slight, but consistent, differences in cell wall mechanics between tissues, with vascular interfaces appearing distinct from ground tissue interfaces. Although the pattern is significant (Friedman test: p=0.0036), only specific pairwise Wilcoxon tests without Holm correction are significant (* indicates $P < 0.05$). Scale bars: 20µm.

Cortical microtubule orientations indicate that the developing lateral root has a dynamic mechanical state with subtle underlying directional stresses

To explore the mechanical stress pattern in the LRP, I examined the cortical microtubule orientation from developmental stages II to VI. Multiphoton microscopy was used to image a (microtubule binding domain (MBD)) fused to GFP, expressed under the UBQ10 promoter. Across all stages, including LRPs undergoing differential growth, cortical microtubule orientation appeared largely isotropic at the organ level (Figure 2.11a).

To quantify this, I measured microtubule orientation in individual cells using FibrilJ [Boudaoud et al., 2014, Louveaux and Boudaoud, 2018]. As differential growth is expected to generate region-specific stresses, quantification was performed in three domains: the provascular region, the surrounding ground tissue precursors, and, for dome-shaped LRPs, the peripheral region (to control for curvature-related effects). This revealed that microtubule orientation in each of these regions was primarily isotropic with no significant differences between different regions (Figure 2.11b). This suggests that the developing LRP exists in a dynamic mechanical state, where tissue growth (and mechanical interactions with overlying tissues) may generate multidirectional mechanical stress components.

Although microtubule orientation appeared largely isotropic, it was not entirely isotropic, suggesting that there is a subtle directional component. It is plausible that such a principal orientation is masked by the dynamic mechanics of LRP development. To reveal these subtle alignment tendencies, microtubule orientations were weighted by anisotropy and averaged across cell-level regions. The resulting orientation were plotted relative to the LR shape (Method 8.4.7). This analysis revealed a supracellular alignment tendency. Namely during early stages (II–V), there was a striking supracellular alignment, whereas in later stages (IV–VI), that undergo differential growth and emerge through the cortex, subtle changes in orientation became apparent in the provascular and peripheral regions. This suggests that the observed supracellular patterns reflect mechanical forces arising during emergence or during differential tissue growth (Figure 2.11c).

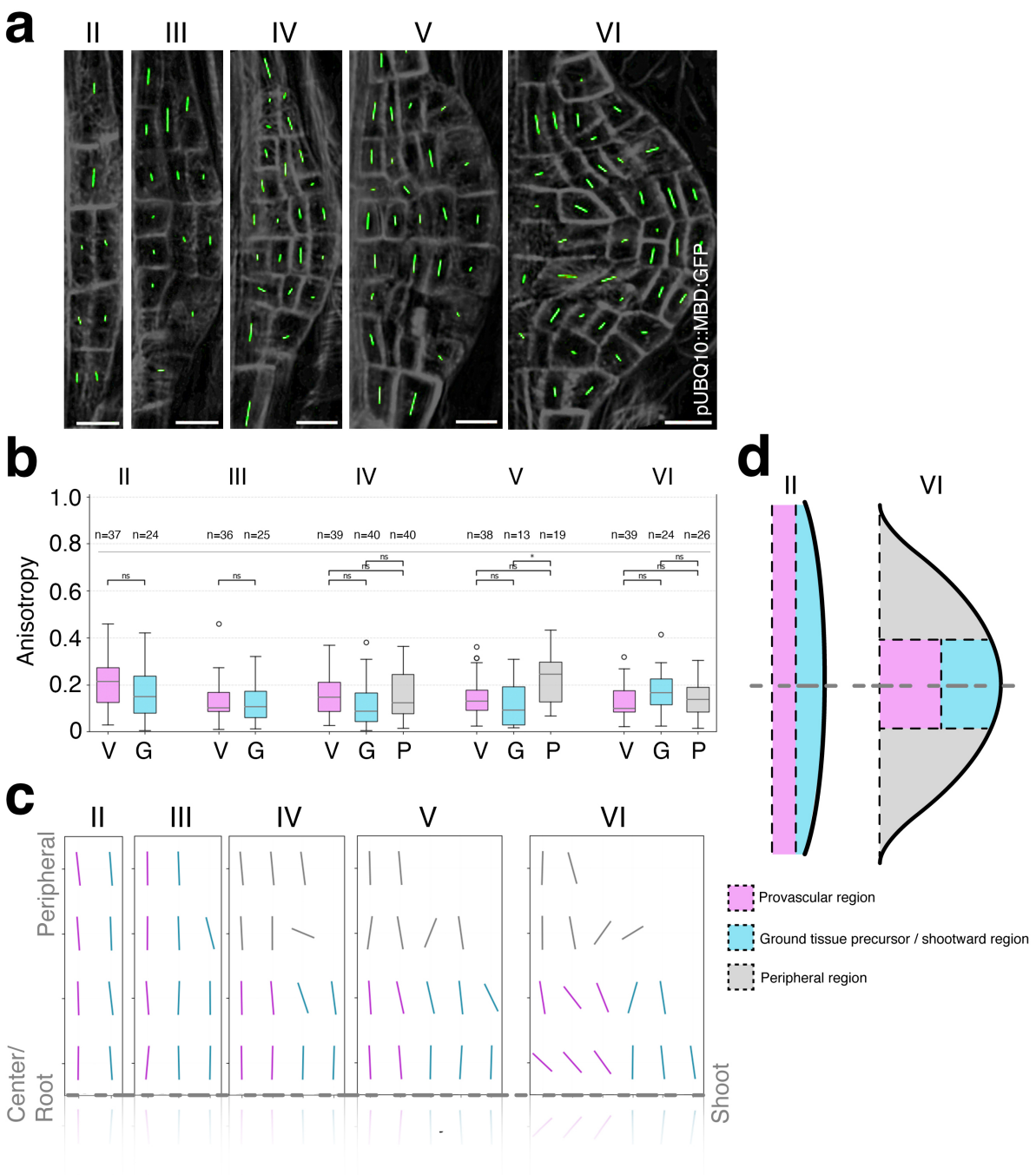

Figure 2.11: Microtubule organization during LRP stages II–VI. (a) *pUBQ10::MBD:GFP* signal (gray) across developmental stages II–VI overlaid with microtubule orientation as measured by FibrilJ (green) [Boudaoud et al., 2014, Louveaux and Boudaoud, 2018]; bar length indicates anisotropy. (b) Mean anisotropy in the provascular domain (magenta), ground-tissue precursors (cyan), and peripheral region (gray) at developmental stages II–VI. Sample sizes (n=cells) are indicated for each region, per stage. Pairwise comparisons (Bonferroni) show no significant differences between regions. (c) Supracellular alignment tendencies in microtubule orientation. Mean anisotropy-weighted microtubule orientation at cell-level regions are shown and plotted relative to the LRP dimensions (Methods 8.4.7). Dashed gray line indicates the symmetry axis. (d) Schematic of the colored regions (provascular, ground tissue, peripheral domain). Scale bar: 10µm.

2.3 Conclusion

The results suggest that SOK proteins respond to mechanical cues in a magnitude-dependent way, where under high mechanical stress the SOKs internalize, whereas in the developing LR, with a heterogeneous distribution of mechanical stress, the SOKs are permitted to accumulate.

2.4 Discussion

In this chapter, I examined the relationship between mechanical cues and SOK proteins. The emerging model is that SOKs are permitted to accumulate in regions with mechanical heterogeneity but internalize under high mechanical stress.

The CarboTag-BDP pattern and microtubule orientation pattern revealed that the LRP has a heterogenous mechanical state, which may favor SOK accumulation. However, it remains unclear what exactly the CarboTag-BDP and microtubule orientation patterns reveal, and what mechanical features attracts SOKs to specific interfaces, such as the PE interface.

Furthermore, upon targeted cell ablation, SOKs internalized across the entire organ. How this response is transmitted mechanistically remains unclear.

2.4.1 Do CarboTag-BDP patterns reflect mechanical stress patterns?

The CarboTag-BDP probe revealed distinct patterns of cell wall mechanics, with vascular cell walls that differed from the cell walls of ground tissue. Although the observed differences in fluorescence lifetime were subtle, on the order of 0.1 nanoseconds, they were consistent across independent samples and between the developmental context of LR organogenesis and in the RAM (Figure 2.10b, c). Importantly, differences on the nanoscale can reflect biologically meaningful changes, as demonstrated by [Besten et al., 2024]. Furthermore, similar contrasts between vascular and outer tissues have been reported in various zones of PR when using CarboTag-BDP, and comparable graded patterns have been quantified with Brillouin microscopy, where the vasculature has the highest stiffness and the outer tissues the lowest stiffness [Besten et al., 2024, Alonso Baez et al., 2025].

The graded CarboTag-BDP pattern was consistently observed across independent samples, with the vasculature exhibiting higher lifetimes than the outer tissues (Figure 2.10b, c). The samples used for this analysis differed in their absolute fluorescence lifetimes and in their developmental stage, because only a limited number of LRPs could be stained with CarboTag-BDP. This suggests that while the graded pattern is maintained, overall lifetimes differ between developmental stages and likely increase as the organ matures, with mature organs such as the RAM displaying higher lifetimes.

Furthermore, in the RAM, the fluorescence lifetime differed more sharply between vascular and ground tissue than in the LRP, suggesting that in mature roots these tissues may have a more pronounced mechanical difference (Figure 2.10c). It is tempting to speculate that the CarboTag-BDP pattern reflects the mechanical stress distributions of the RAM, where vascular cells are under compression and ground tissue experiences circumferential tension (Figure 2.4a) [Gorelova et al., 2021, Hoermayer et al., 2024, Kutschera and Niklas, 2007, Asaoka et al., 2023]. Testing CarboTag-BDP in the SAM, where mechanical stress patterns are well characterized, may clarify whether CarboTag-BDP patterns do indeed reflect such mechanical stress patterns [Hamant et al., 2008].

Furthermore, in the RAM, the visual pattern in the fluorescence lifetime microscopy images did not reflect the quantified pattern of intensity-weighted fluorescence lifetimes (Figure 2.10b, c). This may be caused by noisy pixels that obscure the pattern deeper in the RAM, whereas the quantification is weighted by pixel intensity, reducing the contribution of noisy pixels, and indicating that the quantified pattern is more reliable.

2.4.2 What does the microtubule orientation pattern reveal in the LR?

The developing LR likely exists in a dynamic mechanical environment, where the intensity of compressive stress on the LRP fluctuates (Figure 2.7a) and additional mechanical stresses arise from tissue growth (Figure 1.22a). This dynamic mechanical environment may cause the observed isotropic orientation of microtubules in the developing LRP (Figure 2.11b). When accounting for this dynamic environment, by weighing microtubule orientation by anisotropy, a supracellular anisotropic microtubule alignment was revealed in stages II to V.

Namely, in the early stages, with minimal differential growth, there was a striking supracellular alignment. This supracellular alignment may reflect compressive stress exerted by the overlying tissues on all cells. Whereas, in stage VI, which is after emergence through the cortex and after the onset of differential growth, the observed misalignments in the supracellular pattern may reflect the onset of differential growth and/or the absence of compressive stress (Figure 2.11c). Furthermore, the persistence of anisotropic alignment in the shootward domain throughout development suggests that this region is mechanically robust or experiences a constant external mechanical force. As these cells are located at the tip of the dome, they likely experience the highest external mechanical stress, and may therefore require enhanced mechanical robustness to penetrate the soil, analogous to a needle tip.

Furthermore, cell contours were often prominently marked by the microtubule marker (Figure 2.11a), suggesting that microtubules also accumulate at cell interfaces that are not observed in the side view of the LRP. Imaging the LRP from a different perspective, such as a frontal view, may help resolve these structures and provide further insight into the mechanical stress that the LR may experience.

2.4.3 Computational models to characterize cell wall mechanics during LR development

Computational modeling offers an additional approach to infer the mechanical state of the developing LRP. Previous modeling studies have successfully integrated mechanical information, such as turgor pressure and mechanical constraints, to simulate pericycle expansion [Ramos et al., 2024]. Extending such models to infer the mechanical state at specific tissue interfaces, such as the PE interface or the cortex–endodermis interface during LR organogenesis, may reveal mechanical signatures at these interfaces that correlate with SOK accumulation.

2.4.4 Potential mechanisms underlying SOK internalization

Ablation in the RAM provided valuable insight into how mechanical cues may influence subcellular SOK localization, where SOKs may detach from the plasma membrane in response to mechanical cues (Section 2.2.2).

Laser ablation is also known to trigger cellular stress responses, such as reactive oxygen species (ROS) production and calcium (Ca^{2+}) waves [Marhavý et al., 2019, Ma et al., 2025, Savatin et al., 2014, Vega-Muñoz et al., 2020]. Therefore, it is plausible that these stress signals contribute to the observed changes in SOK localization.

SOK proteins are thought to anchor into the plasma membrane via post-translational attachment of a palmitoyl group, covalently linked to cysteine residues through a reversible thioester bond [Ren et al., 2008, van Dop, 2018, Linder and Deschenes, 2007]. This modification is catalyzed by protein S-acyltransferases and can be removed by acyl-protein thioesterases. Notably, at least one plant thioesterase has been shown to be redox-sensitive, suggesting that depalmitoylation could be regulated by stress signaling [Ji et al., 2023]. Because Ca^{2+} and ROS signaling are rapid, tightly interconnected, and can be triggered by mechanical cues [Marhavý et al., 2019, Choi et al., 2014, Hansen et al., 2025], it is possible that SOK internalization may be a response to (mechanically-induced) stress-signaling rather than a direct mechanical response.

2.4.5 Is there a bias for anchoring near specific phospholipids?

The CarboTag-BDP pattern and microtubule orientation analysis of the LR did not reveal a distinct mechanical signature near the PE interface that could account for SOK accumulation at this specific region (Section 2.2.3). Thus, although a heterogeneous mechanical state may allow SOK accumulation, molecular factors enabling SOK accumulation remain unclear. The SOKs likely anchor into the lipid bilayer of the plasma membrane through post-transcriptional attachment of a palmitoyl group [van Dop, 2018]. Interestingly, the spatial distribution of specific phospholipids, that can affect LR development, roughly mimics regions where SOKs accumulate [Dubrovsky et al., 2025]. It is plausible that SOKs preferentially anchor near specific phospholipids. Specifically, the distributions of phosphatidylserine (PS) and phosphatidylinositol-4,5-bisphosphate (PIP(4,5)P_2) visually correlate with SOK accumulation patterns, where PS is enriched in regions where SOKs accumulate, whereas PIP(4,5)P_2 is depleted from these regions and instead mark sites where SOKs are absent [Stanislas et al., 2018, Dubrovsky et al., 2025]. These observations suggest that SOKs may preferentially anchor near PS whose charge is different from PIP(4,5)P_2, which may disfavors SOK anchoring [Yeung et al., 2008].

Chapter 3

Stay connected: mechanical continuity as a determinant of SOSEKI polarity

3.1 Introduction

The SOK polarity pattern reflects an organ-level polarity pattern in the developing LR, where the SOKs consistently polarize toward specific interfaces near the PE interface (Figure 1.18, 1.22). Although the heterogeneous mechanical environment of the developing LR appears to allow SOK accumulation, it remains unclear what polarizes them to specific interfaces, such as the PE interface (Chapter 2). Chapter I revealed multiple potential polarization cues. Namely, in addition to mechanical cues, there were indications that SOK polarity may be affected by anisotropic growth, tissue identity, and specific tissues interfaces (Figure 1.16, 1.18, 1.20). These potential cues are connected during organogenesis [Banda et al., 2019], which makes it challenging to pinpoint which cues affect SOK polarity. An insightful approach may be to examine SOK polarity in LRPs with aberrant patterning, such as in mutants or chemical-treated plants that target specific developmental processes.

3.1.1 Regulation and perturbation of lateral root patterning

Auxin

LR organogenesis is triggered by auxin accumulation in XPP cells, which activates the auxin response module SOLITARY ROOT (SLR) - auxin response factor 7 and 19 (ARF7/19) [Banda et al., 2019]. Downstream of this module are several regulators required for the proper execution of asymmetric divisions and patterning (Figure 3.1) [Banda et al., 2019]. When plants are treated with exogenous auxin, such as 1-naphthaleneacetic acid (NAA), lateral root (LR) organogenesis is induced in all XPP cells due to the uniform auxin distribution [Dubrovsky et al., 2008, Benková et al., 2003]. This results in symmetric radial growth with excessive cell divisions, often producing enlarged primordia that develop in close proximity (Figure 3.2), that in rare cases, may fuse together [De Smet et al., 2010].

LATERAL ORGAN BOUNDARIES-DOMAIN Genes

The first asymmetric division depends on LATERAL ORGAN BOUNDARIES-DOMAIN genes (LBD) [Goh et al., 2012a, Lee et al., 2019] transcription factors (Figure 3.1). The LBDs are responsible for polar nuclear migration, cytoskeleton reorganization, and asymmetric radial swelling of founder cells. Suppression of LBDs, using a dominant suppression construct, SUPERMAN REPRESSION DOMAIN X (SRDX), fused to LBD16, abolishes these polar processes and results in a symmetric anticlinal division and symmetric stage I LRP (Figure 3.2) [Goh et al., 2012a, Vilches Barro et al., 2019]. This mutant remains in stage I, continuing to undergo additional anticlinal divisions, and does not progress to stage II (Figure 3.2).

PLETHORAs

The second asymmetric division depends on PLETHORA (PLT) transcription factors [Du and Scheres, 2017a] (Figure 3.1). PLT3, PLT5, and PLT7 (PLT3/5/7) are endogenously expressed in stage I LRP [Hofhuis et al., 2013], where they regulate polar auxin transport, tissue identity, and activation of meristematic genes. In *plt3/5/7* triple mutants, the local auxin maximum becomes broadened across the central domain, rather than being confined to the shootward domain of the LRP. This is accompanied by aberrant expression of meristematic and tissue identity markers [Du and Scheres, 2017a]. Importantly, the crucial asymmetric periclinal division that normally transitions the LRP from stage I to stage II rarely occurs. As a result, the LRP continues to grow asymmetrically without proper division (Figure 3.2), leading to an aberrant organ pattern lacking the PE interface [Du and Scheres, 2017a].

SCARECROW

Downstream of the PLTs, the transcription factor SCARECROW (SCR) is required for the asymmetric division that transitions the LRP from stage II to stage III (Figure 3.1) [Di Laurenzio et al., 1996, Goh et al., 2016a]. SCR is expressed in the outer central cells of stage II LRP, where it is required for the establishment of ground tissue identity [Goh et al., 2016b]. In *scr* mutants, the asymmetric division from stage II to III does not occur, resulting in an aberrant cell pattern in stage III, which is more pronounced in stage IV, lacking a ground tissue interface (Figure 3.2) [Goh et al., 2016b]. Despite this, *scr* mutants are still able to form emerged lateral roots.

AURORA KINASES

Orienting the division plane during asymmetric divisions is essential to proper patterning. This is particularly important during the early developmental stages of LR organogenesis, where the orientation of the division plane switches between the first and second asymmetric divisions, and is deterministic for subsequent development [Schütz et al., 2021, Von Wangenheim et al., 2016] (Figure 3.1). Correct division plane orientation has been shown to require the AURORA kinases (AUR), AUR1 and AUR2, in various organisms, including *Arabidopsis* [van Damme et al., 2011, Willems et al., 2018, Li et al., 2008, Ali and Stukenberg, 2023]. Aurora kinases are activated during mitosis and play essential roles from spindle assembly to cytokinesis. In the *Arabidopsis aur1/2* double mutant, division plane orientation becomes randomized, leading to aberrant cell patterns that progressively worsen with each subsequent misoriented division (Figure 3.2) [van Damme et al., 2011]. Interestingly, the characteristic dome shape of the LR is maintained in the *aur1/2* mutant, indicating that organ patterning is not required to generate the dome shape. In fact, it has been experimentally verified that canalization through the overlying tissues (subsection 2.1.3) is responsible for the formation of the dome shape [Ramos et al., 2024, Lucas et al., 2013, Péret et al., 2012, Stöckle et al., 2022, Von Wangenheim et al., 2016].

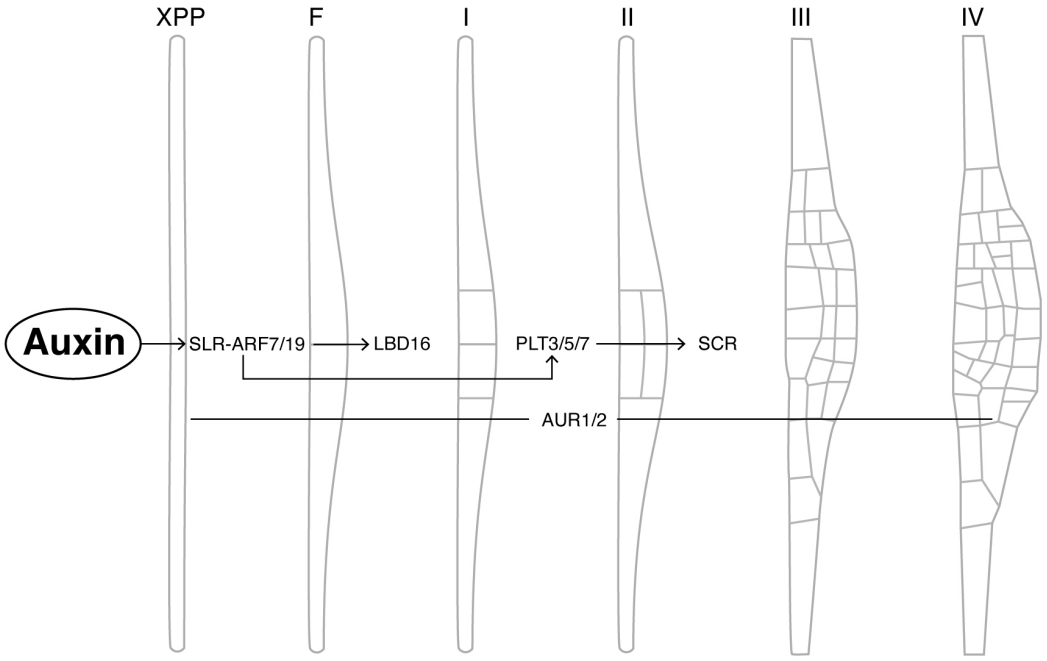

Figure 3.1: Regulation of asymmetric cell division and tissue patterning during early LR development. The transcription factors LBD16, PLT3/5/7, and SCR, together with AUR kinases, are integrated at the indicated developmental transitions.

3.1.2 Additional methods to perturb LR patterning

Genetic mutants often perturb multiple components of developments, such as growth and tissue identity, whereas the effects of chemical or laser perturbations are usually more specific (Table 3.1).

Oryzalin

Oryzalin, a microtubule-depolymerizing chemical, causes excessive radial swelling in LRP [Vilches Barro et al., 2019].

Taxol

Taxol, a microtubule-stabilizing chemical, causes symmetric swelling in LRP [Vilches Barro et al., 2019].

Previous studies indicate that SOK localization is robust and remains unaffected by various chemical treatments, including treatments that disrupt cytoskeletal organization [Yoshida et al., 2019]. This suggests that the microtubule organization defects caused by treatments with oryzalin or taxol do not affect SOK polarization, and allowing the investigation of growth defects or abnormal cell geometry on SOK polarity.

Laser ablation

Laser cell ablation directly disrupts the organ's cell layout and may provide insight into how structural cell layouts influences SOK polarity. However, it cannot be excluded that stress signaling induced by ablation also affects SOK polarity, because it may affect SOK localization (Section 2.4.4).

Table 3.1: Overview of how different perturbations influence organ patterning through effects on cell growth, cell identity, or asymmetric divisions. A (+) indicates that the perturbation affects the mechanism, while a (–) indicates no effect or that the effect is unknown.

	Growth	**Identity**	**Division**
NAA	+	+	+
gLBD16::SRDX	+	-	+
plt3/5/7	+	+	+
scr	-	+	+
aur1/2	-	-	+
oryzalin	+	-	-
taxol	+	-	-
ablation	-	-	-

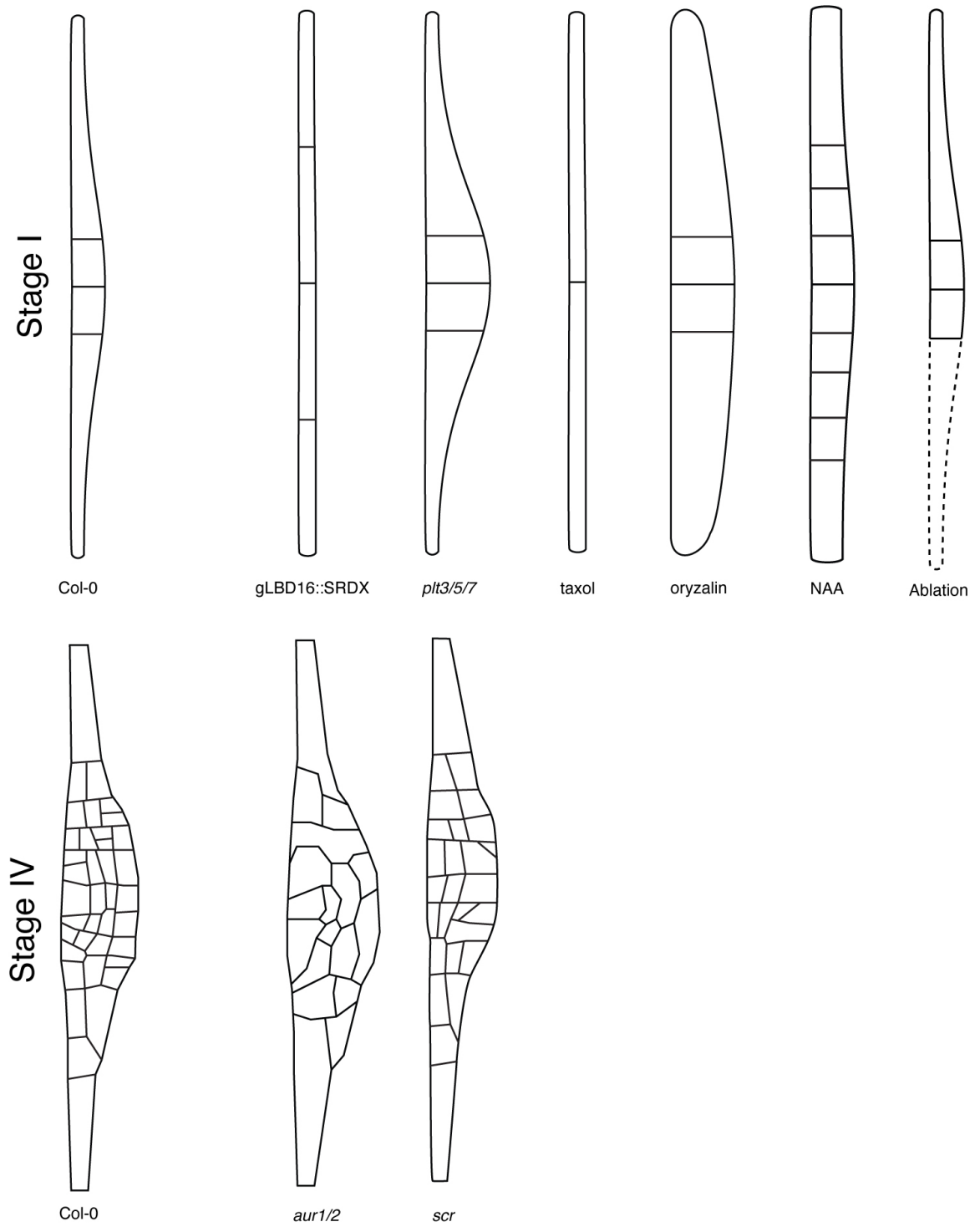

Figure 3.2: Schematic of pertubated organ patterns in mutants, chemically-treated, and ablated samples. Stage IV outlines of Col-0 were replicated from [Torres-Martínez et al., 2019].

3.1.3 Objective

The objective of this chapter is to identify cues that polarize the SOK proteins. To achieve this, I will compare polarity patterns in wildtype LRP with perturbed LRP (Figure 3.2). As a starting point, I will use the PE interface, because the polarization toward this interface is prominent for each SOK (Figure 1.18, 1.22). In particular, I will use the *plt3/5/7* mutant as a starting point because establishment of the PE interface is disrupted in this context [Du and Scheres, 2017b]. Furthermore, to simplify identification of polarity differences, I focus primarily on SOK1 for comparative analysis, as its polarity pattern is the easiest to identify (Figure 1.16). Nevertheless, most experiments were performed with SOK1, SOK2, and SOK5, and all three responded to the perturbations in a similar way (Figure 3.12). Additionally, to clarify, I will use the polarity patterns of genomic and misexpression markers interchangeably as polarity does not seem to be affected by misexpression (Section 1.2.2).

3.2 Results

3.2.1 SOK1 polarity may be linked to the primary root endodermis

In stage II LRP, SOKs polarize toward the PE interface (Figure 1.18). The establishment of this PE interface is dependent on the PLT3/5/7 transcription factors, and in their absence, the PE interface is rarely established [Du and Scheres, 2017a]. To investigate the contribution of the PE interface to SOK polarity, I transformed *pRPS5A::SOK1:mVenus* + pUBQ10::PIP1;4:mScarlet-I in the *plt3/5/7* background and compared the pRPS5A::SOK1:YFP polarity pattern between *plt3/5/7* and wildtype (Col-0) [Hofhuis et al., 2013].

In stage I *plt3/5/7* mutants, the divergent wildtype pRPS5A::SOK1:mVenus corner polarity was maintained, unless the overlying endodermis was thin, in which case corner polarization toward the endodermis was lost (Figure 3.3a, b). This suggests that pRPS5A::SOK1:mVenus polarity may be influenced by (i) PLT3/5/7-dependent gene expression, (ii) excessive radial growth, or (iii) attraction to the interface between the PR endodermis and the LRP.

To disentangle this, I first investigated whether tissue-specific cues play a role. To this end, I observed gSOK1::YFP polarity in oryzalin-treated samples, which mimic the radial swelling phenotype of *plt3/5/7* [Vilches Barro et al., 2019]. The polarization pattern in oryzalin-treated samples was similar to *plt3/5/7*, where mispolarization was only observed after endodermis thinning (Figure 3.3c). Because PLT3/5/7 gene expression is presumably not affected in oryzalin-treated samples, this suggests that the loss of gSOK1::FP corner polarization is due to misgrowth or endodermis thinning.

To examine the contribution of misgrowth on polarity, I analyzed gSOK1::YFP polarity in *gLBD16::SRDX* and taxol-treated samples, both of which exhibit symmetric radial misgrowth [Vilches Barro et al., 2019, Goh et al., 2012b]. In both conditions, the characteristic gSOK1:YFP polarity was maintained (Figure 3.3d), indicating that misgrowth does not directly disrupt SOK1:FP polarity. Instead, these results suggest that the LRP-PR endodermis interface attracts SOK1.

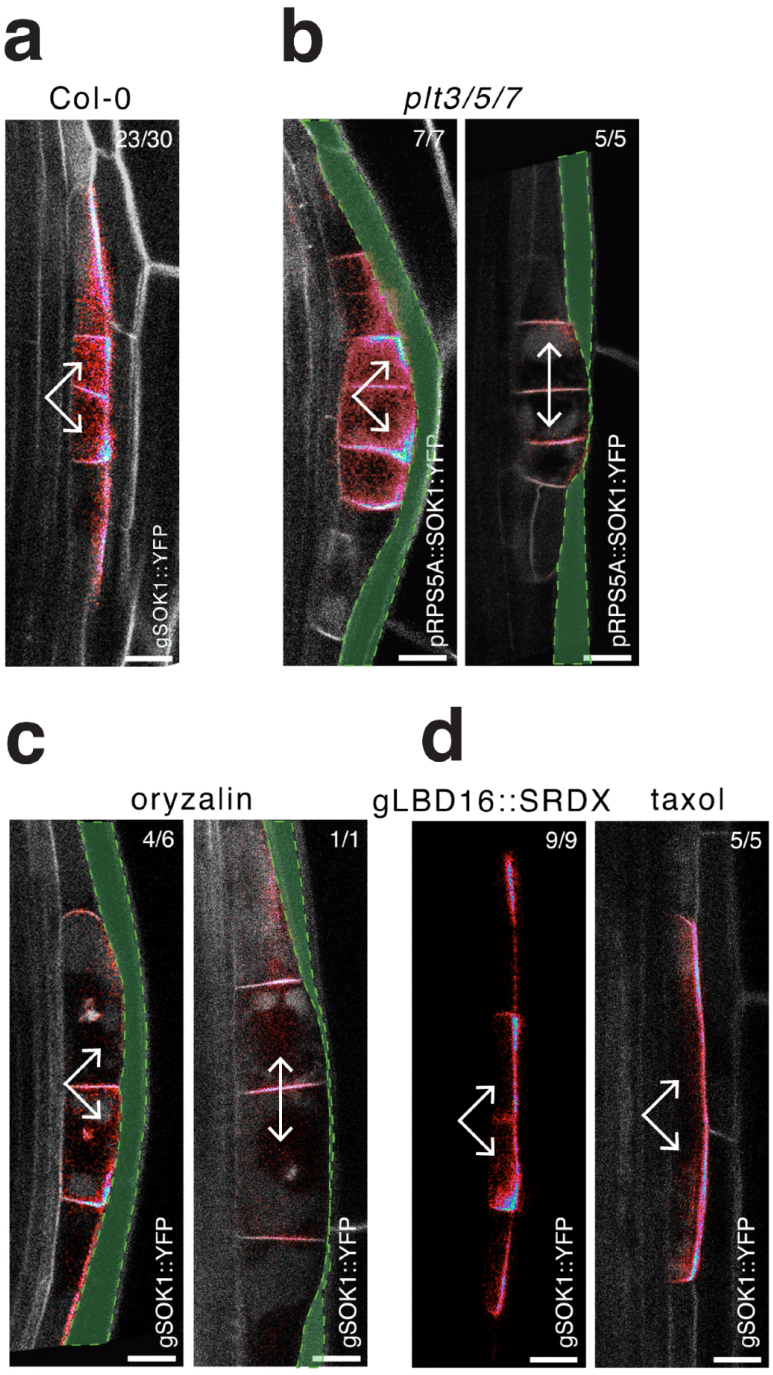

Figure 3.3: SOK1 seems to be attracted to the interface with the PR endodermis, independent of tissue identity and growth. (a) gSOK1::YFP polarization in a wildtype (Col-0) stage I LRP. (b) pRPS5A::SOK1:mVenus polarization in *plt3/5/7* is similar to wildtype and corner polarization is lacking when the endodermis is thin. (c) The gSOK1::YFP polarity pattern in oryzalin-treated plants mimics the polarity pattern of *plt3/5/7*. Data generated jointly with Kathrin Distel. (d) gSOK1::YFP polarization is not affected by symmetric radial misgrowth in *gLBD16::SRDX* and taxol-treated samples. Dashed green area: endodermis. Number of replicate LRP shown in the top right. Scale bar 10µm.

3.2.2 The primary root endodermis attracts SOK1

The PR endodermis appears to attract SOK1 in stage I LRP (Figure 3.3). To investigate the exact contribution of the PR endodermis, I observed the effect of endodermis thinning on gSOK1::YFP polarity in wildtype LRP. In wildtype LRP, endodermis thinning predominantly occurs in stage II. The gSOK1::YFP polarity in wildtype stage II LRP was similar to the *plt3/5/7* mutant and oryzalin-treated samples, where endodermis thinning was associated with a lack of corner polarization in outer central cells (Figure 3.4b). This reiterates that the interface between the LRP and PR endodermis attracts SOK1. To confirm this, I ablated the endodermis overlying a stage II wildtype LRP, and live-imaged gSOK1::YFP post ablation. Indeed, the removal of the endodermis resulted in loss of corner polarization, specifically in outer central cells (Figure 3.4c). This confirms that the PR endodermis attracts SOK1 in cells that are in direct contact with the endodermis.

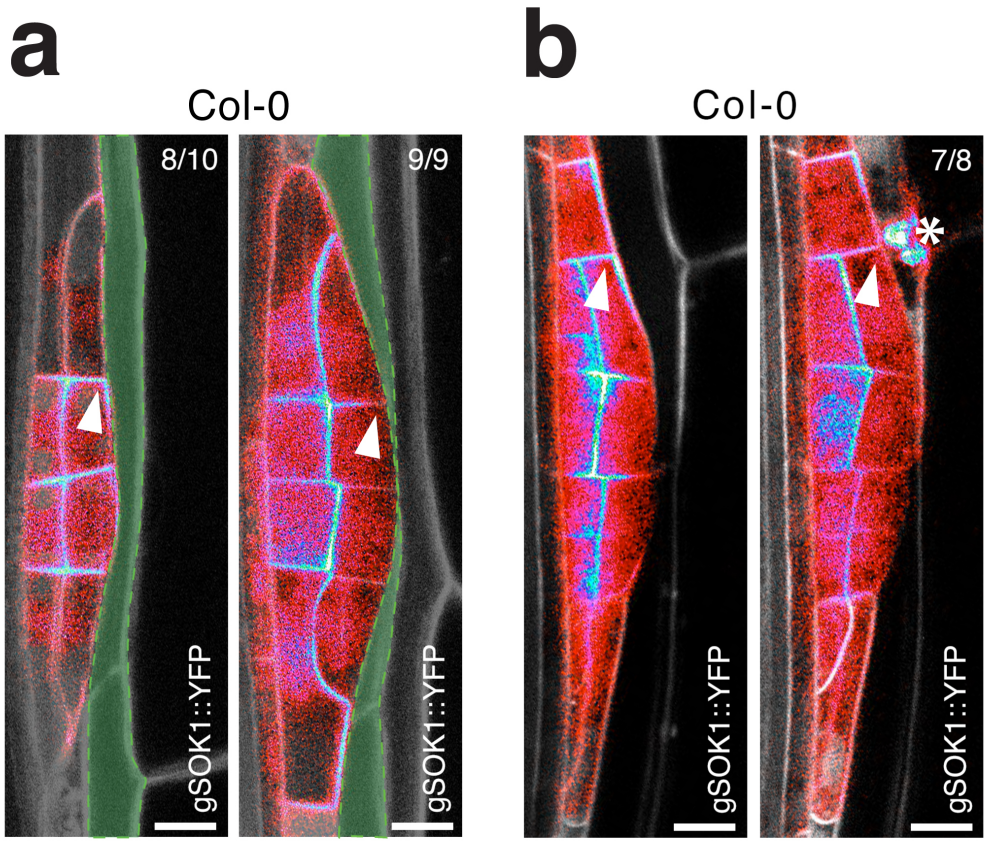

Figure 3.4: The PR endodermis attracts SOK1 in outer central cells. (a) gSOK1::YFP corner localisation is lost when the overlying endermis is thinning. (c) Removal of the overlying endodermis abolishes gSOK1::YFP corner polarization in adjacent LRP cells. Dashed green line: endodermis. Scale bar 10µm.

3.2.3 Mechanically stressed primordia struggle to maintain proper polarization

SOK1 is attracted to several tissue interfaces: the LRP-PR endodermis interface, the PE interface and the ground tissue interface (Figure 1.16, 1.18, 3.3, 3.4) [Yoshida et al., 2019].

Remarkably, *plt3/5/7* LRP do occasionally undergo divisions in stage I, that can result in primordia with a wildtype-like cell pattern and a PE-like interface. To gain more insight on what polarizes SOK1 to the PE interface, I observed pRPS5A::SOK1:mVenus, pRPS5A::SOK2:mScarlet-I, and pRPS5A::SOK5:mVenus in stage I *plt3/5/7* LRP that undergo a rare periclinal division. These polarity patterns were compared with wildtype polarity patterns.

In the resulting *plt3/5/7* stage II LRP, there were conflicting observations, where some LRP had the wildtype polarity pattern and other LRP had an abnormal polarity pattern (Figure 3.5b). Notably, the ability to maintain the wildtype polarity pattern indicates that SOKs polarize to the PE-like interface independently of PLT3/5/7. Instead, the mere physical presence of a periclinal interface in stage II LRP may be sufficient to attract the SOKs to such as an interface.

Interestingly, the mispolarized LRP were specifically located in the upper section of the PR (length-wise), suggesting that “older” primordia were more frequently mispolarized (Figure 3.5b). To examine when polarity changed, I performed live-imaging of pRPS5A::SOK2:mScarlet-I in stage I and II *plt3/5/7* LRP (n=17 timelapses). Prior to endodermis thinning, I detected no mispolarization, reiterating that ’young’ primordia are unlikely to mispolarize.

There was an apparant correlation between SOK::FP signal intensity and growth, where the pRPS5A::SOK2:mScarlet-I signal was intense during periods of active growth and became dimmer when growth was minimal. This phenomenon reflects an earlier observation, where reduced growth reflects compressive stress that leads to the dissipation of SOKs (Figures 2.7, 2.8). Indeed, when measuring the pRPS5A::SOK2:mScarlet-I signal as a function of LR length in a single timelapse, the pRPS5A::SOK2:mScarlet-I signal decreased as the LR length no longer increased (Figure 3.5c), which was consistent with observations in other timelapses. Strikingly, mispolarization of SOK2 occurred specifically during periods of minimal growth (Movie 5; Figure 3.5c) (n=8 similar observations). This suggests that compressive stress, acting on an LRP with aberrant patterning can trigger a polarity change.

Movie 5: pRPS5A::SOK2:YFP mispolarization in *plt3/5/7* mutant LRP.

Click here to view Movie 5
Click here to download Movie 5

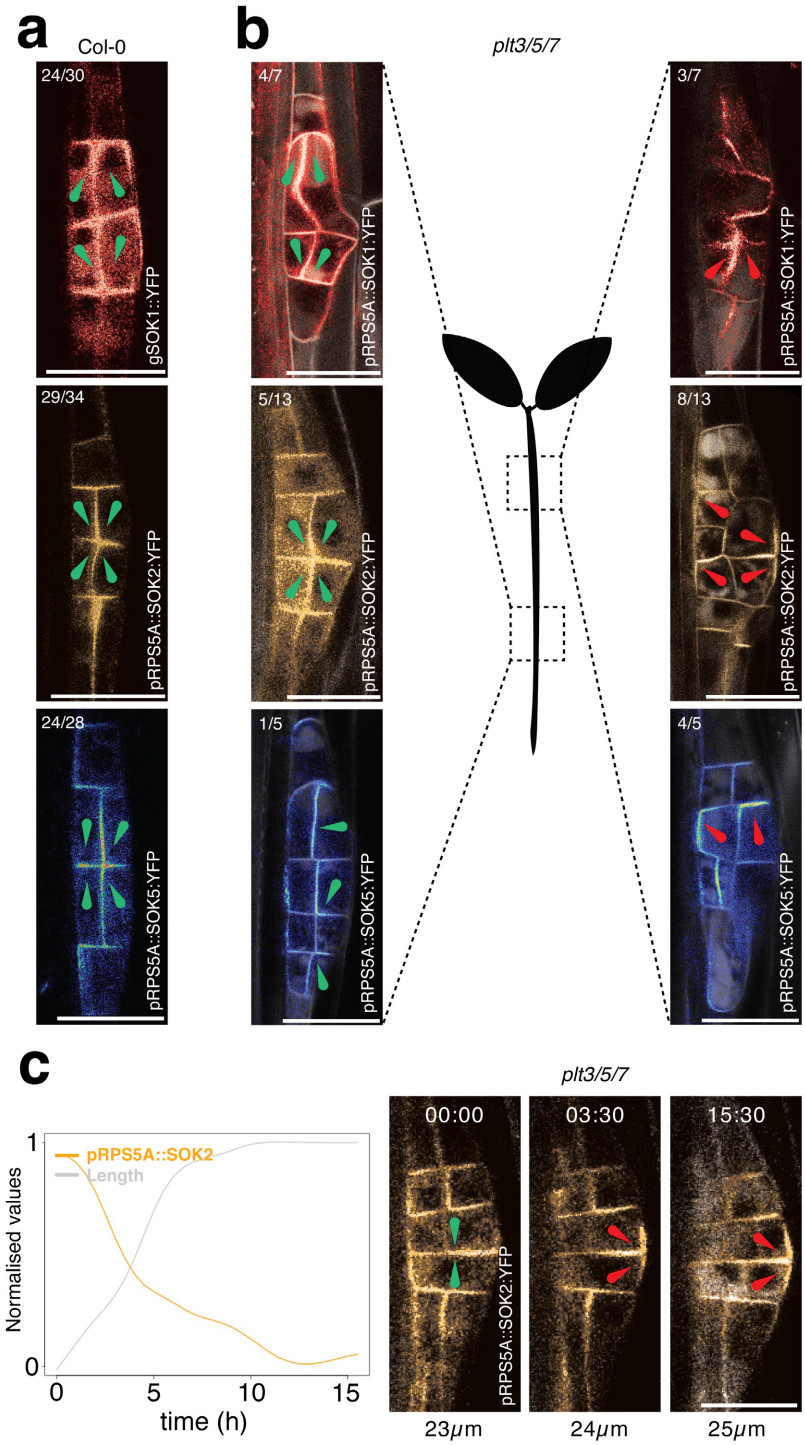

Figure 3.5: SOKs may mispolarize in *plt3/5/7* LRP as a result of compressive stress (a) Consensus of SOK polarization in wildtype (Col-0) stage II LRP. Number in top-left indicates the number of replicates with a similar polarity pattern. (b) "Older" *plt3/5/7* LRP are more likely to mispolarize than "Young" primordia. Number in top-left indicates how many 'young' and how many 'old' LRP were observed. (c) Mispolarization in *plt3/5/7* when there is little to no elongation. Normalized values are SOK5/PM signal scaled from 0 to 1. Length is also scaled from 0 to 1. Timestamp: (hour:min). Scale bar 25μm.

3.2.4 The ground tissue interface is required for proper SOK1 polarization

The mispolarization observed in *plt3/5/7* LRP with minimal growth suggests that compressive stress on an LRP with an aberrant cell layout causes polarization defects (Figure 3.5c). To investigate the extend to which cell layout itself contributes to polarity, I compared the SOK1:YFP (gSOK1::YFP and pRPS5A::SOK1:YFP, used interchangeably) polarity pattern of wildtype with the polarity pattern in the *aur1/2* double mutant 3.1.1), and the *scr* mutant (3.1.1).

In wildtype, convergent SOK1:YFP polarity gradually shifted from the PE interface toward the ground tissue interface during stages II–IV (Figure 1.18, 3.6a). Interestingly, in *aur1/2* this was maintained, whereas in *scr*, the SOK1:YFP polarity pattern was disrupted throughout the organ, including provascular cells that are not known to be affected by SCR (Figure 3.6c). This indicates that cell layout alone does not affect SOK1:YFP polarity. Instead, this suggests that tissue interfaces are required for proper polarity at long range.

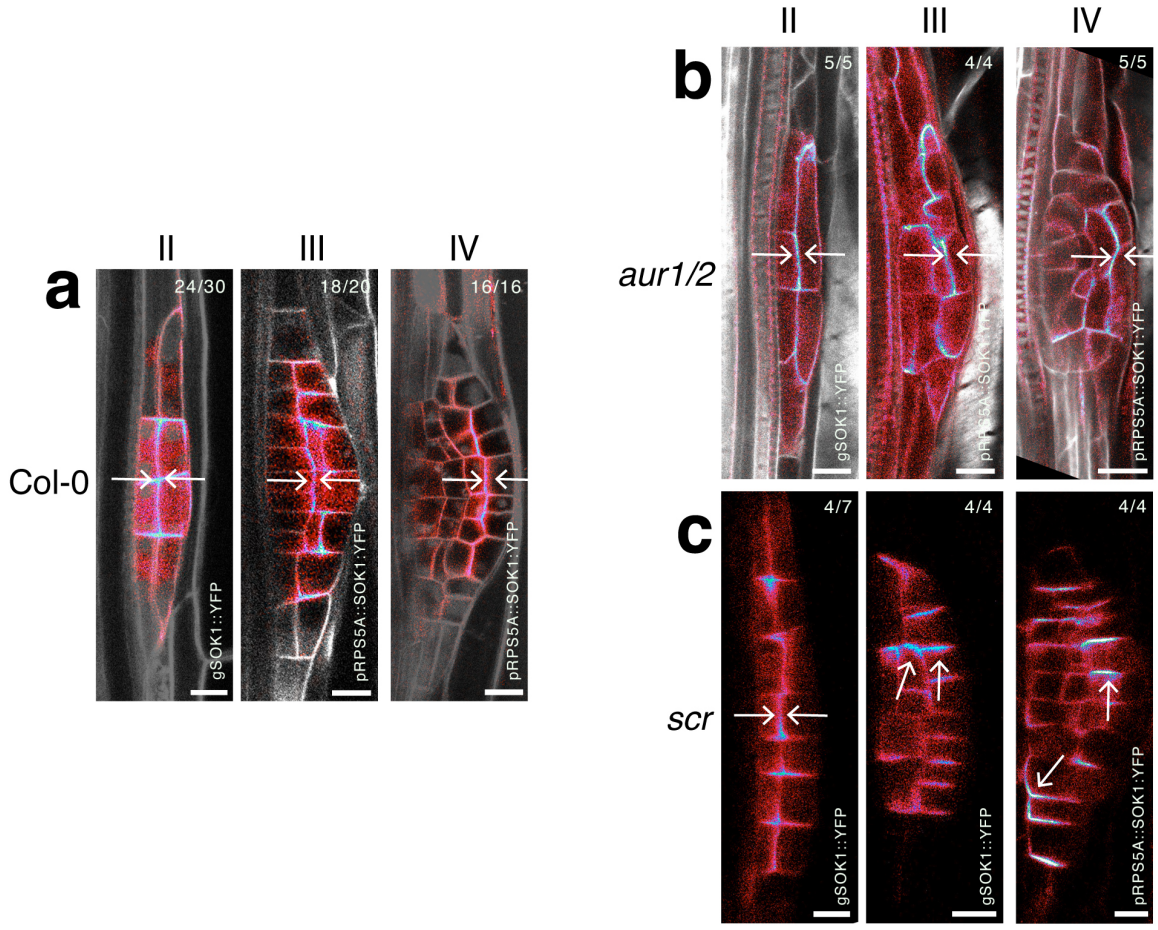

Figure 3.6: The ground tissue interface is required for proper polarization. (a) SOK1 polarity pattern in wildtype stage I to IV LRP. (b) A wildtype-like SOK1 polarity pattern in *aur1/2* double mutants, indicating that an abberrant cell layout is insufficient to alter the SOK1 polarity pattern. Data generated jointly with Kathrin Distel and Laura Schütz. (c) An abnormal SOK1 polarity pattern in the *scr* mutant, when the ground-tissue interface is missing. Scale bar 10µm. gSOK1::YFP and pRPS5A::SOK1:YFP polarity used interchangeably.

3.2.5 SOK1 polarity is shaped by cell–cell contact at long range

Changes in SOK polarization are consistently observed when tissue interfaces are either removed or added. For example, after removal of the LRP–PR endodermis interface (Figure 3.4), after removal of the PE interface combined with compressive stress (Figure 3.5), and after the addition (Figure 1.20) or removal (Figure 3.6c) of the ground tissue interface. These observations suggest that SOK polarity depends on the physical presence of specific tissue interfaces.

To assess whether it is sufficient to disrupt polarity by removal of a cell-cell interface, I ablated a single cell in LRP stages I or II and live-imaged gSOK1::YFP afterwards using light sheet microscopy (n=24 timelapses).

Following single-cell ablation, half of the LRPs (12/24) aborted development immediately, while the others (12/24) continued for some time but ultimately aborted. In LRPs that continued development, gSOK1::YFP signal was usually absent, although transient polarity patterns were occasionally observed. These polarity patterns differed from the pre-ablation pattern. Notably, in a stage I, gSOK1::YFP polarity reoriented in the cell adjacent to the ablation site after 1 hour (Figure 3.7a, Movie 6). In a separate ablation experiment of a stage II LRP, the center of the divergent polarity pattern shifted post ablation after roughly 7 hours (Figure 3.7b, 3.11). This indicates that the removal of individual cell–cell contacts is sufficient to change polarity at the organ level and that such changes operate on a slower timescale than localization/cortical polymerisation, which respond to ablation within seconds (Section 2.2.2).

Movie 6: gSOK1::YFP polarity changes post ablation in stage I LRP

Click here to view Movie 6
Click here to download Movie 6

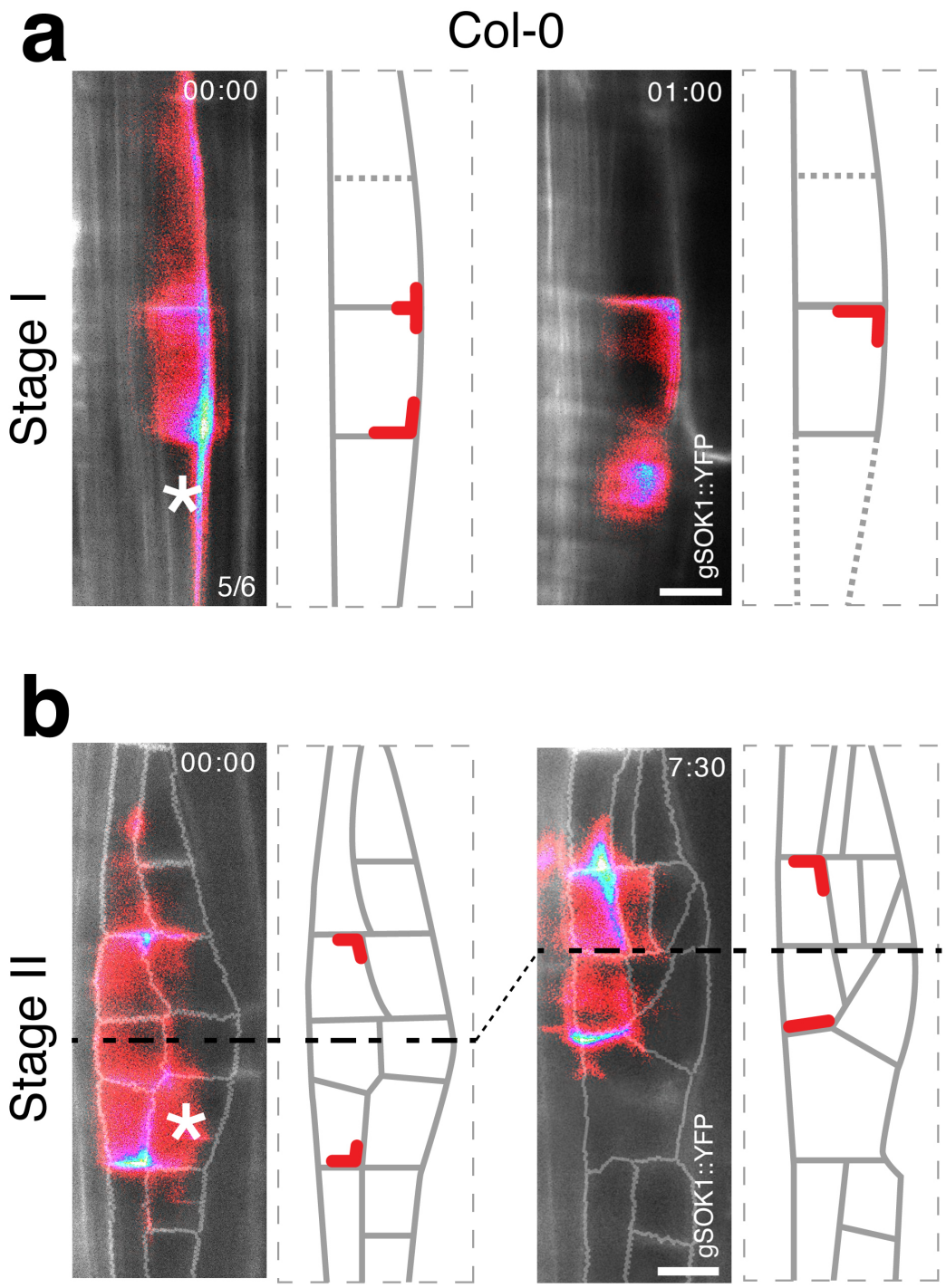

Figure 3.7: gSOK1::YFP polarity changes post ablation. (a) A stage I primordia where a peripheral cell is ablated. Polarization toward the ablated region is lost, and polarization toward a different direction appears to be increased. Dashed gray line in the image, prior to ablation, indicates where the second central cell will be located after its formation in the timelapse. (b) A stage II LRP where an outer central cell is ablated. Post ablation, the polarity pattern shifts upward (black dashed line), indicating that the center of the LRP is adjusting to the new cell layout. Asterisks indicate ablation site. Timestamp: (hour:min). Scale bar 10µm.

To assess whether the addition of cell-cell contacts affects polarity, I used confocal microscopy to live-image gSOK1::YFP in NAA-treated plants, which undergo additional anticlinal divisions in stage I LRP, and occasional organ fusions between adjacent LRP. Interestingly, in independent experiments, I observed that wildtype stage I LRPs can also undergo additional anticlinal division. The polarity pattern of this wildtype LRP was compared with the polarity pattern of NAA-treated samples.

Polarity patterns in the enlarged stage I LRPs were different between wildtype and NAA-treated plants, where gSOK1::YFP tended to polarize toward anticlinal interfaces rather than to corners in NAA-treated samples, indicating that an auxin-dependent signal can influence polarity.

In one timelapse (n=1/10), two adjacent LRPs on opposite sides of the xylem pole fused, and gSOK1::YFP polarity in both organs shifted following the formation of new “bridging” interfaces (Figure 3.8b, Movie 7). This suggests that SOK1 polarity is affected by cell–cell contacts at long range.

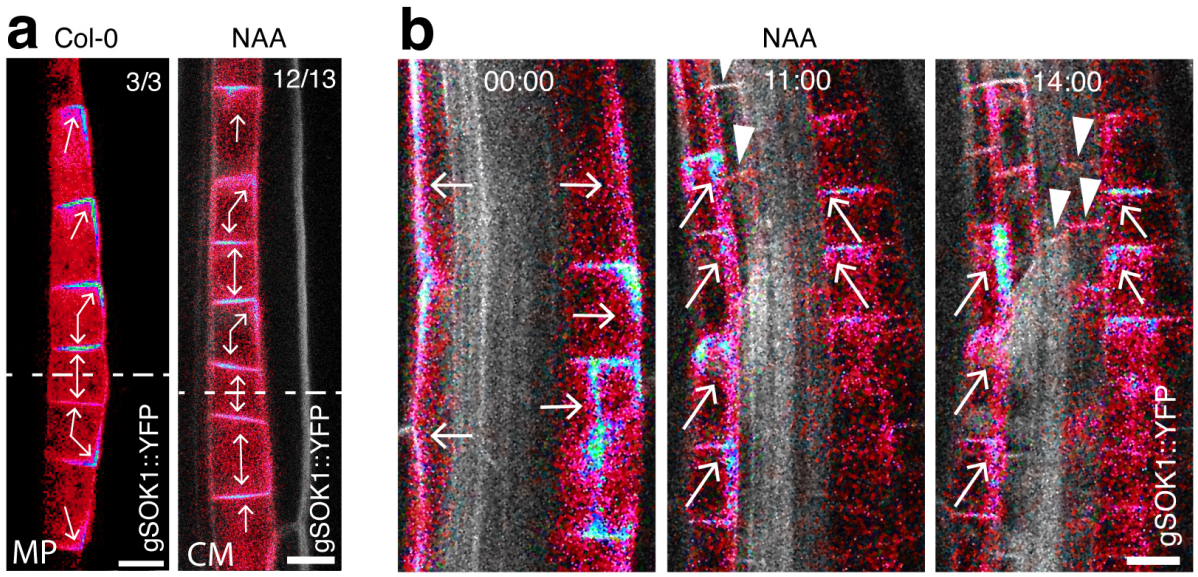

Figure 3.8: SOK1 polarity is shaped by cell-cell contact. (a) gSOK1::YFP has a tendency to polarize to anticlinal interfaces in NAA-treated samples. The number of replicates is shown in the top right. Acquisition method is indicated in bottom left: multiphoton microscopy (MP), confocoal microscopy (CM). Dashed line indicates the symmetry axis. (b) gSOK1::YFP polarity changes when two primordia on opposite xylem poles fuse across the vasculature, by forming a kind of ”bridge” (arrowheads). Scale bar 10µm.

Movie 7: gSOK1::YFP polarity changes at long range after the formation of ”bridging” interfaces during organ fusion.

Click here to view Movie 7
Click here to download Movie 7

3.3 Conclusion

Together, these results show that the removal or addition of tissue interfaces and cell–cell contacts changes the SOK polarity pattern at the organ level, with this effect being further amplified under compressive stress. In contrast, there is no evidence that other proposed cues, such as growth, cell geometry, cell layout, or cell identity, directly influence polarity as perturbation of these cues often results in wildtype-like polarity patterns (Figure 3.9c).

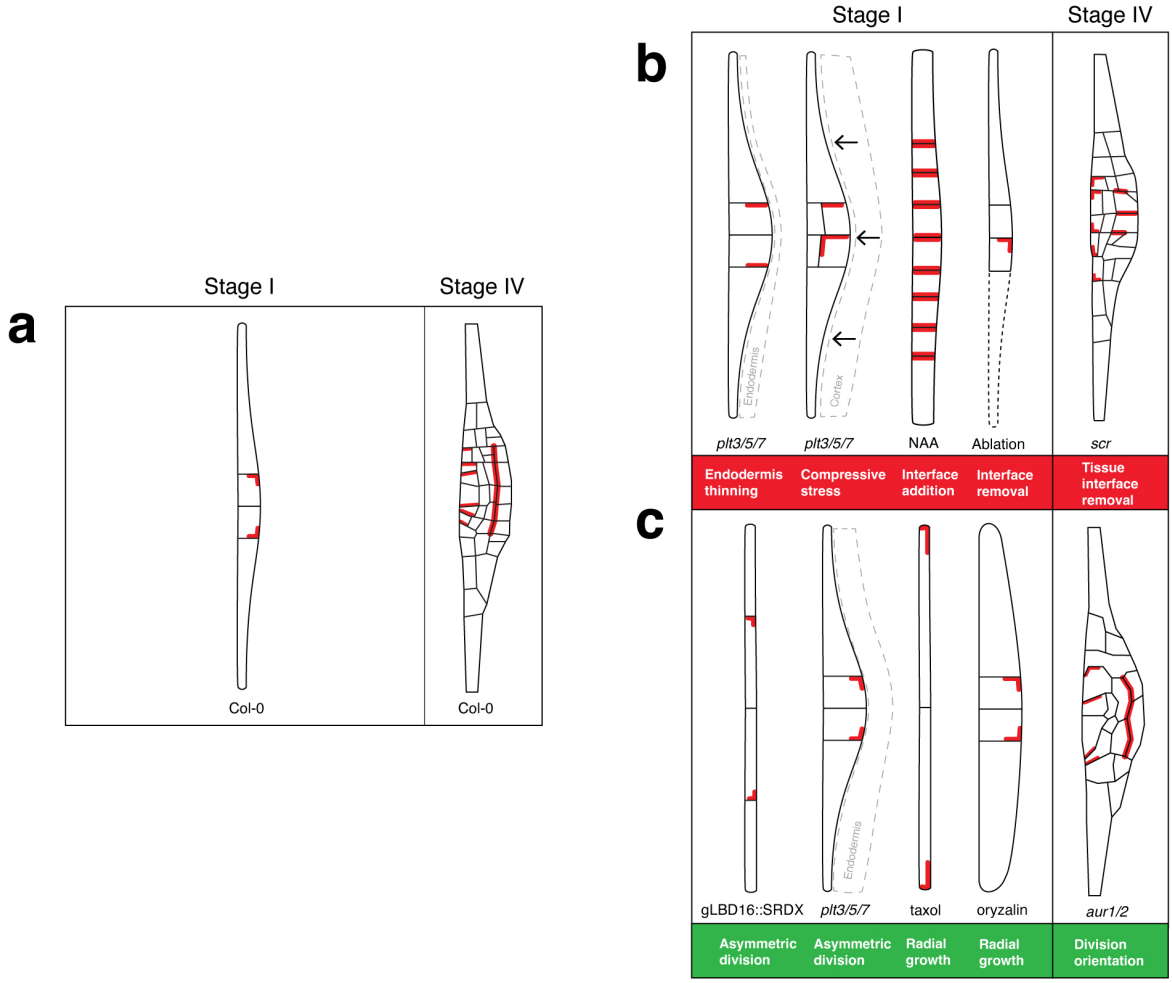

Figure 3.9: Overview of SOK1 polarity in wildtype (Col-0) and abnormal LRP phenotypes. (a) Schematic of SOK1 polarity pattern in wildtype stage I and IV. (b) Abnormal SOK1 polarity patterns in abnormal LRP phenotypes. Below each phenotype, the potential cause of mispolarization is written. (c) Wildtype-like polarity patterns in abnormal LRP phenotypes. The cause of the perturbation is written below each phenotype. Stage IV outlines of Col-0 were replicated from [Torres-Martínez et al., 2020].

3.4 Discussion

3.4.1 The cell wall continuum as a conduit for polarity cues

The results suggest that SOK polarity emerges from an interplay between structural and mechanical cues. This interpretation is consistent with the ability of SOKs to respond to mechanical stimuli (Section 2.2.1, 2.2.2) and their dependence on cell wall integrity [Yoshida et al., 2019].

Mechanical cues are transmitted through the cell wall network, where the structural configuration of cell-cell interfaces determines the directionality of this transmission [Trinh et al., 2021]. Disrupting the mechanical continuity of the cell wall network, for instance, by removing a cell–cell interface, probably changes mechanical transmission patterns and redistributes mechanical stress, thereby shifting mechanical “hot” and “cold” spots [Robinson and Kuhlemeier, 2018, Demes and Verger, 2023, Melogno et al., 2024]. At the cellular level, corresponding mechanics may be perceived and translated into polarity (Figure 3.10).

Consistent with this, phenotypes with disrupted mechanical continuity had abnormal polarity at the organ level (Figure 3.9b). In contrast, perturbations of growth, cell geometry, or division orientation, may not affect mechanical continuity because cell-cell contacts remain intact, and allow transmission of mechanical signals in a way similar to wildtype (Figure 3.9c). Together, this suggests that mechanical continuity (of the cell wall network) is a determinant of polarity.

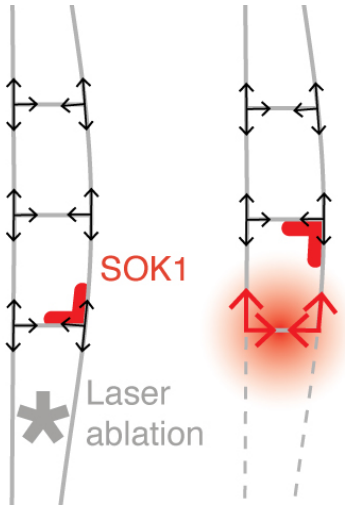

Figure 3.10: Model showing how disruption of mechanical continuity in the cell wall may create mechanical hotspots, to which SOKs respond by polarizing to a different corner.

3.4.2 SOK1 polarity in NAA-treated plants may be affected by cell wall modifications

Despite a similar number of cell–cell interfaces and cell layout, a notable difference in polarity was observed between wildtype and NAA-treated plants (Figure 3.8a). Namely, in NAA-treated plants, SOK1 tended to polarize toward anticlinal interfaces rather than to corners, suggesting that there is an auxin-dependent factor influencing polarity.

In NAA-treated samples, auxin distribution within the LRP is likely homogeneous and accessible throughout the organ, rather than restricted to the central domain as an auxin maximum [Benková et al., 2003]. Since auxin is known to trigger cell wall modifications [Trinh et al., 2021], its widespread availability may induce such modifications across the entire organ, rather than being confined to the central domain. Consistent with this, in wildtype plants, SOK1 polarizes towards the central anticlinal interface, in addition to its divergent corner localization (Figure 3.8a, 1.25, 1.16a). This suggests that there is auxin-dependent polarization toward the central interface.

Additionally, SOK1 polarity may be affected by mechanical changes in the overlying endodermis, which was shown to attract SOK1 (Figure 3.3, 3.4, 3.12). In NAA-treated plants, auxin is readily available in the endodermis, where it can induce cell wall remodeling [Vermeer et al., 2014], thereby altering the mechanical properties of the interface between the LRP and the overlying endodermis, to which SOK1 may respond.

3.4.3 How does cell ablation affect the mechanics of surrounding cell walls?

In Chapter 2, the effect of ablation on SOK localization was rapid (<min), and revealed a potential role of stress signaling that may cause internalization of SOK proteins (Section 2.4.4). In contrast, in this chapter, polarization changes appear to occur later, and were typically observed after at least 1 hour (Figure 3.7, 3.11, Movie 6). This suggest that polarization cues change at a slower timescale. Polarity changes on this timescale may reflect changes in cell wall mechanics, such as stress-induced or mechanically triggered modifications of the cell wall [Denness et al., 2011, Vega-Muñoz et al., 2020, Hansen et al., 2025, Di Fino et al., 2025]. Biologically, it may be advantageous for polarity mechanisms to operate slowly, ensuring that overall polarity is not disturbed by short-lived (mechanical) signals.

Testing the effect of single cell–cell removal on cell wall mechanics in computational models of the LR may provide insight into how mechanics and polarity are linked [Ramos et al., 2024].

3.4.4 Mechanics outweigh cell-cell contact in polarity determination

Post endodermal thinning or post laser ablation of the endodermis, SOK1 no longer polarizes toward the affected interface (Figure 3.3, 3.4). In contrast, during endodermal thinning in *plt3/5/7*, SOK2 mispolarizes toward the corresponding interface, where physical connections are likely minimal (Figure 3.12). These observations suggest that a physical connection between adjacent cells may not be required for SOK polarization. Instead, it suggests that polarity is primarily shaped by changes in mechanics. To directly test whether a physical connection between neighboring cells is required for SOK polarization, it may be insightful to analyze polarity in a simplified system such as protoplasts or liposomes.

3.4.5 gSOK expression as a potential indicator of functional organogenesis

In most of the post ablation timelapses the genomic SOK1:YFP signal was absent. Similarly, the absence of genomic SOK2:YFP signal has been reported during failed regeneration of the shoot from callus, where SOK2 was only observed in progenitor cells that gave rise to functional primordia, and was absent in dysfunctional primordia. [Varapparambath et al., 2022]. Given that SOK1:YFP was not observed in ablated primordia that discontinued development, the expression of *SOK* genes may mark proper organogenesis.

3.4.6 Is the response to missing cell–cell interfaces universal to all SOSEKIs?

In the PR, SOK1 polarity has been reported to be disrupted in *scr* mutants [Yoshida et al., 2019], where SOK1 mispolarizes in cells lacking an endodermis–cortex separation. In this thesis, SOK1 polarity is altered throughout the entire LRP in *scr* mutants, suggesting that the absence of the endodermis–cortex interface affects polarity at long range (Figure 3.6c). However, it is unknown whether such a response is universal to all SOKs in *scarecrow*. Although the polarity of SOK2 and SOK5 has been investigated in several abnormal backgrounds and generally mirror that of SOK1 (Figure 3.12), it remains unknown whether they have comparable polarity changes specifically in the *scr* mutant. To determine whether structural perturbations have a universal response among SOKs, it would be important to assess SOK2 and SOK5 polarity in the *scr* mutant.

3.5 Supplemental figures

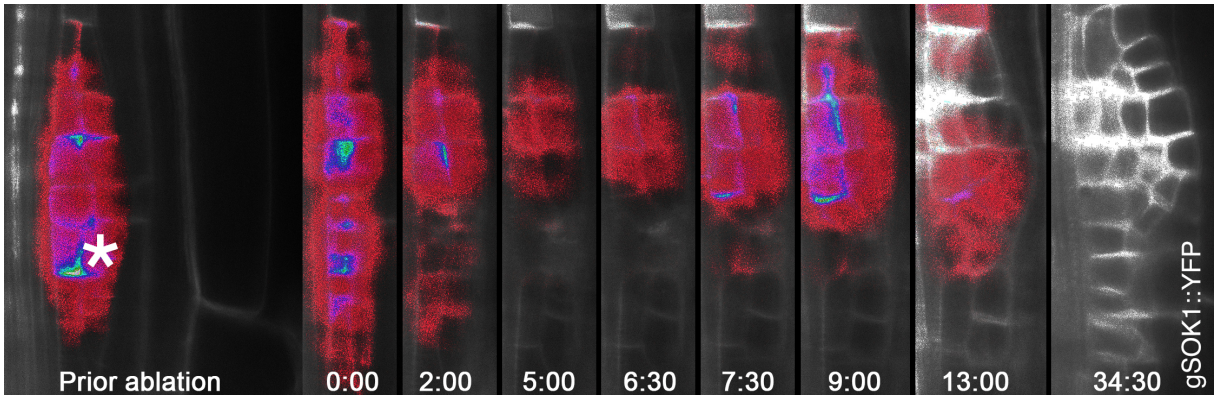

Figure 3.11: gSOK1::YFP polarity change post ablation in stage II LRP. The new polarity pattern suggests that the position of the LRP center moved upwards post ablation.

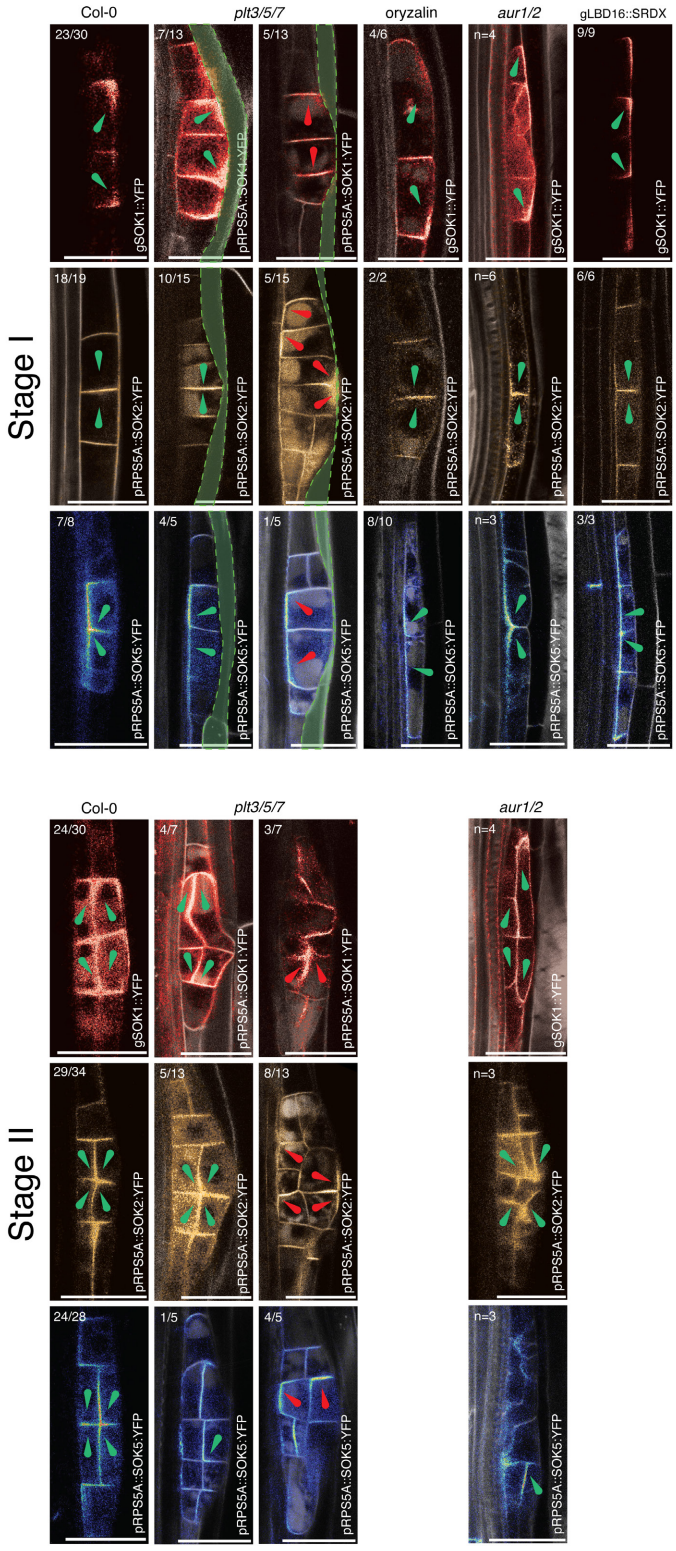

Figure 3.12: The polarization of SOK1, SOK2 and SOK5 appears to be affected in a similar manner in aberrant stage I and II LRP. Green arrows indicate wild-type–like polarization, and red arrows indicate mispolarization. Dashed green line: endodermis. Scale bar 25µm.

Chapter 4

Punctual divisions: temporal regulation of cell division may depend on SOSEKI5

4.1 Introduction

During plant development, mechanical signals play a key role in the coordination of development, where they are transmitted through the cell wall continuum to affect cellular processes, such as growth and cell division orientation [Robinson, 2021, Fruleux et al., 2019, Zhao et al., 2018, Louveaux et al., 2016, Hoermayer et al., 2024]. Given the mechano-sensitive nature of the SOK proteins (Chapter 2), it is plausible that SOKs link mechanical cues to a cellular response.

The function of SOKs remains speculative, but they seem to play a role in development because they are predominantly expressed in meristematic regions. Furthermore, over- and/or misexpression of *SOK1* may trigger oblique cell divisions in the RAM [Yoshida et al., 2019], and SOK polymers recruit the effector ANGUSTIFOLIA [van Dop et al., 2020], which is implicated in developmental processes such as division orientation, cell size, and organ size [Bai et al., 2013, Tsuge et al., 1996]. SOK1 also appears to dissipate during mitosis, suggesting a link to the cell cycle [Yoshida et al., 2019]. To elucidate the biological function of SOK proteins, a critical step is the analysis of LOF mutants.

4.1.1 SOSEKI mutants

Single LOF mutants of individual *SOK* genes do not display an apparent phenotype [van Dop, 2018], likely due to functional redundancy among *SOK* family members. Indeed, LOF of *SOK1* leads to upregulation of *SOK4*, indicating a compensatory role [van Dop, 2018]. Overlap in expression and localization patterns between the SOKs further indicates redundancy between SOK2 and SOK5 in the RAM, between SOK2 and SOK3 in the leaf, and among SOK2, SOK3, and SOK5 in the gynoecium [van Dop, 2018].

To overcome the challenge of functional redundancy within the *SOK* gene family, the generation of higher-order mutants is required. Higher-order CRISPR/Cas-derived mutants have been made (Andriy Volkov, pers. comm.). However, even quadruple mutants do not exhibit obvious developmental phenotypes, underscoring the high degree of redundancy. Interestingly, LOF mutants that also include *SOK5* LOF have not been recovered, and attempts to generate pentuple mutants result in lethality. This suggests that *SOK5* plays an essential role in plant development (results from A. Volkov & Dr. Reyes-Hernández).

To overcome the lethality associated with pentuple LOF mutants and to investigate the cellular function of the *SOKs*, a strategy was developed that combines a *sok1/2/3/4* LOF quadruple mutant with the inducible KD of *SOK5*, simulating a pentuple mutant (Andriy Volkov & Dr. Reyes-Hernández). Specifically, an inducible two-component expression system targeting *SOK5* was introduced into the *sok1/2/3/4* quadruple mutant, generating an inducible pentuple mutant (*sok1/2/3/4»5*) (Andriy Volkov & Dr. Reyes-Hernández). This *sok1/2/3/4»5* mutant serves as a valuable tool for investigating SOK function.

The *sok1/2/3/4»5* mutant exhibits impaired RAM development, characterized by proper tissue organization but a reduced meristem size (Data from Dr. Reyes-Hernández; Figure 4.1). In this mutant, fewer cells undergo division, and cells seem to remain longer in the gap 2 phase (G2) phase of the cell cycle (Data from Dr. Reyes-Hernández). Given that cell size is probably linked to cell cycle progression [Echevarria et al., 2022], these findings suggest that *SOK* genes play a role in regulating cell size. Although *SOK* expression is known to be dynamic and absent during mitosis [Yoshida et al., 2019], the timing of *SOK* expression in relation to specific cell cycle phases remains unclear. Elucidating the temporal relationship between *SOK* expression and the cell cycle may provide valuable insight into the function of the SOKs.

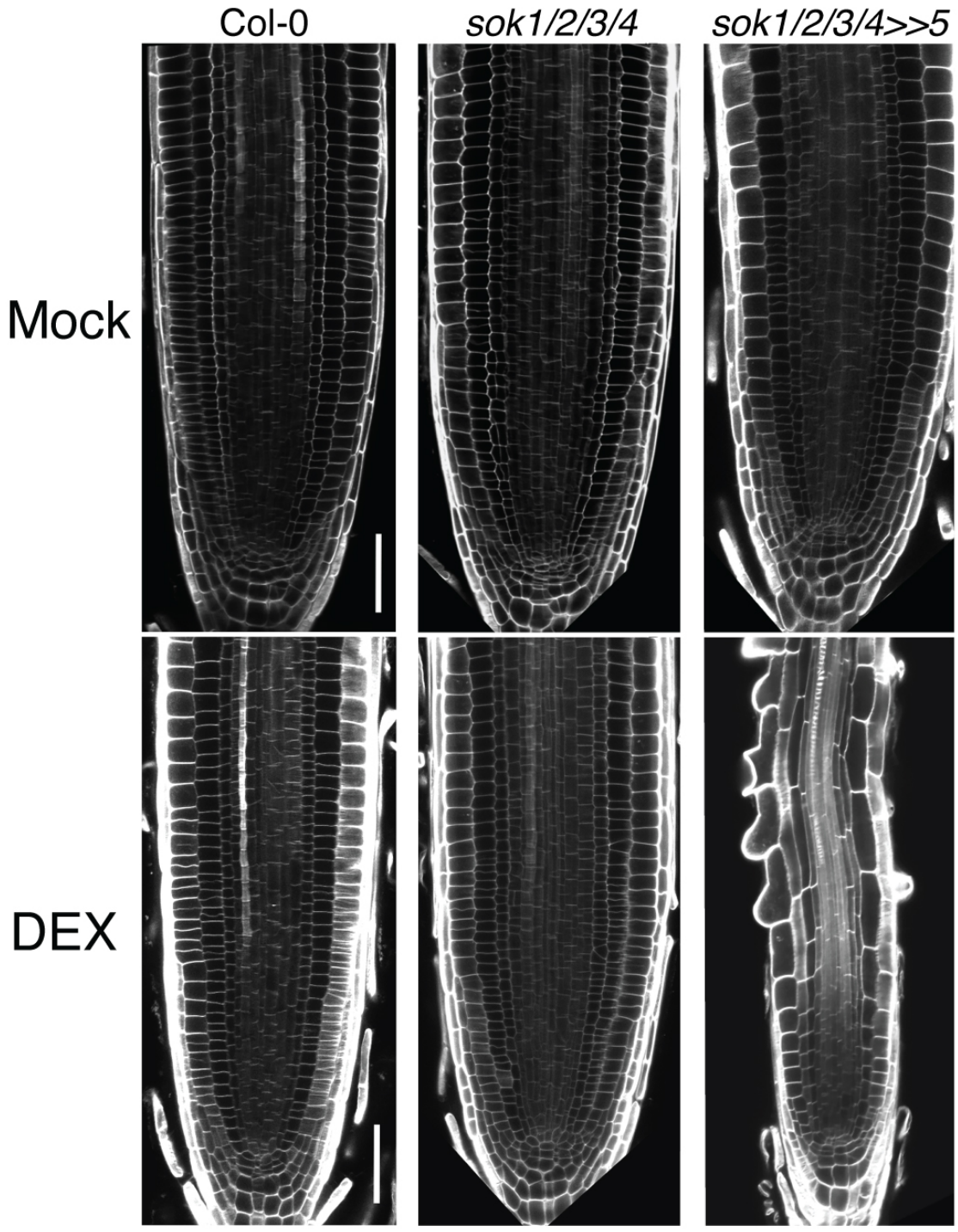

Figure 4.1: The inducible *sok1/2/3/4»5* pentuple mutant has impaired RAM development. The meristem size of the *sok1/2/3/4* quadruple mutant (LOF) is comparable to wild type (Col-0), whereas the *sok1/2/3/4»5* pentuple mutant (LOF + KD) exhibits a reduced meristem size following SOK5 knockdown. Data and images are unpublished and were acquired and provided by Dr. Jazmín Reyes-Hernández. Figure adapted from the original figure created by Dr. Reyes-Hernández. Scale bar 40µm.

4.1.2 The cell cycle in *Arabidopsis*

Dividing cells progress through the cell cycle, which consists of four main phases: G1, S, G2, and M. In the G1 phase, cells increase in size, duplicate their organelles, and synthesize the proteins and RNA required for DNA replication. The synthesized biomaterials are then used in the subsequent S phase to replicate the chromosomes. In the subsequent G2 phase, growth continues and proteins necessary for subsequent mitosis are produced. Mitosis follows, involving the segregation of the replicated chromosomes and the division of the cytoplasm. At the end of mitosis, cytokinesis takes place, leading to the formation of a new cell wall and the production of two daughter cells. These daughter cells either reenter the cycle in G1 or transition into a quiescent state, known as G0, where they temporarily or permanently withdraw from the cell cycle [Alberts et al., 2002a].

Progression through the plant cell cycle is controlled at checkpoints where intrinsic and extrinsic cues are integrated. These cues include the monitoring of DNA integrity and cell size, as well as inputs from hormonal signals, abiotic stress, the cell wall, and nutrient availability. Together this ensures that cell division is coordinated with developmental status and environmental conditions [Gutierrez, 2022, Soni and Bacete, 2023, Bouchez et al., 2024, Qi and Zhang, 2020, Rawat and Laxmi, 2024]. There are four major checkpoints: the G1 to S checkpoint, which determines whether the cell is ready to initiate DNA replication; the S-phase checkpoint, which monitors the progression of DNA synthesis; the G2 to M checkpoint, which ensures that DNA replication is complete; and the M-phase checkpoint, which verifies that all chromosomes are properly aligned before division proceeds [D'Ario and Sablowski, 2019].

The total duration of the cell cycle varies depending on developmental context. Below, the cell cycle is described for the RAM, during LR organogenesis, and in wound healing.

In the RAM of *Arabidopsis* the average cell cycle duration is estimated to be 17 hours [Campilho et al., 2006, Yin et al., 2014, Desvoyes et al., 2021, Hayashi et al., 2013]. Each cell cycle phase has a different duration, which can further differ between tissues. In the ground tissue, the G1 phase shows considerable variation, ranging from 1 to 20 hours depending on the position of the cell relative to the root tip and its tissue identity [Echevarria et al., 2022]. The following S phase is relatively brief and can be as short as 20 minutes across all tissue layers. The duration of the G2 phase is cell type–dependent, lasting approximately 3.5 hours in the pericycle and over 4.5 hours in the epidermis. And finally, the length of mitosis is unclear, and may range from 20 minutes to 2 hours [Desvoyes et al., 2020, Yin et al., 2014, Pasternak et al., 2022] (Figure 4.2).

The cell cycle duration during LR organogenesis is even more dynamic, where the cell cycle in the early stages is rapid, and the duration increases progressively with each developmental stage, starting at approximately 6 hours in the transition from founder cells to stage I [Torres-Martínez et al., 2020] and roughly 40 hours in stage VII [Napsucialy-Mendivil et al., 2025]. Furthermore, the cell cycle in the central cell file (as observed in frontal or transversal view) is shorter than in the adjacent cell files [Von Wangenheim et al., 2016, Schütz et al., 2021]. Detailed phase-specific durations are not yet available for LR organogenesis, making the RAM a more suitable context for studying a potential relationship between *SOK* expression and specific phases of the cell cycle.

The regenerative cell cycle that occurs during wound healing in the RAM is distinct from the regular meristematic one. Its total dutation is considerably shorter, ranging from 5 to 20 hours. Notably, the G1 phase is thought to be dramatically shortened [Lee et al., 2025], and a canonical phase transition from the G1 to S phase may not be required. Furthermore, G2 markers appear roughly 30 minutes prior to the end of mitosis [Marhavý et al., 2016].

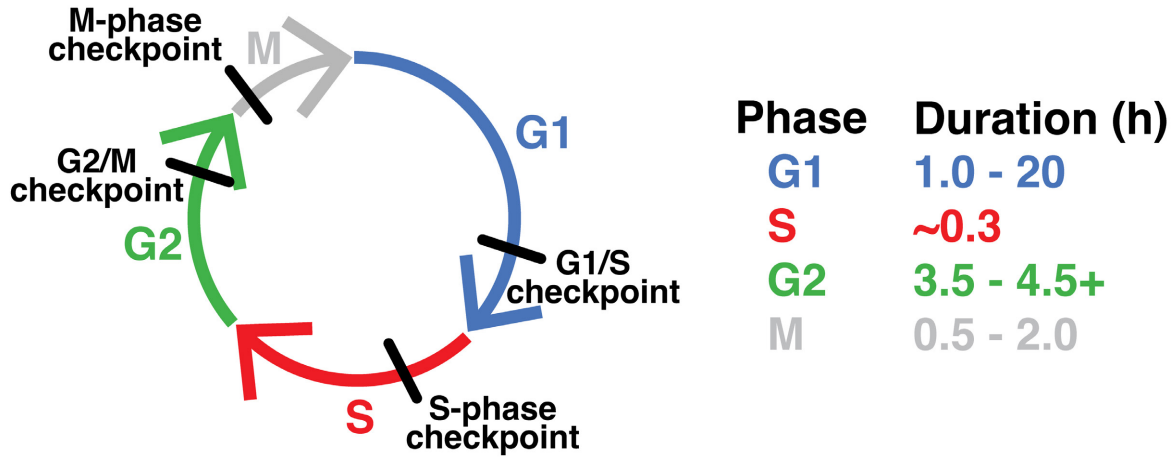

Figure 4.2: The cell cycle and its checkpoints that monitor cell size to regulate progression through each phase. The estimated duration of each phase (in hours) is shown for the RAM of *Arabidopsis*. Figure based on [Alberts et al., 2002a].

4.1.3 Cell size control during the cell cycle

Cell size control is essential to limit cell size variability, maintain meristem function, and ensure optimal cell function [D'Ario and Sablowski, 2019, Serrano-Mislata et al., 2015, Jones et al., 2017]. This regulation is achieved by coupling cell growth to the cell cycle, with critical checkpoints at the G1 to S, and G2 to M checkpoint [D'Ario and Sablowski, 2019].

Four theoretical models have been proposed to explain how cells may control their size: the sizer (i), timer (ii), adder (iii), and the plant-specific ruler model (iv). (i) In the sizer model, a cell divides upon reaching a critical size threshold. (ii) In the timer model, cells divide after a fixed period of time, regardless of their size. (iii) In the adder model, cells grow by adding a constant volume before each division, independent of their initial size. (iv) And, in the ruler model, cell growth is linked to the distance from the meristem. Fitting experimental data to these models has yielded varying results. Bacterial species tend to follow the adder model, while studies in mammalian cells support either the adder or sizer models [Cadart et al., 2018, Deforet et al., 2015, Varsano et al., 2017, Campos et al., 2014]. In plants, both *in silico* and *in vivo* measurements support the sizer model [Echevarria et al., 2022, Jones et al., 2017, Pavelescu et al., 2018]. It is also possible that cells integrate the features of multiple models at different checkpoints [Chandler-Brown et al., 2017].

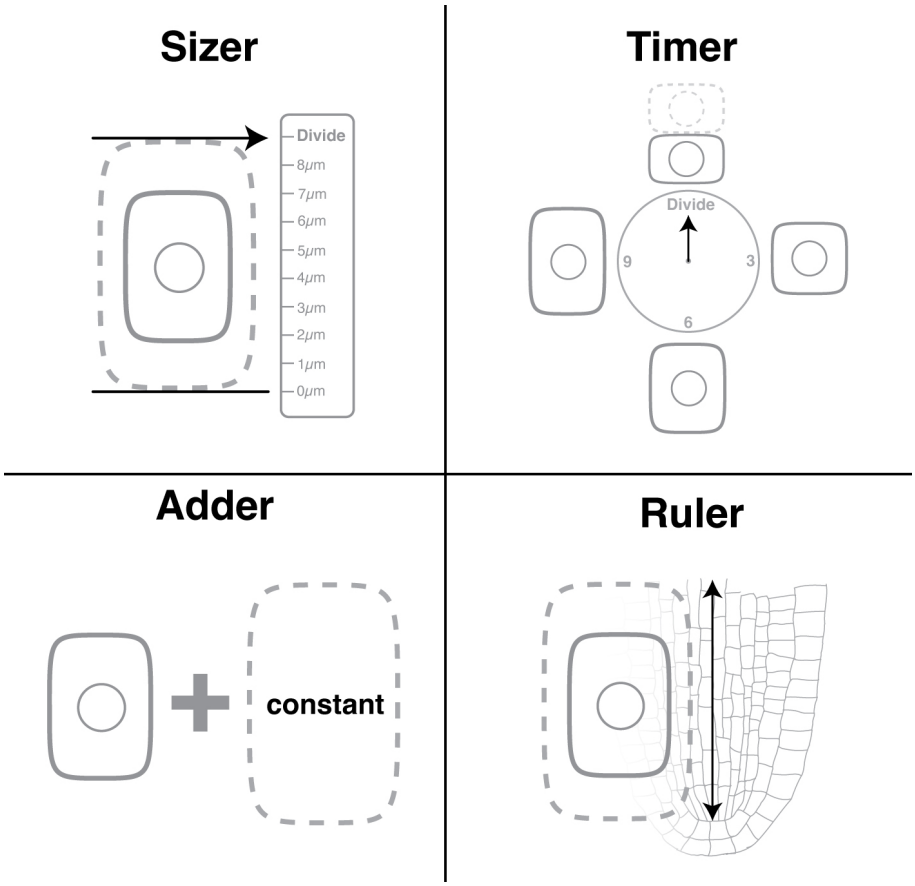

Figure 4.3: Schematic representation of four theoretical models that explain cell size control. Sizer model: cells divide upon reaching a specific size. Timer model: cells divide after a fixed period of time. Adder model: cells grow by adding a constant volume before division. Ruler model: a plant-specific mechanism in which cell growth is relative to the distance from the meristem. The dashed lines represent the size added in each model before division, except for the timer model. The RAM outlines were inspired by [Detlef Weigel and Peter Doerner, 1996].

To clarify which model plants use, the corresponding molecular mechanism needs to be identified. However, although plants are generally thought to follow a sizer model, the underlying molecular "size-sensing" mechanisms remain only partially described [Sablowski and Gutierrez, 2022]. Evidence from other model organisms suggests that size-dependent regulation of the cell cycle may occur at the G1-to-S transition or at the G2-to-M transition [D'Ario and Sablowski, 2019]. In the G1 to S transition, regulation often relies on measuring the size-dependent concentration of specific biomolecules to a fixed reference, such as their interaction with the constant amount of DNA [D'Ario and Sablowski, 2019].

Intriguingly, in the fission yeast *Schizosaccharomyces pombe* (*S. pombe*), progression from the G2 to M phase depends on the polarization of specific proteins at the plasma membrane, a process that loosely resembles SOK protein polarization (Figure 4.4). In *S. pombe*, a kinase cascade regulates cell size by spatially organizing signaling components. The membrane-associated kinase Pom1p is localized to the cell poles and inhibits another kinase, Cdr2p, from accumulating at these sites. As a result, Cdr2p forms cortical nodes at the cell center. These nodes are essential for recruiting and organizing downstream regulators of the cell cycle. Studies in wildtype and mutant strains, as well as computational models, have shown that the formation and distribution of Cdr2p nodes scales specifically with cell surface area, where node formation at the cell center increases as the surface area expands [Pan et al., 2014, D'Ario and Sablowski, 2019].

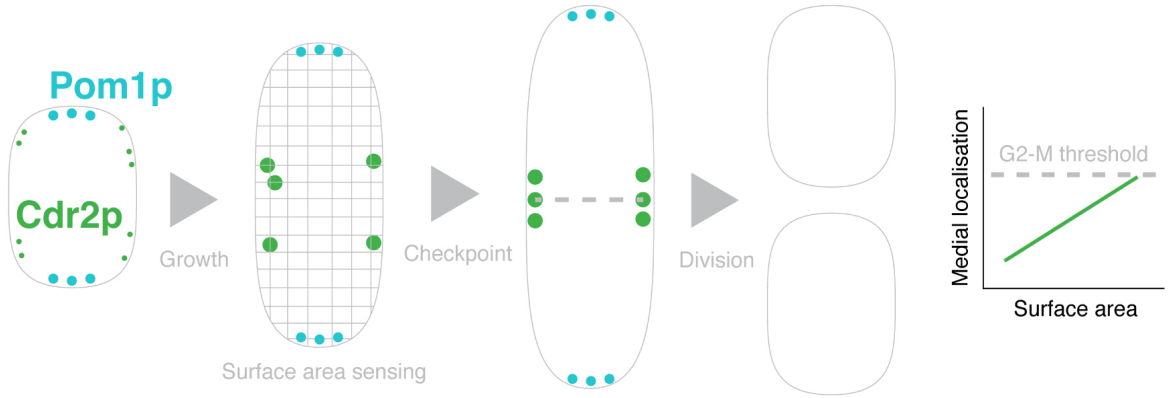

Figure 4.4: Schematic of cell size regulation in fission yeast. As cell surface area increases, Cdr2p localizes to the medial cortex, forming cortical nodes that function as signaling hubs. These nodes recruit regulators of mitotic entry, helping to determine when the cell is large enough to divide. Figure inspired by [D'Ario and Sablowski, 2019]

4.1.4 Objective

The precise function of SOK proteins remains unclear. The inability to generate higher-order mutants with a *SOK5* LOF allele suggests that SOK5 plays an essential role in plant development (Andriy Volkov). In the pentuple mutant (*sok1/2/3/4»5*), reduced cell division and abnormal cell size point to a potential role for SOK5 in cell size regulation (Dr. Reyes-Hernández). A working hypothesis is that SOK proteins internalize in response to mechanical stress generated during cell growth (Prof. Dr. Alexis Maizel & Dr. Reyes-Hernández), which is supported by the results in Chapter 2. Once a mechanical threshold is exceeded, SOKs may internalize to promote cell cycle progression. Consistent with this, data from Dr. Reyes-Hernández suggest that higher-order *SOK* mutants remain longer in the G2 phase, indicating that this regulation could occur at the G2-to-M checkpoint (Figure 4.5).

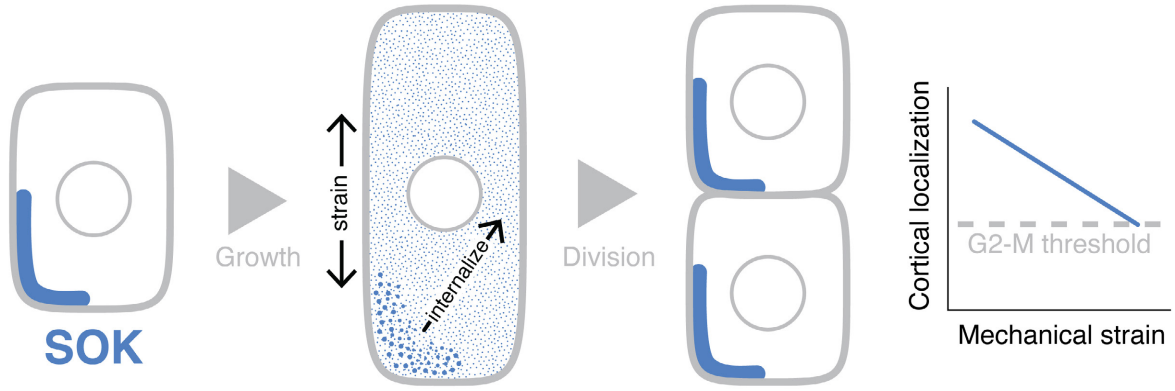

Figure 4.5: Hypothetical model of SOK function. SOK proteins act as sensors of mechanical strain. Once mechanical stress surpasses a critical threshold, SOKs become internalized and trigger progression through the cell cycle, specifically at the G2-to-M checkpoint. This model is inspired by conceptual work from Prof. Dr. Alexis Maizel.

The aim of this chapter is to investigate whether SOK5 activity correlates with the cell cycle and to identify the subcellular processes influenced by SOK proteins. To this end, gSOK5::YFP signal will be monitored during LR development and in the RAM. LR development provides a context with frequent cell divisions, whereas in the RAM, divisions occur less frequently but the timing of cell cycle phases is better characterized [Desvoyes et al., 2021, Pasternak et al., 2022, Echevarria et al., 2022]. To investigate SOK5 function, the phenotype of the *sok1/2/3/4»5* pentuple mutant will be analyzed in the wound-healing assay (Section 2.1.4), where changes in the mechanical landscape affect cell divisions [Hoermayer et al., 2024], thereby providing a context to assess how SOK proteins influence this process.

4.2 Results

4.2.1 SOSEKI5 expression peaks prior to the end of mitosis

To investigate whether *SOK5* expression correlates with the cell cycle, I live imaged gSOK5::YFP during LR development from stage II to emergence using light sheet microscopy (n=2 timelapses) [Yoshida et al., 2019]. In these timelapses, gSOK5:YFP signal appeared relatively low during early stages compared to later stages, possibly due to increased mechanical compression exerted by overlying tissues in the early LRP (Section 2.2.1. Nevertheless, gSOK5:YFP signal intensity consistently exhibited a transient increase prior to cell division throughout organogenesis (Figure 4.6a; Movie 8). These observations were consistent with independent multiphoton live imaging experiments of gSOK5::YFP during early LR development (n=12 timelapses; see Section 1.2.1).

To quantify when SOK5 signal intensity peaked, I calculated the normalized mean signal intensities in individual cells undergoing division during developmental stages IV to VI (n=12 cell divisions from two different light sheet timelapses), and plotted this over time, relative to the end of mitosis. This analysis revealed that gSOK5::YFP signal intensity peaked approximately 45 minutes prior to the end of mitosis (Figure 4.6a).

To determine whether this peak was transcriptionally regulated or influenced by mechanical cues, I quantified the signal intensity of pRPS5A::SOK5:YFP, which is constitutively expressed, in LRPs where the overlying cortex and epidermis were ablated (to exclude that mechanical compression affects the signal intensity). To account for variation in cell cycle phase duration, I did the analysis in the same developmental stages (IV–VI) as quantifications for gSOK5::YFP (n=12 cell divisions; Movie 9).

Under these conditions, pRPS5A::SOK5:YFP signal remained stable prior to division, suggesting that the increase in gSOK5::YFP signal reflects transcriptional upregulation. Interestingly, the decrease in signal intensity, 30 minutes before the end of mitosis, was consistent between pRPS5A::SOK5:YFP and gSOK5::YFP, where SOK5 appeared to internalize. This suggests that the decrease in signal intensity 30 minutes prior to the end of mitosis is not transcriptionally regulated. Instead, there may be an alternative (mechanical-dependent) cue triggering internalization (Figure 4.6a, b).

To investigate during which cell cycle phase gSOK5::YFP signal peaks, I extended this analysis to the RAM, where cell divisions are less frequently observed but the durations of the cell cycle phases are characterized in more detail [Yin et al., 2014, Pasternak et al., 2022, Echevarria et al., 2022]. To this end, live imaging of gSOK5::YFP was performing during RAM development using light sheet microscopy (n=2 timelapses; movies made in collaboration with Dr. Reyes-Hernández) [Yoshida et al., 2019]. Notably, unlike in the LR, a relatively high gSOK5:YFP signal intensity in the RAM was not strictly associated with cell division, particularly in the root cap where the signal was constitutively high, suggesting that SOK5 expression is not exclusively linked to the cell cycle. Nevertheless, in dividing cells, a transient flare-up of gSOK5:YFP signal was consistently observed prior to division (Movie 10). Quantification of these events (n=6 cell divisions) revealed a temporal pattern similar to that observed during LR organogenesis, with gSOK5:YFP signal intensity peaking approximately 30 minutes before the end of mitosis and declining over the final 30 minutes. Similar to the LR, during this final phase, SOK5 appeared to internalize (Figure 4.6c).

Together, these findings suggest that SOK5 expression peaks at the end of the G2 phase or during mitosis, while SOK5 may internalize during mitosis.

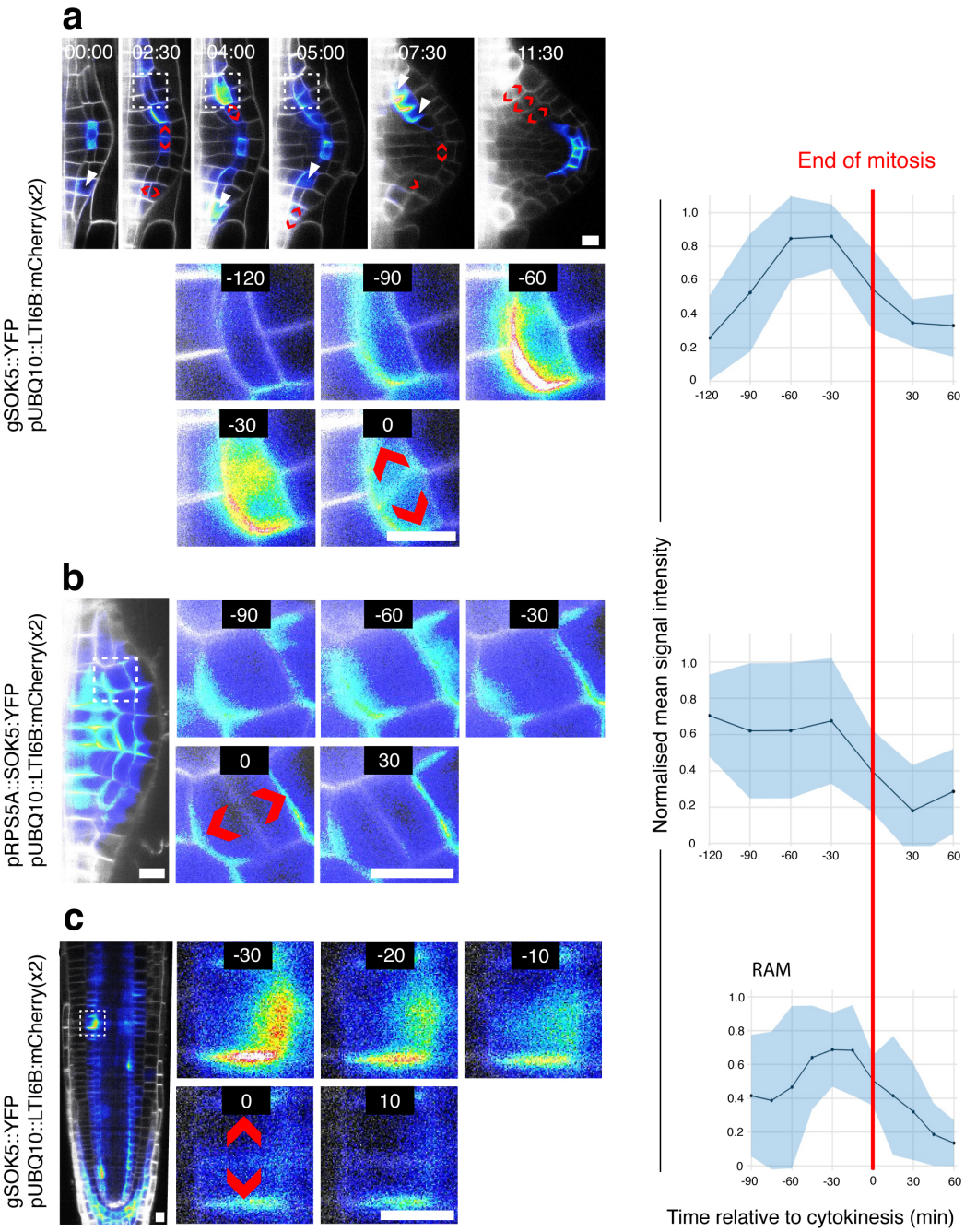

Figure 4.6: *SOK5* expression peaks roughly 30 minutes prior to then end of mitosis. (a) During LR organogenesis, *gSOK5::YFP* is expressed in the endodermis precursor prior to most divisions. Quantification of normalized signal intensity over time (n=12 cell division) indicates that the gSOK5:YFP signal peaks roughly 45 minutes prior to the end of mitosis. (b) Timelapse close-up of pRPS5A::SOK5:YFP signal during a cell division in a stage IV LRP. pRPS5A::SOK5:YFP signal remains relatively stable prior to division but shows a notable decrease approximately 30 minutes before division (n=12 cell divisions). Note that the overlying cortex and epidermis were ablated to eliminate mechanical influences from surrounding tissues, ensuring that changes in pRPS5A::SOK5:YFP signal intensity reflect intrinsic cellular dynamics rather than external mechanical inputs. (c) gSOK5::YFP signal intensity in a dividing cortical cell of the RAM (n=6 cell divisions). Signal intensity over time indicates that signal intensity peaks at roughly 30 minutes prior to the end of mitosis. Zoomed-in regions are indicated by dashed squares. Time: (hour:min) in images; (min relative to the end of mitosis/cytokinesis) in zoomed-in imaged. Scale bars 10µm

Movie 8: gSOK5::YFP signal flares up prior to divisions during LR organogenesis.

Click here to view Movie 8
Click here to download Movie 8

Movie 9: pRPS5A::SOK5:YFP signal intensity is constant prior to cell divisions in LR organogenesis but drops in the 30 minutes prior to division.

Click here to view Movie 9
Click here to download Movie 9

Movie 10: gSOK5::YFP signal flares up prior to cortex cell division in the RAM.

Click here to view Movie 10
Click here to download Movie 10

4.2.2 The *sok1/2/3/4»5* pentuple mutant has few regenerative divisions

SOK proteins respond to mechanical cues and are upregulated during the cell cycle (Chapter 2, Section 4.2.1). However, it remains unclear what the function of the SOK proteins is. The wound healing assay (Section 2.1.4), in which mechanical cues influence regenerative divisions, may provide a useful context to explore this.

To investigate whether SOK5 contributes to wound-induced regeneration, I live imaged gSOK5::YFP and pRPS5A::SOK5:YFP following targeted ablation of epidermal cells in the RAM, and quantified the normalized mean signal intensity of both [Yoshida et al., 2019]. Strikingly, gSOK5::YFP signal was weak both before and immediately after ablation, but increased markedly 1.5 hours post ablation, visually peaking at 3 hour post ablation (Movie 11). In contrast, pRPS5A::SOK5:YFP signal intensity remained stable post ablation, suggesting that *SOK5* is upregulated roughly 1.5 post ablation and that *SOK5* has a function in wound healing (Figure 4.7).

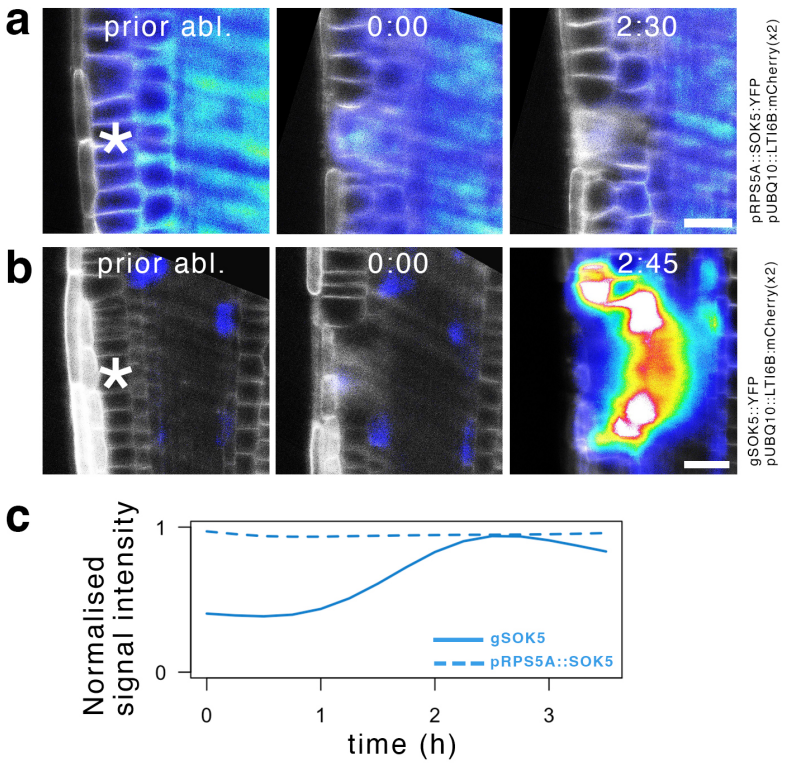

Figure 4.7: SOK5 may play a role in wound healing. (a) pRPS5A::SOK5:YFP signal appears to be constant post ablation (n=2 timelapses). (b) Whereas, gSOK5::YFP flares up roughly 2.5 hours post ablation (n=2 timelapses). Asterisks indicate ablation site. Scale bar 20µm. (c) Quantification of mean signal intensity ratio of both markers (SOK5:YFP over LTI6B:mCherry(x2)), normalized between 0 and 1). pRPS5A::SOK5:YFP signal intensity is constant post ablation, whereas the gSOK5::YFP signal flares up roughly 2.5h post ablation.

Movie 11: gSOK5::YFP signal flares up during wound healing. Time: (hour:min). Scale bar 20µm. This movie consists of three separate recordings region stitched together (hence the z-frame shifts).

Click here to view Movie 11
Click here to download Movie 11

To investigate the role of SOK5 in wound healing, I used the inducible *sok1/2/3/4»5* pentuple mutant, which under uninduced conditions functions as a quadruple mutant (Andriy Volkiv, Dr. Reyes-Hernández). I ablated single cortex cells of uninduced *sok1/2/3/4»5* quadruple mutants (Mock) and induced *sok1/2/3/4»5* pentuple mutants (DEX) in parallel. Additionally, as a control for lack of division, uninduced *sok1/2/3/4»5* quadruple mutants were treated with hydroxy urea (HU), a known inhibitor of cell divisions [Francis, 2007]. After ablation, plants were allowed to recover for 8 or 16 hours under their respective treatments and were then fixed and stained with a cell wall marker to visualize cell contours. Z-stacks of the ablated regions were acquired using confocal microscopy and analyzed for phenotypic differences.

As expected, there were no apparent divisions in the control (HU-treated) samples. In contrast, in both the Mock and DEX-treated sample, divisions were observed at both 8 and 16 hours post ablation. Surprisingly, there were no apparent phenotypic differences between the Mock and DEX-treated samples. However, upon closer inspection, subtle differences in the number of regenerative divisions appeared, indicated by the number of oblique divisions (Figure 4.8). To quantify this, oblique cell divisions were counted in a double-blind way across all treatments (Method 8.4.6). The counting revealed a significant reduction in oblique cell divisions in the pentuple mutant at both 8 and 16 hours post-ablation (Figures 4.8, 4.10). Notably, due to practical constraints, it was not possible to ablate all samples simultaneously. As a result, the DEX-treated pentuple mutants were intentionally ablated first and had approximately one additional hour of recovery time. Despite this longer recovery window, the pentuple mutants still exhibited significantly fewer divisions, further reinforcing the significance of the reduction in regenerative cell division.

Together, these results indicate that there are less regenerative divisions in the inducible *sok1/2/3/4»5* pentuple mutants compared to the uninduced *sok1/2/3/4»5* quadruple mutant, which suggests that SOK5 has a function in cell cycle progression.

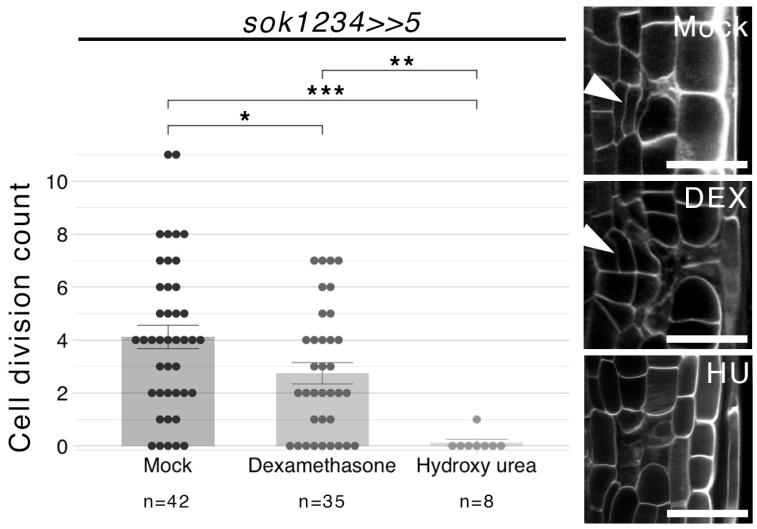

Figure 4.8: The *sok1/2/3/4»5* pentuple mutant has a significant reduction in regenerative cell divisions 16 hours post-wounding in. Although no obvious phenotype is visible in the microscopy images stained with calcofluor white, quantitative analysis via double-blind counting reveal that Mock-treated samples displayed a higher number of regenerative (oblique) divisions (arrowhead) compared to DEX-treated samples. HU-treated samples, which served as a control for a divsion-less phenotype, accordingly exhibited no regenerative divisions. Scale bar: 20µm. Due to technical limitations, DEX-treated samples were ablated first and thus had approximately one additional hour of recovery, yet still showed significantly fewer divisions. Statistical test: Wilcoxon rank-sum test (*: $p<0.05$; **:$p<0.01$; ***:$p<0.001$).

4.3 Conclusion

The results indicate that SOK5 is linked to the cell cycle, with upregulation during the G2 phase and a peak either at the G2 to M transition or during mitosis. Following this expression peak, SOK5 appears to internalize during mitosis in a manner independent of transcription, suggesting a mechanically triggered process. Furthermore, the reduced frequency of regenerative divisions observed in the wound healing assay of the *sok1/2/3/4»5* pentuple mutant implies a delay in cell cycle progression. Together with collaborative data where the *sok1/2/3/4»5* pentuple mutant has a prolonged residence in the later stages of the cell cycle, my findings support a potential role for SOK5 in cell cycle progression.

4.4 Discussion

In this chapter, I showed that SOK5 expression is upregulated during the G2 phase of the cell cycle, with signal intensity peaking near the end of the G2 phase or during mitosis (Figure 4.6). Following this peak, the SOK5 signal appears to internalize prior to cytokinesis (Figure 4.6). The wound healing assay revealed that suboptimal levels of SOK5 in the *sok1/2/3/4»5* lead to a reduced number of regenerative divisions (Figure 4.8).

Furthermore, the *sok1/2/3/4»5* mutant has impaired RAM development, with a meristem that depletes over time, and a longer residence in the late stages of the cell cycle (Dr. Reyes-Hernández).

Together, this implicates SOK5 in the punctual execution of cell division (Figure 4.9). Open question in this model are: what triggers the upregulation of SOK5? The upregulation of *SOK5* post ablation may provide insight on this (Figre 4.7). Furthermore, what causes the internalization of SOK5? These questions are addressed below. Additionally, I speculate how suboptimal levels of SOK5 may deplete a meristem over time.

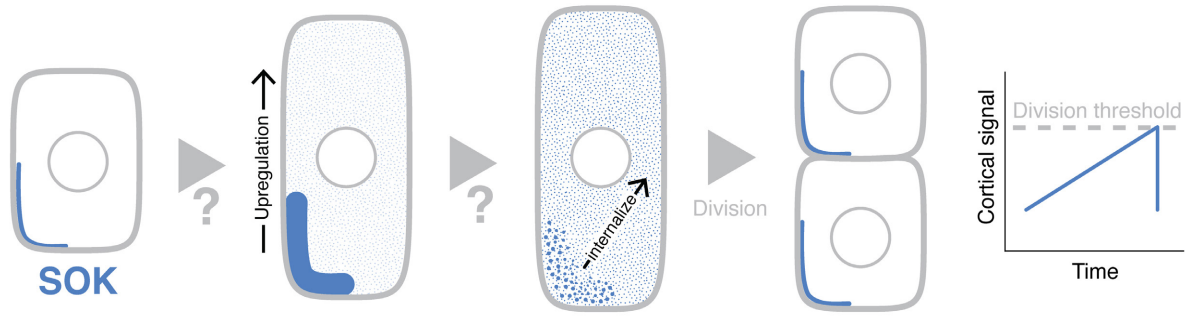

Figure 4.9: Hypothetical model of SOK5 function. SOK5 is upregulated during the cell cycle. Upon reaching a signal intensity (accumulation) threshold, SOK5 may promote division.

4.4.1 What triggers the upregulation of SOK5 in neighboring cells after wound healing?

SOK5 is upregulated approximately 1.5 hours after ablation in cells adjacent to the wound site, with expression peaking around 3 hours post-ablation (Figure 4.7). Since regenerative divisions follow an atypical cell cycle [Marhavý et al., 2016, Lee et al., 2025, Hoermayer et al., 2024], and because SOK5 is constitutively expressed in the root cap (Movie 11), this suggests that SOK5 expression is not strictly coupled to cell cycle progression. Instead, additional regulatory factors may be involved.

During the 1.5 to 3 hour window post-ablation, neighboring cells show an auxin response [Hoermayer et al., 2020], Ca^{2+}-dependent ethylene signaling [Marhavý et al., 2019, Ma et al., 2025], and mechanically induced microtubule reorientation [Hoermayer et al., 2024], all of which represent potential mechanistic links to SOK5 upregulation. An explanation for SOK5 upregulation may be auxin signalling, as *SOK5* is downstream of auxin signalling in the embryo [Yoshida et al., 2019].

4.4.2 What causes internalization of SOKs prior to cell division?

SOK5 is upregulated prior to division, where in the 30 minutes before cytokinesis, the protein appears to internalize. This is similar to what has been observed for SOK1, which internalizes prior to division and has been described as an unstable protein [Yoshida et al., 2019]. Yet, it is unknown what causes this internalization prior to division. Given that internalization has also been observed as a response to targeted cell ablation (Figure 2.9; Section 2.4.4) and SOKs additionally appear to internalize in response to high mechanical stress in different mechanical contexts (Figure 1.24, 2.7), it is plausible that internalization is triggered by a mechanical change or associated stress signaling. Although stress signaling can play a role during the cell cycle [Mhamdi and Van Breusegem, 2018, De Simone et al., 2017], it is unknown whether mechanically induced stress signaling plays a role during mitosis [Sablowski and Gutierrez, 2022, Soni and Bacete, 2023]). A logical next step would be to determine whether SOKs respond to stress signaling.

4.4.3 How does the punctuality of divisions contribute to meristem maintenance?

The wound healing assay performed on the *sok1/2/3/4»5* pentuple mutant revealed that there may be a delay in divisions in the pentuple mutant. Furthermore, the pentuple mutant has been shown to be impaired in meristem maintenance and is affected in cell size (Data from Dr. Reyes-Hernández). This may highlight the importance of punctual divisions in meristem maintenance.

Given that the reduction in regenerative cell division is relatively subtle compared to HU treatment, this suggests that the *sok1/2/3/4»5* pentuple mutant experiences only a modest delay in cell cycle progression. This may be caused by residual amounts of SOK5 following KD, that may be sufficient to progress the cell cycle. In contrast, a complete LOF for all SOK genes seems to be lethal (Data from Andriy Volkov), suggesting that in the absence of SOK5, cell divisions may not occur.

Furthermore, collaborative data indicate that higher-order *sok* mutants with KD of SOK5 remain longer in the G2 phase than wildtype, approximately 2 to 3 hours longer (Data from Dr. Reyes-Hernández). Such a delay likely accounts for the observed reduction in regenerative divisions in the pentuple mutant during wound healing. Notably, the effect on RAM development has been shown to become more pronounced over time, where two days post SOK5 KD, the pentuple mutant displays a visibly shorter RAM compared to wildtype-like plants (Data from Dr. Reyes-Hernández). These findings imply that a moderate delay in cell cycle progression may be sufficient to deplete the RAM over time.

Computational modeling studies have shown that reproducing wildtype-like meristem behavior requires the RAM to be divided into two distinct zones, a proliferative domain with constant proliferative potential, and a transition domain in which proliferative potential gradually decreases [Baskin, 2000, Desvoyes et al., 2021]. These findings suggest that meristem size is maintained by preserving proliferative potential within the proliferative domain and allowing a gradual reduction of proliferation in the transition domain. As such, interference with the temporal regulation of cell division, as seen in higher-order *sok* mutants, may disrupt this spatiotemporal pattern and lead to depletion of the meristem over time. Furthermore, in shrinking meristems, the relative position of the QC changes, which may disrupt hormonal patterns or feedback signaling [Smet and Blilou, 2023], and ultimately result in meristem collapse.

4.5 Supplemental figure

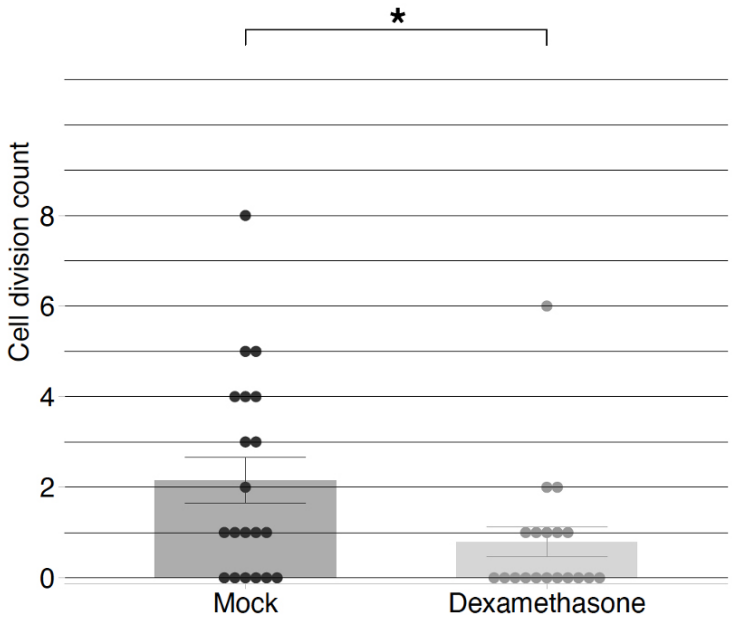

Figure 4.10: There are less regenerative division in the *sok1/2/3/4»5* pentuple mutant 8h post ablation. Statistical test: Wilcoxon rank-sum test (*: $p<0.05$)

Conclusion

The SOK polarity system was previously thought to reflect a global polarity system. Surprisingly, the findings presented in this thesis indicate that the SOK polarity system reflects a local, mechano-sensitive system. In this system, the SOK proteins respond to mechanics in a magnitude-dependent way, where they dissipate from regions with mechanical stress, while environments with mechanical heterogeneity allow SOK accumulation. Their subcellular localization appears to be able to respond to relatively fast signals, and is possibly influenced by stress signaling, whereas their specific polarization may depend on slower structural signals linked to the mechanical continuity of the cell wall network. Together, these observations support a model in which SOK proteins are sensitive to mechanical signals transmitted through the cell wall network. Perceiving these mechanical signals may modulate intracellular responses, one of which appears to ensure the punctual execution of cell division.

To build towards a model that links multicellular mechanics to developmental responses, a logical next step would be to determine whether SOK proteins respond to stress signaling, and to identify corresponding mechanisms that operate late in the cell cycle.

In addition, because the precise mechanical signature that polarizes SOKs remains unclear, it may be informative to investigate SOK polarization in simplified contexts with a limited set of potential polarization cues. Furthermore, computational mechanics may provide additional insight to pinpoint which mechanical signature (tensile stress or tensile strain) is enriched at sites where SOK proteins accumulate.

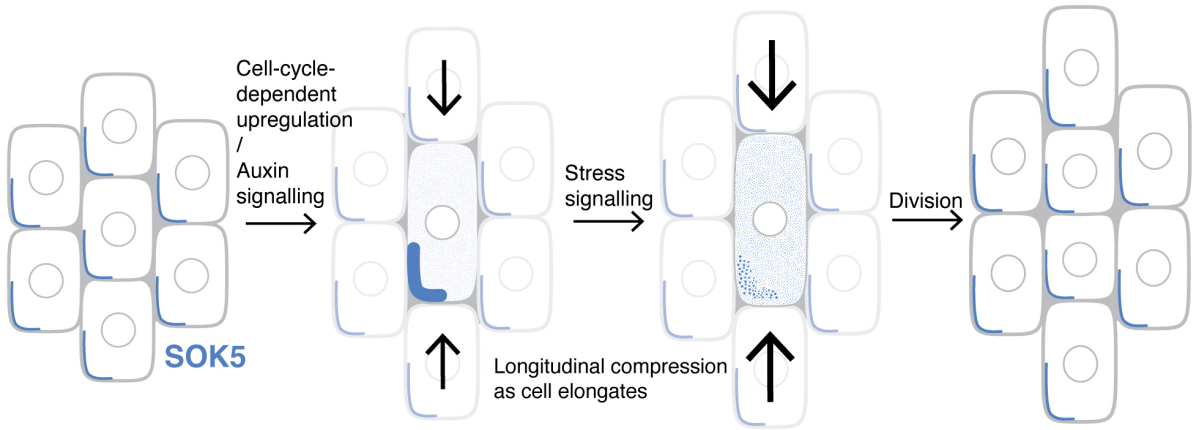

Figure 5.11: Final model: During cell growth, SOK5 may be upregulated either through auxin signaling or via cell cycle–dependent regulation. A longitudinal compressive force generated during cell elongation may cause SOK5 internalization, thereby triggering the onset of cell division.

Annex 1: Towards plant optogenetics at the cellular level

6.1 Introduction

Optogenetics is a method that enables controlled gene expression by exposing organisms to light. In animals, this technique is particularly useful for studying the effects of targeted transgene expression [Krut et al., 2024]. However, applying optogenetics to plants presents additional challenges, since plants depend on broad-spectrum light for growth, which inadvertently activates optogenetic systems constitutively. To address this limitation, researchers have developed more sophisticated strategies, such as using additional transcriptional repressors that can suppress optogenetic expression under normal growth conditions [Christie and Zurbriggen, 2021, Ochoa-Fernandez et al., 2020].

PULSE is an optogenetic system that regulates transcription using two artificial transcription factors, an activator and a repressor, each fused to distinct photoreceptors [Ochoa-Fernandez et al., 2020]. The activator consists of phytochrome B (PhyB) fused to virion protein 16 (VP16), which promotes transcription under red light and is inactivated by far-red light [Müller et al., 2014]. To further suppress transcription under normal growth conditions, PULSE also employs a repressor composed of a dominant SRDX domain fused to the blue-light-sensitive bacterial transcription factor erythrobacter litoralis 222 (EL222) [Motta-Mena et al., 2014].

These artificial transcription factors bind to an artificial promoter that drives the expression of a reporter gene of choice. The artificial promoter has binding sites for the red-light activator $((etr)_8)$ and blue-light repressor $((C120)_5)$, which are flanked by an enhancer sequence from 35S promoter, and a minimal promoter domain of human cytomegalovirus (hCMV) (Figure6.12) [Odell et al., 1985, Chan et al., 1996]. This system has been demonstrate to activate gene expression in *Arabidopsis* protoplasts, control an artificial immune response in *Nicotiana benthamiana* (*N. benthamiana*) leaves, and trigger a luminescence response in whole *Arabidopsis* seedlings [Ochoa-Fernandez et al., 2020].

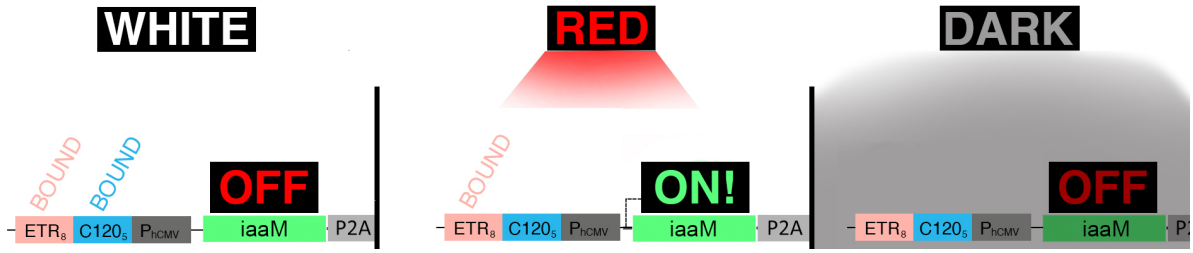

Figure 6.12: Schematic of PULSE response to different light conditions. Under white light the activating component and repressing component bind to the artificial promoter. Because the repressor is dominant, transcription is repressed. Under red light, only the activator promotes transcription. And finally in darkness, one half of the activator binds to the promoter but lacks the red-light-induced binding with PhyB fused to VP16, required for transcriptional activation. Graphical elements from [Ochoa-Fernandez et al., 2020] were reused in this figure.

The PULSE system has primarily been applied *ex-vivo* and at the organ or organismal level. Here I pilot the use of PULSE at the cellular level, for this I used a published version of PULSE to assess light conditions for plant growth in *N. benthamiana* leaves and in *Arabidopsis* roots [Ochoa-Fernandez et al., 2020]. And, I designed and tested an ambitious system to initiate LR organogenesis in *Arabidopsis* with cellular precision.

6.2 Results

6.2.1 Growth under white light appears to sufficiently suppress reporter expression

To assess the optimal light conditions for normal plant growth while suppressing basal optogenetic expression, I used a published version of the PULSE system, which I name C-PULSE [Ochoa-Fernandez et al., 2020]. In C-PULSE, transcription of each component is driven by the UBQ10 promoter, with the reporter expressing a nuclear-localized mVenus:H2B fusion protein. Additionally, in C-PULSE there is a constitutively expressed, nuclear-localized mCerulean:NLS fluorescent marker, to constitutively label all nuclei (Figure 6.13) [Ochoa-Fernandez et al., 2020].

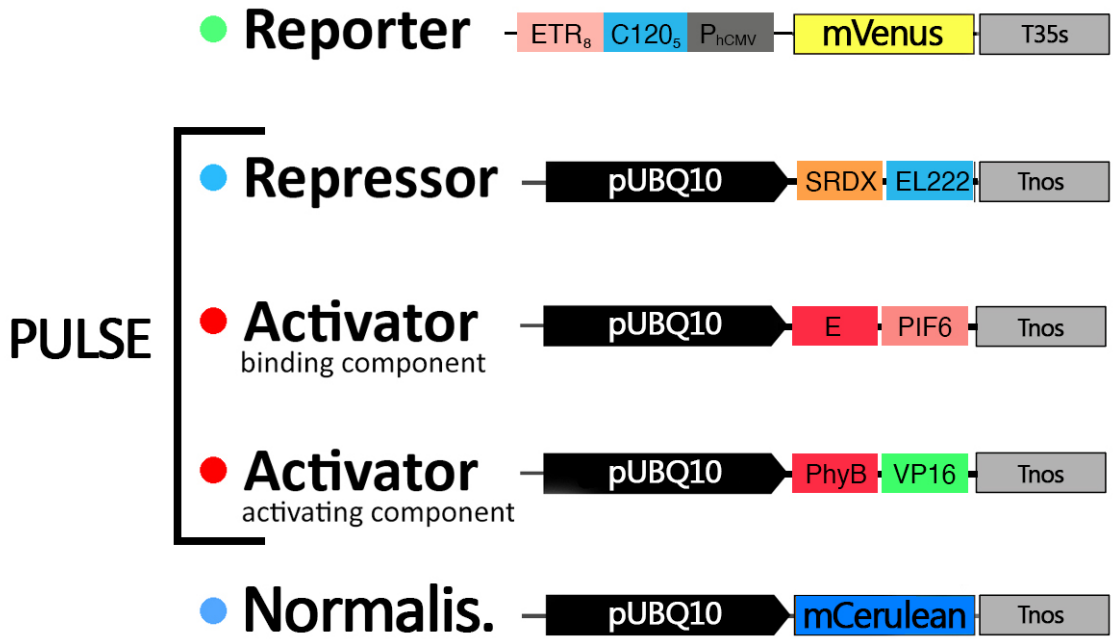

Figure 6.13: The C-PULSE system where each component is under control of pUBQ10, the reporter drives expression of mVenus:H2B, and there is an additional normalisation component with mCerulean:NLS, that is used to mark all nuclei constitutively. The activator consists of two transgenes, a binding component that binds to DNA and red-light induced activating component. Graphical elements from [Ochoa-Fernandez et al., 2020] were reused in this figure.

C-PULSE system was transiently expressed in *N. benthamiana* leaves, and the plants were subsequently exposed to one of three light treatments using FloraLED growth chambers that allow independent control of white, blue, red, and far-red light intensities.

To assess the efficiency of transcriptional repression, plants were exposed for 4 days to either darkness (D), blue light (B; 440-500nm), or white light (WL; 440-700nm) supplemented with blue and far-red light (FR; 720-780nm). Following this initial light treatment, the same plants were exposed to red light (R; 650-700nm) overnight to induce reporter expression. After both the initial 4 day suppressive treatment and the overnight inductive treatment, the constitutive nuclei marker (mCerulean:NLS) and the reporter (mVenus:H2B) were imaged in leaf sections using confocal microscopy. The labeled nuclei were counted in both channels, and the congruence (mVenus:H2B over mCerulean:NLS) was calculated and plotted in a boxplot (Figure 6.14). Additionally this treatment was done for plants that were infiltrated with a mock (water) solution, which showed no fluorescent activity.

For the initial suppressive treatment, comparison between the supplemented white light (WL+B+FR) and darkness indicated that there is significant basal reporter expression in darkness. Comparison between WL+B+FR and blue light indicated that the inclusion of WL, which contains red light, does not significantly increase reporter gene expression (Figure 6.14). Whereas, upon red-light induction, the congruence increased significantly for each treatment, indicating that gene suppression can be reversed, independent of suppressive treatment (Figure 6.14b).

Altogether, WL+B+FR appears to be a suitable ”daylight” condition for experiments requiring suppression of optogenetic gene expression, as it included broad-spectrum light required for normal plant growth while minimizing reporter activation. In contrast, complete darkness may not be appropriate as a ”night” condition due to elevated basal expression. To mitigate this basal expression, a suitable ”night” condition may be either blue and/or far-red light to suppress basal reporter expression.

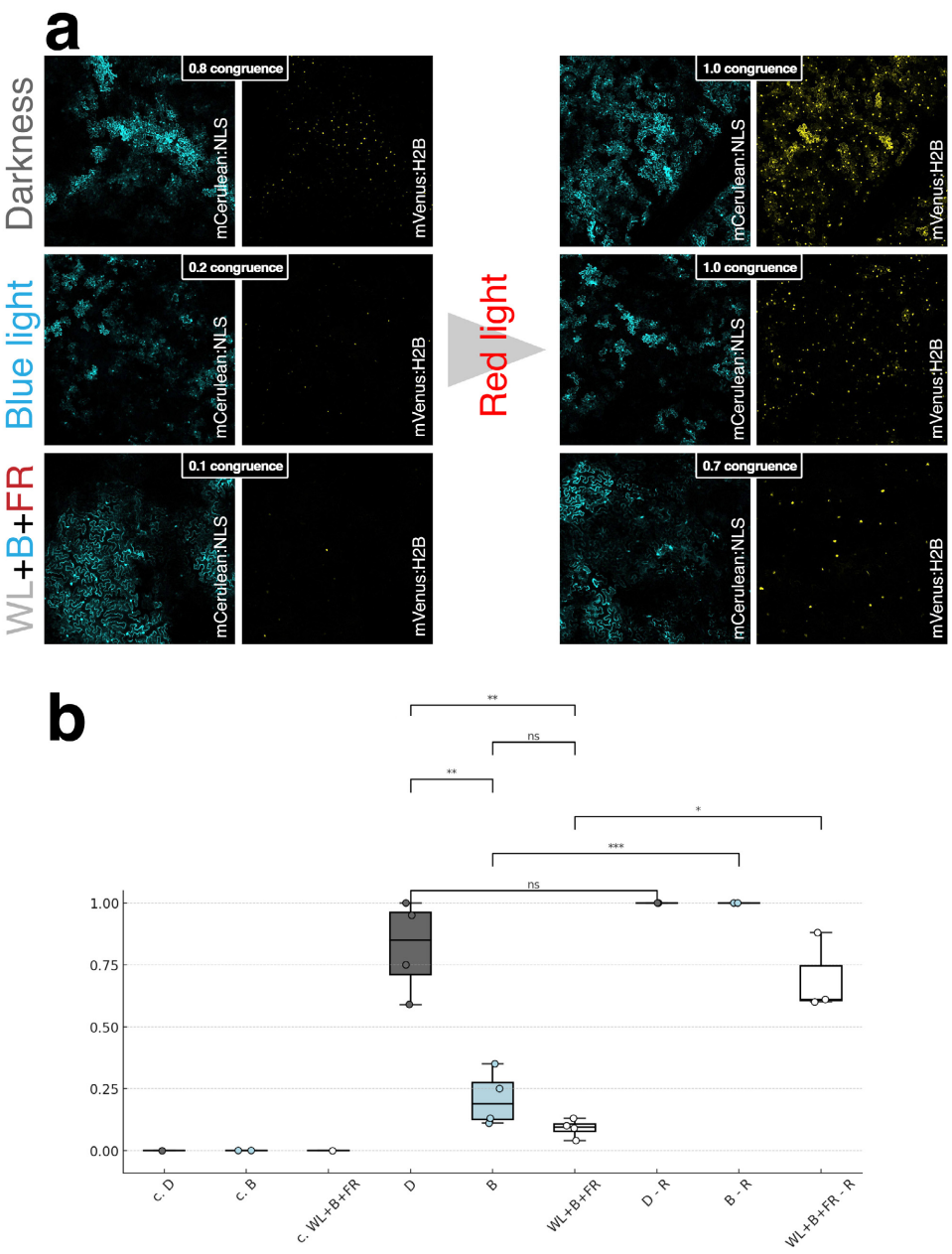

Figure 6.14: Probing how different light conditions activate C-PULSE in transiently transformed *N. benthamiana* leaves (a) Images show sections after 4 days under the indicated light conditions: darkness, blue light, or white light supplemented with blue and far-red light (WL+B+FR). The normalization marker mCerulean:NLS (constitutively expressed) is shown alongside red-light-induced mVenus:H2B. After the 4 day incubation, plants were exposed to red light overnight, and new sections of the same plant were imaged to assess light-induced reporter expression. (b) Reporter activation is shown as the congruence (mVenus/mCerulean ratio) for each condition (darkness, blue light, WL+B+FR), and their corresponding post-red-light exposure groups. Control samples were infiltrated with a mock (water) solution. In some cases, the calculated ratio exceeded 1, which were capped at 1, because values above 1 are not biologically meaningful. Statistical test: Welch's t-test (*: p<0.05; **:p<0.01; ***:p<0.001). Data generated jointly with Babette Knoblauch.

6.2.2 PULSE may not be suitable to control optogenetic expression at the cellular level in *Arabidopsis*

The tobacco-based experiment provided valuable insight into the light conditions suitable for regulating PULSE gene expression. However, transient expression in *N. benthamiana* does not fully replicate the behavior of stable transgenes in *Arabidopsis*, as agroinfiltration typically results in high and variable expression levels [Voinnet et al., 2003, Sparkes et al., 2006].

To test whether the PULSE system functions reliably in a stable genetic background, I generated transgenic *Arabidopsis* plant lines with the C-PULSE construct [Ochoa-Fernandez et al., 2020]. For T1 selection, plants underwent light-dependent kanamycin selection for 2 days and were grown under WL+B+FR for an additional 2 days. Basal reporter expression was monitored at this timepoint by capturing the constitutive nuclei marker (mCerulean:NLS) and the reporter (mVenus:H2B) confocal microscopy. Among the transformants analyzed (n=26), the majority (20/26) showed no detectable mVenus expression, indicating the absence of basal reporter activity. Plants were then transferred to red light overnight. Surprisingly, none of the transformants exhibited a clear response to red light in the RAM. In a few cases, a few cells displayed mVenus fluorescence after red-light treatment, suggesting partial activation of the system (Figure 6.15).

These promising lines were maintained under white light and later transferred to soil for propagation under long-day conditions in a plant room (Section 8.1.3). During growth in the plant room, the plants developed abnormal phenotypes (Figure 6.15). This abnormal development was likely caused by transgene load, because similar phenotypes were observed in other (non-optogenetic) plants with more than four transgenes (Figure 7.24.

Altogether the results indicate that PULSE may not be suitable for reliable induction of reporter expression at the cellular level, and that transgene load of the PULSE system causes developmental stress.

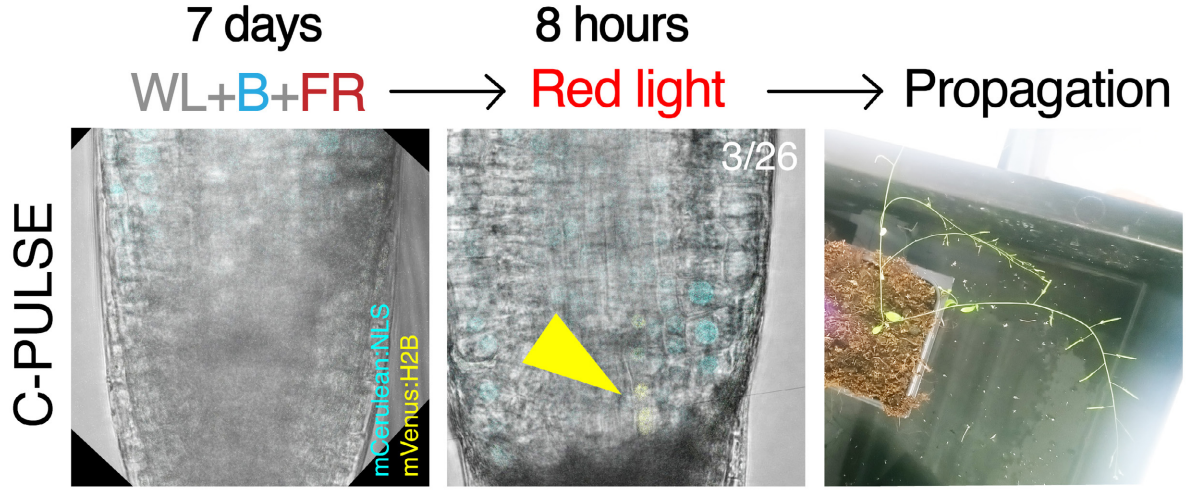

Figure 6.15: T1 selection of C-PULSE in *Arabidopsis*. Microscopy images show red-light–induced reporter expression (nuclear mVenus in a few cells of the RAM) and constitutively expressed mCerulean:NLS, overlayed on a brightfield image. The same lines showed developmental defects during propagation. Data generated jointly with Babette Knoblauch.

6.2.3 Reiteration that a PULSE-derived system may not function at the cellular level in *Arabidopsis*

Despite the indications that PULSE may not be suitable for optogenetic control at the cellular level, I continued my ambitious attempt to initiate LR organogenesis with cellular precision, as most experiments were conducted in parallel rather than direct follow-ups. For this, a modified version of PULSE was designed (together with Prof. Dr. Alexis Maizel, and Prof. Dr. Matthias Zurbriggen), which I named X-PULSE, which combined a constitutively active blue-light repressor with an XPP-specific red-light activator, and a reporter gene encoding the auxin biosynthesis catalyst indoleacetic acid tryptophan monooxygenase (iaaM) fused to mScarlet-I:NLS via a self-cleaving peptide. In principle, targeted red light illumination of XPP cells would trigger iaaM expression, thereby catalyzing auxin biosynthesis upon providing a substrate, a process previously shown to be sufficient for initiating LR organogenesis (Figure 6.16) [Dubrovsky et al., 2008].

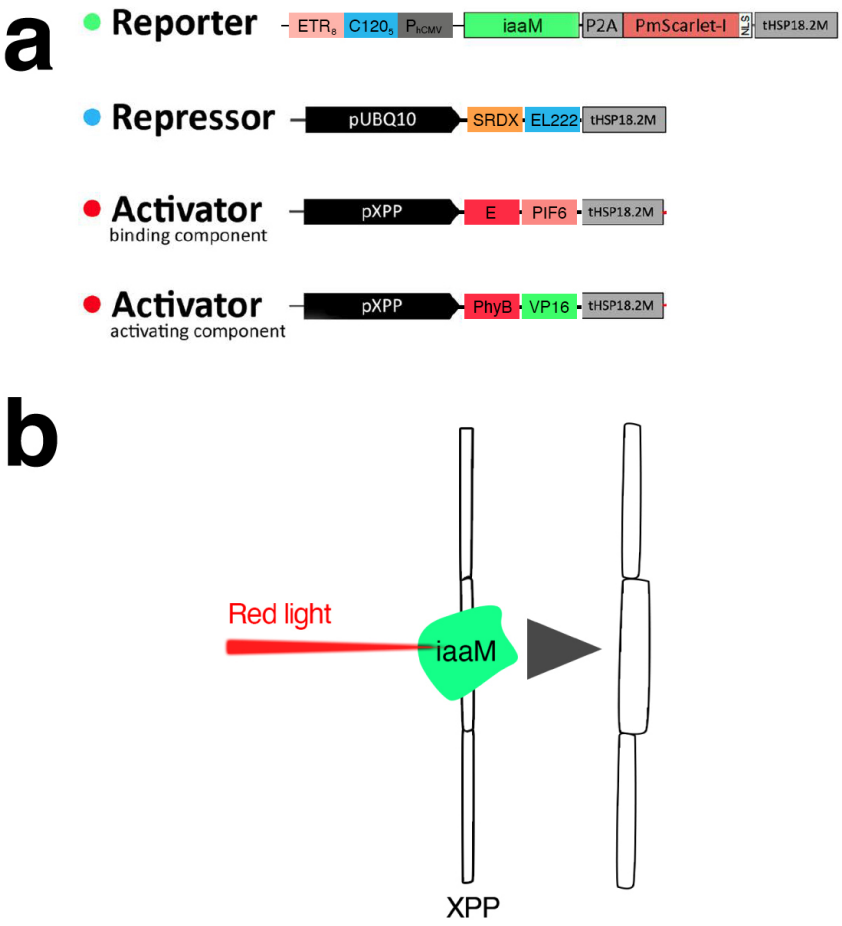

Figure 6.16: The X-PULSE system, an optogenetic approach to induce iaaM expression in XPP cells. (a) The transgenes of the X-PULSE system, including the reporter, repressor, and two components of the activator. The reporter expresses a catalyst of auxin synthesis (iaaM) linked to mScarlet-I:NLS via a self-cleavage-peptide. The repressor is constitutively active under the pUBQ10 promoter. The activator consists of two constructions, both of which are specifically active in XPP cells. Graphical elements where reused from [Ochoa-Fernandez et al., 2020]. (b) Intended purpose of X-PULSE: expresss iaaM with cellular precision in XPP cells by shining red light on single cells. Graphical elements from [Ochoa-Fernandez et al., 2020] were reused in this figure.

The X-PULSE system was cloned (jointly with Anika Seppelt) and was transformed into a plant line carrying gSOK1::YFP and pUBQ10::LTI6B:mCherry(x2), allowing polarity to be monitored post LR induction. T1 seedlings were grown for 4 days under white light, after which basal PULSE expression was monitored by capturing mScarlet-I:NLS using confocal microscopy. Plants were then exposed to red light overnight and induction of PULSE expression was monitored by capturing the mScarlet-I:NLS signal again. During this T1 selection, challenges similar to those encountered with the C-PULSE system were observed.

Prior to red-light induction, mScarlet signal was absent in most plants (43/55). After red light exposure, mScarlet-I signal was rarely observed in XPP cells, indicating partial activation of the reporter. Plants that had mScarlet-I in very few cells after red light exposure were transferred to soil for propagation. However, they developed similar abnormal phenotypes as those observed in C-PULSE and other plants with transgenic load (Figure 6.17, 7.24). These results indicate that the PULSE system may not be suitable for reliable optogenetic expression at the cellular level, and reiterate that transgene load of the PULSE system may cause developmental stress.

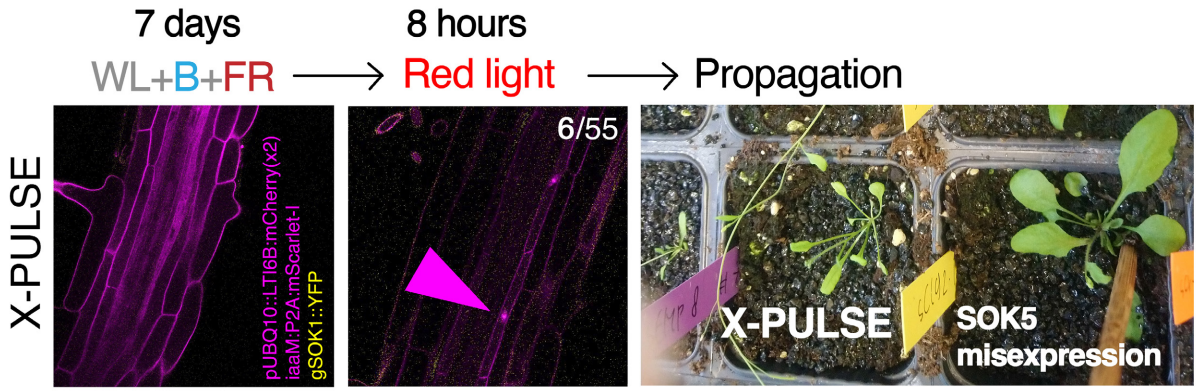

Figure 6.17: T1 selection of X-PULSE in *Arabidopsis*. Microscopy images show red-light–induced reporter expression: nuclear mScarlet-I fluorescence in XPP cells. Cell outlines are pUBQ10::LTI6B:mCherry(x2), and the gSOK1::YFP marker was not observed in these XPP cells, but was visible in the RAM (not shown). The same lines showed developmental defects during propagation.

6.3 Conclusion

In transient transformation of *N. benthamiana*, PULSE responded to light conditions as expected. Basal expression was suppressed under white light, while red light successfully induced PULSE expression. However, in stably transformed *Arabidopsis*, PULSE performed less effectively, with red light inducing expression in very few cells. In addition, the high transgene load required for PULSE may limit its applicability in mature plants, and hinder propagation.

6.4 Discussion

6.4.1 The optogenetic PULSE tool may not function at the cellular level in *Arabidopsis*

I aimed to employ the PULSE tool for cell-specific optogenetic manipulation. However, red-light induction produced an inconsistent cellular response, with iaaM expression detected in only a few cells rather than in all cells exposed to red light. By contrast, previous successful applications in *Arabidopsis* have been restricted to whole organism responses [Ochoa-Fernandez et al., 2020]. This suggests that the PULSE system is better suited for optogenetic regulation at higher organizational levels, such as the organ or whole-plant level.

Annex 2: GreenBraid - convenient stacking of transcriptional units

7.1 Introduction

Molecular cloning is a fundamental technique in biological research, enabling the assembly of a transcriptional unit (TU) that is subsequently used to genetically transform an organism. Traditionally, molecular cloning involved the use of restriction enzymes and DNA ligase to cut and join DNA fragments, a method that remains essential in many modern cloning workflows [Jackson et al., 1972, Cohen et al., 1973]. Since its inception, a variety of cloning strategies have emerged, including restriction-free and ligation-free methods, as well as modular and recombination-based approaches [Stevenson et al., 2013, Bomfiglio et al., 2025, Tian et al., 2014].

Modular cloning methods are hierarchical, scalable, and rely on libraries of standardized, reusable DNA modules [Lampropoulos et al., 2013, Sarrion-Perdigones et al., 2013a]. In these systems, ”Level 0” modules, containing basic genetic parts such as promoters, coding sequences, and terminators, can be assembled into a ”Level 1” TU. A level 1 TUs may then be combined with another level 1 TU to create ”Level 2” multi-TU construct.

Golden Gate cloning introduced the core principles that enables modular TU assembly [Engler et al., 2008]. Namely, directional ligation of DNA modules through the use of type IIS restriction enzymes. These enzymes cleave outside their recognition sequences, resulting in customizable overhangs, that are typically 4 basepairs in length, and enable the directional and seamless assembly of DNA modules. Each DNA module is stored in a circular vector with strategically oriented type IIS restriction sites. That is, they are oriented in such a way that, upon digestion, the recognition sites are absent from the module, and thus unable to interfere with subsequent cloning steps. Moreover, the released modules are flanked by unique 4 basepair overhangs that allow directional ligation in a predefined order. That is achieved by have complementing overhangs between adjacent DNA modules. Such a directional assembly reaction can be done in a single cyclic restriction-ligation reaction where the end product is a restriction-site-free destination vector containing the TU [Engler et al., 2008] (Figure 7.18). This reaction is cyclic, with restriction and ligation steps occurring in succession, progressively accumulating the desired destination vector while eliminating unstable byproducts that retain type IIS restriction sites.

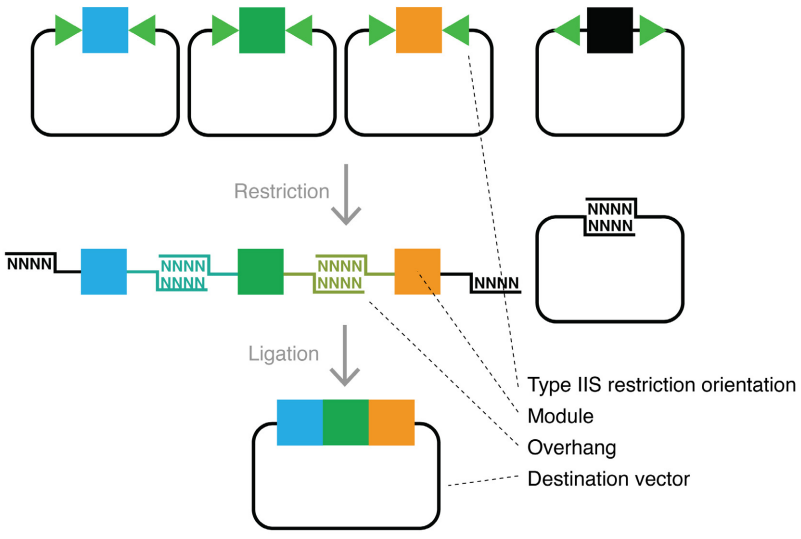

Figure 7.18: The GoldenGate cloning principle, where DNA modules are stored in entry vectors. The orientation of the type IIS restriction enzyme recognition sites is crucial for directional ligation. And, each overhang must be unique to ensure the assembly of modules in the desired order.

Several modular cloning systems that are based on this Golden Gate principle have been developed, each with distinct characteristics. These systems typically differ in their choice of type IIS restriction enzymes and their DNA module libraries, which are often tailored to specific kingdoms of life [Andreou and Nakayama, 2018, Weber et al., 2011, Lampropoulos et al., 2013, Sarrion-Perdigones et al., 2011].

GreenGate is a plant-focused modular cloning method that exclusively uses the BsaI (also known as Eco31I) restriction enzyme. In GreenGate, ”Level 0” DNA modules are assembled using a classical restriction-ligation reaction. Up to six Level 0 modules can be combined in a single assembly reaction to form a complete TU. These TUs can then be stacked into Level 2 multi-TU constructs using one of two strategies: (i) through the use of intermediate vectors to create constructs with two TUs, or (ii) by sequentially adding individual TUs with the help of an adapter module, enabling the construction of vectors with more than two TUs [Lampropoulos et al., 2013].

However, GreenGate has several inconveniences. First, construction of Level 0 modules via classical restriction-ligation can be time-consuming, particularly when modules must be domesticated, which is the removal of internal BsaI/Eco31I sites. Second, the system is restricted to the use of six modules per TU assembly, which limits its utility for building complex genetic tools, such as methods employing CRISPR/Cas. Third, TU stacking is often inefficient likely due to the exclusive use of a single type IIS enzyme and can laborious due to the inherently linear nature of the stacking process [Lampropoulos et al., 2013].

To overcome the inconveniences of the original system, a largely backward compatible upgrade, GreenGate 2.0, was developed. GreenGate 2.0 introduces three key improvements. First, it includes a universal entry vector generator (pUEG), which enables the assembly of DNA fragments into Level 0 modules in a single reaction, streamlining module generation in a manner similar to TU assembly. Second, the system expands the range of Level 0 modules, allowing the assembly of TUs with up to twelve modules, thereby accommodating more complex genetic constructs. Third, GreenGate 2.0 introduces GreenBraid, a new TU stacking method that enables efficient, scalable assemblies, with exponential progression rather than linear progression (Figure 7.19) [Piepers et al., 2023].

My primary contribution to GreenGate 2.0 was the development of GreenBraid. I constructed new Level 1 and Level 2 destination vectors that enable efficient, iterative stacking of TUs. This method proved to be highly effective, as demonstrated by a proof-of-principle. In addition, a set of pre-assembled plasma membrane and nuclear marker modules was constructed, which can be readily used in GreenBraid-based constructions to facilitate subcellular localization studies.

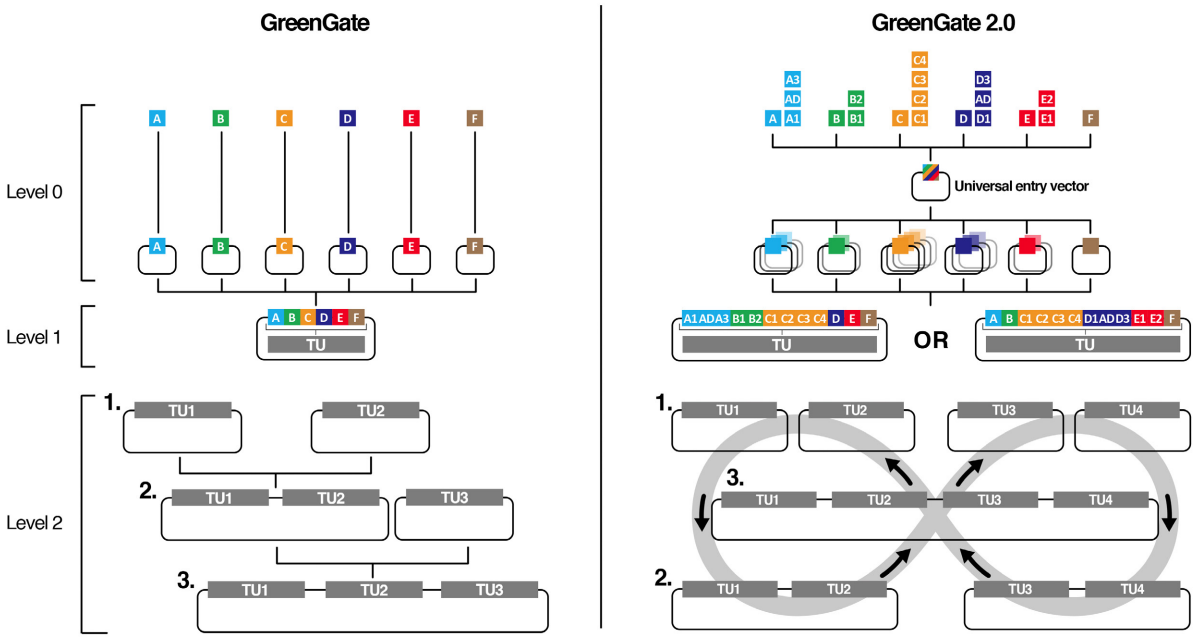

Figure 7.19: GreenGate mechanisms and innovations introduced in GreenGate 2.0. In GreenGate 2.0, Level 0 modules can be generated using a universal entry vector generator, streamlining the cloning workflow. At Level 1, TUs can be assembled from more than six entry modules, enhancing flexibility for the construction of complex genetic constructs. At Level 2, TU stacking is achieved through GreenBraid, a streamlined iterative mechanism with exponential scalability, enabling efficient assembly of multi-TU constructs. Figure taken from [Piepers et al., 2023].

7.2 Results

7.2.1 The GreenBraid vectors toolkit

(Disclaimer: parts of this section were rephrased from [Piepers et al., 2023]).

The original TU stacking strategy in GreenGate relied on the use of a single type IIS restriction enzyme, BsaI/Eco31I. This resulted in intermediate vectors that retained a BsaI site, which likely prevented efficient accumulation of the desired product during the cycling assembly reaction [Lampropoulos et al., 2013]. Second, the alternative stacking method, designed for more than two TUs, relied on an adapter module to add TUs sequentially, which was inefficient and time consuming [Lampropoulos et al., 2013].

To address both these inconveniences, I developed the GreenBraid system, which was inspired by the GoldenBraid strategy for transgene stacking [Sarrion-Perdigones et al., 2011]. GreenBraid introduces a new type IIS restriction enzyme, PaqCI (also known as AarI), which recognizes a 7 bp site rather than the typical 6 bp recognition sites of enzymes. This longer recognition sequence reduces the likelihood of internal PaqCI sites in existing GreenGate modules, thereby minimizing the need for domestication and largely maintaining backward compatibility with the GreenGate module library.

To facilitate a stacking process with exponential scalability, GreenBraid introduces a set of new destination vectors that also function as entry vectors in subsequent stacking reactions. The core GreenBraid vector set consists of four destination vectors: Z1, Z2, Y1, and Y2. The Z vectors serve as level 1 destination vectors, analogous to the original GreenGate destination vectors. They contain divergent BsaI/Eco31I sites to assemble Level 1 TUs using the standard GreenGate ”a” (ACCT) and ”g” (GTAT) overhangs, and can be readily transformed into plants. Additionally, they contain convergent PaqCI/AarI sites that target the ”a” or ”g” overhang and a new ”gb” (GTCA) overhang, which enables the subsequent stacking of two Z vectors (exclusively Z1 and Z2). That is, these Z vectors are used as entry vectors in a level 2 assembly, where one of the Y vectors (either Y1 or Y2) is used as a destination vector (Figure 7.20). Conversely, the Y vectors have divergent PaqCI/AarI sites and convergent BsaI/Eco31I sites to allow the efficient TU stacking. Furthermore, a combination of Y vectors (exclusively Y1 and Y2) can be used in a subsequent ”level 2+” stacking reaction, where a Z vector (either Z1 or Z2) is used as a destination vector, essentially returning to the starting vector. This allows indefinite stacking at Level 2+, where one must alternate between Y and Z vectors as entry and destination vectors in successive rounds (Figure 7.21). Furthermore, to allow control over the orientation of the TU, a reverse orientation version of each core vector was also constructed (Z1r, Z2r, Y1r, Y2r). And, joker/dummy vectors (Z1j, Z2j, Y1j, Y2j) were created containing a non-functional 162 bp module, allowing the assembly of constructs with an uneven number of TUs by filling empty positions in the assembly scheme.

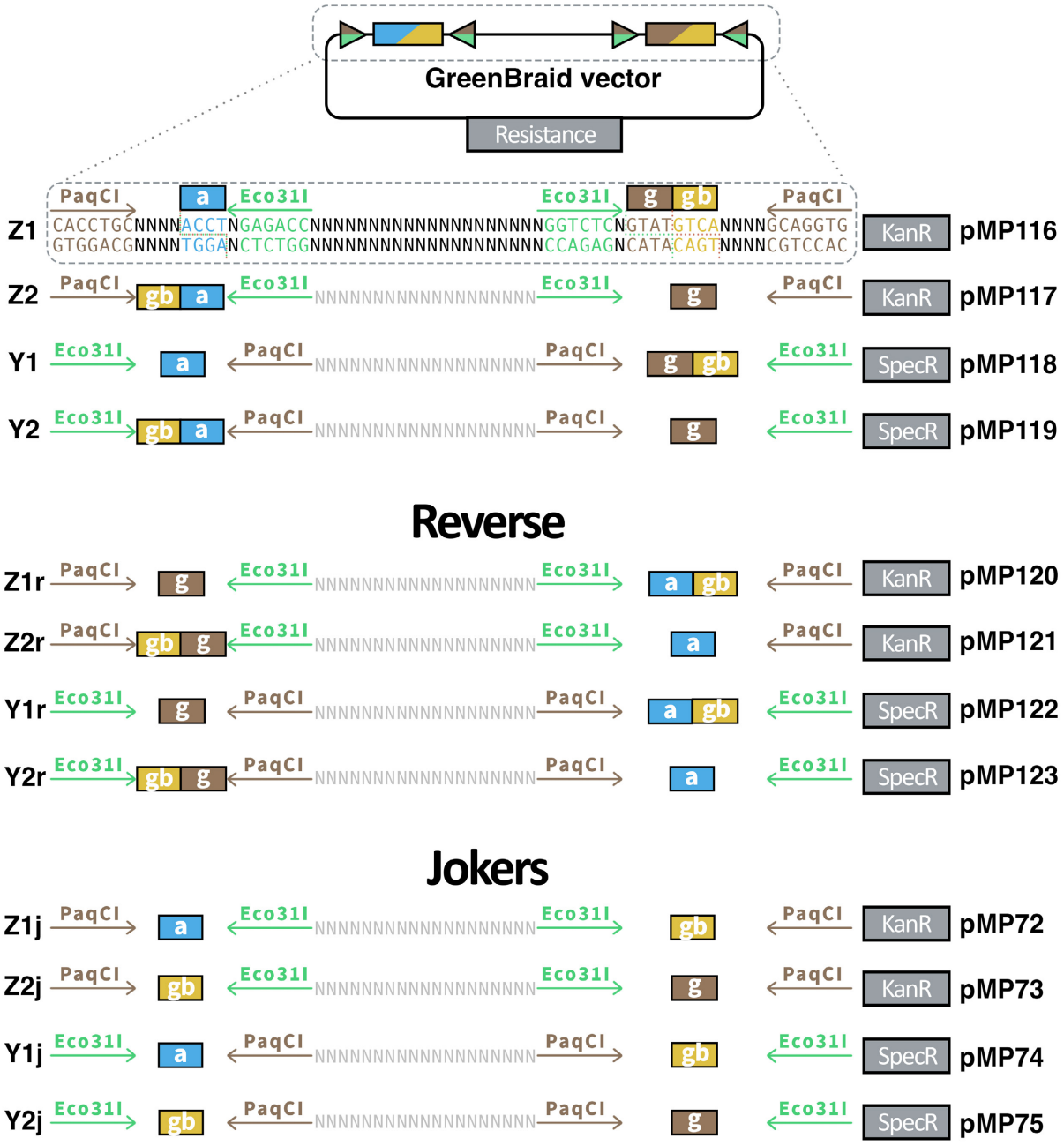

Figure 7.20: Overview of the GreenBraid vector system. The core set consists of four vectors: Z1, Z2, Y1, and Y2. Z vectors serve as destination vectors for 'level 1' reactions and as entry vectors for 'level 2' stacking. Y vectors function as destination vectors in 'level 2' stacking reactions. Reverse vectors enable control of the orientation of TU on the transformation construct. Joker vectors substitute for Z or Y vectors to accommodate the stacking of an uneven number of TUs. Figure taken from [Piepers et al., 2023].

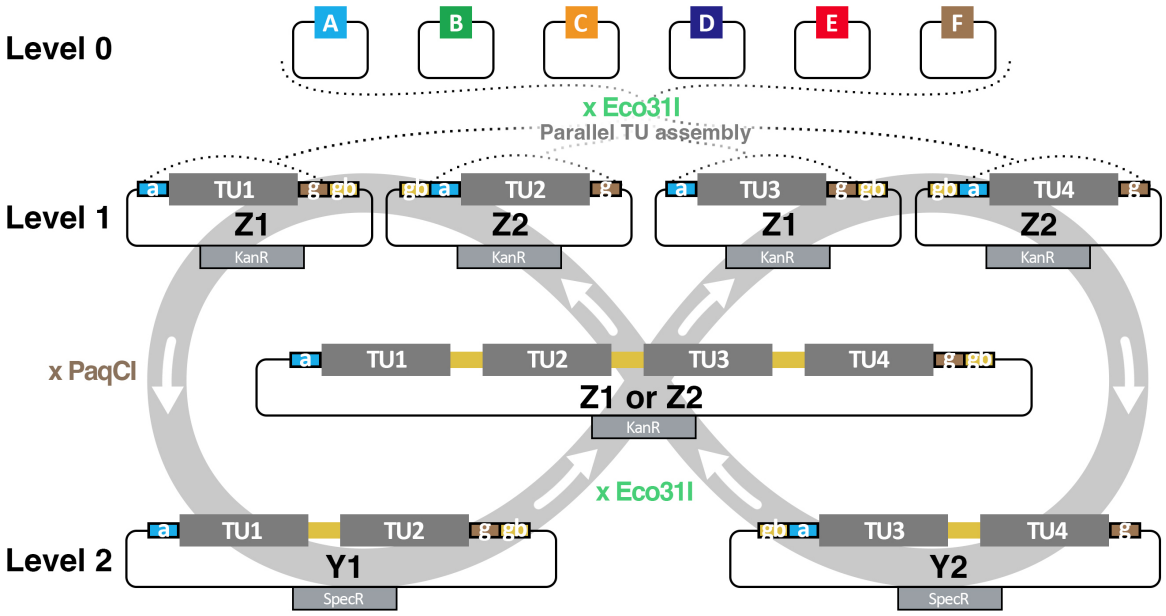

Figure 7.21: The GreenBraid Principle: GreenBraid builds on the GreenGate cloning system by enabling iterative TU stacking. In a 'level 1' reaction, TUs are assembled into Z1 or Z2 destination vectors. These Z vectors can be directly transformed into plants, or serve as entry modules in a subsequent 'level 2' stacking reaction, with Y1 or Y2 as the destination vector. These Y vectors can be transformed into plants, or be used to continue stacking, where the Y vectors serve as entry vectors and Z vectors as destinations, effectively cycling back to the initial step. This iterative design enables unlimited and modular stacking of TUs. Figure taken from [Piepers et al., 2023].

All GreenBraid vectors were built on the pCAMBIA backbone [Sarrion-Perdigones et al., 2011], which is compatible with plant transformation. Z vectors carry a kanamycin resistance marker for bacterial selection, while Y vectors carry spectinomycin resistance. To further aid bacterial screening, Z vectors contain a spisPink chromoprotein and Y vectors contain sfGFP in their cloning sites [Pollak et al., 2019] [Geldner et al., 2009]. Upon successful assembly, these chromoprotein genes are replaced by the desired insert, allowing for visual discrimination between positive (wildtype color) and negative (colored) colonies.

To enhance the convenience of GreenBraid, a comprehensive set of pre-assembled, ubiquitously expressed (pUBQ10) plasma membrane (PIP1;4) and nuclear markers (H2B) were pre-assembled in Z vectors (Figure 7.22) (Generated jointly with Kathrin Distel) . These vectors are immediately compatible with Level 2 GreenBraid assemblies. To allow easy integration in any cloning setup, the marker set offers flexibility with 22 fluorescent markers. Each marker was assembled in various versions, with one of three distinct fluorescent proteins (mTurquoise2, mVenus, or mScarlet), in both Z1 and Z2 vectors, and is available in with or without a FastRed plant selection marker [Shimada et al., 2010].

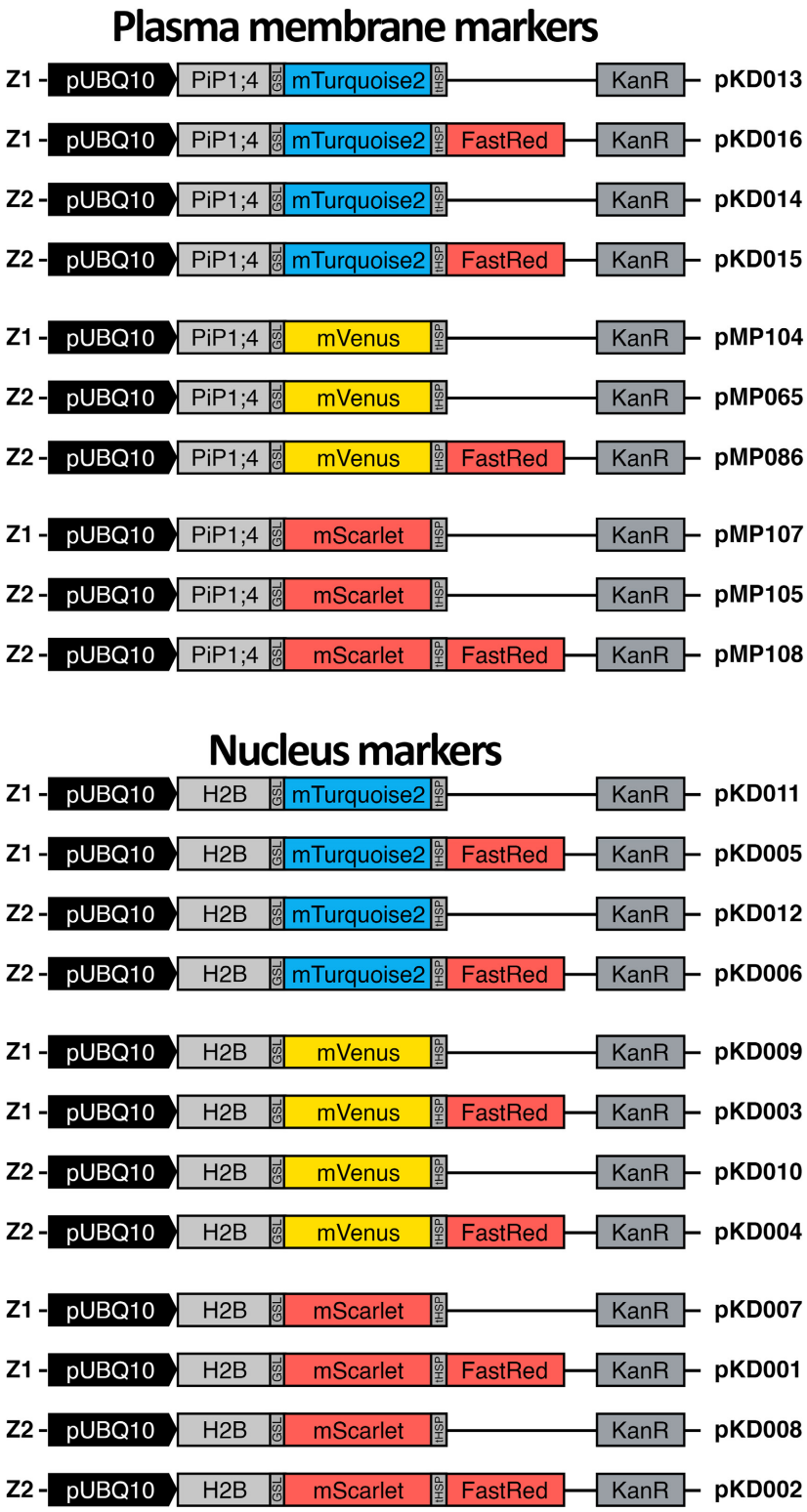

Figure 7.22: Overview of pre-assembled plasma membrane and nuclear markers. These constructs are designed for ease of use, and can be directly employed in stacking reactions. Figure taken from [Piepers et al., 2023].

7.2.2 GreenBraid proof-of-principle

(Disclaimer: parts of this section were rephrased from [Piepers et al., 2023]).

To validate the GreenBraid system, a proof-of-principle plant transformation vector, containing four TUs, was assembled and introduced into *Arabidopsis*. Each TU was first assembled in parallel using Level 1 GreenGate reactions in GreenBraid Z vectors (Figure 7.23a).

- (TU1) pRPS5A::H2B:mTurquoise2 (meristematic nuclear marker).
- (TU2) pUBQ10::PIP1;4:mVenus (constitutive plasma membrane marker).
- (TU3) pGATA23::Vha-a3:mScarlet (LRP-specific vacuolar marker).
- (TU4) pXPP::Vha-a3:mScarlet (XPP-specific vacuolar marker).

The vacuolar markers were created as translational fusions between the tonoplast-localized proton pump subunit Vha-a3 and mScarlet, driven by a LRP- (pGATA23) or XPP-specific promoter [Dettmer et al., 2006, De Rybel et al., 2010, Andersen et al., 2018]. In all four TUs, a 14–37 amino acid Glycine-Serine linker was inserted between the proteins and the fluorescent tag, and each used the terminator of heat shock protein 18.2 (tHSP18.2) [Nagaya et al., 2010]. Specifically in TU4, a FastRed plant selection marker was included [Shimada et al., 2010], while the other markers included a newly constructed dummy module.

The four Level 1 TUs were stacked two-by-two into Level 2 Y vectors, followed by a final stacking assembly where both Level 2 constructs were combined into a single Z destination vector (Figure 7.23a). An optimized assembly protocol using a high concentration T4 DNA ligase was used for this efficient GreenBraid stacking, with a success rate of 83%, producing a 26 kb plasmid, verified by sequencing.

The construct was successfully transformed into *Agrobacterium tumefaciens* (*Agrobacterium*) (strain GV3101 [Koncz and Schell, 1986]), where it remained intact in 100% of tested colonies (Figure 7.23b). Upon transformation into *Arabidopsis*, approximately 5% of primary transformants exhibited expression of all four reporters in the expected tissues (Figure 7.23c).

This expression pattern was stable across generations. However, during propagation, a subset of plants displayed developmental abnormalities, such as smaller leaves, narrow vascular stele, and reduced seed set (Figure 7.24). Notably, these phenotypes were only observed in lines with more than four TUs (including the selection marker) and were not detected in plants transformed with up to four TUs using GreenBraid. This indicates that the abnormalities are likely due to transgene load.

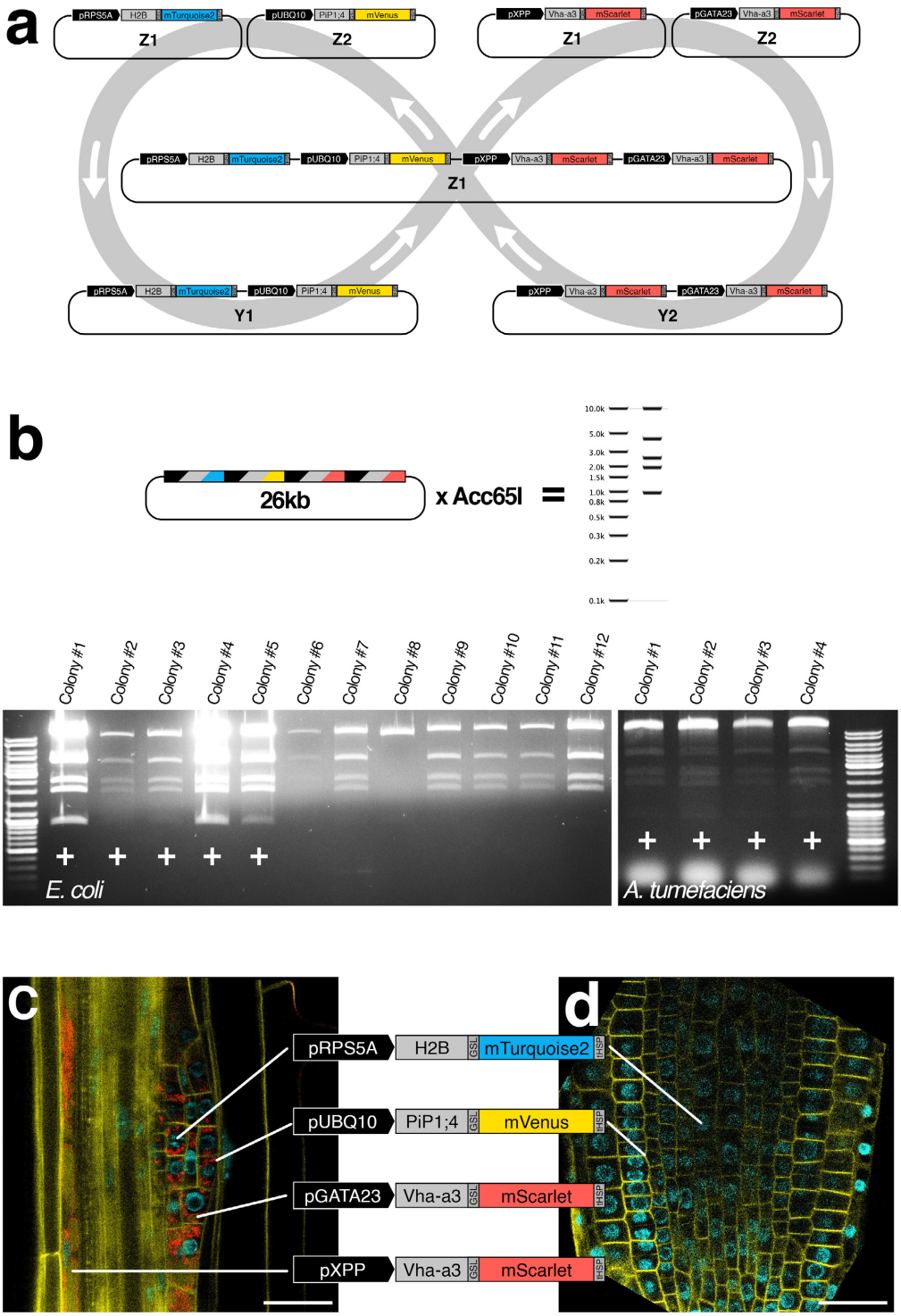

Figure 7.23: GreenBraid proof-of-principle. (a) Four fluorescent transcriptional markers were assembled in parallel into Z-level vectors and subsequently stacked into Y-level vectors. A final stacking reaction into a Z1 vector completed the construct. (b) The final Z1 assembly was highly efficient, with most colonies showing the expected digestion pattern (marked with "+"). (c–d) Functional expression of the complete GreenBraid construct in *Arabidopsis*. (c) All four markers—including constitutive, XPP-specific, and LRP-specific reporter, are expressed in a stage III LRP. (d) Constitutive markers are also expressed in the RAM. Figure taken from [Piepers et al., 2023].

7.3 Conclusion

To address the inconvenience of the original GreenGate TU stacking system, GreenBraid offers a streamlined and efficient alternative that remains largely backward compatible with the existing GreenGate module library. The system improves assembly efficiency, introduces convenient color-based bacterial selection, and enables recursive TU stacking with minimal changes to existing workflows.

Notably, GreenBraid destination vectors can be used as direct replacements for standard GreenGate Level 1 vectors. Aside from differences in bacterial resistance markers and the rare need for domestication of PaqCI/AarI sites, there are no practical disadvantages. A key advantage is that assembled Level 1 TUs can be stacked at any time, making GreenBraid Z vectors valuable substitutes for existing GreenGate destination vectors. This feature enhances modularity by supporting the growth of a library of preassembled Level 1 TU modules.

7.4 Supplemental figure

Figure 7.24: Developmental phenotype of T1 GreenBraid proof-of-principle plants. Two same-age transgenic T1 plants exhibit developmental abnormalities during propagation, including reduced leaf size, a thinner stele, and few or absent siliques. The plant on the left displays a more severe phenotype.

Materials and Methods

8.1 Plant protocols

8.1.1 Plant material

Plant material used in this thesis is from *Arabidipsis* with ecotype Columbia-0 (Col-0), unless mentioned otherwise. An overview of plant lines used can be found in table 8.1.

Table 8.1: Overview of plant lines used in this thesis. Marker, genotype (Gtype), ID, and references to articles are listed. (+) indicates transformation, (x) indicates a plant crossing

Marker		Genotype	ID	Reference
gSOK1::YFP		Col-0	sR562	Yoshida et al (2019)
gSOK2::YFP		Col-0	sR563	Yoshida et al (2019)
gSOK3::YFP		Col-0	sR564	Yoshida et al (2019)
gSOK4::YFP		Col-0	sR565	Yoshida et al (2019)
gSOK5::YFP		Col-0	sR566	Yoshida et al (2019)
p35S::GFP:BASL		Col-0	sR210	Dong et al (2009)
pRPS5A::BOR1:mCitrine		Col-0	sR671	Liao and Weijers (2017)
pRPS5A::NIP5;1:mCitrine		Col-0	sR689	Liao and Weijers (2017)
gSOK1::YFP x pUBQ10::LTi6B:mCherry(x2)		Col-0	sC149	Yoshida et al (2019); Elsayad et al (2016)
gSOK2::YFP x pUBQ10::LTi6B:mCherry(x2)		Col-0	sC152	Yoshida et al (2019); Elsayad et al (2016)
gSOK5::YFP x pUBQ10::LTi6B:mCherry(x2)		Col-0	sC162	Yoshida et al (2019); Elsayad et al (2016)
pRPS5A::SOK1::YFP pUBQ10::LTi6B:mCherry(x2)	x	Col-0	sC192	Yoshida et al (2019); Elsayad et al (2016)
pRPS5A::SOK2::YFP pUBQ10::LTi6B:mCherry(x2)	x	Col-0	sC193	Yoshida et al (2019); Elsayad et al (2016)
pRPS5A::SOK5::YFP pUBQ10::LTi6B:mCherry(x2)	x	Col-0	sC194	Yoshida et al (2019); Elsayad et al (2016)
pRPS5A::SOK4::mVenus pUBQ10::PiP1;4:mScarlet-I	+	Col-0	stMP46	
pXPP::SOK1:Gamillus pUBQ10::LTi6B:mCherry(x2)	+	Col-0	stMP14	Elsayad et al (2016)
gSOK1::YFP		aur1/2	stMP16	Yoshida et al (2019); van Damme et al (2011)
pRPS5A::SOK1:YFP		aur1/2	stMP17	Yoshida et al (2019); van Damme et al (2011)
pRPS5A::SOK2:YFP		aur1/2	stMP12	Yoshida et al (2019); van Damme et al (2011)
pRPS5A::SOK5:YFP		aur1/2	stMP29	Yoshida et al (2019); van Damme et al (2011)
pRPS5A::SOK1:mVenus pUBQ10:PiP1;4:mScarlet-I	+	plt3/5/7	stMP43	Hofhuis et al (2013)
pRPS5A::SOK2:mVenus pUBQ10:PiP1;4:mScarlet-I	+	plt3/5/7	stMP38/40	Hofhuis et al (2013)
pRPS5A::SOK5:mVenus pUBQ10:PiP1;4:mScarlet-I	+	plt3/5/7	stMP33/34	Hofhuis et al (2013)
gSOK1::YFP		scr-4	sR618	Yoshida et al (2019)
pRPS5A::SOK1:YFP		scr-3	stMP20	Yoshida et al (2019)
gLBD16:SRDX + gSOK1::YFP		Col-0	sC170	Goh et al (2012); Yoshida et al (2019)

Marker	Genotype	ID	Reference
gLBD16:SRDX + pRPS5A::SOK2:YFP x pUBQ10::LTI6B:mCherry(x2)	Col-0	sC217	Goh et al (2012); Yoshida et al (2019)
gLBD16:SRDX + pRPS5A::SOK5:YFP x pUBQ10::LTI6B:mCherry(x2)	Col-0	sC218	Goh et al (2012); Yoshida et al (2019)
pCASP1::LhG4:GR + p6xOP::PHS1deltaP:mCherry + pRPS5A::SOK5:YFP x pUBQ10::LTi6B:mCherry(x2)	Col-0	sC227	Stöckle et al (2022)
pUBQ10::LhG4:GR + p6xOP::AmiRNA-SOK5 + pUBI::GFP(x3):PIP1;4 + GATA23::H2B:mCherry(x3)	sok1/3/4	stJR111	Dr. Jazmín Reyes-Hernández; Andriy Volkov
pUBQ10::LhG4:GR + p6xOP::AmiRNA-SOK5	sok1/2/3/4	stJR133	Dr. Jazmín Reyes-Hernández; Andriy Volkov
pUBQ10::MBD:GFP	Col-0	stJR117	

8.1.2 Seed sterilization

Seeds were sterilized by incubation in 70% ethanol and 0.05% sodium dodecyl sulfate for 10min. They were then rinsed with 99% ethanol and air-dried in a sterile cabinet.

8.1.3 Plant growth conditions

Nutrient-rich ½ Murashige and Skoog (MS) solid medium plates were prepared in transparent square Petri dishes [Murashige and Skoog, 1962]. The medium contained 8 mg/ml phytoagar, 2.15 mg/ml MS salts, and 5 mg/ml 2-(N-Morpholino)-ethane sulphonic acid (MES), adjusted to pH 5.7 with potassium hydroxide (KOH). Occasionally, the medium was supplemented with 10 mg/ml sucrose to synchronize growth or for O/N live imaging in darkness.

Sterilized seeds were sown on the ½ MS plates and sealed with micropore tape. The plates were placed O/N in darkness at 4 °C for stratification. Subsequently, they were transferred to a growth chamber with long-day conditions (16 h light / 8 h dark) at 22 °C. In this thesis, the transfer to the growth chamber is defined as 0days after germination (DAG). After at least 4 DAG up to 8 DAG, seedlings were either used for experiments or transferred to soil. Soil-grown seedlings were maintained under long-day conditions at 22°C. Once siliques of mature plants turned yellow to brown, plants were loosely wrapped in breathable plastic bags and transferred to a drying room until fully desiccated, after which seeds were harvested.

For experiments involving boron transporters, borosilicate glassware was avoided during medium preparation, as it can leach boron and interfere with transporter activity.

8.1.4 Optogenetics - FloraLEDs conditions

Arabidopsis seeds and N. benthamiana plants were germinated/incubated in FloraLEDs chambers, which were light-isolated and maintained at room temperature (RT). To suppress basal reporter expression, white light (440-700nm, 10µE) supplemented with blue (440-500nm, 10µE) and far-red light (720-780nm, 10µE) was used (Figure 8.25). To activate reporter expression, red light (640-700nm, 10µE) was used.

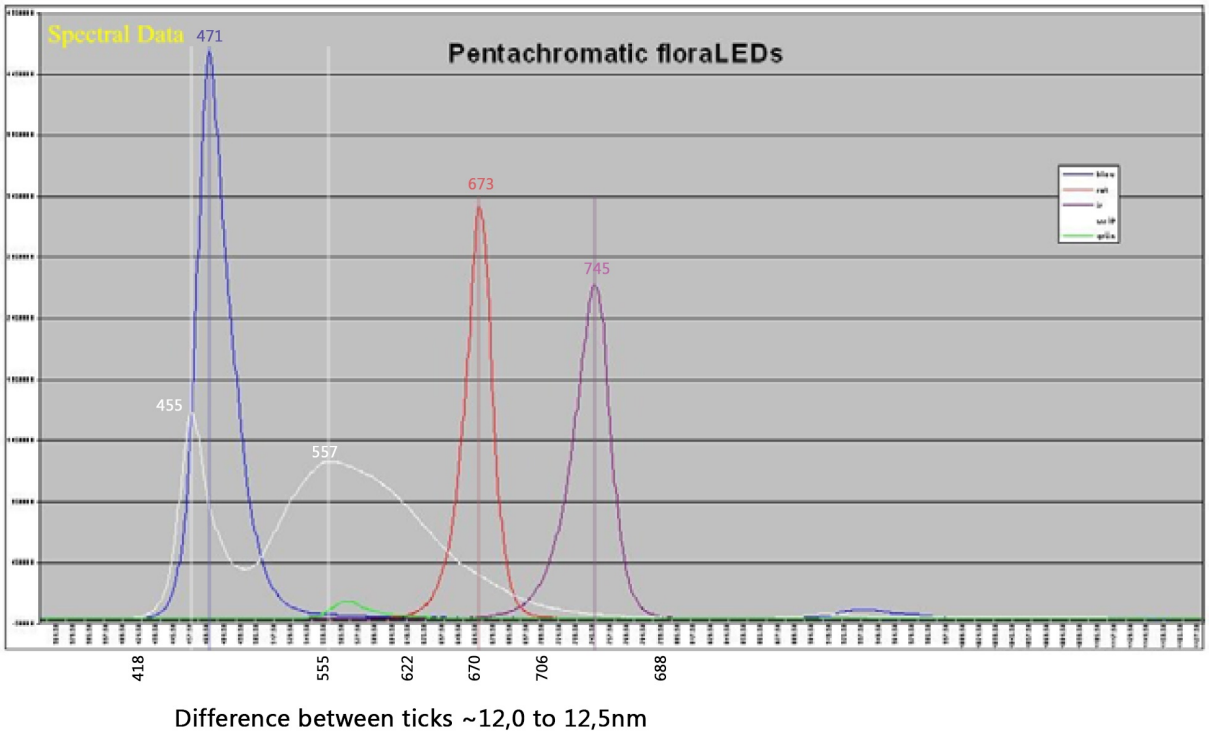

Figure 8.25: FloraLEDs spectrum received from a FloraLEDs representative. Figure is edited with wavelength and a discription about the x-axis ticks for clarify.

8.1.5 Plant crossing

A dissection microscope (Zeiss Stemi 2000-CS) was used to emasculate flower buds at developmental stages 10 to 12 as described by [Smyth, 1990]. For manual pollination, anthers from stage 13 flowers were used to transfer pollen directly onto the stigma of the emasculated bud.

8.1.6 Plant selection

Antibiotic resistance selection

Sterilized seeds were sown on ½MS medium supplemented with the appropriate antibiotic (Table 8.2) [Murashige and Skoog, 1962]. Plants were grown under similar conditions described in the plant growth conditions (Section 8.1.3). Between 5 and 10 DAG, transformant seedlings were identified based on hypocotyl color and plant size. For kanamycin resistance, a rapid selection protocol was employed as described by [Harrison et al., 2006].

Table 8.2: Working concentrations of antibiotics for plant selection.

Antibiotic	**Working concentration (µg/ml)**
Glufosinate ammonium / phosphinothricin ammonium (BASTA)	10
Hygromycin	25
Kanamycin	50
Sulfadiazine	7.5

Rapid and non-destructive screenable marker selection

Transgenic seeds carried an selection marker that allowed their identification using fluorescence-accumulating seed technology (FAST). This allowed non-destructive selection of transgenic seeds based on their fluorescence under a dissection microscope equipped with a fluorescence light source [Shimada et al., 2006].

8.1.7 Plant transformation

Stable Arabidopsis transformation

Stable transformation of *Arabidopsis* was performed using the floral dip method [Clough and Bent, 1998]. To promote flower formation prior to transformation, stalks approximately 15–20 cm in length were cut at the base of five to six week-old plants. Cut plants were supplemented with a fertilizer (Wuxal, 10 ml/L) and allowed to recover for one to two weeks until new stalks regrew.

An *Agrobacterium* (strain GV3101, [Koncz and Schell, 1986]) solution was prepared two days before transformation. Specifically, a 4 ml preculture was inoculated in LB medium supplemented with the appropriate antibiotics (Table 8.2) and incubated O/N at 28°C in a shaking incubator. The following day, 2 ml of the preculture was used to inoculate a 250 ml main culture in LB medium with the same antibiotics. After O/N incubation, cells were harvested by centrifugation at 4000 round per minute (RPM), and the pellet was resuspended in 100 ml of liquid ½MS medium supplemented with 5% sucrose.

Before floral dip, the surfactant Silwet L-77 (15 µl/100 ml) was added to the solution. Plants were dipped into the *Agrobacterium* suspension for 30 seconds to 2 min. Approximately 30 plants were treated per transformation. After dipping, plants were placed in trays and loosely covered with a plastic bag O/N to maintain humidity. The next day, the plastic bag was removed, and plants were grown under the conditions described in the plant growth conditions (Section 8.1.3).

Transient N. benthamiana transformation

Two separate Agrobacterium cultures were grown for 2 days at 28°C: one carrying the p19 gene (a suppressor of gene silencing) and the other containing the transgenic construct of interest. The two cultures were mixed so that the final optical density (OD600) of the p19 culture was 0.1 and the OD600 of the culture containing the construct was 0.3, in a total volume of 1mL. This mixed culture was centrifuged at 14680 RPM for 30s at room temperature, and the supernatant was discarded. The pellet was re-suspended in transformation solution composed of 10mM MES (pH 5.7), 10 mM $MgCl_2$, and 0.1mM acetosyringone (added last). This suspension was then infiltrated into *N. benthamiana* leaves using a 1 mL syringe without a needle. Prior to transformation, plants were watered the evening before.

8.1.8 Gravistimulation

Gravistimulation was applied by inverting plants (placing them upside down). This reorientation induces root bending and leads to the formation of an auxin maximum at the bend site, which serves as a morphogenetic trigger for LR initiation [Ditengou et al., 2008].

8.1.9 Inducible expression

For inducible expression experiments, the LhG4/p6xOP two-component system was used, where the synthetic transcription factor LhG4 was expressed in a tissue-specific manner, depending on the experiment. This system drives expression of a gene of interest from a synthetic promoter containing six

tandem repeats of the LhG4 binding site (p6xOP) [Moore et al., 2006, Stöckle et al., 2022].

For endodermis remodeling experiments, seedlings were transferred at 7DAG to ½MS plates containing 15µM dexamethasone (DEX), and immediately subjected to gravistimulation for roughly 24 hours, after which fluorescence was captured using confocal microscopy.

For the inducible KD of SOK in the RAM ablation experiments involving *sok* mutants, seedlings were transferred at 5 DAG to ½MS + 1% sucrose plates containing 20 µM DEX. They were treated for 1 day prior to ablation.

8.1.10 Drug treatments

At 6 DAG, seedlings were transferred to ½MS plates supplemented with the appropriate chemical (Table 8.3). For certain treatments, seedlings were gravistimulated two to three hours after transfer to ensure the compound was active at the root bend prior to LR initiation. Seedlings were subsequently grown under the conditions described in the plant growth conditions (Section 8.1.3). In some cases, to stain cell walls, seedlings were fixed, cleared, and then stained at as indicated in (Table 8.3).

Table 8.3: Working concentrations of chemicals used for seedling treatments and indication of cell wall staining.

Chemical	Working concentration (µM)	Gravistimulation duration (h)	Cell wall stain
Auxin	5000	–	No
Oryzalin	500	21–24	Yes
Taxol	17000	21–24	Yes

8.1.11 Plant fixation

At 5–7 DAG, seedlings were transferred to six-well plates (one to three seedlings per well). Fixation was performed by submerging the seedlings in a fixation solution containing 4% paraformaldehyde (PFA) in 1× phosphate-buffered saline (PBS). Samples were incubated in this solution for 2 hours at room temperature (RT) with gentle agitation (70 RPM), or alternatively O/N at 4°C without agitation. Subsequently, fixed seedlings were washed for 30 min with gentle agitation at 70 RPM [Ursache et al., 2018].

8.1.12 Plant clearing and staining

Fixed seedlings were simultaneously cleared and stained using the ClearSee method [Kurihara et al., 2015]. This was achieved by submerging the seedlings in a staining solution composed of ClearSee (100 mg/mL xylitol, 150 mg/mL sodium deoxycholate, 250 mg/mL urea) supplemented with 1 mg/mL calcofluor white for cell wall staining. The six-well plate was wrapped in aluminum foil, and seedlings were incubated for 30–60 min at 70 RPM with gentle agitation. Seedlings were either imaged directly by mounting in ClearSee on microscope slides or stored for later imaging. During storage, samples were kept under gentle agitation at 70 RPM, and the ClearSee solution was refreshed every two to three days [Kurihara et al., 2015].

8.2 Molecular cloning

GreenGate molecular cloning was used to generate transformation vectors [Lampropoulos et al., 2013]. An overview of oligos used and plasmids made can be found in (Tables 8.7, 8.8).

8.2.1 Entry vector construction

GreenGate module sequences were amplified from template DNA (either genomic or plasmid) using primers containing GreenGate-specific overhangs. In cases where domestication was required, modules were amplified in multiple fragments using additional primers that introduced silent mutations at the recognition sites. PCR products were either column- or gel-purified prior to further use, and subsequently inserted into entry vectors using a conventional restriction-ligation reaction. Following the release of GreenGate 2.0, the universal entry vector generation (UEG) method was used instead [Piepers et al., 2023].

8.2.2 Transcriptional unit construction

Entry vectors were used to assemble transcriptional units using the GreenGate reaction, resulting in plant transformation vectors (Table 8.4, Table 8.5). For transcriptional unit stacking, single-transcriptional-unit vectors were further combined through a GreenBraid assembly [Piepers et al., 2023]. The resulting plant transformation vectors were subsequently transformed into *Agrobacterium* (strain GV3101) for use in plant transformation.

Table 8.4: GreenGate reaction components and volumes for each type of assembly. Components were added in the order listed from top to bottom.

Level 0 Entry module	**Level 1 TU assembly**	**Level 2 GreenBraid**	**Volume (µl)**
Purified PCR product	Entry vector A (pGGA)	TU1 entry vector (pGB)	1.5
	Entry vector B (pGGB)		1.5
	Entry vector C (pGGC)		1.5
	Entry vector D (pGGD)	TU2 entry vector (pGB)	1.5
	Entry vector E (pGGE)		1.5
	Entry vector F (pGGF)		1.5
pUEG	Destination vector Z (pGBZx)	Destination vector (pGB)	1.0
10x T4 ligase buffer with ATP (B0202S)	10x Fast Digest buffer	10x T4 ligase buffer with ATP (B0202S)	2.0
	ATP 10mM		2.0
PaqCI Activator (5pmol)		PaqCI Activator (5pmol)	1.0
H_2O	H_2O	H_2O	Up to 20.0
400 Units T4 Ligase (M0202S)	30 Units T4 Ligase (EL0013)	400 Units T4 Ligase (M0202S)	0.5
PaqCI (R0745L)	Eco31I (FD0293)	PaqCI (R0745L)	0.5
Total			**20.0**

Table 8.5: GreenGate reaction thermal cycling protocol.

Temperature (°C)	**Time O/N (min:sec)**	**Time 2h (min:sec)**	**Cycles (x)**	**Purpose**
37	5:00	1:00	50–60	Digestion
16	5:00	1:00		Ligation
70	5:00	5:00		Heat-inactivat ion enzymes

8.2.3 GreenBraid vector construction

For construction of the new GreenBraid vectors, the cloning site of the pCAMBIA-based GoldenBraid vectors [Sarrion-Perdigones et al., 2013b] was replaced with a GreenBraid cloning site using restriction-ligation. The GreenBraid cloning sites were ordered as two complementary oligos that were annealed by slowly decreasing the temperature from 90°C to RT over a period of 20 min. Additionally, the annealed oligos were phosphorylated (NEB M0201S). These annealed and phosphorylated oligos were ligated in EcoRI-opened pDGB3α1 for pGBZs and BamHI-opened pDGB3Ω1 for pGBYs. Resulting ligations were transformed into *Escherichia coli* (*E.coli*), and desired clones were identified through vector extraction, digestion and sequencing. The chromogenic bacterial selection markers were added to each GreenBraid vector (spisPink for Z1, Z2, Z1r, and Z2r; sfGFP for Y1, Y2, Y1r, and Y2r). The chromogenic marker genes (sfGFP & spisPink) [Andreou and Nakayama, 2018] were amplified by PCR and inserted in the GreenBraid vectors by restriction-ligation between PstI and BamHI sites. The GreenBraid Z and Y jokers (Z1j, Z2j, Y1j, and Y2j) were obtained by NcoI and XhoI restriction-ligation of 200–208 bp joker sequences that were PCR amplified from GoldenBraid dummy vectors (pDGB1α1_SF for Z1j, pDGB1α2_SF for Z2j, pDGB1Ω1_SF for Y1j, and pDGB1Ω2_SF for Y2j).

The set of pre-assembled Level 1 GreenBraid vectors containing plasma membrane markers or nucleus markers were constructed using a level 1 GreenGate reaction protocol [Lampropoulos et al., 2013]. The resulting vectors were then verified by sequencing.

8.2.4 Digestion

DNA digestion was performed using FastDigest enzymes (ThermoFisher) of which reactions were incubated for approximately 1 hour at 37°C. The digested DNA was separated by electrophoresis on a 1% agarose gel at 100V for 30min. Resulting fragment patterns were compared to *in silico* digestion patterns generated in Geneious.

8.2.5 Ligation

For restriction–ligation reactions, pre-digested insert and vector DNA were combined at a 5:1 molar ratio. The subsequent ligation was carried out using a T4 DNA ligase (NEB, EL0011) and incubation O/N at 4°C.

8.2.6 Bacterial transformation

E.coli transformation

Chemically-competent *E. coli* (strain DH5α1) was used for transformations via heat shock. Approximately 1 µg of plasmid DNA was gently mixed with 30 µl of competent cells and incubated on ice for 30 min. Heat shock was performed at 42°C for 30 seconds, after which the cells were returned to ice for 2 min. Subsequently, 500 µl of LB medium was added, and the mixture was incubated for 1 hour at 37°C in a shaking incubator at 200 RPM. The transformed cells were then plated on solid LB agar supplemented with the appropriate antibiotic for transformant selection (Table 8.6).

Agrobacterium transformation

Chemically-competent *Agrobacterium* (strain GV3101) was used for transformation. Deep-frozen bacterial cells, stored at –80°C, were thawed on ice and mixed with approximately 1 µg of plasmid DNA. The mixture was incubated on ice for 10 min, flash-frozen in liquid nitrogen for 5 min, and then subjected to heat shock by incubation at 37°C for 5 min. Following heat shock, 800 µl of LB medium was added, and

the cells were incubated at 28°C for 3–4 hours in a shaking incubator at 200 RPM. Transformed cells were plated on LB agar containing rifampicin (for chromosomal resistance), gentamicin (for Ti plasmid maintenance), and the appropriate antibiotic for vector selection (Table 8.6).

Table 8.6: Working concentrations of bacterial antibiotics, and respective solvent.

Antibiotic	**Working concentration (µg/ml)**	**Solvent**
Ampicillin	100	Water
Kanamycin	50	Water
Spectinomycin	100	Water
Rifampicin	50	Methanol
Gentamycin	10	Water
Tetracyclin	5	Ethanol

8.2.7 Bacterial culture growth

Bacterial cultures were initiated by inoculating 4 ml of liquid LB medium supplemented with the appropriate antibiotics. Cultures were grown in a shaking incubator at 200 RPM. *E.coli* was cultured at 37°C for 14–20 hours, while *Agrobacterium* was cultured at 28°C for 2 days.

8.2.8 Plasmid extraction

Plasmid DNA was extracted from 2 ml bacterial cultures, which was transferred to a 2 ml microcentrifuge tube and centrifuged at 8500 RPM to pellet the cells. Another 2 ml of the same culture was stored at 4°C to make a glycerol stock later, post verification of the plasmid DNA.

The bacterial pellet was resuspended in 200 µl Tris-EDTA buffer (50mM Tris, 10mM Na_2EDTA, 1mg/L RNase, pH8.0). Then, 200 µl of lysis buffer (200mM NaOH, 35mM SDS) was added, and the suspension was incubated at RT for 2 min. Following this, 200 µl of neutralization buffer (3M potassium acetate, pH5.5) was added, and the suspension was centrifuged for 10 min at 13000 RPM. 500 µl of the supernatant was transferred to a fresh 1.5 ml microcentrifuge tube. 500 µl isopropanol was added, and the mixture was gently inverted to mix. This mixture was centrifuged for 10 min at 14680 RPM, after which the supernatant was discarded. The DNA pellet was washed with 500 µl of 70% ethanol, followed by centrifugation for 2 min at 14680 RPM. The supernatant was discarded, and the pellet was air-dried at 65°C for 15 min. The dried pellet was then resuspended in 65 µl MilliQ H_2O.

8.2.9 Sequencing

To verify the accuracy of the constructed vectors, Sanger sequencing was performed using the Mix2Seq service provided by Eurofins Genomics.

8.2.10 Oligos

Table 8.7: Overview of oligos used in this thesis.

Purpose	ID	Sequence
SOK1 amiRNA1 I	P-2219	GATTCGTCCAATAAATCTTGCCGTCTCTCTTTTGTATTCC
SOK1 amiRNA1 II	P-2220	GACGGCAAGATTTATTGGACGAATCAAAGAGAATCAATGA
SOK1 amiRNA1 III	P-2221	GACGACAAGATTTATAGGACGATTCACAGGTCGTGATATG
SOK1 amiRNA1 IV	P-2222	GAATCGTCCTATAAATCTTGTCGTCTACATATATATTCCT
SOK1 amiRNA2 I	P-2223	GATAGGATGGTCAACGCGACCCGTCTCTCTTTTGTATTCC
SOK1 amiRNA2 II	P-2224	GACGGGTCGCGTTGACCATCCTATCAAAGAGAATCAATGA
SOK1 amiRNA2 III	P-2225	GACGAGTCGCGTTGAGCATCCTTTCACAGGTCGTGATATG
SOK1 amiRNA2 IV	P-2226	GAAAGGATGCTCAACGCGACTCGTCTACATATATATTCCT
SOK2 amiRNA1 I	P-2227	GATTATTGTGATGTCATGCGCTTTCTCTCTTTTGTATTCC
SOK2 amiRNA1 II	P-2228	GAAAGCGCATGACATCACAATAATCAAAGAGAATCAATGA
SOK2 amiRNA1 III	P-2229	GAAAACGCATGACATGACAATATTCACAGGTCGTGATATG
SOK2 amiRNA1 IV	P-2230	GAATATTGTCATGTCATGCGTTTTCTACATATATATTCCT
SOK2 amiRNA2 I	P-2231	GATTGCTAAGTCATTCGACACAATCTCTCTTTTGTATTCC
SOK2 amiRNA2 II	P-2232	GATTGTGTCGAATGACTTAGCAATCAAAGAGAATCAATGA
SOK2 amiRNA2 III	P-2233	GATTATGTCGAATGAGTTAGCATTCACAGGTCGTGATATG
SOK2 amiRNA2 IV	P-2234	GAATGCTAACTCATTCGACATAATCTACATATATATTCCT
SOK3 amiRNA1 I	P-2235	GATAATTGGGCTAAAGTGATCTCTCTCTCTTTTGTATTCC
SOK3 amiRNA1 II	P-2236	GAGAGATCACTTTAGCCCAATTATCAAAGAGAATCAATGA
SOK3 amiRNA1 III	P-2237	GAGAAATCACTTTAGGCCAATTTTCACAGGTCGTGATATG
SOK3 amiRNA1 IV	P-2238	GAAAATTGGCCTAAAGTGATTTCTCTACATATATATTCCT
SOK3 amiRNA2 I	P-2239	GATTACACTTTGTACTCAGCCACTCTCTCTTTTGTATTCC
SOK3 amiRNA2 II	P-2240	GAGTGGCTGAGTACAAAGTGTAATCAAAGAGAATCAATGA
SOK3 amiRNA2 III	P-2241	GAGTAGCTGAGTACATAGTGTATTCACAGGTCGTGATATG
SOK3 amiRNA2 IV	P-2242	GAATACACTATGTACTCAGCTACTCTACATATATATTCCT
SOK4 amiRNA1 I	P-2243	GATAATCGTACCAGACGAAACTGTCTCTCTTTTGTATTCC
SOK4 amiRNA1 II	P-2244	GACAGTTTCGTCTGGTACGATTATCAAAGAGAATCAATGA
SOK4 amiRNA1 III	P-2245	GACAATTTCGTCTGGAACGATTTTCACAGGTCGTGATATG
SOK4 amiRNA1 IV	P-2246	GAAAATCGTTCCAGACGAAATTGTCTACATATATATTCCT
SOK4 amiRNA2 I	P-2247	GATAATGAAGTGTGGGTGGTCGATCTCTCTTTTGTATTCC
SOK4 amiRNA2 II	P-2248	GATCGACCACCCACACTTCATTATCAAAGAGAATCAATGA
SOK4 amiRNA2 III	P-2249	GATCAACCACCCACAGTTCATTTTCACAGGTCGTGATATG
SOK4 amiRNA2 IV	P-2250	GAAAATGAACTGTGGGTGGTTGATCTACATATATATTCCT
SOK5 amiRNA1 I	P-2251	GATAGTAGAGACTTGCGATGCCTTCTCTCTTTTGTATTCC
SOK5 amiRNA1 II	P-2252	GAAGGCATCGCAAGTCTCTACTATCAAAGAGAATCAATGA
SOK5 amiRNA1 III	P-2253	GAAGACATCGCAAGTGTCTACTTTCACAGGTCGTGATATG
SOK5 amiRNA1 IV	P-2254	GAAAGTAGACACTTGCGATGTCTTCTACATATATATTCCT
SOK5 amiRNA2 I	P-2255	GATGACTTTCCGGTTAACGACCGTCTCTCTTTTGTATTCC
SOK5 amiRNA2 II	P-2256	GACGGTCGTTAACCGGAAAGTCATCAAAGAGAATCAATGA

Purpose	ID	Sequence
SOK5 amiRNA2 III	P-2257	GACGATCGTTAACCGCAAAGTCTTCACAGGTCGTGATATG
SOK5 amiRNA2 IV	P-2258	GAAGACTTTGCGGTTAACGATCGTCTACATATATATTCCT
pGBZ1 cloning site	P-2409	AATTACCATGGCACCTGCTGCAACCTAGAGACCCTGCAGATCGTACGGGATCCGGT CTCTGTATGTCATATGGCAGGTGCTCGAGCTGACAGGATATATTGGCGGGTAAACC TAAG
pGBZ1 cloning site	P-2410	CATGCTTAGGTTTACCCGCCAATATATCCTGTCAGCTCGAGCACCTGCCATATGACA TACAGAGACCGGATCCCGTACGATCTGCAGGGTCTCTAGGTTGCAGCAGGTGCCA TGGT
pGBZ2 cloning site	P-2411	AATTACCATGGCACCTGCTACAGTCAACCTAGAGACCCTGCAGATCGTACGGGATC CGGTCTCTGTATATCGGCAGGTGCTCGAGCTGACAGGATATATTGGCGGGTAAACC TAAG
pGBZ2 cloning site	P-2412	CATGCTTAGGTTTACCCGCCAATATATCCTGTCAGCTCGAGCACCTGCCGATATACA GAGACCGGATCCCGTACGATCTGCAGGGTCTCTAGGTTGACTGTAGCAGGTGCCAT GGT
pGBZ1r cloning site	P-2313	AATTACCATGGCACCTGCTACAACCTATACAGAGACCCTGCAGATCGTACGGGATC CGGTCTCTAGGTGTCAATCGGCAGGTGCTCGAGC
pGBZ1r cloning site	P-2314	AATTGCTCGAGCACCTGCCGATTGACACCTAGAGACCGGATCCCGTACGATCTGCA GGGTCTCTGTATAGGTTGTAGCAGGTGCCATGGT
pGBZ2r cloning site	P-2315	AATTACCATGGCACCTGCTACAGTCAATACAGAGACCCTGCAGATCGTACGGGATC CGGTCTCTAGGTGTATATCGGCAGGTGCTCGAGC
pGBZ2r cloning site	P-2316	AATTGCTCGAGCACCTGCCGATATACACCTAGAGACCGGATCCCGTACGATCTGCA GGGTCTCTGTATTGACTGTAGCAGGTGCCATGGT
pGBY1 cloning site	P-2317	GATCACCATGGGGTCTCAACCTATCGGCAGGTGCTGCAGATCGTACGGGATCCCA CCTGCTACAGTATGTCATGAGACCCTCGAGA
pGBY1 cloning site	P-2318	GATCTCTCGAGGGTCTCATGACATACTGTAGCAGGTGGGATCCCGTACGATCTGC AGCACCTGCCGATAGGTTGAGACCCCATGGT
pGBY2 cloning site	P-2319	GATCACCATGGGGTCTCAGTCAACCTATCGGCAGGTGCTGCAGATCGTACGGGAT CCCACCTGCTACAGTATTGAGACCCTCGAGA
pGBY2 cloning site	P-2320	GATCTCTCGAGGGTCTCAATACTGTAGCAGGTGGGATCCCGTACGATCTGCAGCA CCTGCCGATAGGTTGACTGAGACCCCATGGT
pGBY1r cloning site	P-2321	GATCACCATGGGGTCTCAACCTATACATCGGCAGGTGCTGCAGATCGTACGGGAT CCCACCTGCTGCAAGGTGTCATGAGACCCTCGAGA
pGBY1r cloning site	P-2322	GATCTCTCGAGGGTCTCATGACACCTTGCAGCAGGTGGGATCCCGTACGATCTGCA GCACCTGCCGATGTATAGGTTGAGACCCCATGGT
pGBY2r cloning site	P-2323	GATCACCATGGGGTCTCAGTCAATACATCGGCAGGTGCTGCAGATCGTACGGGATC CCACCTGCTGCAAGGTGTATTGAGACCCTCGAGA
pGBY2r cloning site	P-2324	GATCTCTCGAGGGTCTCAATACACCTTGCAGCAGGTGGGATCCCGTACGATCTGCA GCACCTGCCGATGTATTGACTGAGACCCCATGGT
pGBZ1 joker cloning site	P-2326	CGCGCGCCATGGCACCTGCTACAACCTTCTCAATGGTAACTTTACTC
pGBZ1 joker cloning site	P-2327	CGCGCGCTCGAGCACCTGCTACATGACAGCGAAATGATTGATGAAGAAC
pGBZ2 joker cloning site	P-2328	CGCGCGCCATGGCACCTGCTACAGTCAGGAGTCTCAATGGTAACTTTAC
pGBZ2 joker cloning site	P-2329	CGCGCGCTCGAGCACCTGCTACAATACAAATGATTGATGAAGAACAATG
pGBY1 joker cloning site	P-2330	CGCGCGCCATGGGGTCTCAACCTCTCAATGGTAACTTTACTCTTTATTTAAC
pGBY1 joker cloning site	P-2331	CGCGCGCTCGAGGGTCTCATGACAGCGAAATGATTGATGAAGAACAATG
pGBY2 joker cloning site	P-2332	CGCGCGCCATGGGGTCTCAGTCAGGAGTCTCAATGGTAACTTTACTC
pGBY2 joker cloning site	P-2333	CGCGCGCTCGAGGGTCTCAATACAAATGATTGATGAAGAACAATG
GreenGate module F dummy amplification	P-2334	ACTAAGTGACACATGACCATAGGAGAAC
GreenGate module F dummy amplification	P-2335	ATACGTTCTCCTATGGTCATGTGTCACT
pOPTO optogenetics promoter	P-2336	TGAACTGGTCTCTACCTTCGGAGCTTCGAAGTTTAAAC
pOPTO optogenetics promoter	P-2337	TAGACCGGTCTCATGTTGTCATTAGGCTGGATCGGTCCCGGTG

Purpose	ID	Sequence
Optogenetics repressor	P-2417	TGAACTGGTCTCAAACAATGCTTGATCTTGAACTTAGACTTGGTT
Optogenetics repressor	P-2416	TAGACCGGTCTCTGCAGTTAGATTCCGGCTTCGACGGCAATG
Optogenetics activator component 1 part 1	P-2340	TGAACTGGTCTCAAACAATGCCCCGCCCCAAGCTCAAG
Optogenetics activator component 1 part 1	P-2341	TGCGGCCCTGCGCCTATCGGTATCGCATTCAGGTAATGCCGCACTTGCTCGACGC
Optogenetics activator component 1 part 2	P-2342	TAGGCGCAGGGCCGCAAGGGCTCTGGGAATTTTTGCAAGTGCTCGTTCG
Optogenetics activator component 1 part 2	P-2415	TAGACCGGTCTCTGCAGCTACACCTTCCTCTTCTTCTTTGGGTC
Optogenetics activator component 2	P-2344	TGAACTGGTCTCTAACAATGGTTTCCGGAGTCGGGGGTAG
Optogenetics activator component 2	P-2414	AACAGGTCTCTGCAGCTACTTCCTCTTCTTCTTTGGCCCACC
iaaM amplification	P-2536	ACAGTCGACACTTACTTGGTCTAC
iaaM amplification	P-2537	TCCCAATCATGAGGAAAACTCCAT
iaaM site directed mutagenesis	P-2552	GGGTGCTATTCAGACCGCGTGTAACGCCGTCTGTGC
iaaM site directed mutagenesis	P-2553	GCACAGACGGCGTTACACGCGGTCTGAATAGCACCC
iaaM site directed mutagenesis	P-2555	GCACAGACGGCGTTACACG
iaaM site directed mutagenesis	P-2556	GCTATTCAGACCGCGTGTAA
pSOK1 entry module	P-2883	GCTTGGTCTCAACCTTGAGTCGTTCCGTGGTGAATC
pSOK1 entry module	P-2884	ATTCGGTCTCATGTTCTCTCTTTCTTTTTGTTTTGGTCTTCG
SOK1 CDS entry module	P-2885	GCTTGGTCTCAGGCTCCATGGAAAGTAATGGTGGAGG
SOK1 CDS entry module	P-2886	ATTCGGTCTCACTGACTCTTTGAGAGTAGTCGTC
SOK2 CDS entry module	P-2887	GCTTGGTCTCAGGCTCCATGGAAGCTGTAAGATGCAG
SOK2 CDS entry module	P-2888	ATTCGGTCTCACTGATTTCTTGATTTGCTTCGATG
Gamillus entry module	P-2896	GCTTGGTCTCATCAGGTGCCGTTAACGCTGGTTCGATG
Gamillus entry module	P-2897	ATTCGGTCTCAGCAGTTACTTGTACAGCTCGTCCATGC
SOK4 CDS block 1	P-3199	ATAACACCTGCAACACTCAGGCTCCATGGCGTTGGTGAGTTCAAG
SOK4 CDS block 1	P-3230	GTCCCACCTGCTGTTACATCTTTGAGATAGAGATCGTTGTGAG
SOK4 CDS block 2	P-3231	CAGGCACCTGCAACAATGTAATCAATAGATTAAATGATCTACG
SOK4 CDS block 2	P-3232	GTCCCACCTGCTGTTAGTTCGTTTTGAGGACCAAGAG
SOK4 CDS block 3	P-3233	CAAGCACCTGCAACAAACTTACAAGAACGGTTTC
SOK4 CDS block 3	P-3234	GTCCCACCTGCTGTTACTCCTATCAATATTGTAAGAAGATGAC
SOK4 CDS block 4	P-3235	CAGGCACCTGCAACAGAGTTCAAGGATGGGGTTG
SOK4 CDS block 4	P-3321	GTCCCACCTGCTGTTACATCTTTGAGATAGAGGCCGTTGTGAG
SOK4 CDS mutagenesis block 1	P-3324	GGCACCTGCCTCAACCTCCATAATCGTGAG
SOK4 CDS mutagenesis block 1	P-3325	GGCACCTGCTAGAGACCGTTGTGAGAAGAGAG
SOK4 CDS mutagenesis block 2	P-3326	GGCACCTGCCAACGGTCTCTATCTCAAAGATG
SOK4 CDS mutagenesis block 2	P-3327	GGCACCTGCTGACATACGTTCTCCTATGGTC

8.2.11 Plasmids

Table 8.8: Overview of plasmids constructed in this thesis.

Name	GG Type	Content
pMP001	I	amiRNA1 targeting SOK1
pMP002	Z003	amiRNA1 targeting SOK1
pMP003	N	amiRNA1 targeting SOK1
pMP004	Z	UBIQ10-LGh4::AmiRNA1-SOK1-pGGZ03
pMP005	Z	GATA23-LGh4::AmiRNA1-SOK1-pGGZ03
pMP006	I	amiRNA2 targeting SOK1
pMP007	Z	amiRNA2 targeting SOK1
pMP008	N	amiRNA2 targeting SOK1
pMP009	Z	UBIQ10-LGh4::AmiRNA2-SOK1-pGGZ03
pMP010	Z	GATA23-LGh4::AmiRNA2-SOK1-pGGZ03
pMP011	I	amiRNA1 targeting SOK2
pMP012	Z	AmiRNA1-SOK2-pGGZ03
pMP013	N	amiRNA1 targeting SOK2
pMP014	Z	UBIQ10-LGh4::AmiRNA1-SOK2-pGGZ003
pMP015	Z	GATA23-LGh4::AmiRNA1-SOK2-pGGZ003
”	I	amiRNA2 targeting SOK2
”	Z	amiRNA2 targeting SOK2
pMP018	N	AmiRNA2-SOK2-pGGN
pMP019	Z	UBIQ10-LGh4::AmiRNA2-SOK2-pGGZ003
pMP020	Z	GATA23-LGh4::AmiRNA2-SOK2-pGGZ003
pMP021	I	amiRNA1 targeting SOK3
pMP022	Z003	amiRNA1 targeting SOK3
pMP023	N	AmiRNA1-SOK3-pGGN
pMP024	Z	UBIQ10-LGh4::AmiRNA2-SOK3-pGGZ03
pMP025	Z	GATA23-LGh4::AmiRNA1-SOK3-pGGZ003
pMP026	I	amiRNA2 targeting SOK3
pMP027	Z003	amiRNA2 targeting SOK3
pMP028	N	AmiRNA2-SOK3-pGGN
pMP029	Z	UBIQ10-LGh4::AmiRNA2-SOK3-pGGZ003
pMP030	Z	GATA23-LGh4::AmiRNA2-SOK3-pGGZ003
pMP031	I	amiRNA1 targeting SOK4
pMP032	Z003	amiRNA1 targeting SOK4
pMP033	N	amiRNA1 targeting SOK4
pMP034	Z	UBIQ10-LGh4::AmiRNA1-SOK4-pGGZ003
pMP035	Z	GATA23-LGh4::AmiRNA1-SOK4-pGGZ003
pMP036	I	amiRNA2 targeting SOK4
pMP037	Z003	amiRNA2 targeting SOK4
pMP038	N	AmiRNA2-SOK4-pGGN

Name	GG Type	Content
pMP039	Z	UBIQ10-LGh4::AmiRNA2-SOK4-pGGZ003
pMP040	Z	GATA23-LGh4::AmiRNA2-SOK4-pGGZ003
pMP041	I	amiRNA1 targeting SOK5
pMP042	Z	amiRNA1 targeting SOK5
pMP043	N	AmiRNA1-SOK5-pGGN
pMP044	Z	UBIQ10-LGh4::AmiRNA1-SOK5-pGGZ003
pMP045	Z	GATA23-LGh4::AmiRNA1-SOK5-pGGZ003
pMP046	I	amiRNA2 targeting SOK5
pMP047	Z003	amiRNA2 targeting SOK5
pMP048	N	AmiRNA2-SOK5-pGGN
pMP049	Z	UBIQ10-LGh4::AmiRNA2-SOK5-pGGZ003
pMP050	Z	GATA23-LGh4::AmiRNA2-SOK5-pGGZ003
pMP051	GB-Z1	GreenBraid pGBZ1
pMP052	GB-Z2	GreenBraid pGBZ2
pMP053	GB-Y1	GreenBraid pGBY1
pMP054	GB-Y2	GreenBraid pGBY2
pMP055	GB-Z1r	GreenBraid pGBZ1r(everse)
pMP056	GB-Z2r	GreenBraid pGBZ2r(everse)
pMP057	GB-Y1r	GreenBraid pGBY1r(everse)
pMP058	GB-Y2r	GreenBraid pGBY2r(everse)
pMP059	F	Entry clone dummy F
pMP060	C	Coding sequence P2A-PmScarlet-I
pMP062	GB-Z1	pRPS5A::H2B:mTurquoise2:tHSP18.2M
pMP063	GB-Z1	pXPP::Vhaa3:PmScarlet-I:tHSP18.2M
pMP064	GB-Z2	pGATA23::Vhaa3:PmScarlet-I:tHSP18.2M:FastRed
pMP065	GB-Z2	pUBQ10::PiP1;4:mVenus:tHSP18.2M
pMP066	GB-Y1	pRPS5A::H2B:mTurquoise2:tHSP18.2M + pUBQ10::PiP1;4:mVenus:tHSP18.2M
pMP067	GB-Y2	pXPP::Vhaa3:PmScarletI:tHSP18.2M + pGATA23::Vhaa3:PmScarletI:tHSP18.2M:FastRed
pMP068	GB-Z1	pRPS5A::H2B:mTurquoise2:tHSP18.2M + pUBQ10::PiP1;4:mVenus:tHSP18.2M + pXPP::Vhaa3:PmScarletI:tHSP18.2M + pGATA23::Vhaa3:PmScarletI:tHSP18.2M:FastRed
pMP069	GB-Z2	pUBQ10::SRDX:NLS:EL222:tHSP18.2M
pMP070	GB-Z1	pXPP::PhyB(1to600):VP16:NLS:tHSP18.2M
pMP071	GB-Z2	pXPP::E:PIF6(1to600):NLS:tHSP18.2M:FastRedGene
pMP072	GB-Z1	GreenBraid pGBZ1 joker
pMP073	GB-Z2	GreenBraid pGBZ2 joker
pMP074	GB-Y1	GreenBraid pGBY1 joker
pMP075	GB-Y2	GreenBraid pGBY2 joker
pMP076	B	Coding sequence iaaM
pMP077	GB-Z1	pOPTO::iaaM:P2A:PmScarlet-I:NLSx3
pMP078	GB-Y1	pOPTO::iaaM:P2A:PmScarlet-I:NLSx3 + pUBQ10::SRDX:NLS:EL222:tHSP18.2M
pMP079	GB-Z1	pXPP::PhyB(1to600):VP16:NLS:tHSP18.2M
pMP080	GB-Y2	pXPP::PhyB(1to600):VP16:NLS:tHSP18.2M + pXPP::E:PIF6(1to600):NLS:tHSP18.2M

Name	GG Type	Content
pMP081	GB-Z1	pGATA23::PhyB(1to600):VP16:NLS:tHSP18.2M
pMP082	GB-Z2	pGATA23::E:PIF6(1to600):NLS:tHSP18.2M
pMP083	GB-Y1	pOPTO::iaaM:P2A:PmScarletI:NLSx3 + pXPP::E:PIF6(1to600):NLS:tHSP18.2M:FastRed
pMP084	GB-Y2	pXPP::PhyB(1to600):VP16:NLS:tHSP18.2M + pUBQ10::SRDX:NLS:EL222:tHSP18.2M
pMP085	GB-Z1	pUBQ10::H2B:mTurquoise2:tHSP18.2M
pMP086	GB-Z2	pUBQ10::PiP1;4:mVenus:tHSP18.2M:FastRed
pMP087	GB-Z2	pOPTO::iaaM:P2A:PmScarletI:NLSx3 + pXPP::E:PIF6(1to600):NLS:tHSP18.2M + pXPP::PhyB(1to600):VP16:NLS:tHSP18.2M + pUBQ10::SRDX:NLS:EL222:tHSP18.2M
pMP094	GB-Z1	pUBQ10:SYP122:GSL:linker:pHusion2:tHSP18.2M:FastRed
pMP095	GB-Z1	pUBQ10:SP:pHusion4:GSL:TM26:tHSP18.2M:FastRed
pMP096	GB-Z1	pUBQ10:SP:pHusion3:GSL:TM26:tHSP18.2M:FastRed
pMP097	GB-Z1	pUBQ10:SYP122:GSL:pHusion3:tHSP18.2M:FastRed
pMP098	GB-Y1	pOPTO::iaaM:P2A:PmScarlet:NLSx3 + pGATA23::E:PIF6(1-600):NLS:tHSP18.2M
pMP099	GB-Y2	pGATA23::PhyB(1-600):VP16:NLS:tHSP18.2M + pUBQ10::SRDX:NLS:EL222:tHSP18.2M
pMP100	GB-Z1	pOPTO::iaaM:P2A:PmScarlet:NLSx3 + pGATA23::E:PIF6(1-600):NLS:tHSP18.2M + pGATA23::PhyB(1-600):VP16:NLS:tHSP18.2M + pUBQ10::SRDX:NLS:EL222:tHSP18.2M
pMP101	GB-Z1	pUBQ10::H2B:pHusion4:tHSP18.2M:FastRed
pMP102	GB-Z1	pSOK1::SOK1:mVenus:tHSP18.2M
pMP103	GB-Z1	pSOK2::SOK2:PmScarlet-I:tHSP18.2M:Sulf
pMP104	GB-Z1	pUBQ10::PiP1;4:mVenus:tHSP18.2M
pMP105	GB-Z2	pUBQ10::PiP1;4:PmScarlet-1:tHSP18.2M
pMP106	GB-Z1	pRPS5A::SOK5:mVenus:tHSP18.2M
pMP107	GB-Z1	pUBQ10::PiP1;4:PmScarlet-1:tHSP18.2M
pMP108	GB-Z2	pUBQ10::PiP1;4:PmScarlet-1:tHSP18.2M:FastRed
pMP109	GB-Y2	pRPS5A::H2B:mTurquoise2:tHSP18.2M + pUBQ10:PiP1;4:PmScarlet:tHSP18.2M:FastRed
pMP110	GB-Y2	pRPS5A::SOK5:mVenus:tHSP18.2M + pUBQ10:PiP1;4:PmScarlet-I:tHSP18.2M:FastRed
pMP111	GB-Z2	pSOK5::SOK5:mTurquoise2:tHSP18.2M
pMP112	GB-Z1	pRPS5A::SOK1:mVenus:tHSP18.2M
pMP113	GB-Z1	pRPS5A::SOK2:PmScarlet:tHSP18.2M:Sulf
pMP114	GB-Y1	pSOK1::SOK1:mVenus:tHSP18.2M + pUBQ10::PiP1;4:PmScarletI:tHSP18.2M:FastRed
pMP116	GB-Z1	pGBZ1 with pink chromatic marker
pMP117	GB-Z2	pGBZ2 with pink chromatic marker
pMP118	GB-Y1	pGBY1 with green chromatic marker
pMP119	GB-Y2	pGBY2 with green chromatic marker
pMP120	GB-Z1r	pGBZ1r with pink chromatic marker
pMP121	GB-Z2r	pGBZ2r with pink chromatic marker
pMP122	GB-Y1r	pGBY1r with green chromatic marker
pMP123	GB-Y2r	pGBY2r with green chromatic marker
pMP124	GB-Z2	pRPS5A::SOK5:mTurquoise2:tHSP18.2M
pMP125	GB-Y1	pSOK1::SOK1:mVenus + Z2joker
pMP126	GB-Y1	pRPS5A::SOK1:mVenus + Z2joker
pMP127	GB-Y1	pRPS5A::SOK1:mVenus + pUBQ10:PiP1;4:mScarlet:FastRed

Name	GG Type	Content
pMP128	GB-Y2	pRPS5A::SOK2:PmScarletI:SulfR + pUBQ10:PiP1;4:mVenus:FastRed
pMP129	GB-Y2	pRPS5A::SOK2:PmScarletI:SulfR + pRPS5A::SOK5:mTurquoise2
pMP130	GB-Z2	pRPS5A::SOK1:mVenus + pRPS5A::SOK2:mScarlet + pRPS5A::SOK5:mTurquoise2:SulfR
pMP131	GB-Y2	pRPS5A::SOK5:mTurquoise2
pMP132	GB-Y2	pSOK1::SOK1:mVenus + pSOK5::SOK5:mTurquoise2
pMP133	GB-Y2	Z1joker + pSOK5::SOK5:mTurquoise2
pMP134	GB-Y2	pSOK2::SOK2:PmScarlet-I:tHSP18.2M:SulfR + pSOK5::SOK5:mTurquoise2:tHSP18.2M
pMP135	GB-Z2	pSOK1::SOK1:mVenus:tHSP18.2M + pSOK2::SOK2:PmScarletI:tHSP18.2M:SulfR + pSOK5::SOK5:mTurquoise2:tHSP18.2M
pMP136	C	SOK4 CDS
pMP139	GB-Z1	pRPS5A::SOK4:mVenus:tHSP18.2M:FastRed
pMP140	GB-Z2	pRPS5A::SOK5:mTagBFP2:tHSP18.2M
pMP141	GB-Z2	pUBQ10::SOK5:mVenus:tHSP18.2M:FastRed
pMP142	GB-Z2	pTCTP1::SOK5:mVenus:tHSP18.2M:FastRed
pMP143	GB-Z2	pSOK5::SOK5:mTagBFP2:tHSP18.2M
pMP144	GB-Y2	pSOK2::SOK2:mScarlet + pSOK5::SOK5:BFP
pMP145	GB-Y1	pRPS5A::SOK4:mVenus:FastRed + pUBQ10::PIP4;1:mScarlet
pMP146	GB-Y1	pUBQ10:PIP4;1:mScarlet + pUBQ10::SOK5:mVenus:FastRed
pMP147	GB-Y2	pRPS5A::SOK2:mScarlet + pRPS5A::SOK5:BFP
pMP148	GB-Y1	pUBQ10:PM:mScarlet + pTCTP1::SOK5:mVenus:FR
pMP149	GB-Y2r	pRPS5A::SOK5:mVenus + Z2joker
pMP150	GB-Y1	pRPS5A::SOK4:mVenus:FR + pUBQ10::PIP4;1:mScarlet

8.3 Microscopy

8.3.1 Sample preparation

Slide mounting

Up to ten seedlings were mounted in the appropriate mounting medium (ClearSee or H_2O) on a microscope slide. These samples were covered with a 22 × 60mm cover slip.

Chamber mounting

Up to ten seedlings were mounted on a slice of solid ½MS medium (43×20mm), which was then inverted into a single-well Lab-Tek® coverglass chamber of similar dimensions (43×20mm).

Light sheet sample mounting

For light sheet microscopy, seedlings were grown on ½MS medium in glass capillary tubes (44.5mm × 1mm, 1.7mm outer diameter) or fluorinated ethylene-propylene (FEP) tubes (44.5mm × 1mm, 1.6mm outer diameter). The composition of the ½MS medium was identical to that described in the section plant growth conditions, except that phyta-gel (8mg/mL) was used instead of phyto-agar. The same growth conditions applied (Section 8.1.3).

8.3.2 Confocal microscopy

From 2020 to 2024, a Leica TCS SP5II confocal microscope was used with a 63×/1.20 water-immersion objective. The system was equipped with an argon laser (operated at 30% output, 458–514nm), a 401nm diode laser, and a 561nm diode-pumped solid-state (DPSS) HeNe laser. These lasers were used to excite fluorophores at the wavelengths indicated in Table 8.9. In most cases, emission light was detected using a Hybrid (HyD) detector at 100–500% gain, depending on fluorophore signal intensity.

For fluorophores with weak signals (e.g., majority of gray values $<$150 at 15% excitation power), laser power was increased up to 50%, and/or the same frame was captured multiple times (up to 8× using frame accumulation) with gray values accumulated across frames. Bidirectional scanning was used in most cases, and frames were often rotated to align seedlings along the shoot–root axis. Images were acquired at 1024×1024 resolution for static 2D images, and at 512×512 resolution for time-lapse experiments. For timelapse experiments, z-stacks of multiple positions were captured within the same imaging chamber every 30 min, where z-stacks had a step size of 1µm between frames.

From 2024 onward, two different Leica SP8 Stellaris systems were used, the AGM/AGS and the AGW system. Both were equipped with a white-light laser, whereas the AGW system was additionally equiped with a multi-photon module. Experiments using white-light excitation were performed on the AGM/AGS system similarly to the SP5II setup. Key differences included increased white-light laser power (up to 80%) and occasional use of z-step spacing optimization. Two-photon excitation and ablation experiments were performed on the AGW system, with image acquisition similar to the single-photon setup, but using different excitation wavelengths (Table 8.9).

Table 8.9: Excitation and emission wavelengths used to capture fluorescent signal in the confocal and multi-photon setup.

Fluorophore	**WL argon excitation wavelength** (nm)	**MP excitation wavelength** (nm)	**Emission wavelength range** (nm)
Calcofluor white	405	–	410–450
mTurquoise2	458	–	470–500
Gamillus	504	–	510–530
mVenus	514	–	520–550
sYFP2	514	970	520–550
mScarlet-I	561	–	580–630
mCherry	561	1060	600–650

8.3.3 Light sheet microscopy

Live-imaging was performed using a MuViSPIM light sheet microscope (Luxendo, Bruker) equipped with a Nikon NIR Apo 40× NA=1.2 water-immersion objective for detection. The magnification was increased to 60× for most time-lapse experiments, except those focused on the root apical meristem. Sample preparation was done as described in the section light sheet sample mounting (Section 8.3.1). Mounted samples were placed in the MuViSPIM imaging chamber, which was filled with liquid ½MS medium.

Fluorescent proteins were excited using diode lasers, and the emitted light was filtered through band pass (BP) filter cubes (Table 8.10). Emission light was detected simultaneously from two opposing angles by scanning cameras. However, for most time-lapse recordings, only one of the captured angles was processed. Timelapse series were acquired by capturing z-stacks (100 µm total depth with a 0.5µm step size) at a 30 min interval for up to three days. Manual drift correction was performed in the Fiji plugin BigDataProcessor2.

Table 8.10: Excitation and emission wavelengths used to capture fluorescent signal in the MuViSPIM.

Fluorescent protein	**Excitation wavelength (nm)**	**Filter cube (nm)**
mTurquoise2	458	BP458-500
mVenus	514	BP520-543
sYFP2	514	BP520-543
mScarlet-I	561	BP610-628
mCherry	561	BP610-628

8.3.4 Laser ablation

Two-photon ablation

The two-photon excitation module of the AGW SP8 setup was exploited to induce targeted cellular damage. The laser was set to 960nm and operated at 20–30% power, focused on a zoomed-in (40x) region encompassing a single cell (LRP, epidermal, or cortex). The exposure duration, approximately 1 second, corresponded to the frame acquisition time when using the following settings: 600 Hz scan speed, 512×512 px resolution, single frame per line, no frame averaging, and bidirectional scanning disabled.

For ablation of the *sok1/2/3/4»5* pentuple mutant, samples were transferred to 1/2MS + 1% sucrose + 20µM DEX or 50mM HU 1 day prior to ablation, and plants recovered at the same conditions prior to fixation and staining (8 h or 16 h post ablation).

UV laser ablation

The light sheet microscope was equipped with an UV ablation laser (High Q, TDK-LAMBDA, Z36-12 REV:2.210 controller) with an output power of approximately 1.8W. Ablation was performed via point illumination at the center of the target cell. Exposure times varied widely, due to variability in the required exposure time to induce visible cellular damage, illumination was often repeated or continued until structural changes became apparent.

8.3.5 Image processing

Image processing was performed in the software Fiji. Specific methods used are described below.

Big Data processor (1 & 2)

Luxendo light sheet microscopy data was visualized using the Big Data Processor (BDP) plugin. For manual drift correction, BDP2 was used. Additionally, the timelapse stacks were cropped along all spatial and temporal dimensions (x, y, z, and t) in BDP2.

Fiji image registration

Drift correction of confocal timelapses were performed using the 3D drift correction function of the Fiji *Registration* plugin. Key parameters for effective correction included the selection of relevant channels and z-slices, a gray value threshold to exclude background noise from the analysis, and the specification of the maximum expected drift in pixels.

Maximum intensity projections

In most cases, a single representative z-slice is shown. However, when fluorescent signal intensity was low, a maximum or sum intensity projection was generated by combining the highest pixel intensities across multiple adjacent z-slices (typically 2 to 10 slices).

Brightness and contrast

In most cases, pixel values below 25 were excluded to reduce background noise. When signal intensity was low, the color mapping of pixel values was compressed. For example, mapping the same display color to a range of gray values (e.g., 25–150, where everything between 150 and 255 has the same color), to enhance visibility. In cases of oversaturation, the gray value range was artificially extended (e.g., from 25-255 to 25–365), allowing pixels to retain their acquired intensity values while being assigned a less intense display color to preserve detail.

8.4 Data analysis

The scripts used in this thesis can be found on github and were created with the help of ChatGPT (https://github.com/mjcpiepers/thesis).

Click here to go to GitHub

8.4.1 SOSEKI accumulation plot

Timelapses and static images were used to determine LR width and SOK maxima at each developmental stage. Image preprocessing was done in Fiji. That is, a 6µm maximum projection of the SOK signal was taken at the midpoint of the z-stack, corresponding to the center of the LRP. The image was rotated so that the LR grew towards the right. It was then cropped precisely to ensure identical image height across samples, and the width was cropped to exactly include the organ from base to apex.

To smooth signal intensity, a median filter with a 25px radius was applied. The image was converted to 8-bit, and background signal outside the primordium was removed using thresholding.

In static images, LR dimensions and the three SOK maxima were determined manually. For timelapses, this information was extracted using a Python script (see GitHub). The resulting CSV file recorded the position of three maxima and LR width per timepoint. All output tables were combined and passed to a second Python script that plotted the relative SOK maxima positions per developmental stage (see GitHub).

8.4.2 Image segmentation

Cell shapes were manually segmented using the Pencil Tool (feathering off) in Adobe Photoshop CC (16-bit grayscale), using a plasma membrane marker as a template.

8.4.3 MorphoGraphX growth quantification

In MorphoGraphX, the principal direction of cell growth and anisotropic growth were quantified. First, a mesh was generated from a Bézier cutting surface. This blank mesh was refined by subdivision and smoothing to increase resolution (`Process` → `Mesh` → `Structure`). A 2D segmentation was imported into MorphoGraphX and projected onto the cell mesh (`Process` → `Segmentation` → `Project 3D labels on mesh`; `min = -2`; `max = +2`). The resulting labels were eroded (`Process` → `Segmentation` → `Erode labels`; `radius = 0.4`), after which a watershed segmentation was applied to generate individual cells (`Process` → `Segmentation` → `Watershed segmentation`).

This workflow was repeated for every time point. Cell labels were then linked across consecutive time points with the Grab Label tool, and their correspondence was verified via `Mesh` → `Cell Axis` → `PDG` → `Check Correspondence`. If mismatches were detected,

the mesh vertices were manually adjusted until the correspondence was correct. The anisotropic growth and principal direction of growth were quantified between each pair of adjacent timepoints (`Mesh` → `Cell Axis` → `PDG` → `Compute Growth Directions`). To generate maps of cellular SOK signal intensity, the SOK signal image was projected onto the mesh (`Quantify` → `Project Signal`).

8.4.4 CarboTag-BDP lifetime plot

The intensity-weighted mean fluorescence lifetime was measured at specific junctions using the Leica LAS X software. ROIs were manually selected using the brush tool. A two-component exponential decay model was applied to fit the fluorescence decay curves within each ROI. The resulting lifetime values were exported from Leica LAS X and imported into RStudio for further analysis. A custom R script was used to generate bar plots displaying the mean lifetime values for each junction.

8.4.5 Signal intensity quantification

For signal intensity measurements, drift-corrected time-lapses were used. A ROI that remained consistently present across all timepoints was selected. At each timepoint, the mean signal intensity within this ROI was measured. To normalize the data, the mean intensity of the marker of interest was divided by the mean intensity of the plasma membrane signal. The resulting ratio was then scaled linearly to a range of 0 to 1 using linear regression. These normalized intensity values were plotted over time using RStudio.

8.4.6 Double blind counting

To quantify the number of oblique cell divisions in the *sok1/2/3/4»5* mutant, Z-stack images of recovered plants were anonymized by assigning a unique identifier, concealing the corresponding treatment condition (Mock, HU, or DEX). Two independent observers manually counted the number of oblique divisions per identifier. After scoring, the treatment identities were revealed and the counts from both observers were averaged for each sample. These averaged values were then visualized in a boxplot.

8.4.7 Microtubule orientation quantification

Two-dimensional images of the cell cortex were acquired by positioning the image plane to capture the cortex. The microtubule fluorescence channel was processed in Fiji using the following workflow. Background subtraction using the rolling ball algorithm (radius = 100 pixels). Gaussian blur (σ = 1) to reduce noise. Contrast enhancement (saturation = 0.3, equalized) to improve visibility of microtubules. Unsharp masking (radius = 2 pixels, mask weight = 0.6) to enhance microtubule edges. Processed images were rotated to generate a rightward side view of the LRP and cropped so that the image width corresponded exactly to the measured LRP width.

ROIs were manually selected using the freehand selection tool in Fiji. Microfibril orientation and anisotropy were quantified for each ROI using the batch-processing version of FibrilJ [Boudaoud et al., 2014, Louveaux and Boudaoud, 2018]. The resulting measurements were grouped according to developmental stage and their relative X and Y coordinates within the LRP. Coordinates were corrected for differences in zoom level between images, and orientations for measurements in the bottom half of the LRP were mirrored to match those in the top half. This allowed pooling of equivalent positions between the top and bottom halves. Each group corresponded to a set of measurements representing a single cell..

The mean anisotropy-weighted microfibril orientation was calculated for each group in Microsoft Excel using the following procedure. The measured orientation (in degrees) was converted to radians and doubled to account for the fact that orientations 180° apart correspond to the same microtubule axis. For each measurement, the anisotropy value was multiplied by the cosine and sine of the doubled orientation, producing weighted X and Y vector components. Weighted cosine and sine values were summed across all ROIs in the group. The mean doubled orientation (in radians) was obtained using the ATAN2 function. The doubled mean angle was halved to return to axial space and converted back to degrees. This method was validated using test inputs (e.g., 5° and 10° at equal anisotropy weight), which produced the expected mean of 7.5°. Mean group orientations were plotted onto schematic coordinate systems to represent cell positions relative to the LRP outline. Additionally, mean anisotropy values were calculated over multiple groups and visualized as boxplots to illustrate regional variation in microtubule alignment.

8.5 Graphic design

8.5.1 Figure mounting

Microscopy images were mounted using Adobe Illustrator and Adobe Photoshop. In some cases, an adjustment layer was applied to modify the hue of the lookup table for improved visual clarity. When images lacked an embedded scale bar, the pixel-to-µm ratio was calculated, and a corresponding scale bar was generated within the software. The layout of graphs or box plots, generated in R or Python, were adjusted in Adobe Photoshop or Illustrator to enhance clarity, such as by increasing font-size or adding graphical elements or text.

8.5.2 Animation and movies

Animations and movies were created using Adobe After Effects. Final rendering and export of the animations were performed using Adobe Media Encoder.

8.5.3 Cell Outlines

Cell outlines were manually drawn by tracing the contours of a plasma membrane marker using the Pen Tool in Adobe Illustrator.

8.5.4 Schematic creation

Schematics were created using Adobe Illustrator and Adobe Photoshop to illustrate experimental designs and biological processes.

8.5.5 Cartoon creation

Cartoon illustrations were initially generated using ChatGPT by providing descriptive prompts. The resulting images were then edited in Adobe Photoshop to correct inaccuracies and better align with the intended visual narrative. In some cases, individual elements were extracted and reused in subsequent cartoons to ensure visual consistency and to meet the specific conceptual requirements of this thesis

8.5.6 Color adjustments

The LUT/colors of processed images were occasionally altered in Adobe Photoshop to enhance contrast and visual clarity of the images.

8.6 Writing

8.6.1 Proofreading

Structured written text was reviewed using ChatGPT, which was prompted to enhance clarity and correct grammar. The text editor Overleaf provided grammatical corrections. The suggested revisions were manually evaluated, selectively integrated, and refined where they improved the clarity of the intended message. Furthermore, a handful of people read the thesis and provided useful feedback. Finally, the translation of the abstract to the Zusammenfassung was done with the help of ChatGPT.

Acknowledgments

I would like to thank all the people listed below for their invaluable contributions. I have tried to keep this section concise while conveying the essential support. I sincerely hope I have not overlooked anything or anyone.

Dr. Ranjith Papareddy
For proofreading and providing incredibly helpful feedback.

Dr. Xinai Zhao
For providing an EDU staining kit.

Dr. Diego Orzáez
For supplying GoldenBraid vectors.

Dr. Uriel Urquiza and Prof. Dr. Matias Zurbriggen
For their feedback on the optogenetic system and for supplying transgenic plant lines.

Dr. Pascal Hunziker
For an introduction to the Stellaris 8 microscope system.

Dr. Rodrigo Vena
For propagation of GreenBraid plant lines.

Prof. Dr. Kasper van Gelderen, Prof. Dr. Josephine Bageritz, Prof. Dr. Lázaro Centanin, and Prof. Dr. Gislene Pereira
For valuable feedback on presentations.

Prof. Dr. Joseph Dubrovsky
For valuable feedback during my presentations, his guidance in nomenclature usage, and his broad knowledge of plant literature, which directed me toward insightful publications.

Prof. Dr. Jan Lohmann and Prof. Dr. Thomas Greb
For enabling the exchange of lab resources and providing feedback on the research conducted in this thesis.

Andriy Volkov
For making the *SOK* LOF mutants that were consequently used in this thesis.

Dr. Xiaomin Li
For additional results (not included in this thesis) supporting that SOSEKIs respond to mechanical cues in the hypocotyl.

Dr. Vera Gorelova
For sending boron transporter lines and SOSEKI transgenic lines.

Vesta Petrasiunaite, Katarina Erbstein, and Naja Faerber
For their work on GreenGate 2.0, which resulted in valuable new additions to GreenGate molecular cloning, and a joint publication.

Dr. Melanie Krebs
For technical support with microscopy.

Dr. Athul Vijayan and Dr. Sören Strauss
For fast and helpful guidance with issues in MorphoGraphX.

Jana Fuss and Joergen Benjaminsen
For technical support and help setting up ablation experiments using the multi-photon system.

Dr. Christian Wenzl
For assistance in setting up imaging experiments to capture the root apical meristem.

Maarten Besten and Prof. Dr. Joris Sprakel
For initial support during preliminary CarboTag experiments and for supplying the lab with CarboTags.

Prof. Dr. Kay Schneitz and Prof. Dr. Karin Schumacher
For their evaluation of the thesis progress and insightful feedback on the research.

Prof. Dr. Dolf Weijers
For targeted feedback that helped shape the direction of this thesis, supplying transgenic plant lines, and initiating the collaboration that led to the CarboTag experiments.

Christina Godel
For guidance with administrative tasks.

Barbara Jesenofsky
For organizing and ordering lab supplies.

Neva Bölke
For constructing SOSEKI coding sequences in plasmids.

Babette Knoblauch
For testing light conditions for the optogenetic approach and summarizing the results.

Laura Schütz
For acquiring and summarizing preliminary results investigating whether SOSEKIs respond to mechanical cues.

Anika Seppelt
For constructing promoter and coding sequences of optogenetic components in plasmids and providing essential feedback that enabled progress in cloning.

Kathrin Distil
For constructing plasma membrane and nuclear markers for GreenGate 2.0, and for obtaining and summarizing polarity patterns resulting from drug treatments.

Dr. Michael Stitz, Dr. Béatrice Berthet, Dr. Tomás Tessi, Dr. Harshita Singh, Dr. Changzheng Song, Dr. Amaya Vilches-Barro, Dr. Zhaoxue Ma, and Anamrija Primc
For continuous feedback during lab meetings and their availability to support lab work.

Dr. Jazmín Reyes-Hernández
For being a kind and unconditionally supportive colleague throughout this work.

Prof. Dr. Alexis Maizel
For securing funding, providing access to lab resources, fostering a pleasant work environment, proofreading, and offering continuous and constructive support throughout my thesis, that helped me grow as a scientist and person.

Bibliography

[Abas et al., 2022] Abas, R., Masrudin, S. S., Harun, A. M., and Omar, N. S. (2022). Gastrulation and Body Axes Formation: A Molecular Concept and Its Clinical Correlates. *Malaysian Journal of Medical Sciences*, 29(6):6–14.

[Alassimone et al., 2010] Alassimone, J., Naseer, S., and Geldner, N. (2010). A developmental framework for endodermal differentiation and polarity. *Proceedings of the National Academy of Sciences of the United States of America*, 107(11):5214–5219.

[Alberts et al., 2002a] Alberts, B., Johnson, A., Lewis, J., and et al (2002a). The Plant Cell Cycle. In *Molecular Biology of the Cell. 4th edition.* Garland Science, New York, 4th edition.

[Alberts et al., 2002b] Alberts, B., Johnson, A., Lewis, J., and et al (2002b). The Plant Cell Wall. In *Molecular Biology of the Cell. 4th edition.* Garland Science, New York, 4th edition.

[Ali and Stukenberg, 2023] Ali, A. and Stukenberg, P. T. (2023). Aurora kinases: Generators of spatial control during mitosis.

[Alonso Baez et al., 2025] Alonso Baez, L., Bjørkøy, A., Saffioti, F., Morghen, S., Amanda, D., Tichá, M., Besten, M., Ivanova, A., Sprakel, J., Stokke, B. T., and Hamann, T. (2025). The mechanical properties of Arabidopsis thaliana roots adapt dynamically during development and to stress.

[Alonso-Serra et al., 2024] Alonso-Serra, J., Cheddadi, I., Kiss, A., Cerutti, G., Lang, M., Dieudonné, S., Lionnet, C., Godin, C., and Hamant, O. (2024). Water fluxes pattern growth and identity in shoot meristems. *Nature Communications*, 15(1):1–14.

[Andersen et al., 2018] Andersen, T. G., Naseer, S., Ursache, R., Wybouw, B., Smet, W., De Rybel, B., Vermeer, J. E., and Geldner, N. (2018). Diffusible repression of cytokinin signalling produces endodermal symmetry and passage cells. *Nature*, 555(7697):529–533.

[Andreou and Nakayama, 2018] Andreou, A. I. and Nakayama, N. (2018). Mobius assembly: A versatile golden-gate framework towards universal DNA assembly. *PLoS ONE*, 13(1):1–18.

[Arkowitz, 2009] Arkowitz, R. A. (2009). Chemical gradients and chemotropism in yeast. *Cold Spring Harbor perspectives in biology*, 1(2):1–20.

[Armenta-Medina et al., 2021] Armenta-Medina, A., Gillmor, C. S., Gao, P., Mora-Macias, J., Kochian, L. V., Xiang, D., and Datla, R. (2021). Developmental and genomic architecture of plant embryogenesis: from model plant to crops.

[Asaoka et al., 2023] Asaoka, M., Sakamoto, S., Gunji, S., Mitsuda, N., Tsukaya, H., Sawa, S., Hamant, O., and Ferjani, A. (2023). Contribution of vasculature to stem integrity in Arabidopsis thaliana. *Development (Cambridge)*, 150(3).

[Asnacios and Hamant, 2012] Asnacios, A. and Hamant, O. (2012). The mechanics behind cell polarity. *Trends in Cell Biology*, 22(11):584–591.

[Bai et al., 2013] Bai, Y., Vaddepalli, P., Fulton, L., Bhasin, H., Hülskamp, M., and Schneitz, K. (2013). ANGUSTIFOLIA is a central component of tissue morphogenesis mediated by the atypical receptor-like kinase STRUBBELIG. *BMC plant biology*, 13:16.

[Banda et al., 2019] Banda, J., Bellande, K., von Wangenheim, D., Goh, T., Guyomarc'h, S., Laplaze, L., and Bennett, M. J. (2019). Lateral Root Formation in Arabidopsis: A Well-Ordered LRexit. *Trends in Plant Science*, 24(9):826–839.

[Baskin, 2000] Baskin, T. I. (2000). On the constancy of cell division rate in the root meristem. *Plant Molecular Biology*, 43:545–554.

[Baskin, 2005] Baskin, T. I. (2005). Anisotropic expansion of the plant cell wall. *Annual Review of Cell and Developmental Biology*, 21:203–222.

[Baskin et al., 2010] Baskin, T. I., Peret, B., Baluška, F., Benfey, P. N., Bennett, M., Forde, B. G., Gilroy, S., Helariutta, Y., Hepler, P. K., Leyser, O., Masson, P. H., Muday, G. K., Murphy, A. S., Poethig, S., Rahman, A., Roberts, K., Scheres, B., Sharp, R. E., and Somerville, C. (2010). Shootward and rootward: Peak terminology for plant polarity. *Trends in Plant Science*, 15(11):593–594.

[Benková et al., 2003] Benková, E., Michniewicz, M., Sauer, M., Teichmann, T., Seifertová, D., Jürgens, G., and Friml, J. (2003). Local, Efflux-Dependent Auxin Gradients as a Common Module for Plant Organ Formation. *Cell*, 115(5):591–602.

[Besten et al., 2024] Besten, M., Hendriksz, M., Michels, L., Charrier, B., Smakowska-Luzan, E., Weijers, D., Borst, J. W., and Sprakel, J. (2024). CarboTag: a modular approach for live and functional imaging of plant cell walls. *bioRxiv*, 22(May):2024.07.05.597952.

[Bomfiglio et al., 2025] Bomfiglio, I. F., Seiler De Medeiros Mendes, I., and Bonatto, D. (2025). A review of DNA restriction-free overlapping sequence cloning techniques for synthetic biology. *Arxiv*.

[Bouchez et al., 2024] Bouchez, D., Uyttewaal, M., and Pastuglia, M. (2024). Spatiotemporal regulation of plant cell division. *Current Opinion in Plant Biology*, 79.

[Boudaoud et al., 2014] Boudaoud, A., Burian, A., Borowska-Wykręt, D., Uyttewaal, M., Wrzalik, R., Kwiatkowska, D., and Hamant, O. (2014). FibrilTool, an ImageJ plug-in to quantify fibrillar structures in raw microscopy images. *Nature Protocols*, 9(2):457–463.

[Breuninger et al., 2008] Breuninger, H., Rikirsch, E., Hermann, M., Ueda, M., and Laux, T. (2008). Differential Expression of WOX Genes Mediates Apical-Basal Axis Formation in the Arabidopsis Embryo. *Developmental Cell*, 14(6):867–876.

[Butler and Wallingford, 2017] Butler, M. T. and Wallingford, J. B. (2017). Planar cell polarity in development and disease. *Nature Reviews Molecular Cell Biology*, 18(6):375–388.

[Cadart et al., 2018] Cadart, C., Monnier, S., Grilli, J., Sáez, P. J., Srivastava, N., Attia, R., Terriac, E., Baum, B., Cosentino-Lagomarsino, M., and Piel, M. (2018). Size control in mammalian cells involves modulation of both growth rate and cell cycle duration. *Nature Communications*, 9(1).

[Campilho et al., 2006] Campilho, A., Garcia, B., Toorn, H. V., Wijk, H. V., Campilho, A., and Scheres, B. (2006). Time-lapse analysis of stem-cell divisions in the Arabidopsis thaliana root meristem. *Plant Journal*, 48(4):619–627.

[Campos et al., 2014] Campos, M., Surovtsev, I. V., Kato, S., Paintdakhi, A., Beltran, B., Ebmeier, S. E., and Jacobs-Wagner, C. (2014). A constant size extension drives bacterial cell size homeostasis. *Cell*, 159(6):1433–1446.

[Chan et al., 1996] Chan, Y.-J., Tseng, W.-P., and Hayward, G. S. (1996). Two Distinct Upstream Regulatory Domains Containing Multicopy Cellular Transcription Factor Binding Sites Provide Basal Repression and Inducible Enhancer Characteristics to the Immediate-Early IES (US3) Promoter from Human Cytomegalovirus. *JOURNAL OF VIROLOGY*, 70(8):5312–5328.

[Chandler-Brown et al., 2017] Chandler-Brown, D., Schmoller, K. M., Winetraub, Y., and Skotheim, J. M. (2017). The Adder Phenomenon Emerges from Independent Control of Pre- and Post-Start Phases of the Budding Yeast Cell Cycle. *Current Biology*, 27(18):2774–2783.

[Choi et al., 2014] Choi, W. G., Toyota, M., Kim, S. H., Hilleary, R., and Gilroy, S. (2014). Salt stress-induced Ca2+ waves are associated with rapid, long-distance root-to-shoot signaling in plants. *Proceedings of the National Academy of Sciences of the United States of America*, 111(17):6497–6502.

[Christie and Zurbriggen, 2021] Christie, J. M. and Zurbriggen, M. D. (2021). Optogenetics in plants. *New Phytologist*, 229(6):3108–3115.

[Clough and Bent, 1998] Clough, S. J. and Bent, A. F. (1998). Floral dip: A simplified method for Agrobacterium-mediated transformation of Arabidopsis thaliana. *Plant Journal*, 16(6):735–743.

[Coen and Cosgrove, 2023] Coen, E. and Cosgrove, D. J. (2023). The mechanics of plant morphogenesis. *Science*, 379(6631).

[Cohen et al., 1973] Cohen, S. N., Chang, A. C. Y., Boyert, H. W., and Hellingt, R. B. (1973). Construction of Biologically Functional Bacterial Plasmids In Vitro (R factor/restriction enzyme/transformation/endonuclease/antibiotic resistance). *PNAS*, 70(11):3240–3244.

[Cosgrove, 2005] Cosgrove, D. J. (2005). Growth of the plant cell wall. *Nature Reviews Molecular Cell Biology*, 6(11):850–861.

[Cosgrove, 2016] Cosgrove, D. J. (2016). Plant cell wall extensibility: Connecting plant cell growth with cell wall structure, mechanics, and the action of wall-modifying enzymes. *Journal of Experimental Botany*, 67(2):463–476.

[D'Ario and Sablowski, 2019] D'Ario, M. and Sablowski, R. (2019). Cell Size Control in Plants. *Annual Review of Genetics*, 53:45–65.

[de Reuille et al., 2015] de Reuille, P. B., Routier-Kierzkowska, A. L., Kierzkowski, D., Bassel, G. W., Schüpbach, T., Tauriello, G., Bajpai, N., Strauss, S., Weber, A., Kiss, A., Burian, A., Hofhuis, H., Sapala, A., Lipowczan, M., Heimlicher, M. B., Robinson, S., Bayer, E. M., Basler, K., Koumoutsakos, P., Roeder, A. H., Aegerter-Wilmsen, T., Nakayama, N., Tsiantis, M., Hay, A., Kwiatkowska, D., Xenarios, I., Kuhlemeier, C., and Smith, R. S. (2015). MorphoGraphX: A platform for quantifying morphogenesis in 4D. *eLife*, 4(MAY):1–20.

[De Rybel et al., 2010] De Rybel, B., Vassileva, V., Parizot, B., Demeulenaere, M., Grunewald, W., Audenaert, D., Van Campenhout, J., Overvoorde, P., Jansen, L., Vanneste, S., Möller, B., Wilson, M., Holman, T., Van Isterdael, G., Brunoud, G., Vuylsteke, M., Vernoux, T., De Veylder, L., Inzé, D., Weijers, D., Bennett, M. J., and Beeckman, T. (2010). A novel Aux/IAA28 signaling cascade activates GATA23-dependent specification of lateral root founder cell identity. *Current Biology*, 20(19):1697–1706.

[De Simone et al., 2017] De Simone, A., Hubbard, R., De La Torre, N. V., Velappan, Y., Wilson, M., Considine, M. J., Soppe, W. J., and Foyer, C. H. (2017). Redox Changes during the Cell Cycle in the Embryonic Root Meristem of Arabidopsis thaliana. *Antioxidants and Redox Signaling*, 27(18):1505–1519.

[De Smet et al., 2010] De Smet, I., Lau, S., Voß, U., Vanneste, S., Benjamins, R., Rademacher, E. H., Schlereth, A., De Rybel, B., Vassileva, V., Grunewald, W., Naudts, M., Levesque, M. P., Ehrismann, J. S., Inzé, D., Luschnig, C., Benfey, P. N., Weijers, D., Van Montagu, M. C., Bennett, M. J., Jürgens, G., and Beeckman, T. (2010). Bimodular auxin response controls organogenesis in Arabidopsis. *Proceedings of the National Academy of Sciences of the United States of America*, 107(6):2705–2710.

[Deforet et al., 2015] Deforet, M., Van Ditmarsch, D., and Xavier, J. B. (2015). Cell-Size Homeostasis and the Incremental Rule in a Bacterial Pathogen. *Biophysical Journal*, 109(3):521–528.

[Demes and Verger, 2023] Demes, E. and Verger, S. (2023). High-throughput characterization of cortical microtubule arrays response to anisotropic tensile stress. *BMC Biology*, 21(1).

[Denness et al., 2011] Denness, L., McKenna, J. F., Segonzac, C., Wormit, A., Madhou, P., Bennett, M., Mansfield, J., Zipfel, C., and Hamann, T. (2011). Cell wall

damage-induced lignin biosynthesis is regulated by a reactive oxygen species- and jasmonic acid-dependent process in arabidopsis. *Plant Physiology*, 156(3):1364–1374.

[Desvoyes et al., 2020] Desvoyes, B., Arana-Echarri, A., Barea, M. D., and Gutierrez, C. (2020). A comprehensive fluorescent sensor for spatiotemporal cell cycle analysis in Arabidopsis. *Nature Plants*, 6(11):1330–1334.

[Desvoyes et al., 2021] Desvoyes, B., Echevarría, C., and Gutierrez, C. (2021). A perspective on cell proliferation kinetics in the root apical meristem.

[Detlef Weigel and Peter Doerner, 1996] Detlef Weigel and Peter Doerner (1996). Cell–cell interactions: Taking cues from the neighbors. *Current Biology*, 6(1).

[Dettmer and Friml, 2011] Dettmer, J. and Friml, J. (2011). Cell polarity in plants: When two do the same, it is not the same.... *Current Opinion in Cell Biology*, 23(6):686–696.

[Dettmer et al., 2006] Dettmer, J., Hong-Hermesdorf, A., Stierhof, Y. D., and Schumacher, K. (2006). Vacuolar H+-ATPase activity is required for endocytic and secretory trafficking in Arabidopsis. *Plant Cell*, 18(3):715–730.

[Di Fino et al., 2025] Di Fino, L. M., Anjam, M. S., Besten, M., Mentzelopoulou, A., Papadakis, V., Zahid, N., Baez, L. A., Trozzi, N., Majda, M., Ma, X., Hamann, T., Sprakel, J., Moschou, P. N., Smith, R. S., and Marhavý, P. (2025). Cellular damage triggers mechano-chemical control of cell wall dynamics and patterned cell divisions in plant healing. *Developmental Cell*, 60(10):1411–1422.

[Di Laurenzio et al., 1996] Di Laurenzio, L., Wysocka-Diller, J., Malamy, J. E., Pysh, L., Helariutta, Y., Freshour, G., Hahn, M. G., Feldmann, K. A., and Benfey, P. N. (1996). The SCARECROW gene regulates an asymmetric cell division that is essential for generating the radial organization of the Arabidopsis root. *Cell*, 86(3):423–433.

[Ditengou et al., 2008] Ditengou, F. A., Teale, W. D., Kochersperger, P., Flittner, K. A., Kneuper, I., Van Der Graaff, E., Nziengui, H., Pinosa, F., Li, X., Nitschke, R., Laux, T., and Palme, K. (2008). Mechanical induction of lateral root initiation in Arabidopsis thaliana. *Proceedings of the National Academy of Sciences of the United States of America*, 105(48):18818–18823.

[Dolan et al., 1993a] Dolan, L., Janmaat, K., Willemsen, V., Linstead, P., Poethig, S., Roberts, K., and Scheres, B. (1993a). Cellular organisation of the Arabidopsis thaliana root. *Development*, 119(1):71–84.

[Dolan et al., 1993b] Dolan, L., Janmaat, K., Willemsen, V., Linstead, P., Poethig, S., Roberts, K., and Scheres, B. (1993b). Cellular organisation of the Arabidopsis thaliana root. *Development*, 119(1):71–84.

[Dong et al., 2009] Dong, J., MacAlister, C. A., and Bergmann, D. C. (2009). BASL Controls Asymmetric Cell Division in Arabidopsis. *Cell*, 137(7):1320–1330.

[Drubin and Nelson, 1996] Drubin, D. G. and Nelson, W. J. (1996). Origins of Cell Polarity Review. *Cell*, 84:335–344.

[Du and Scheres, 2017a] Du, Y. and Scheres, B. (2017a). PLETHORA transcription factors orchestrate de novo organ patterning during Arabidopsis lateral root outgrowth. *Proceedings of the National Academy of Sciences of the United States of America*, 114(44):11709–11714.

[Du and Scheres, 2017b] Du, Y. and Scheres, B. (2017b). PLETHORA transcription factors orchestrate de novo organ patterning during Arabidopsis lateral root outgrowth. *Proceedings of the National Academy of Sciences of the United States of America*, 114(44):11709–11714.

[Dubrovsky et al., 2025] Dubrovsky, J. G., Li, J., Bouziri, S., Bormann, E., Geiger, C., Reyes-Hernandez, J., and Maizel, A. (2025). Spatiotemporal Dynamics of Anionic Phospholipids Orchestrate Lateral Root Initiation and Morphogenesis in Arabidopsis thaliana.

[Dubrovsky et al., 2008] Dubrovsky, J. G., Sauer, M., Napsucialy-Mendivil, S., Ivanchenko, M. G., Friml, J., Shishkova, S., Celenza, J., and Benková, E. (2008). Auxin acts as a local morphogenetic trigger to specify lateral root founder cells. *Proceedings of the National Academy of Sciences of the United States of America*, 105(25):8790–8794.

[Echevarria et al., 2022] Echevarria, C., Desvoyes, B., Marconi, M., Franco-Zorrila, J. M., Lee, L., Umeda, M., Sablowski, R., Birnbaum, K. D., Wabnik, K., and Gutierrez, C. (2022). Stem cell regulators control a G1 duration gradient in the plant root meristem.

[Elsayed et al., 2016] Elsayed, K., Werner, S., Gallemí, M., Kong, J., Sánchez Guajardo, E. R., LZhang, L., Jaillais, Y., Greb, T., and Belkhadir, Y. (2016). Mapping the subcellular mechanical properties of live cells in tissues with fluorescence emission–Brillouin imaging. *Science Signaling*, 9(435).

[Engler et al., 2008] Engler, C., Kandzia, R., and Marillonnet, S. (2008). A one pot, one step, precision cloning method with high throughput capability. *PLoS ONE*, 3(11).

[Feng et al., 2018] Feng, W., Kita, D., Peaucelle, A., Cartwright, H. N., Doan, V., Duan, Q., Liu, M. C., Maman, J., Steinhorst, L., Schmitz-Thom, I., Yvon, R., Kudla, J., Wu, H. M., Cheung, A. Y., and Dinneny, J. R. (2018). The FERONIA Receptor Kinase Maintains Cell-Wall Integrity during Salt Stress through Ca2+ Signaling. *Current Biology*, 28(5):666–675.

[Francis, 2007] Francis, D. (2007). The plant cell cycle - 15 Years on. *New Phytologist*, 174(2):261–278.

[Friml et al., 2003] Friml, J., Vieten, A., Sauer, M., Weijers, D., Schwarz, H., Hamann, T., Offringa, R., and Jürgens, G. (2003). Efflux-dependent auxin gradients establish the apical-basal axis of Arabidopsis. *Nature*, 426(6963):147–153.

[Fruleux et al., 2019] Fruleux, A., Verger, S., and Boudaoud, A. (2019). Feeling stressed or strained? A biophysical model for cell wall mechanosensing in plants. *Frontiers in Plant Science*, 10.

[Fuchs and Lohmann, 2020] Fuchs, M. and Lohmann, J. U. (2020). Aiming for the top: non-cell autonomous control of shoot stem cells in Arabidopsis. *Journal of Plant Research*, 133(3):297–309.

[Fujita et al., 2013] Fujita, S., Pytela, J., Hotta, T., Kato, T., Hamada, T., Akamatsu, R., Ishida, Y., Kutsuna, N., Hasezawa, S., Nomura, Y., Nakagami, H., and Hashimoto, T. (2013). An atypical tubulin kinase mediates stress-induced microtubule depolymerization in arabidopsis. *Current Biology*, 23(20):1969–1978.

[Geldner et al., 2003] Geldner, N., Anders, N., Wolters, H., Keicher, J., Kornberger, W., Muller, P., Delbarre, A., Ueda, T., Nakano, A., and Jürgens, G. (2003). The Arabidopsis GNOM ARF-GEF mediates endosomal recycling, auxin transport, and auxin-dependent plant growth. *Cell*, 112(2):219–230.

[Geldner et al., 2009] Geldner, N., Dénervaud-Tendon, V., Hyman, D. L., Mayer, U., Stierhof, Y.-D., and Chory, J. (2009). Rapid, combinatorial analysis of membrane compartments in intact plants with a multicolor marker set. *Plant J*, 59(1):169–178.

[Goehring et al., 2011] Goehring, N. W., Hoege, C., Grill, S. W., and Hyman, A. A. (2011). PAR proteins diffuse freely across the anterior-posterior boundary in polarized C. elegans embryos. *Journal of Cell Biology*, 193(3):583–594.

[Goh et al., 2012a] Goh, T., Joi, S., Mimura, T., and Fukaki, H. (2012a). The establishment of asymmetry in Arabidopsis lateral root founder cells is regulated by LBD16/ASL18 and related LBD/ASL proteins. *Development*, 139(5):883–893.

[Goh et al., 2012b] Goh, T., Joi, S., Mimura, T., and Fukaki, H. (2012b). The establishment of asymmetry in Arabidopsis lateral root founder cells is regulated by LBD16/ASL18 and related LBD/ASL proteins. *Development*, 139(5):883–893.

[Goh et al., 2016a] Goh, T., Toyokura, K., Wells, D. M., Swarup, K., Yamamoto, M., Mimura, T., Weijers, D., Fukaki, H., Laplaze, L., Bennett, M. J., and Guyomarc'h, S. (2016a). Quiescent center initiation in the Arabidopsis lateral root primordia is dependent on the SCARECROW transcription factor. *Development (Cambridge)*, 143(18):3363–3371.

[Goh et al., 2016b] Goh, T., Toyokura, K., Wells, D. M., Swarup, K., Yamamoto, M., Mimura, T., Weijers, D., Fukaki, H., Laplaze, L., Bennett, M. J., and Guyomarc'h, S. (2016b). Quiescent center initiation in the Arabidopsis lateral root primordia is dependent on the SCARECROW transcription factor. *Development (Cambridge)*, 143(18):3363–3371.

[Gorelova et al., 2021] Gorelova, V., Sprakel, J., and Weijers, D. (2021). Plant cell polarity as the nexus of tissue mechanics and morphogenesis. *Nature Plants*, 7(12):1548–1559.

[Gutierrez, 2022] Gutierrez, C. (2022). A Journey to the Core of the Plant Cell Cycle. *International Journal of Molecular Sciences*, 23(15).

[Hamant and Haswell, 2017] Hamant, O. and Haswell, E. S. (2017). Life behind the wall: Sensing mechanical cues in plants.

[Hamant et al., 2008] Hamant, O., Heisler, M. G., Jönsson, H., Krupinski, P., Uyttewaal, M., Bokov, P., Corson, F., Sahlin, P., Boudaoud, A., Meyerowitz, E. M., Couder, Y., and Traas, J. (2008). Developmental patterning by mechanical signals in Arabidopsis. *Science*, 322(5908):1650–1655.

[Hansen et al., 2025] Hansen, A., Gladala-Kostarz, A., Hindhaugh, R., Doonan, J. H., and Bosch, M. (2025). Mechanical stimulation in plants: molecular insights, morphological adaptations, and agricultural applications in monocots.

[Harrison et al., 2006] Harrison, S. J., Mott, E. K., Parsley, K., Aspinall, S., Gray, J. C., and Cottage, A. (2006). A rapid and robust method of identifying transformed Arabidopsis thaliana seedlings following floral dip transformation. *Plant Methods*, 2(1):1–7.

[Hayashi et al., 2013] Hayashi, K., Hasegawa, J., and Matsunaga, S. (2013). The boundary of the meristematic and elongation zones in roots: Endoreduplication precedes rapid cell expansion. *Scientific Reports*, 3.

[Hoermayer et al., 2020] Hoermayer, L., Montesinos, J. C., Marhava, P., Benková, E., Yoshida, S., and Friml, J. (2020). Wounding-induced changes in cellular pressure and localized auxin signalling spatially coordinate restorative divisions in roots. *Proceedings of the National Academy of Sciences of the United States of America*, 117(26):15322–15331.

[Hoermayer et al., 2024] Hoermayer, L., Montesinos, J. C., Trozzi, N., Spona, L., Yoshida, S., Marhava, P., Caballero-Mancebo, S., Benková, E., Heisenberg, C. P., Dagdas, Y., Majda, M., and Friml, J. (2024). Mechanical forces in plant tissue matrix orient cell divisions via microtubule stabilization. *Developmental Cell*, 59(10):1333–1344.

[Hofhuis et al., 2013] Hofhuis, H., Laskowski, M., Du, Y., Prasad, K., Grigg, S., Pinon, V., and Scheres, B. (2013). Phyllotaxis and rhizotaxis in Arabidopsis are modified by three plethora transcription factors. *Current Biology*, 23(11):956–962.

[Jackson et al., 1972] Jackson, D. A., Symonst, R. H., Berg, P., Lobban, D. P., and Kaiser, A. D. (1972). Biochemical Method for Inserting New Genetic Information into DNA of Simian Virus 40: Circular SV40 DNA Molecules Containing Lambda Phage Genes and the Galactose Operon of Escherichia coli (molecular hybrids/DNA joining/viral transformation/genetic transfer). *PNAS*, 69(10):2904–2909.

[Jacques et al., 2013] Jacques, E., Verbelen, J. P., and Vissenberg, K. (2013). Mechanical stress in Arabidopsis leaves orients microtubules in a 'continuous' supracellular pattern. *BMC Plant Biology*, 13(1).

[Jarvis et al., 2003] Jarvis, M. C., Briggs, S. P., and Knox, J. P. (2003). Intercellular adhesion and cell separation in plants. *Plant, Cell and Environment*, 26(7):977–989.

[Ji et al., 2023] Ji, T., Zheng, L., Wu, J., Duan, M., Liu, Q., Liu, P., Shen, C., Liu, J., Ye, Q., Wen, J., Dong, J., and Wang, T. (2023). The thioesterase APT1 is a bidirectional-adjustment redox sensor. *Nature Communications*, 14(1).

[Jones et al., 2017] Jones, A. R., Forero-Vargas, M., Withers, S. P., Smith, R. S., Traas, J., Dewitte, W., and Murray, J. A. (2017). Cell-size dependent progression of the cell cycle creates homeostasis and flexibility of plant cell size. *Nature Communications*, 8:1–13.

[Jonsson et al., 2022a] Jonsson, K., Hamant, O., and Bhalerao, R. P. (2022a). Plant cell walls as mechanical signaling hubs for morphogenesis. *Current Biology*, 32(7):R334–R340.

[Jonsson et al., 2022b] Jonsson, K., Hamant, O., and Bhalerao, R. P. (2022b). Plant cell walls as mechanical signaling hubs for morphogenesis. *Current Biology*, 32(7):R334–R340.

[Kania et al., 2014] Kania, U., Fendrych, M., and Friml, J. (2014). Polar delivery in plants; Commonalities and differences to animal epithelial cells. *Open Biology*, 4(4).

[Klunder et al., 2017] Klunder, L. J., Faber, K. N., Dijkstra, G., and Van Ijzendoorn, S. C. (2017). Mechanisms of cell polarity – Controlled epithelial homeostasis and immunity in the intestine. *Cold Spring Harbor Perspectives in Biology*, 9(7):1–15.

[Koncz and Schell, 1986] Koncz, C. and Schell, J. (1986). The promoter of TL-DNA gene 5 controls the tissue-specific expression of chimaeric genes carried by a novel type of Agrobacterium binary vector. *Molecular and General Genetics*, 204:383–396.

[Kostareli et al., 2025] Kostareli, M. M., Westerink, T., Couillaud, G., Peippo, M., Govers, F., Weijers, D., and Evangelisti, E. (2025). Diversification of DIX domain-containing proteins in the SAR supergroup. *mBio*, 16(5).

[Krut et al., 2024] Krut, V. G., Kalinichenko, A. L., Maltsev, D. I., Jappy, D., Shevchenko, E. K., Podgorny, O. V., and Belousov, V. V. (2024). Optogenetic and chemogenetic approaches for modeling neurological disorders in vivo. *Progress in Neurobiology*, 235.

[Kurihara et al., 2015] Kurihara, D., Mizuta, Y., Sato, Y., and Higashiyama, T. (2015). ClearSee: A rapid optical clearing reagent for whole-plant fluorescence imaging. *Development (Cambridge)*, 142(23):4168–4179.

[Kutschera and Niklas, 2007] Kutschera, U. and Niklas, K. J. (2007). The epidermal-growth-control theory of stem elongation: An old and a new perspective.

[Lampropoulos et al., 2013] Lampropoulos, A., Sutikovic, Z., Wenzl, C., Maegele, I., Lohmann, J. U., and Forner, J. (2013). GreenGate - A novel, versatile, and efficient cloning system for plant transgenesis. *PLoS ONE*, 8(12).

[Lee et al., 2019] Lee, H. W., Cho, C., Pandey, S. K., Park, Y., Kim, M. J., and Kim, J. (2019). LBD16 and LBD18 acting downstream of ARF7 and ARF19 are involved in adventitious root formation in Arabidopsis. *BMC Plant Biology*, 19(1).

[Lee et al., 2025] Lee, L. R., Guillotin, B., Rahni, R., Hutchison, C., Desvoyes, B., Gutierrez, C., and Birnbaum, K. D. (2025). Glutathione accelerates the cell cycle

and cellular reprogramming in plant regeneration. *Developmental Cell*, 60(8):1153–1167.

[Li et al., 2008] Li, H., Chen, Q., Kaller, M., Nellen, W., Gräf, R., and De Lozanne, A. (2008). Dictyostelium Aurora kinase has properties of both Aurora A and Aurora B kinases. *Eukaryotic Cell*, 7(5):894–905.

[Li et al., 2023] Li, J., Szymanski, D. B., and Kim, T. (2023). Probing stress-regulated ordering of the plant cortical microtubule array via a computational approach. *BMC Plant Biology*, 23(1).

[Li and Bowerman, 2010] Li, R. and Bowerman, B. (2010). Symmetry breaking in biology. *Cold Spring Harbor perspectives in biology*, 2(3):1–5.

[Liao and Weijers, 2018] Liao, C. Y. and Weijers, D. (2018). A toolkit for studying cellular reorganization during early embryogenesis in Arabidopsis thaliana. *Plant Journal*, 93(6):963–976.

[Linder and Deschenes, 2007] Linder, M. E. and Deschenes, R. J. (2007). Palmitoylation: Policing protein stability and traffic.

[Louveaux and Boudaoud, 2018] Louveaux, M. and Boudaoud, A. (2018). FibrilTool Batch: an automated version of the ImageJ/Fiji plugin FibrilTool.

[Louveaux et al., 2016] Louveaux, M., Julien, J. D., Mirabet, V., Boudaoud, A., and Hamant, O. (2016). Cell division plane orientation based on tensile stress in Arabidopsis thaliana. *Proceedings of the National Academy of Sciences of the United States of America*, 113(30):E4294–E4303.

[Lu et al., 2025] Lu, C., Li, W., Feng, X., Chen, J., Hu, S., Tan, Y., and Wu, L. (2025). The Dynamic Remodeling of Plant Cell Wall in Response to Heat Stress. *Genes*, 16(6):628.

[Lucas et al., 2013] Lucas, M., Kenobi, K., Von Wangenheim, D., Voß, U., Swarup, K., De Smet, I., Van Damme, D., Lawrence, T., Péret, B., Moscardi, E., Barbeau, D., Godin, C., Salt, D., Guyomarc'h, S., Stelzer, E. H., Maizel, A., Laplaze, L., and Bennett, M. J. (2013). Lateral root morphogenesis is dependent on the mechanical properties of the overlaying tissues. *Proceedings of the National Academy of Sciences of the United States of America*, 110(13):5229–5234.

[Ma et al., 2025] Ma, X., Hasan, M. S., Anjam, M. S., Mahmud, S., Bhattacharyya, S., Vothknecht, U. C., Mendy, B., Grundler, F. M., and Marhavý, P. (2025). Ca2+ waves and ethylene/JA crosstalk orchestrate wound responses in Arabidopsis roots. *EMBO Reports*, 26(12):3187–3203.

[Malamy and Benfey, 1997] Malamy, J. E. and Benfey, P. N. (1997). Organization and cell differentiation in lateral roots of Arabidopsis thaliana. *Development*, 124(1):33–44.

[Malivert et al., 2021] Malivert, A., Erguvan, □., Chevallier, A., Dehem, A., Friaud, R., Liu, M., Martin, M., Peyraud, T., Hamant, O., and Verger, S. (2021). FERONIA and microtubules independently contribute to mechanical integrity in the Arabidopsis shoot. *PLoS Biology*, 19(11).

[Mammoto and Ingber, 2010] Mammoto, T. and Ingber, D. E. (2010). Mechanical control of tissue and organ development. *Development*, 137(9):1407–1420.

[Marhava et al., 2019] Marhava, P., Hoermayer, L., Yoshida, S., Marhavý, P., Benková, E., and Friml, J. (2019). Re-activation of Stem Cell Pathways for Pattern Restoration in Plant Wound Healing. *Cell*, 177(4):957–969.

[Marhavý et al., 2019] Marhavý, P., Kurenda, A., Siddique, S., Dénervaud Tendon, V., Zhou, F., Holbein, J., Hasan, M. S., Grundler, F. M., Farmer, E. E., and Geldner, N. (2019). Single□cell damage elicits regional, nematode□restricting ethylene responses in roots. *The EMBO Journal*, 38(10).

[Marhavý et al., 2016] Marhavý, P., Montesinos, J. C., Abuzeineh, A., Van Damme, D., Vermeer, J. E. M., Duclercq, J., Rakusová, H., Nováková, P., Friml, J. I., Geldner, N., and Benková, E. (2016). Targeted cell elimination reveals an auxin-guided biphasic mode of lateral root initiation. *Genes Dev.*, pages 471–483.

[Marhavý et al., 2013] Marhavý, P., Vanstraelen, M., De Rybel, B., Zhaojun, D., Bennett, M. J., Beeckman, T., and Benková, E. (2013). Auxin reflux between the endodermis and pericycle promotes lateral root initiation. *EMBO Journal*, 32(1):149–158.

[Matsumoto and Ueda, 2024] Matsumoto, H. and Ueda, M. (2024). Polarity establishment in the plant zygote at a glance. *Journal of Cell Science*, 137(5):1–6.

[Maure et al., 2008] Maure, C., Verdoucq, L., Luu, D. T., and Santoni, V. (2008). Plant aquaporins: Membrane channels with multiple integrated functions.

[Melogno et al., 2024] Melogno, I., Takatani, S., Llanos, P., Goncalves, C., Kodera, C., Martin, M., Lionnet, C., Uyttewaal, M., Pastuglia, M., Trehin, C., Bouchez, D., Dumais, J., and Hamant, O. (2024). A transient radial cortical microtubule array primes cell division in Arabidopsis. *Proceedings of the National Academy of Sciences of the United States of America*, 121(29).

[Meyerowitz, 1997] Meyerowitz, E. M. (1997). Genetic control of cell division patterns in developing plants. *Cell*, 88(3):299–308.

[Mhamdi and Van Breusegem, 2018] Mhamdi, A. and Van Breusegem, F. (2018). Reactive oxygen species in plant development. *Development (Cambridge)*, 145(15).

[Michels et al., 2020] Michels, L., Gorelova, V., Harnvanichvech, Y., Borst, J. W., Albada, B., Weijers, D., and Sprakel, J. (2020). Complete microviscosity maps of living plant cells and tissues with a toolbox of targeting mechanoprobes. *Proceedings of the National Academy of Sciences of the United States of America*, 117(30):18110–18118.

[Moore et al., 2006] Moore, I., Samalova, M., and Kurup, S. (2006). Transactivated and chemically inducible gene expression in plants. *Plant Journal*, 45(4):651–683.

[Motta-Mena et al., 2014] Motta-Mena, L. B., Reade, A., Mallory, M. J., Glantz, S., Weiner, O. D., Lynch, K. W., and Gardner, K. H. (2014). An optogenetic gene expression system with rapid activation and deactivation kinetics. *Nature Chemical Biology*, 10(3):196–202.

[Müller et al., 2014] Müller, K., Siegel, D., Rodriguez Jahnke, F., Gerrer, K., Wend, S., Decker, E. L., Reski, R., Weber, W., and Zurbriggen, M. D. (2014). A red light-controlled synthetic gene expression switch for plant systems. *Molecular BioSystems*, 10(7):1679–1688.

[Murashige and Skoog, 1962] Murashige, T. and Skoog, F. (1962). A Revised Medium for Rapid Growth and Bio Assays with Tobacco Tissue Cultures. *Physiologia Plantarum*, 15(3):473–497.

[Nagaya et al., 2010] Nagaya, S., Kawamura, K., Shinmyo, A., and Kato, K. (2010). The HSP terminator of arabidopsis thaliana increases gene expression in plant cells. *Plant and Cell Physiology*, 51(2):328–332.

[Napsucialy-Mendivil et al., 2025] Napsucialy-Mendivil, S., Torres-Martínez, H. H., Rodríguez-Alonso, G., Rivera-Toro, D. M., Alvarez-Venegas, R., Júarez-Verdayes, M. A., Shishkova, S., and Dubrovsky, J. G. (2025). ARABIDOPSIS HOMOLOG OF TRITHORAX1 impacts lateral root development by epigenetic regulation of targets involved in root system architecture. *New Phytologist*.

[Nelson, 2003] Nelson, W. J. (2003). Generating polarity in single cells for mitotic division. *Nature*, 422(6933):766–774.

[Obomighie et al., 2025] Obomighie, I., Prentice, I. J., Lewin-Jones, P., Bachtiger, F., Ramsay, N., Kishi-Itakura, C., Goldberg, M. W., Hawkins, T. J., Sprittles, J. E., Knight, H., and Sosso, G. C. (2025). Understanding pectin cross-linking in plant cell walls. *Communications Biology*, 8(1).

[Ochoa-Fernandez et al., 2020] Ochoa-Fernandez, R., Abel, N. B., Wieland, F. G., Schlegel, J., Koch, L. A., Miller, J. B., Engesser, R., Giuriani, G., Brandl, S. M., Timmer, J., Weber, W., Ott, T., Simon, R., and Zurbriggen, M. D. (2020). Optogenetic control of gene expression in plants in the presence of ambient white light. *Nature Methods*, 17(7):717–725.

[Odell et al., 1985] Odell, J. T., Nagy, F., and Chua, N.-H. (1985). Identification of DNA sequences required for activity of the cauliflower mosaic virus 35S promoter. *Nature*, 313:810–812.

[Pan et al., 2014] Pan, K. Z., Saunders, T. E., Flor-Parra, I., Howard, M., and Chang, F. (2014). Cortical regulation of cell size by a sizer cdr2p. *eLife*, 2014(3):1–24.

[Pasternak et al., 2022] Pasternak, T., Kircher, S., Pérez-Pérez, J. M., and Palme, K. (2022). A simple pipeline for cell cycle kinetic studies in the root apical meristem. *Journal of Experimental Botany*, 73(14):4683–4695.

[Pavelescu et al., 2018] Pavelescu, I., Vilarrasa□Blasi, J., Planas□Riverola, A., González□García, M., Caño□Delgado, A. I., and Ibañes, M. (2018). A Sizer model for cell differentiation in Arabidopsis thaliana root growth . *Molecular Systems Biology*, 14(1).

[Peaucelle et al., 2012] Peaucelle, A., Braybrook, S., and Höfte, H. (2012). Cell wall mechanics and growth control in plants: The role of pectins revisited. *Frontiers in Plant Science*, 3.

[Péret et al., 2012] Péret, B., Li, G., Zhao, J., Band, L. R., Voß, U., Postaire, O., Luu, D. T., Da Ines, O., Casimiro, I., Lucas, M., Wells, D. M., Lazzerini, L., Nacry, P., King, J. R., Jensen, O. E., Schäffner, A. R., Maurel, C., and Bennett, M. J. (2012). Auxin regulates aquaporin function to facilitate lateral root emergence. *Nature Cell Biology*, 14(10):991–998.

[Petersen and Reddien, 2009] Petersen, C. P. and Reddien, P. W. (2009). Wnt Signaling and the Polarity of the Primary Body Axis. *Cell*, 139(6):1056–1068.

[Piepers et al., 2023] Piepers, M., Erbstein, K., Reyes-Hernandez, J., Song, C., Tessi, T., Petrasiunaite, V., Faerber, N., Distel, K., and Maizel, A. (2023). GreenGate 2.0: Backwards compatible addons for assembly of complex transcriptional units and their stacking with GreenGate. *PLoS ONE*, 18(9 September):1–17.

[Pollak et al., 2019] Pollak, B., Matute, T., Nuñez, I., Cerda, A., Lopez, C., Vargas, V., Kan, A., Bielinski, V., Von Dassow, P., Dupont, C. L., and Federici, F. (2019). Universal loop assembly: Open, efficient and cross-kingdom DNA fabrication. *Synthetic Biology*, 5(1).

[Qi and Zhang, 2020] Qi, F. and Zhang, F. (2020). Cell Cycle Regulation in the Plant Response to Stress. *Frontiers in Plant Science*, 10.

[Ramalho et al., 2022a] Ramalho, J. J., Jones, V. A. S., Mutte, S., and Weijers, D. (2022a). Pole position: How plant cells polarize along the axes. *Plant Cell*, 34(1):174–192.

[Ramalho et al., 2022b] Ramalho, J. J., Jones, V. A. S., Mutte, S., and Weijers, D. (2022b). Pole position: How plant cells polarize along the axes. *Plant Cell*, 34(1):174–192.

[Ramos et al., 2024] Ramos, J. R., Reyes-Hernández, B. J., Alim, K., and Maizel, A. (2024). Auxin-mediated stress relaxation in pericycle and endoderm remodeling drives lateral root initiation. *Biophysical Journal*, 124(26).

[Rawat and Laxmi, 2024] Rawat, S. S. and Laxmi, A. (2024). Sugar signals pedal the cell cycle! *Frontiers in Plant Science*, 15.

[Ren et al., 2008] Ren, J., Wen, L., Gao, X., Jin, C., Xue, Y., and Yao, X. (2008). CSS-Palm 2.0: An updated software for palmitoylation sites prediction. *Protein Engineering, Design and Selection*, 21(11):639–644.

[Robert et al., 2013] Robert, H. S., Grones, P., Stepanova, A. N., Robles, L. M., Lokerse, A. S., Alonso, J. M., Weijers, D., and Friml, J. (2013). Local auxin sources orient the apical-basal axis in arabidopsis embryos. *Current Biology*, 23(24):2506–2512.

[Roberts and Oparka, 2003] Roberts, A. G. and Oparka, K. J. (2003). Plasmodesmata and the control of symplastic transport.

[Robinson, 2021] Robinson, S. (2021). Mechanobiology of cell division in plant growth. *New Phytologist*, 231(2):559–564.

[Robinson and Kuhlemeier, 2018] Robinson, S. and Kuhlemeier, C. (2018). Global Compression Reorients Cortical Microtubules in Arabidopsis Hypocotyl Epidermis and Promotes Growth. *Current Biology*, 28(11):1794–1802.

[Roppolo et al., 2011] Roppolo, D., De Rybel, B., Tendon, V. D., Pfister, A., Alassimone, J., Vermeer, J. E., Yamazaki, M., Stierhof, Y. D., Beeckman, T., and Geldner, N. (2011). A novel protein family mediates Casparian strip formation in the endodermis. *Nature*, 473(7347):381–384.

[Roth and Lynch, 2009] Roth, S. and Lynch, J. A. (2009). Symmetry breaking during Drosophila oogenesis. *Cold Spring Harbor perspectives in biology*, 1(2):1–22.

[Sablowski and Gutierrez, 2022] Sablowski, R. and Gutierrez, C. (2022). Cycling in a crowd: Coordination of plant cell division, growth, and cell fate.

[Sampathkumar, 2020] Sampathkumar, A. (2020). Mechanical feedback-loop regulation of morphogenesis in plants. *Development (Cambridge)*, 147(16).

[Sampathkumar et al., 2014] Sampathkumar, A., Krupinski, P., Wightman, R., Milani, P., Berquand, A., Boudaoud, A., Hamant, O., Jönsson, H., and Meyerowitz, E. M. (2014). Subcellular and supracellular mechanical stress prescribes cytoskeleton behavior in Arabidopsis cotyledon pavement cells. *eLife*, 3:1–20.

[Sarrion-Perdigones et al., 2011] Sarrion-Perdigones, A., Falconi, E. E., Zandalinas, S. I., Juárez, P., Fernández-del Carmen, A., Granell, A., and Orzaez, D. (2011). GoldenBraid: An iterative cloning system for standardized assembly of reusable genetic modules. *PLoS ONE*, 6(7).

[Sarrion-Perdigones et al., 2013a] Sarrion-Perdigones, A., Vazquez-Vilar, M., Palací, J., Castelijns, B., Forment, J., Ziarsolo, P., Blanca, J., Granell, A., and Orzaez, D. (2013a). Goldenbraid 2.0: A comprehensive DNA assembly framework for plant synthetic biology. *Plant Physiology*, 162(3):1618–1631.

[Sarrion-Perdigones et al., 2013b] Sarrion-Perdigones, A., Vazquez-Vilar, M., Palací, J., Castelijns, B., Forment, J., Ziarsolo, P., Blanca, J., Granell, A., and Orzaez, D. (2013b). Goldenbraid 2.0: A comprehensive DNA assembly framework for plant synthetic biology. *Plant Physiology*, 162(3):1618–1631.

[Savatin et al., 2014] Savatin, D. V., Gramegna, G., Modesti, V., and Cervone, F. (2014). Wounding in the plant tissue: The defense of a dangerous passage. *Frontiers in Plant Science*, 5(SEP).

[Schütz et al., 2021] Schütz, L. M., Louveaux, M., Vilches Barro, A., Bouziri, S., Cerrone, L., Wolny, A., Kreshuk, A., Hamprecht, F. A., and Maizel, A. (2021). Integration of Cell Growth and Asymmetric Division during Lateral Root Initiation in Arabidopsis thaliana. *Plant and Cell Physiology*, 62(8):1269–1279.

[Schwarz-Romond et al., 2007] Schwarz-Romond, T., Fiedler, M., Shibata, N., Butler, P. J. G., Kikuchi, A., Higuchi, Y., and Bienz, M. (2007). The DIX domain of Dishevelled confers Wnt signaling by dynamic polymerization. *Nature Structural and Molecular Biology*, 14(6):484–492.

[Serrano-Mislata et al., 2015] Serrano-Mislata, A., Schiessl, K., and Sablowski, R. (2015). Active Control of Cell Size Generates Spatial Detail during Plant Organogenesis. *Current Biology*, 25(22):2991–2996.

[Serrano-Ron et al., 2021a] Serrano-Ron, L., Perez-Garcia, P., Sanchez-Corrionero, A., Gude, I., Cabrera, J., Ip, P. L., Birnbaum, K. D., and Moreno-Risueno, M. A. (2021a). Reconstruction of lateral root formation through single-cell RNA sequencing reveals order of tissue initiation. *Molecular Plant*, 14(8):1362–1378.

[Serrano-Ron et al., 2021b] Serrano-Ron, L., Perez-Garcia, P., Sanchez-Corrionero, A., Gude, I., Cabrera, J., Ip, P. L., Birnbaum, K. D., and Moreno-Risueno, M. A. (2021b). Reconstruction of lateral root formation through single-cell RNA sequencing reveals order of tissue initiation. *Molecular Plant*, 14(8):1362–1378.

[Shi et al., 2018] Shi, B., Guo, X., Wang, Y., Xiong, Y., Wang, J., Hayashi, K. i., Lei, J., Zhang, L., and Jiao, Y. (2018). Feedback from Lateral Organs Controls Shoot Apical Meristem Growth by Modulating Auxin Transport. *Developmental Cell*, 44(2):204–216.

[Shimada et al., 2010] Shimada, T. L., Shimada, T., and Hara-Nishimura, I. (2010). A rapid and non-destructive screenable marker, FAST, for identifying transformed seeds of Arabidopsis thaliana: TECHNICAL ADVANCE. *Plant Journal*, 61(3):519–528.

[Shimada et al., 2006] Shimada, Y., Yonemura, S., Ohkura, H., Strutt, D., and Uemura, T. (2006). Polarized transport of Frizzled along the planar microtubule arrays in Drosophila wing epithelium. *Developmental Cell*, 10(2):209–222.

[Smet and Blilou, 2023] Smet, W. and Blilou, I. (2023). A blast from the past: Understanding stem cell specification in plant roots using laser ablation. *Quantitative Plant Biology*, 4.

[Smyth, 1990] Smyth, D. R. (1990). Early Flower Development in Arabidopsis. *the Plant Cell Online*, 2(8):755–767.

[Soni and Bacete, 2023] Soni, N. and Bacete, L. (2023). The interplay between cell wall integrity and cell cycle progression in plants.

[Sparkes et al., 2006] Sparkes, I. A., Runions, J., Kearns, A., and Hawes, C. (2006). Rapid, transient expression of fluorescent fusion proteins in tobacco plants and generation of stably transformed plants. *Nature Protocols*, 1(4):2019–2025.

[St Johnston and Ahringer, 2010] St Johnston, D. and Ahringer, J. (2010). Cell polarity in eggs and epithelia: Parallels and diversity. *Cell*, 141(5):757–774.

[Stanislas et al., 2018] Stanislas, T., Platre, M. P., Liu, M., Rambaud-Lavigne, L. E., Jaillais, Y., and Hamant, O. (2018). A phosphoinositide map at the shoot apical meristem in Arabidopsis thaliana. *BMC Biology*, 16(1).

[Stevenson et al., 2013] Stevenson, J., Krycer, J. R., Phan, L., and Brown, A. J. (2013). A practical comparison of ligation-independent cloning techniques. *PLoS ONE*, 8(12).

[Stöckle et al., 2022] Stöckle, D., Reyes-Hernández, B. J., Barro, A. V., Nenadić, M., Winter, Z., Marc-Martin, S., Bald, L., Ursache, R., Fujita, S., Maizel, A., and Vermeer, J. E. (2022). Microtubule-based perception of mechanical conflicts controls plant organ morphogenesis. *Science Advances*, 8(6):1–19.

[Sunchu and Cabernard, 2020] Sunchu, B. and Cabernard, C. (2020). Principles and mechanisms of asymmetric cell division. *Development (Cambridge)*, 147(13).

[Swarup et al., 2008] Swarup, K., Benková, E., Swarup, R., Casimiro, I., Péret, B., Yang, Y., Parry, G., Nielsen, E., De Smet, I., Vanneste, S., Levesque, M. P., Carrier, D., James, N., Calvo, V., Ljung, K., Kramer, E., Roberts, R., Graham, N., Marillonnet, S., Patel, K., Jones, J. D., Taylor, C. G., Schachtman, D. P., May, S., Sandberg, G., Benfey, P., Friml, J., Kerr, I., Beeckman, T., Laplaze, L., and Bennett, M. J. (2008). The auxin influx carrier LAX3 promotes lateral root emergence. *Nature Cell Biology*, 10(8):946–954.

[Szymanowska-Pułka, 2007] Szymanowska-Pułka, J. (2007). Application of a changing field of growth rates to a description of root apex formation. *Journal of Theoretical Biology*, 247(4):650–656.

[Szymanowska-Pułka et al., 2012] Szymanowska-Pułka, J., Potocka, I., Karczewski, J., Jiang, K., Nakielski, J., and Feldman, L. J. (2012). Principal growth directions in development of the lateral root in Arabidopsis thaliana. *Annals of botany*, 110(2):491–501.

[Takahashi et al., 2021] Takahashi, K., Takahashi, H., Furuichi, T., Toyota, M., Furutani-Seiki, M., Kobayashi, T., Watanabe-Takano, H., Shinohara, M., Numaga-Tomita, T., Sakaue-Sawano, A., Miyawaki, A., and Naruse, K. (2021). Gravity sensing in plant and animal cells.

[Takano et al., 2010] Takano, J., Tanaka, M., Toyoda, A., Miwa, K., Kasai, K., Fuji, K., Onouchi, H., Naito, S., and Fujiwara, T. (2010). Polar localization and degradation of Arabidopsis boron transporters through distinct trafficking pathways. *Proceedings of the National Academy of Sciences of the United States of America*, 107(11):5220–5225.

[Tang et al., 2017] Tang, L. P., Zhou, C., Wang, S. S., Yuan, J., Zhang, X. S., and Su, Y. H. (2017). FUSCA3 interacting with LEAFY COTYLEDON2 controls lateral root formation through regulating YUCCA4 gene expression in Arabidopsis thaliana. *New Phytologist*, 213(4):1740–1754.

[ten Hove et al., 2015] ten Hove, C. A., Lu, K.-J., and Weijers, D. (2015). Building a plant: cell fate specification in the early Arabidopsis embryo. *Development*, 142(3):420–430.

[Tian et al., 2014] Tian, H., Jia, Y., Niu, T., Yu, Q., and Ding, Z. (2014). The key players of the primary root growth and development also function in lateral roots in Arabidopsis. *Plant Cell Reports*, 33(5):745–753.

[Torres-Martínez et al., 2020] Torres-Martínez, H. H., Hernández-Herrera, P., Corkidi, G., and Dubrovsky, J. G. (2020). From one cell to many: Morphogenetic field of lateral root founder cells in Arabidopsis thaliana is built by gradual recruitment. *Proceedings of the National Academy of Sciences of the United States of America*, 117(34):20943–20949.

[Torres-Martínez et al., 2019] Torres-Martínez, H. H., Rodríguez-Alonso, G., Shishkova, S., and Dubrovsky, J. G. (2019). Lateral root primordium morphogenesis in angiosperms. *Frontiers in Plant Science*, 10(March):1–19.

[Trinh et al., 2021] Trinh, D. C., Alonso-Serra, J., Asaoka, M., Colin, L., Cortes, M., Malivert, A., Takatani, S., Zhao, F., Traas, J., Trehin, C., and Hamant, O. (2021). How Mechanical Forces Shape Plant Organs.

[Tsuge et al., 1996] Tsuge, T., Tsukuba, H., and Uchimiya, H. (1996). Two independent and polarized processes of cell elongation regulate leaf blade expansion in Arabidopsis thaliana (L.) Heynh. *Development*, 122:1589–1600.

[Ursache et al., 2018] Ursache, R., Andersen, T. G., Marhavý, P., and Geldner, N. (2018). A protocol for combining fluorescent proteins with histological stains for diverse cell wall components. *Plant Journal*, 93(2):399–412.

[Uyttewaal et al., 2012] Uyttewaal, M., Burian, A., Alim, K., Landrein, B., Borowska-Wykrt, D., Dedieu, A., Peaucelle, A., Ludynia, M., Traas, J., Boudaoud, A., Kwiatkowska, D., and Hamant, O. (2012). Mechanical stress acts via Katanin to amplify differences in growth rate between adjacent cells in Arabidopsis. *Cell*, 149(2):439–451.

[van Damme et al., 2011] van Damme, D., de Rybel, B., Gudesblat, G., Demidov, D., Grunewald, W., de Smet, I., Houben, A., Beeckman, T., and Russinova, E. (2011). Arabidopsis α Aurora kinases function in formative cell division plane orientation. *Plant Cell*, 23(11):4013–4024.

[van Dop, 2018] van Dop, M. (2018). *Function, localization and evolution of SOSEKI polar proteins*. PhD thesis, Wageningen University & Research, Wageningen.

[van Dop et al., 2020] van Dop, M., Fiedler, M., Mutte, S., de Keijzer, J., Olijslager, L., Albrecht, C., Liao, C. Y., Janson, M. E., Bienz, M., and Weijers, D. (2020). DIX Domain Polymerization Drives Assembly of Plant Cell Polarity Complexes. *Cell*, 180(3):427–439.

[Vanneste and Friml, 2009] Vanneste, S. and Friml, J. (2009). Auxin: A Trigger for Change in Plant Development. *Cell*, 136(6):1005–1016.

[Varapparambath et al., 2022] Varapparambath, V., Mathew, M. M., Shanmukhan, A. P., Radhakrishnan, D., Kareem, A., Verma, S., Ramalho, J. J., Manoj, B., Vellandath, A. R., Aiyaz, M., Radha, R. K., Landge, A. N., Mähönen, A. P., Heisler, M. G., Weijers, D., and Prasad, K. (2022). Mechanical conflict caused by a cell-wall-loosening enzyme activates de novo shoot regeneration. *Developmental Cell*, 57(17):2063–2080.

[Varsano et al., 2017] Varsano, G., Wang, Y., and Wu, M. (2017). Probing Mammalian Cell Size Homeostasis by Channel-Assisted Cell Reshaping. *Cell Reports*, 20(2):397–410.

[Vega-Muñoz et al., 2020] Vega-Muñoz, I., Duran-Flores, D., Fernández-Fernández, □. D., Heyman, J., Ritter, A., and Stael, S. (2020). Breaking Bad News: Dynamic Molecular Mechanisms of Wound Response in Plants.

[Vermeer et al., 2014] Vermeer, J. E. M., von Wangenheim, D., Barberon, M., Lee, Y., Stelzer, E. H. K., Maizel, A., and Geldner, N. (2014). A Spatial Accommodation by Neighboring Cells Is Required for Organ Initiation in Arabidopsis. *Science*, 343(6167):178–183.

[Vilches-Barro and Maizel, 2015] Vilches-Barro, A. and Maizel, A. (2015). Talking through walls: Mechanisms of lateral root emergence in Arabidopsis thaliana. *Current Opinion in Plant Biology*, 23:31–38.

[Vilches Barro et al., 2019] Vilches Barro, A., Stöckle, D., Thellmann, M., Ruiz-Duarte, P., Bald, L., Louveaux, M., von Born, P., Denninger, P., Goh, T., Fukaki, H., Vermeer, J. E., and Maizel, A. (2019). Cytoskeleton Dynamics Are Necessary for Early Events of Lateral Root Initiation in Arabidopsis. *Current Biology*, 29(15):2443–2454.

[Voinnet et al., 2003] Voinnet, O., Rivas, S., Mestre, P., and Baulcombe, D. (2003). An enhanced transient expression system in plants based on suppression of gene silencing by the p19 protein of tomato bushy stunt virus. *Plant Journal*, 33(5):949–956.

[Von Wangenheim et al., 2016] Von Wangenheim, D., Fangerau, J., Schmitz, A., Smith, R. S., Leitte, H., Stelzer, E. H., and Maizel, A. (2016). Rules and self-organizing properties of post-embryonic plant organ cell division patterns. *Current Biology*, 26(4):439–449.

[Waadt et al., 2022] Waadt, R., Seller, C. A., Hsu, P. K., Takahashi, Y., Munemasa, S., and Schroeder, J. I. (2022). Plant hormone regulation of abiotic stress responses. *Nature Reviews Molecular Cell Biology*, 23(10):680–694.

[Weber et al., 2011] Weber, E., Engler, C., Gruetzner, R., Werner, S., and Marillonnet, S. (2011). A modular cloning system for standardized assembly of multigene constructs. *PLoS ONE*, 6(2).

[Weijers et al., 2001] Weijers, D., Franke-van Dijk, M., Vencken, R. J., Quint, A., Hooykaas, P., and Offringa, R. (2001). An Arabidopsis minute-like phenotype caused

by a semi-dominant mutation in a RIBOSOMAL PROTEIN S5 gene. *Development*, 128(21):4289–4299.

[Willats et al., 2001] Willats, W. G., Orfila, C., Limberg, G., Buchholt, H. C., Van Alebeek, G. J. W., Voragen, A. G., Marcus, S. E., Christensen, T. M., Mikkelsen, J. D., Murray, B. S., and Knox, J. P. (2001). Modulation of the degree and pattern of methyl-esterification of pectic homogalacturonan in plant cell walls: Implications for pectin methyl esterase action, matrix properties, and cell adhesion. *Journal of Biological Chemistry*, 276(22):19404–19413.

[Willems et al., 2018] Willems, E., Dedobbeleer, M., Digregorio, M., Lombard, A., Lumapat, P. N., and Rogister, B. (2018). The functional diversity of Aurora kinases: A comprehensive review.

[Xiao et al., 2017] Xiao, J., Jin, R., and Wagner, D. (2017). Developmental transitions: Integrating environmental cues with hormonal signaling in the chromatin landscape in plants. *Genome Biology*, 18(1):1–14.

[Yeung et al., 2008] Yeung, T., Gilbert, G. E., Shi, J., Silvius, J., Kapus, A., and Grinstein, S. (2008). Membrane Phosphatidylserine Regulates Surface Charge and Protein Localization. *Science*, 319.

[Yin et al., 2014] Yin, K., Ueda, M., Takagi, H., Kajihara, T., Aki, S. S., Nobusawa, T., Umeda-Hara, C., and Umeda, M. (2014). A dual-color marker system for in vivo Visualization of cell cycle progression in Arabidopsis. *Plant Journal*, 80(3):541–552.

[Yoshida et al., 2019] Yoshida, S., van der Schuren, A., van Dop, M., van Galen, L., Saiga, S., Adibi, M., Möller, B., ten Hove, C. A., Marhavy, P., Smith, R., Friml, J., and Weijers, D. (2019). A SOSEKI-based coordinate system interprets global polarity cues in Arabidopsis.

[Zhang et al., 2022] Zhang, Y., Umeda, M., and Kakimoto, T. (2022). Pericycle cell division competence underlies various developmental programs.

[Zhao et al., 2018] Zhao, F., Chen, W., and Traas, J. (2018). Mechanical signaling in plant morphogenesis. *Current Opinion in Genetics and Development*, 51:26–30.